Tampere University

MUHAMMAD ZEESHAN WAHEED

Passive Intermodulation Distortion in Radio Communication Systems

Signal Models and Digital Cancellation

Tampere University Dissertations 1050

Tampere University Dissertations 1050

MUHAMMAD ZEESHAN WAHEED

Passive Intermodulation Distortion in Radio Communication Systems

Signal Models and Digital Cancellation

ACADEMIC DISSERTATION
To be presented, with the permission of
The Faculty of Information Technology and Communication Sciences
of Tampere University,
for public discussion in the auditorium TB 109,
of the Tietotalo, Korkeakoulunkatu 1, Tampere,
on 30th of August, 2024, at 12 o'clock.

ACADEMIC DISSERTATION

Tampere University, Faculty of Information Technology and Communication Sciences
Finland

Responsible supervisor and Custos	Professor Mikko Valkama Tampere University Finland	
Supervisors	Dr. Lauri Anttila Tampere University Finland	Dr. Adnan Qamar Kiayani Tampere University Finland
Pre-examiners	Professor Mario Huemer Johannes Kepler University Linz Austria	Professor Alexios Balatsoukas-Stimming Eindhoven University of Technology Netherlands
Opponent	Professor Timo Rahkonen University of Oulu Finland	

The originality of this thesis has been checked using the Turnitin OriginalityCheck service.

Cover design: Roihu Inc.

ISBN 978-952-03-3510-6 (print)
ISBN 978-952-03-3511-3 (pdf)
ISSN 2489-9860 (print)
ISSN 2490-0028 (pdf)
http://urn.fi/URN:ISBN:978-952-03-3511-3

Carbon dioxide emissions from printing Tampere University dissertations have been compensated.

PunaMusta Oy – Yliopistopaino
Joensuu 2024

To my parents Waheed and Rafia.

ABSTRACT

Cellular networks and technology have evolved substantially since the late 1970s, with successive generations bringing a variety of new features. Each upcoming generation is better and more advanced in technology when compared to the previous generation. To this end, a huge amount of research in the field of wireless communications has been dedicated to the following two major aspects: the increasing demand for user data rate requirements and the exponential growth of internet-dependent devices around the world. It is undeniable that the outcome of this phenomenon is a heavy congestion of the available spectral resources. This has inspired the utilization of many innovative solutions for improving the spectral efficiency in wireless communication systems by facilitating simultaneous transmission at a high data rate without having the need for additional spectrum. Some of these technologies include in-phase/quadrature (I/Q) modulation, multiple-input-multiple-output (MIMO) systems, and orthogonal frequency-division multiplexing (OFDM). In part because of these existing solutions, the spectral efficiency of wireless communication has improved considerably. However, more advanced techniques are necessary if future data transfer requirements are to be met, for example in the sub-6 GHz band. Given this, the frequency division duplex (FDD) in Long Term Evolution-Advanced (LTE-Advanced) has suggested carrier aggregation (CA) technology as another step towards the better utilization of the spectral resources. The CA techniques enable the utilization of multiple con-

tiguous or noncontiguous parts of the spectrum, thus allowing for flexibility in transmission bandwidth. By using CA, spectral resources can be combined from the same operating frequency band (intraband CA) or from multiple frequency bands (interband CA). In CA, multiple transmitters and receivers are integrated into a single chip to reduce costs, space, and power consumption. Additionally, the industry is moving towards low-cost radio frequency (RF)-front-end solutions containing duplex filters with limited isolation capabilities in order to cope with ever-increasing CA combinations. This results in the leakage of the own transmit (TX) signal and other so-called blocker signals. One of the challenges in the utilization of the CA is when the combined noncontiguous signal propagates through the TX chain passing through the RF front-end passive components, the cross-modulation of the transmitted signal further creates unwanted passive intermodulation (PIM) products. These PIM products in some cases may fall onto their own receiver (RX) band and may cause receiver desensitization.

In this thesis, we present novel solutions for modeling and suppressing PIM distortion and passive harmonic distortion (PHM) in FDD based radio transceivers. This distortion results from nonlinear RF components and simultaneous transmission and reception, with a particular focus on modern carrier aggregation networks. PIM-induced distortion terms generally have a higher power than the weak received signal, even with state-of-the-art RF components, because of the linearity characteristics of the passive components. Consequently, it is necessary to minimize the harmful impact of such distortion, which can be achieved by taking a variety of approaches. A simple technique can be to decrease the transmit power or relax the receiver reference sensitivity requirements. This is known as maximum power reduction (MPR) and maximum sensitivity degradation (MSD), respectively, for LTE-Advanced and new radio (NR) user equipment (UEs).

In addition to preventing receiver desensitization, these approaches will negatively affect coverage, so they are not very appealing. Uplink (UL) and downlink (DL) resource allocation and scheduling can also be optimized to avoid in-band distortion. This approach, however, will be very complex, and could also result in reduced peak throughput and spectrum utilization. The PIM/PHM distortion power can, however, be controlled by improving RF component qual-

ity and isolation. Nevertheless, this solution has the drawback of increasing the overall cost of the device. In addition, even with the more expensive components PIM-induced distortion might not be avoided. In this thesis, we take an alternative approach by using the original transmit data as a reference to cancel such PIM in the transceiver digital front-end. For the generation of an accurate cancellation signal, we derive different advanced signal models for the observable intermodulation distortion in the receiver band that incorporate also power amplifier nonlinearities, together with the passive component nonlinearities and the frequency-selective responses of the duplex filters. Real-life RF measurements are conducted with an actual LTE-Advanced user equipment (UE) transceiver system to evaluate the performance and processing complexity of the devised digital cancellation and parameter estimation solutions. The experiments show that PIM-induced self-interference is almost 20 dB above the noise floor even while utilizing state-of-the-art RF components. However, the results show that each of the proposed signal models and the related digital cancellers in this thesis are able to cancel the PIM-induced interference up to 15 dB. The results also indicate that in many cases it is necessary to account for nonlinear distortions caused by amplifiers. This is even if the individual component carriers are combined after the amplification stage. In general, when the nonlinear distortion of the power amplifiers is taken into account the amount of cancellation is further improved by 4-5 dB, in contrast to the linear power amplifier based cancellers.

PREFACE

This thesis is based on research work carried out during the years 2017-2022 in the Department of Electrical Engineering, Tampere University, Tampere, Finland. Ph.D. studies and research is a long and tiring journey but there are many people that I am thankful to who helped me and guided me throughout this journey.

First and foremost, I am grateful to my supervisor Prof. Mikko Valkama for providing me with such a fascinating thesis topic. I am also grateful for the opportunity to be a part of his research group. His hard work, dedication, and expertise have inspired me and motivated me to complete this thesis under his supervision. I must also express my sincere gratitude to my thesis co-supervisors, Dr. Lauri Anttila and Dr. Adnan Kiayani for their time, guidance and all the support during the thesis work. All the things I learned from them proved useful to me throughout my career. I would also like to thank Dr. Dani Korpi for his initial guidance and support during my Ph.D. studies.

I wish to thank Tampere University for providing an excellent environment and support for students to carry out their research work.

In addition, I wish to thank also my numerous co-workers in our research group. As a result of our fruitful and friendly discussions, I was able to accomplish a great deal and overcome many challenges thanks to Matias Turunen, Pablo Pascual Campo, Alberto Brihuega Garcia, and Vesa Lampu.

Furthermore, I would like to thank all the people I have been working with at

Nokia for their trust in me. I am grateful for their support in every way possible. Special thanks to Joose Tamminen, Aleksi Jokela, and Jussi Kilpeläinen for having wonderful coffee breaks every afternoon and listening to me whenever needed.

At the end I would like to thank my parents and family, especially my mom and dad for their continuous support and love throughout my life. In addition, I would like to thank Stanley Mwangi, Ihtisham Ali, and especially Fahad Sohrab for their continuous support. Thank you!

Tampere, June, 2024.
Muhammad Zeeshan Waheed

TABLE OF CONTENTS

LIST OF ABBREVIATIONS

3G	Third generation
3GPP	Third-Generation Partnership Project
4G	Fourth generation
5G	Fifth generation
5GC	Fifth generation core network
6G	Sixth generation
ACLR	Adjacent channel leakage ratio
ADC	Analog-to-digital converter
BW	Bandwidth
CA	Carrier aggregation
CC	Component carrier
CF	Carrier Frequency
CFs	Carrier Frequencies
CP	Cyclic prefix
CP-OFDM	Cyclic prefix orthogonal frequency-division multiplexing
DC	Direct current

DCR	Direct Conversion Receiver
DFE	Digital front-end
DFT-s-OFDM	Discrete Fourier transform single-carrier OFDM
DL	Downlink
DPD	Digital predistortion
DSS	Dynamic spectrum sharing
eMBB	Enhanced mobile broadband
ET	Electro-thermal
EVM	Error vector magnitude
FDD	Frequency-division duplexing
FFT	Fast Fourier transform
FR1	Frequency range 1
FR2	Frequency range 2
GHz	Gigahertz
gNB	5G node B
gNB-CU	gNB central unit
gNB-DU	gNB Distributed Unit
I-V	Current-Voltage
I/Q	In-phase/Quadrature
IF	Intermediate frequency
IIoT	Industrial in- ternet of things
IM	Intermodulation
IM3	Third-order intermodulation
IMD	Intermodulation distortion
IMT-2020	International mobile telecommunication 2020
IP3	Third-order intercept point
ISI	Inter symbol interference

ITU	international telecommunication union
ITU-R	ITU radio-communication Sector
LMS	Least mean squares
LO	Local Oscillator
LS	Least squares
LTE	Long-term evolution
MAC	Medium access control
MIM	Metal-insulator-metal
MIMO	Multiple-input-multiple-output
MM	Metal-metal
mMIMO	Massive multiple-input-multiple-output
mMTC	Massive machine type communications
MPR	Maximum power reduction
MSD	Maximum sensitivty degradation
NI	National Instrument
NR	New radio
NSA	Non-standalone
NTL	Nonlinear transmission line
NTN	Non-terrestrial network
OFDM	orthogonal frequency-division multiplexing
OOB	Out-of-band
PA	Power amplifier
PAPR	Peak-to-average power ratio
PAs	Power amplifiers
PDCP	Packet data convergence protocol
PHM	Passive harmonic distortion
PIM	Passive intermodulation

PO	Physical-optics
PRB	Physical resource block
PSDs	Power spectral densities
QPSK	Quadrature phase-shift keying
RAN	Radio access network
RedCap	Reduced capability
RF	Radio Frequency
RX	Receiver
SA	Standalone
SBFD	subband full duplex
SC-FDMA	single carrier frequency division multiple access
SCS	Subcarrier spacing
SCSs	Subcarrier spacings
SDAP	Service data adaptation protocol
SI	Self-interference
SINR	signal-to-interference-plus-noise ratio
SNR	signal-to-noise ratio
SoI	Signal-of-interest
TDD	Time-division duplexing
TDM	Time division duplexing
TDPO	Time domain physical-optics
TX	Transmitter
UE	User equipment
UHF	Ultra high frequency
UL	Uplink
URLLC	Ultra-reliable-low-latency-communications
V2X	Vehicle to anything

VST	Vector Signal transceiver

LIST OF PUBLICATIONS

Publication I M. Z. Waheed, D. Korpi, A. Kiayani, L. Anttila and M. Valkama. Digital self-interference cancellation in inter-band carrier aggregation transceivers: Algorithm and digital implementation perspectives. In: *2017 IEEE International Workshop on Signal Processing Systems (SiPS), Lorient, France* (2017), 1–5. DOI: 10.1109/SiPS.2017.8109983.

Publication II M. Z. Waheed, P. P. Campo, D. Korpi, A. Kiayani, L. Anttila and M. Valkama. Digital Cancellation of Passive Intermodulation in FDD Transceivers. In: *2018 52nd Asilomar Conference on Signals, Systems, and Computers* (2018), 1375–1381. DOI: 10.1109/ACSSC.2018.8645262.

Publication III M. Z. Waheed, D. Korpi, A. Kiayani, L. Anttila and M. Valkama. Digital Cancellation of Passive Intermodulation: Method, Complexity and Measurements. In: *2019 IEEE MTT-S International Microwave Conference on Hardware and Systems for 5G and Beyond (IMC-5G)* (2019), 1–3. DOI: 10.1109/IMC-5G47857.2019.9160361.

Publication IV M. Z. Waheed, D. Korpi, L. Anttila, A. Kiayani, M. Kosunen, K. Stadius, P. P. Campo, M. Turunen, M. Allén, J. Ryynänen

and M. Valkama. Passive Intermodulation in Simultaneous Transmit–Receive Systems: Modeling and Digital Cancellation Methods. In: *IEEE Transactions on Microwave Theory and Techniques* 68.9 (2020), 3633–3652. DOI: 10.1109/TMTT.2020.2996206.

Publication V M. Z. Waheed, V. Lampu, A. Kiayani, M. Fleischer, L. Anttila and M. Valkama. Modeling and Digital Suppression of Passive Nonlinear Distortion in Simultaneous Transmit–Receive Systems. In: *2022 56th Asilomar Conference on Signals, Systems, and Computers* (2022). DOI: 10.1109/IEEECONF56349.2022.10051880.

Author's contribution

This dissertation is a compound thesis with a summary of above listed five publications together with a literature review. The author and co-authors contributions are as following:

Publication I The research topic for developing digital cancellation solutions for passive intermodulation distortion was proposed by Prof. Mikko Valkama and Dr. Adnan Kiayani. This idea was built on top of the earlier works on digital mitigation of transmitter-induced desensitization in [46, 47]. The analysis, signal models, and the algorithm were developed by the author with support of Dr. Dani Korpi. The writing of the conference paper was a joint effort of the author and Dr. Adnan Kiayani, while Dr. Lauri Anttila and Prof. Mikko Valkama reviewed the final results and also helped with final publication preparation.

Publication II The issue of PIM interference coupling over the air was identified in [**Publication-I**], thus this publication built on the previous results. The RF measurements were performed by the author with support of Dr. Dani Korpi, while the results were jointly reviewed by all authors. The publication script

was written jointly by the author and Dr. Adnan Kiayani, but other authors naturally contributed to its preparation.

Publication III — The work in this publication focused on the complexity analysis of the suggested digital cancellation solution. The idea of the decoupled memory-based model was proposed by Dr. Dani Korpi while the author performed analysis, as well as carried out the simulation and the measurements. All authors contributed equally in preparation of the manuscript, while Dr. Lauri Anttila and Prof. Mikko Valkama contributed to reviewing and improving the final document.

Publication IV — The work in this publication builds on top of [**Publications I-IV**] and extensively studies the problem of passive intermodulation distortion. The signal models were a result of the joint efforts between the author and Dr. Dani Korpi and Dr. Adnan Kiayani. Moreover, the manuscript was extensively revised and improved based on the reviewers' comments. The author performed all the reported simulation and measurements with support of Dr. Adnan Kiayani, and prepared the journal manuscript together with all authors. Finally, Dr. Lauri Anttila and Prof. Mikko Valkama reviewed the paper and also helped extensively on preparing the final camera ready version of the paper. This version addresses all the comments and changes proposed by the reviewers.

Publication V — The idea of digital cancellation of passive harmonic distortion was originally proposed by Dr. Lauri Anttila. Under the supervision of Dr. Adnan Kiayani, the author and M.Sc Vesa Lampu developed the signal models and carried out the measurements for RF. The author then evaluated the data with the developed digital cancellation methods and confirmed the performance of the cancellers. Dr. Lauri Anttila and Prof. Mikko Valkama reviewed the final paper and also suggested final changes before submission.

CHAPTER 1

INTRODUCTION

1.1 Background and Thesis Motivation

DRIVEN by evolving services and applications there has been a significant increase in the amount of data that is being shared wirelessly over the past decades. As technology advances, an increasing amount of information is transferred over-the-air each day, demanding an increase in the efficiency of wireless communications systems in every aspect. There is, however, a physical limit to the amount of information that can be transferred over radio waves. Therefore, it is imminent that in the future, existing technologies will not be sufficient to satisfy the ever-increasing demand for wireless data transfer requirements. Ultimately, a time will come when the available spectrum has been used as efficiently as physically possible. Only a truly radical solution will be needed to maximize spectrum usability efficiently. Given that, the currently implemented systems are already unable to meet the desired data rate targets specified for the future fifth generation (5G) networks, mainly because of the congestion of the radio spectrum [6, 58, 68]. This is due to the fact that the spectrum in the sub-6GHz band is the most suitable one for radio transmission because of its better coverage properties. However, this also makes the sub-6GHz spectrum the most crowded and hence cannot fulfil the continuous requirement of

data growth. Thus, to meet the demands of increased data speed while simultaneously better utilizing the existing spectrum resources and overcoming the scarcity of the electromagnetic spectrum to meet the wireless data transfer demands of modern society, new and innovative technologies must be developed [38, 77, 85].

To this end, several techniques and solutions have been proposed, namely the employment of the massive multiple-input-multiple-output (mMIMO) technology, where the number of antennas could be increased by tens or even hundreds [11, 17, 18, 64, 84] or alternatively, a higher centre frequency can be utilized for communicating where the bandwidth is abundant for the time being [14, 15, 29, 83, 104]. Enhanced spectral efficiency and higher data rates are indeed possible with these methods that require operation in the milli-meter frequency band where radio design presents unique challenges, meanwhile, there is another fundamental approach to realize increased data rate and capacity where wider transmission bandwidths can be utilized by aggregating spectral resources from multiple frequency channels or bands simultaneously [26, 72]. Third-generation Partnership Projects (3GPP) introduced this technique in Release 10, also known as (LTE)-Advanced [41], also supported on 5G new radio (NR) and later [70]. The carrier aggregation (CA) technique enables simultaneous transmission and reception over several contiguous or noncontiguous parts of the spectrum. As a result, the overall transmission bandwidth can be expanded flexibly. CA allows combining the spectral resources from either the same operating frequency band (intraband CA) or from multiple frequency bands (interband CA). The user equipment (UE) can also be connected to both LTE and NR cells at a time, commonly known as LTE-NR dual connectivity, and thus, having the ability to transmit and receive data at the same time. The dual connectivity also helps operators improve mobility robustness and handovers in macro/micro-cell deployments [59, 82].

An interband CA transmits signals at two or more LTE or NR bands at the same time, with signals transmitted at each band referred to as component carriers (CC) [26, 70]. Given the deployment scenarios, the CA can be further categorized as CA among low-band (< 1 GHz) and high-band (> 1 GHz) carrier frequencies, known as LB-HB CA, and CA among more similar frequencies, known as LB-LB CA or HB-HB CA. Furthermore, in 5G NR, CA can be

utilized at both FR1 (below 6-GHz bands) and FR2 (millimeter-wave bands) [82]. Fig. 1.1 shows an illustrative example of CA in frequency division duplex (FDD) with contiguous and noncontiguous inter and intraband CA.

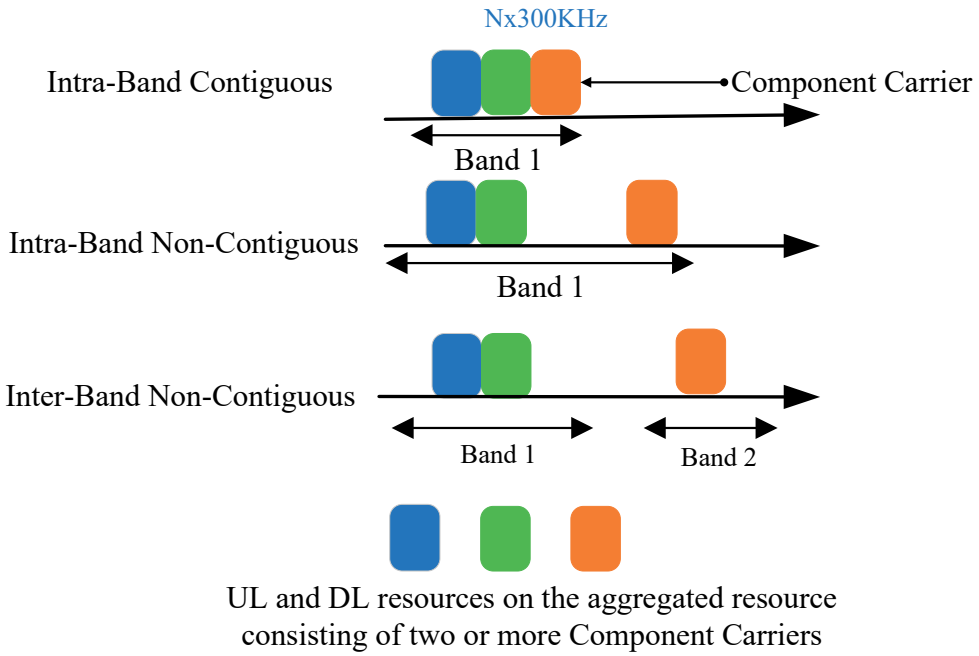

Figure 1.1 Carrier aggregation in FDD, with interband and intraband carrier aggregation alternatives.

The CA technique enables the operators to expand the overall transmission bandwidth flexibly, however, the increasing number of CA frequency band combinations poses a variety of practical implementation-related challenges for the radio frequency (RF) front-end design and implementation, which must also now support several RF paths concurrently [16, 47, 100]. One of the challenges from the undesired emission point of view is the nonlinear distortion in the transmitter (TX) power amplifier (PA), which typically leads to spectral regrowth around the CCs when each of the CC is amplified separately by each PA [16]. However, when the combined noncontiguous signal propagates through the TX chain passing through the RF front-end passive components, the cross-modulation of the transmitted signal further creates unwanted passive intermodulation (PIM) products. PIM can create interference that will

negatively affect receiver sensitivity and even block calls in some cases. This interference not only affects the cell in question but can also affect the other nearby cells. This makes PIM a serious issue for the network operators that want to increase their network reliability and data rate capacity [16, 22, 43, 60, 70, 88].

The physical factors that can cause PIM can be several, such as the passive components present in the radio unit front-end that typically includes for example, connectors, switches, duplexer filters, the cable assembly and even rusty metallic objects in the antenna near field [34, 35, 43, 98]. The PIM that is generated as a result of the presence of rusty metallic objects in the antenna near the field is referred to as the "rusty-bolt effect" which not only affects its own operating cell but also the neighbouring cells on the same site [51]. The generated PIM products are located at specific intermodulation (IM) subbands, which are in fact the integer linear combinations of the CCs center frequencies, which depending on the LTE or NR band combinations or frequency co-allocation may fall into the RX operating band [46, 60, 62, 79, 101]. This phenomenon is illustrated in Fig. 1.2 as an example, where the third-order IM (IM3) falls within the DL frequencies of band B1 when 3GPP-specified interband CA of Band 1 (1920 - 1980 MHz) and Band 3 (1710 - 1785 MHz) is used.

Other band combinations which are prone to similar problems are, e.g., B3+B8, B2+B4, and B5+B7. The PIM is generated after the duplexer TX filter, meaning it only experiences the insertion loss of the duplexer RX filter. The signal, which is substantially stronger than the desired weak received signal, therefore, may directly go into the RX causing self-interference (SI) that could lead to RX desensitization. Furthermore, the PIM can also couple over the air into the RX band causing SI. The generation of PIM in the uplink band results in the increased noise floor which in turn may lead to throughput degradation and poor end-user experience. This problem is expected to become a serious issue in the future with the introduction of several new band combinations.

In recent years, several 3GPP studies have identified this problem for many LTE/NR band combinations in interband CA [1, 26, 80] and at the same time provided some solutions to tackle the problem of PIM. These solutions include for example, decreasing the transmit power or alternatively easing the RX reference sensitivity requirements, known as the maximum power reduction (MPR)

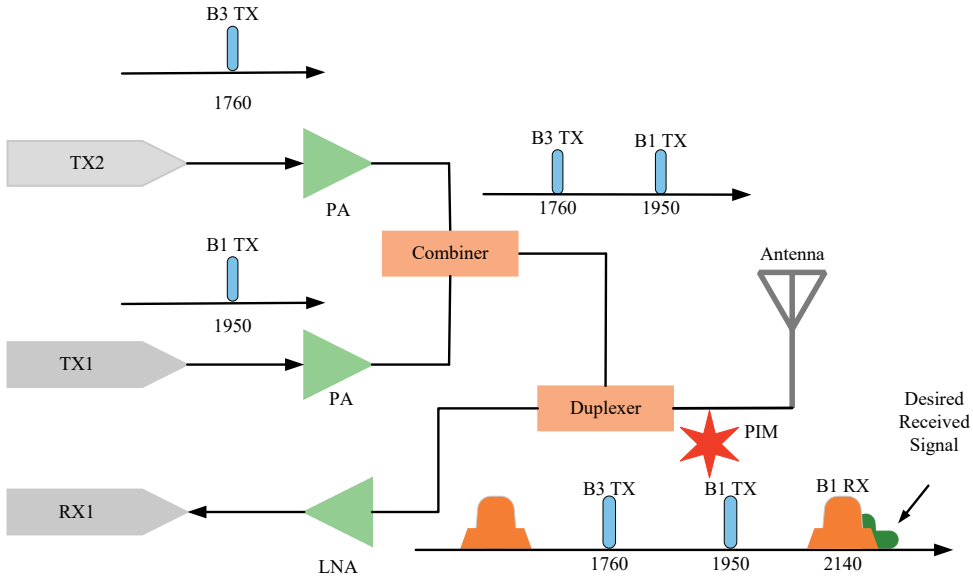

Figure 1.2 Spectral illustration of the undesired PIM products with interband CA of Band 1 and Band 3. In this example, some of the internal PIM products hit the Band 1 receiver.

and maximum sensitivty degredation (MSD), respectively when referring to LTE-Advanced and NR UEs [2, 24, 81]. These solutions may prevent the receiver desensitization but will negatively impact the link budget performance and are thus not very appealing. Another solution to avoid PIM in practice is by ensuring proper frequency planning. However, such planning is almost impractical with the growing number of configured bands on the same radio or on a site where FDD or time-division duplexing (TDD) radios are co-located. Yet, another solution to reduce the power of SI would be to use highly linear RF components with good isolation but the drawback of such a solution is that it would increase the cost of the devices significantly. Given these facts, an appealing solution would be to develop and deploy a digital cancellation algorithm that exploits the deterministic nature of the SI to model and suppress it in the digital front end (DFE).

1.2 Thesis Scope

Radio interference mitigation is a well-known area and is an active research field. The scope of this thesis is to present advanced digital cancellation solutions to suppress the PIM in FDD-based transceivers originating from the passive nonlinear RF components and simultaneous transmission and reception, with a focus on the modern CA transmission. The PIM and passive harmonic distortion (PHM) resulting over-the-air because of the presence of metallic objects in the antenna near the field are also briefly discussed. As discussed above, with certain band combinations e.g., LTE-Advanced and 5G NR mobile radio systems, the resulting PIM can fall onto one of the configured RX band and thus block the desired RX signal. Compared to traditional solutions to this problem such as reducing the transmit power which may affect the link budget performance we develop novel digital cancellation solutions where a replica of the interference is created from the known TX data and is then subtracted from the original interference at the RX end to cancel it out. The benefit of such solutions is that the interference signal can be modelled with great accuracy taking into account the PAs and the passive components' nonlinear characteristics and also the frequency-selective response of the duplex filters.

As we will discuss further in Chapter 4, in this thesis comprehensive behavioural models of the observable PIM waveform that incorporates the joint effects of the combined nonlinearities of PAs and the passive RF front-end components are considered. The substantial filtering or memory effects of the duplexer filter or the RF front-end components are also taken into consideration. PIM can also arise over-the-air or at fundamental harmonic frequencies called PHM distortion which in some cases may fall onto the RX band of a co-located radio and hence modelling of such scenarios is also considered, where a multiple-input-multiple-output (MIMO) antenna setup is adapted [35, 51]. To further facilitate the actual digital cancellation, efficient parameter estimation methods are also derived which are built on top of the derived PIM signal models. These include, e.g., least-squares (LS) or least-mean-squares (LMS). The performance of the proposed cancellation methods is further evaluated with actual real-life RF measurements, utilizing actual NR signals and

LTE-Advanced/NR UE. The obtained results indicate excellent suppression of PIM under realistic scenarios while maintaining acceptable computational complexity from a hardware implementation perspective. To this end, the proposed digital cancellation solutions can suppress PIM, without affecting the RF components' linearity requirements, maintaining the RX sensitivity while also keeping the cost and maintenance at a minimum. Furthermore, the developed advanced digital cancellation solutions can further enable new frequency band combinations, which may have been otherwise avoided because of the SI challenge [**Publication I, Publication II, Publication III, Publication IV, Publication V**].

To achieve the goals that are mentioned above, this thesis attempts to provide an answer to the following research questions:

- RQ1. What kind of benefit do the proposed digital cancellation solutions offer over the traditional methods such as reducing the TX power or relaxing the reference sensitivity requirements, MPR and MSD respectively?
- RQ2. The resulting PIM stems from the nonlinear components in the TX chain such as PAs and the passive components and undergoes the frequency-selective response of the duplexer filter. How accurate are the developed signal models that mimic the SI and what is the computational complexity of the proposed parameter estimation methods and the cancellation solutions?
- RQ3. How easy it is to implement the proposed digital cancellation solutions in practice and whether they can perform efficiently in complex scenarios such as mMIMO communication systems?

1.3 Thesis Contribution and Structure

The main contributions of this thesis are deriving a nonlinear signal model for the PIM induced SI, which results from the cascaded nonlinearity of the PAs and the passive components present in the RF front-end [**Publication I**]. Building on that, while now taking into account the PA memory effects, the suggested digital cancellation solutions are evaluated with real-life RF measurements. This is to provide evidence of the performance of the proposed cancella-

tion method in [**Publication II**]. Furthermore, the computational complexity of the proposed solutions is evaluated and a novel reduced-complexity digital PIM cancellation solution along with self-orthogonalizing decoupled parameter learning rules are presented [**Publication III**]. [**Publication IV**], builds on [**Publication I, Publication II, Publication III**] and presents more advanced PIM induced SI models. This is combined with computational complexity analysis and detailed RF measurement results for the developed signal models and digital cancellation methods suggested. Finally, [**Publication V**] focuses on PHM distortion while considering a MIMO scenario, shedding light briefly on the fact that in addition to PIM, PHM is also an issue that needs to be addressed, especially in co-located scenarios with special band combinations such as FDD/TDD. We further explore this in [**Publication V**] where we consider a co-located scenario in which one radio transmits on Band 3 FDD and another radio receives on Band 78 TDD, with harmonic distortions from Band 3 FDD falling onto Band 78 TDD RX.

The articles comprising this thesis [**Publication I-V**] have been grouped together and presented as a summary in Chapter 4, and Chapter 5 of this thesis. Chapter 3, sheds light on the PIM problem in general in modern radio systems and finally chapter 6 concludes the thesis.

CHAPTER 2

NEW RADIO PHYSICAL LAYER OVERVIEW AND CHALLENGES

The 3GPP project, completed its studies on 5G mobile communications in its Release - 15 in June 2018 and thus laid the foundation of the commercial 5G deployment worldwide [56]. The 3GPP NR is a unified, adaptable air interface that supports three categories of the 5G mobile communications as defined by the International Telecommunication Union (ITU), i.e., enhanced mobile broadband (eMBB), massive machine-type communications (mMTC), and ultra-reliable low-latency communications (URLLC).

In this chapter, we give a basic overview of the 3GPP NR. We also discuss, e.g., the 5G NR frame structure, physical layer characteristics such as waveforms and numerology. Furthermore, we discuss the evolution of the CA technology in cellular networks and some basic principles. Last but not least, we also briefly discuss the transmit signal leakage problems in FDD transceivers.

2.1 An Overview of the 3GPP New Radio

3GPP plays a key role in almost once-in-every-decade progression of cellular networks technology, since the very first phase of the mobile standards in the

1980's. Each generation harvests improvements from the previous generation and is divided as 3GPP releases. Fig. 2.1 shows the 3GPP's evolution roadmap from 5G (Release 15) to 5G-Advanced (Release 18).

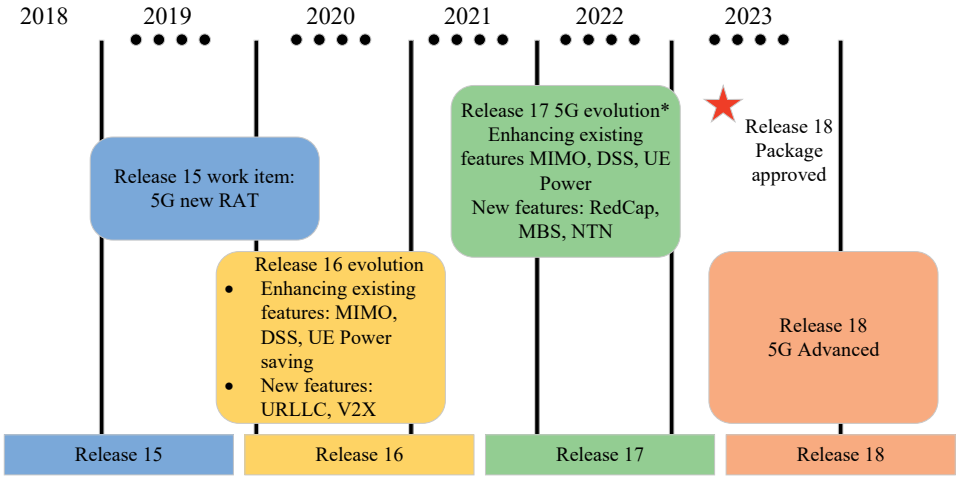

Figure 2.1 3GPP's 5G technology evolution roadmap from 5G to 5G advanced.

3GPP provided a new 5G air interface in its Release 15, known as NR, where the main focus was to address a variety of usage scenarios such as eMBB, URLLC and mMTC [3, 23, 55, 67]. NR supports both non-standalone (NSA) as well as standalone (SA) operation. In NSA mode, NR utilizes LTE for initial access and handling, while in SA model NR does not rely on LTE. Other key features of NR include low latency, flexible spectrum and high-frequency operations, among others [25]. 3GPP continues the journey towards 5G evolution in Release 16, where several significant enhancements are introduced. These enhancements not only improve existing features but also define new use cases and deployment scenarios. Some of the key improvements made to existing features include beam forming enhancements, MIMO, enhanced dynamic spectrum sharing (DSS), CA and UE power saving. Release 16 also addresses some novel use cases and deployment scenarios such as enhanced industrial internet of things (IIoT), operations in unlicensed spectrum and vehicle to anything (V2X) communication. The functionalities proposed in NR Release 15 and 16 were submitted by 3GPP to IMT-2020 and were approved by the International Telecommunication Union radio-communication Sector (ITU-R) in 2020.

3GPP continues NR evolution in Release 17 and 18. The existing features such as, DSS, MIMO, and URLLC are further enhanced. Release 17 further introduces novel use cases and deployment scenarios, including reduced capability (RedCap) UE and non-terrestrial networks (NTN). 3GPP approved the Release 18 (5G-Advanced) package in December 2021, radio access network (RAN) plenary meeting [90]. Several study items were proposed in this package which will further boost network performance and address novel use cases.

Illustratively, the NR 5G system uses the same elements as the previous generations, i.e., a UE, RAN, and a 5G core network (5GC) as shown in Fig. 2.2.

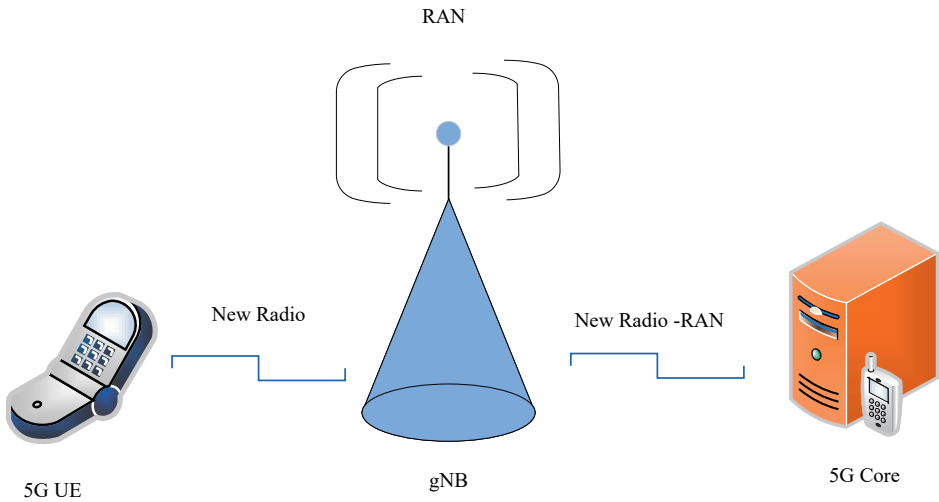

Figure 2.2 An overview of the 5G system.

The main component is the "gNB" where the "g" stands for 5G and "NB" for node B. Node B is used for the radio transceiver since the third generation (3G) and onwards. The gNB can be further split into the gNB-central unit (gNB-CU) and gNB-distributed unit (gNB-DU). The gNB-CU provides support for the higher layers of the protocol stack such as service data adaptation protocol (SDAP), and packet data convergence protocol (PDCP) while DU provides support for the lower layers of the protocol stack such as medium access control (MAC) and physical layer [56]. The 5G UE is a medium of access for the end

user to utilize the network services, while the 5G core establishes a reliable and secure connection to the network for end users and provides access to its services.

2.1.1 5G NR Waveform and Numerology

5G NR DL radio access is achieved via a specific version of orthogonal frequency-division multiplexing (OFDM) called the cyclic prefix orthogonal frequency-division multiplexing (CP-OFDM). CP-OFDM is a multicarrier and multiple access transmission scheme, where the overall bandwidth is divided into narrow bandwidth subcarriers which are orthogonal to each other and carry data as illustrated in Fig. 2.3.

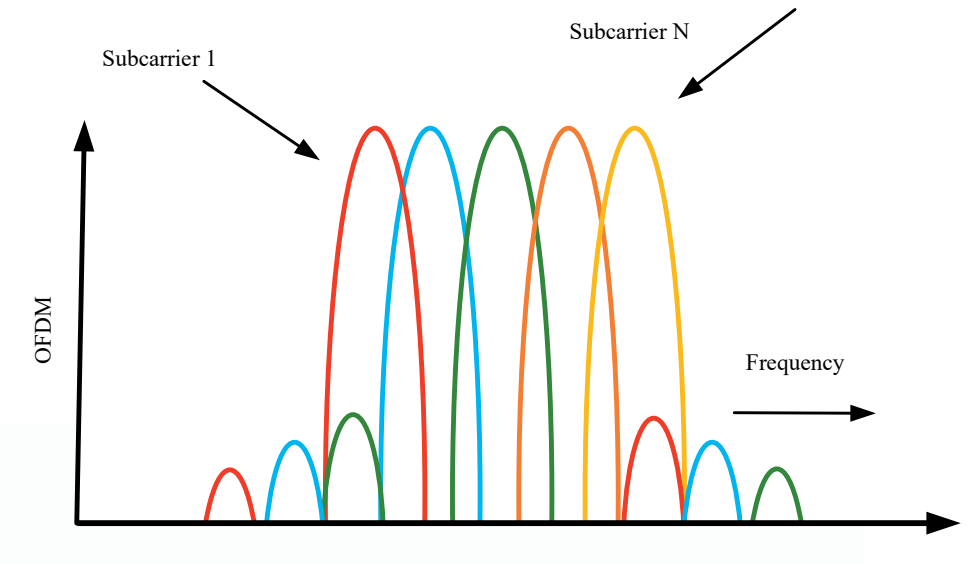

Figure 2.3 Basic concept of OFDM, Orthogonal Frequency Division Multiplexing

Similarly, each active user can be mapped to a particular subset of the overall pool of subcarriers. By allocating a varying number of subcarriers to each user, OFDM becomes more robust to frequency selectivity. OFDM has been widely studied in the literature [40], and it offers various advantages over other waveforms.

OFDM is considered to be highly spectral-efficient. Spectral efficiency is

essential for meeting the demands of an increasing data rate. OFDM is also more robust towards channel time selectivity and channel frequency selectivity compared to the single carrier frequency division multiple access (SC-FDMA). The channel time selectivity is due to the motion of the transmitter or the receiver. The frequency changes due to the Doppler effect depend on the relative motion of the source and the receiver and on the speed of the propagation of the wave, which is dependent on the channel frequency. Channel time selectivity is a crucial factor in high-speed scenarios. This is usually not a concern at lower frequencies, however, at higher frequencies channel time selectivity, which is hugely dependent on the channel frequency is a critical performance indicator. OFDM can be made robust to channel time selectivity by choosing proper subcarrier spacing. OFDM is also robust towards channel frequency selectivity which makes it an excellent choice for scenarios where a signal with large transmission bandwidth is propagated over a wireless channel. In CP-OFDM, some information from the end of an OFDM frame is taken and it is appended to the start of the same OFDM frame while keeping the length of the CP wider than the channel delay spread. This overcomes the inter-symbol interference (ISI) that may result from delays and reflections.

One of the drawbacks of the OFDM transmission scheme is that simultaneous transmission of multiple subcarriers leads to variation in the instantaneous transmit power i.e., a large peak-to-average power ratio (PAPR). A lower PAPR is essential for power-efficient transmissions. When the amplitude of the OFDM signal is greater than the linear range of the PA, the PA may operate in the nonlinear region, thus leading to nonlinear distortion. However, high PAPR can be significantly reduced by well-known PAPR reduction techniques and thus improve the performance of the PA operation [65, 86, 89].

In the uplink NR utilizes both CP-OFDM and single carrier waveforms. Single carrier waveforms are very useful at higher frequencies as they are very power efficient. Single-carrier waveforms can be further divided into two categories, which are the discrete Fourier transform single-carrier OFDM (DFT-s-OFDM) and pure single-carrier. Pure single-carrier waveforms have low PAPR compared to DFT-s-OFDM and OFDM. It should be noted that the PAPR depends on the modulation order and a direct comparison between different waveforms may be vague but in general, single carrier waveforms have low PAPR. Pure

single-carrier waveforms are also more robust to phase noise and Doppler shift with high power efficiency but they do not allow for adequate resource spectrum utilization. They also require a more complex receiver design as it does not allow frequency domain channel equalization, has lower compatibility with MIMO, and is less spectrally efficient in general. DFT-s-OFDM, has better frequency domain equalization compared to pure single-carrier waveforms. It offers better scheduling flexibility and is compatible with MIMO. DFT-s-OFDM has lower PAPR compared to OFDM but not as low as the pure single-carrier waveforms [39]. These properties of the DFT-s-OFDM make it a good choice for uplink (UL) and downlink (DL) transmissions in NR at higher frequencies, particularly for UL transmission where power efficiency is a key factor.

The 5G NR is able to handle several use cases and support a wide range of carrier frequencies thanks to its unique feature of supporting a wide range of subcarrier spacings (SCSs). 3GPP Release 15 has defined two different frequency ranges with different numerologies The frequency range 1 (FR1) which is defined for carrier frequencies (CFs) 410 MHz – 7.125 GHz and supports SCSs of 15/30/60 kHz and the frequency range 2 (FR2) defined for CFs 24.25 GHz – 52.6 GHz and supports 60/120/240 kHz SCSs. These numerologies have a great impact on the performance of the system. For example, if the subcarrier spacing SCS is increased for a given fast Fourier transform (FFT) size, the bandwidth and the symbol rate increase and thus faster processing are required in the transceiver. The time duration of the CP decreases with the increasing SCS, however, this does not always affect the ISI as the channel delay spread for narrow beams at higher frequencies is very small. However, too short CP may become a problem for beam-based transmission if the channel delay spread is almost equal to the CP length. Lower SCSs are useful when it comes to CA and enable better use of legacy systems. Table I shows some of the supported transmission numerologies [4, 5, 40, 92, 103].

2.1.2 5G NR Frame Structure

In the time domain, the length of an NR subframe is 1 ms. Each subframe is composed of 14 OFDM symbols while using a 15 kHz SCS and a normal CP length. A subframe is made up of an integer number of slots each containing

Table I 5G NR WAVEFORM NUMERLOGIES AS DEFINED BY 3GPP.

Numerology μ	$N^{\text{slot}}{}_{\text{symbol}}$	$N^{\text{frame}}{}_{\text{slot}}$	$N^{\text{subframe}}{}_{\text{symbol}}$
0	14	10	1
1	14	20	2
2	14	40	4
3	14	80	8
4	14	160	16

14 OFDM symbols. Each slot can carry control or channel signals either at the start or the end of the given OFDM symbols as illustrated in Fig. 2.4a and Fig. 2.4b. In the frequency domain a full carrier BW is characterized by a resource grid as illustrated in Fig. 2.4c. A resource grid represents information in terms of the number of allocated PRBs and subcarriers in a PRB.

This flexible design allows gNB to quickly allocate resources for URLLC when a data with high data rate arrives. It is also possible for the OFDM symbols to be all UL or all DL or have at least mix one UL and DL part allocation. These features make time division-multiplexing (TDM) in NR more flexible compared to LTE. Additionally, NR introduced the concept of a mini-slot for very small-size packet transmission. Each mini-slot is able to carry UL/DL signals or part of each at the beginning or end of the OFDM symbol(s). A mini slot is the smallest unit of resource allocation/scheduling. In NR different SCS with the same CP overhead can be multiplexed together within a subframe, Fig. 2.4b. However, to maintain the 1 ms duration of a subframe, there needs to be symbol boundary alignment within a subframe. Therefore, for SCSs larger than 15 kHz the sum of these symbol durations including the CP length must be equal to the symbol duration of one symbol of a 15 KHz subcarrier. Similarly, for SCSs lower than 15 kHz, the sum of OFDM symbol durations of a 15 kHz subcarrier should equal 1 symbol duration of SCS less than 15 kHz.

In the frequency domain, the basic scheduling unit in the 5G NR is a physical resource block (PRB). A PRB is composed of 12 subcarriers, where all the subcarriers are of the same spacing and CP overhead. Since NR supports multiple SCSs the range of the PRBs bandwidths also varies. The boundaries of the PRBs must be aligned when PRBs of different bandwidth ranges are multiplexed in the time domain. Therefore, in NR PRBs of the same bandwidth

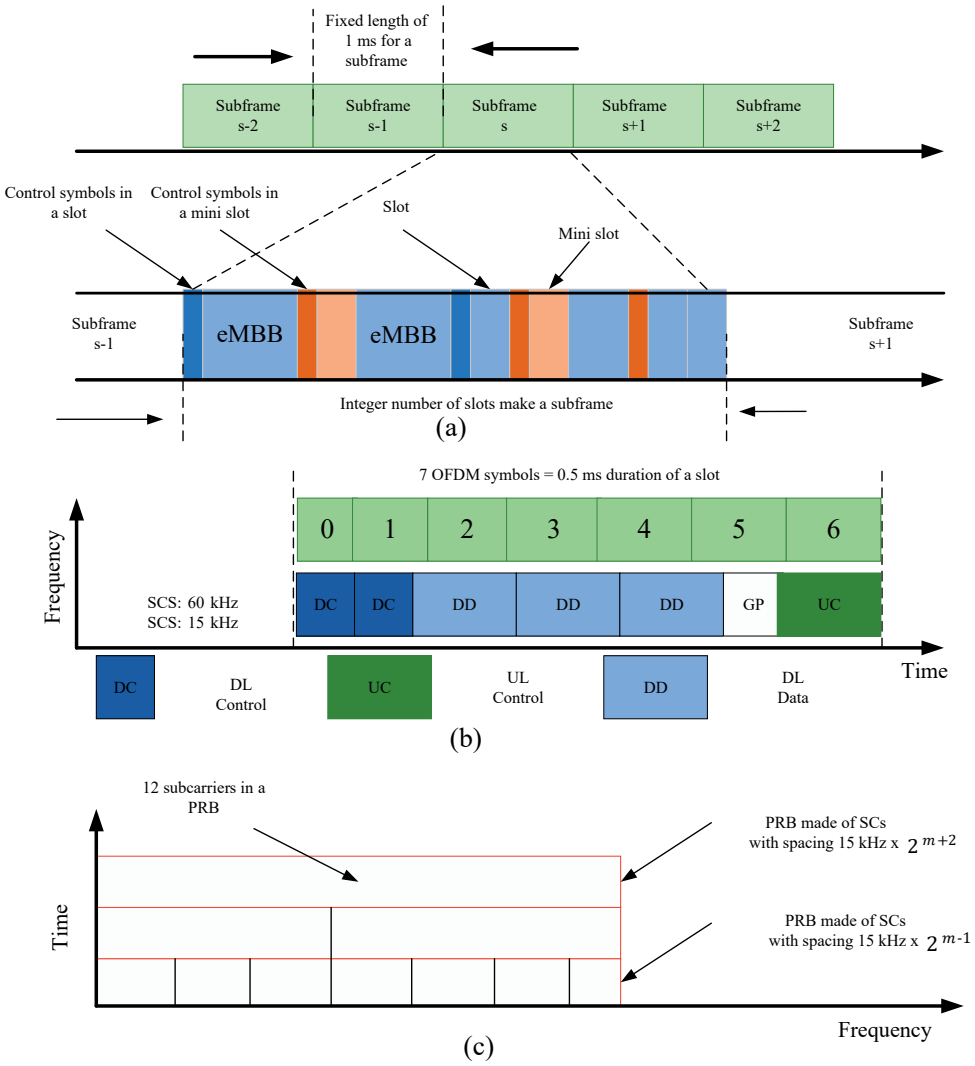

Figure 2.4 Frame structure of the 5G new radio.

range form a PRB grid, as shown in Fig. 2.4c [30, 37, 54].

2.2 Carrier Aggregation and 5G NR

To meet the increasing demand for higher peak data rates by users and improved cell coverage, efficient bandwidth utilization is essential [82]. To fulfil

these demands the concept of CA was introduced in LTE Release 10. CA is a technology introduced to increase data capacity, peak data rates, and network performance. CA allows efficient spectrum utilization by combining the CCs either from the same frequency band or different frequency bands into one single aggregated channel [59, 82]. It also enables the aggregation of FDD and TDD, as well as licensed and unlicensed spectrum.

In CA, as specified by 3GPP the carriers can be aggregated in three different ways:

- Intra Band Contiguous CA: In this scenario, the CCs are aggregated contiguously within the same frequency band. It is a rare scenario however, with the introduction of new spectrum bands in 5G NR such as 3.5 GHz such allocation is made possible. Since the contiguous channels are from the same band, this type of CA is the easiest when it comes to hardware implementation.
- Intra Band Non-Contiguos CA: In this scenario, the CCs are aggregated non-contiguously but within the same band. The middle carriers are usually loaded with other users or utilized when network sharing is considered. The channels are of different or the same sizes within the same frequency band.
- Inter Band Non-Contiguous CA: Inter band non-contiguous CA is achieved when the CCs are combined from different frequency bands,e.g., 5G NR Band 1 and Band 3 (B1+B3). In this scenario, the channels are of the same size but in different frequency bands.

CA technology is critical and plays a major role in the coexistence of fourth generation (4G) and 5G, by allowing operators to combine different 4G and 5G carriers [41, 67, 74, 87].

2.3 Transmitter Architectures and Carrier Aggregation Challenges

There are a variety of challenges and complexities associated with CA transmitter architecture depending on where the CCs are combined in the transmitter

chain. Given a dual-carrier scenario, i.e., CC1 and CC2, there are three possible options to combine these CCs as shown in Fig. 2.5.

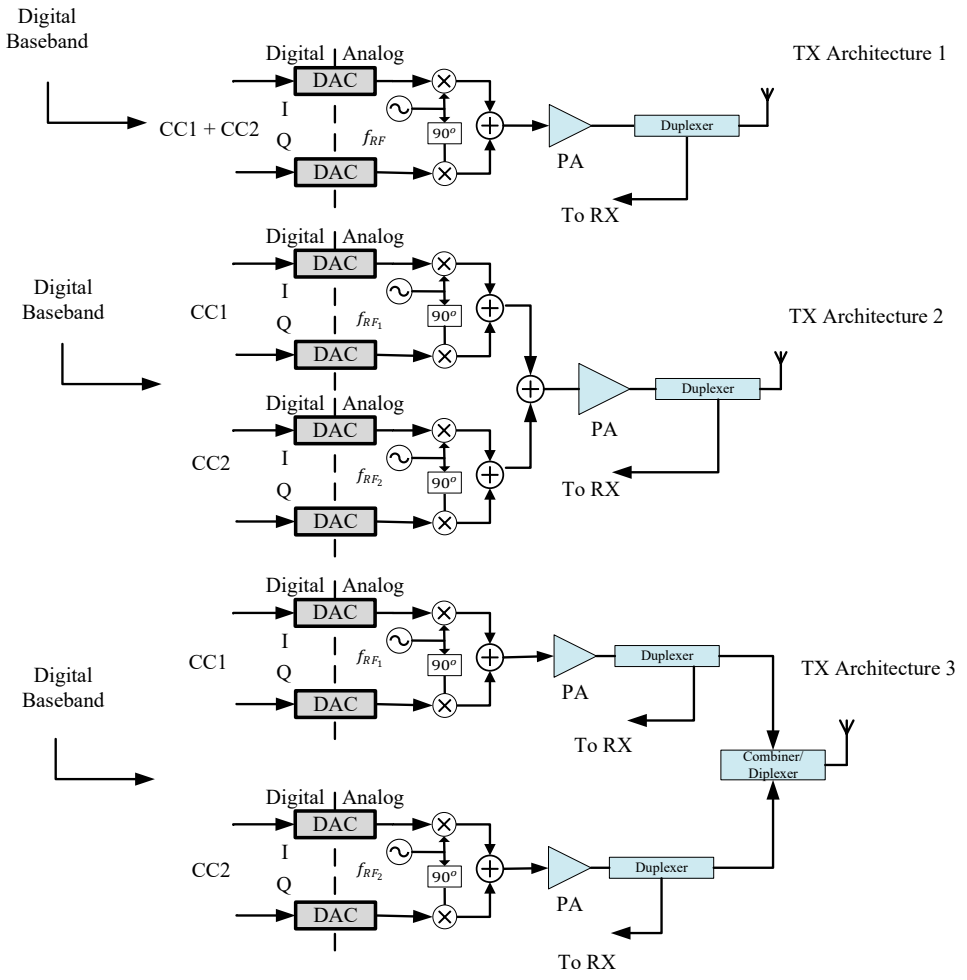

Figure 2.5 Three possible TX architectures for a dual-band CA in 5G NR. An I/Q upconversion based TX architecture is assumed in each case.

- Combining the CC1 and CC2 already at the digital front-end. This is a feasible scenario in the case of intraband contiguous CA. In general, it is possible also in intraband non-contiguos CA scenario. However, a higher sample rate would be required.
- Combining the CC1 and CC2 at the RF, right before the PA. This is a

suitable scenario in case of intraband non-contiguous CA and interband CA, when the bands are not far apart from each other thus making it possible to use a single dual-band PA.

- Combining the CC1 and CC2 at the RF after the PA amplification stages. This is a feasible scenario in case of non-contiguos intraband CA and interband CA.

2.4 Interference Problems in CA-based Cellular Transceivers

In CA based cellular transceivers interference can occur at many levels and in many forms. The interference can occur for example, at the network level, inter-cell level, or chip level such as within the integrated circuit of a UE. In this thesis, we mainly focus on the topics related to chip-level interference, which may occur in the modern RF transceivers, especially the distortion caused by PIM. In general, the receiver is treated as a victim, while the TX signal, on-chip clocks, and other blocker signals are treated as aggressors.

Within the past two decades, cellular transceivers have undergone a remarkable transformation to meet industry demands for high performance while retaining a small area and low power [10]. The superheterodyne receiver has been the receiver of choice for cellular UEs for many years because of its superior performance [9]. A superheterodyne receiver down-converts the incoming RF signal into an intermediate frequency (IF) for amplification and channel selection filtering. Then, in the next step, the filtered signal is down-converted to the baseband, i.e., centred around the direct current (DC), where the signal is demodulated and quantization is carried out. However, the disadvantage of this architecture is that the unwanted image signal that lies at the IF frequency offset to the LO will also fold into the desired received signal after the initial down-conversion stage. To overcome this problem, in front of the IF down-conversion filter, an off-chip, bulky image rejection filter is deployed to block the unwanted image signal and this is not desirable.

To this end, the direct-conversion receivers (DCR) or the homodyne receiver started to gain popularity in the early 1990s [9]. In this type of receiver, the

received RF signal is down-converted to the baseband in a single step, i.e., by programming the LO signal to the carrier centre frequency. As a consequence, the unwanted image signal problem that exists in the superheterodyne receiver is now alleviated and with some digital correction, it is possible to remove the remaining unwanted image. However, the DCR architecture has several cons in some areas where the superheterodyne is more resilient. For example, the down-conversion is performed directly at the RF, therefore, the design of the receiver for minimum amplitude and phase mismatch is essential. Any mismatch between the phase and amplitude will lead to in-phase/quadrature (I/Q) imbalance in the receiver. Furthermore, due to the distortion of the receiver, second and third-order intermodulation products are generated by the unwanted signals which may fall near the DC and interfere with the down-converted signal.

The sensitivity of DL is another challenge related to CA. In designing the duplexer for the CCs, the interference at the DL and the uplink UL should be taken into account. If the frequency separation between the two CCs is very large and an additional duplexer/diplexer or multiplexer is required it will increase the cost of the device as a multiplexer is expensive to develop and it will also increase the area of the component board. This is a serious issue in CA based FDD transceivers [71, 72].

2.5 Transmit Leakage Induced Interference Problems in CA-based Transceivers

As discussed in Section 2.1, 5G supports two duplex modes, i.e., FDD and TDD [32, 76]. 5G NR FDD enables full duplex operation meaning that both TX and RX are operating at the same time but are transmitting and receiving on different frequency bands. This makes the FDD operation more challenging as enough isolation is required between the UL and DL signal to avoid the strong TX signal leaking into the receiver band causing receiver desensitization [50, 78]. To connect the TX and RX to the same antenna it is essential to ensure adequate isolation between them. This is commonly achieved with a duplexer filter. To support a wide dynamic range of transmit and receive signals, a

duplexer filter is composed of two bandpass filters. In the TX path, the duplexer bandpass filter suppresses the out-of-band (OOB) emissions, which commonly result from the PA noise present on the transmit path. On the receiver side, the duplexer bandpass filter suppresses the strong transmitter in-band signal. The restriction on the device size such as a UE, does not allow for designing a duplexer filter that has a good TX-RX isolation. Furthermore, the cost that comes with the utilization of extremely linear components such as PAs is not sustainable. The duplexing distance is becoming even narrower due to the introduction of new frequencies in 5G and NR and the excessive use of CA, in particular the non-contiguous CA. This has also been recognized recently in [21, 28, 46, 48, 49, 91]. The problem of transmit signal leakage is briefly addressed in the following Sections. These Sections cover the TX spectral emissions due to nonlinear PA and TX induced leaks at their own RX.

2.5.1 TX Spurious Emissions at Own RX Band due to a Nonlinear PA

There are three different kinds of undesired emissions that result when a non-contiguous CA signal is applied at the input of a single nonlinear PA. These unwanted emissions affect three different regions of the spectrum. The first kind of emission is in the in-band, i.e., right on top of each CC, which degrades the transmit signal quality, which in turn means it degrades the in-band error vector magnitude (EVM). The second kind of emissions are the OOB emissions, which are emitted in the nearby channels and cause interference to the neighbouring users, that is to say, it degrades the adjacent channel leakage ratio (ACLR). The third kind of unwanted emissions are those that are emitted beyond the spurious domain, outside the adjacent channel region, as illustrated in Fig. 2.6. These kinds of emissions can violate the emission limits or can also lead to RX desensitization.

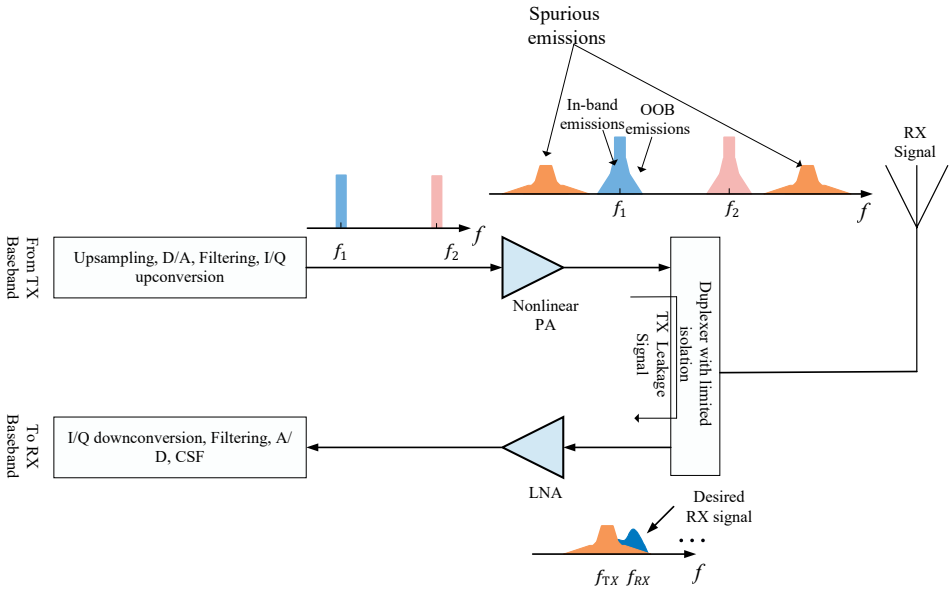

Figure 2.6 Spectral illustration of undesired PA emissions, In-band, OOB and spurious emissions at the RX band due to a limited finite isolation duplexer filter.

2.5.2 TX Induced Leakage at Own RX due to Nonlinear Passive Components

Continuing from the previous Section, in FDD transceivers, besides violating the general spurious emission limits, the generated spurious components can fall into one of the RX bands. This can lead to receiver desensitization. Furthermore, in addition to PAs, the nonlinear passive components present in the TX chain at the DFE, can generate PIM distortions which in some cases may fall into the RX band and also contribute to receiver desensitization. Considering a 5G, NR interband CA example, in which the two CCs from band 1 and band 3 after being presented to the nonlinear passive components undergo PIM distortions, where the 3rd order PIM distortion may fall onto the RX band and thus lead to RX desensitization [**Publication I-IV**]. In addition, the PIM distortion can also couple over-the-air into RX band, if there are for example rusty metal objects in the antenna near field or from nearby antennas

in MIMO, scenarios [35, 51, 52],[**Publication V**]. As discussed in Chapter 1, there are several methods to mitigate PIM distortions such as MPR, MSD or increasing the TX/RX isolation of the duplexer filter. However, all these methods are costly and drastically affect the performance of the whole system. An alternative and efficient solution is digital cancellation of the PIM distortions. In this case, a replica of the interference is created from the known TX data and is then simply subtracted from the received signal. Before We dive into the topic of digital cancellation of PIM distortion, We will discuss PIM distortion in detail in the following chapter.

CHAPTER 3

PASSIVE INTERMODULATION DISTORTION IN RADIO SYSTEMS

Linearity is a fundamental concept in physics, mathematics and more. The linear relationship in mathematics and science refers to a direct and proportional relationship between two variables. This relationship can be described by a straight-line equation in which one variable changes as the other does. The general form of a linear relationship between two variables, let's call them "x" and "y" is expressed by the equation:

$$y = mx + b.$$

where "y" is the dependent variable, "x" is the independent variable, "m" is the slope of the line indicating how much "y" changes for a unit change in "x" and "b" is the y-intercept, indicating the value of "y" when "x" is zero. On the other hand, a nonlinear system is one where the output is not directly proportional to the input. This can be elaborated by a simple equation:

$$y = x^2.$$

where "y" is not directly proportional to "x^2", i.e., if $x = 2$, $y = 4$, but when $x = -2$, "y" is still equal to "4".

As discussed in Chapter 2, to meet the increasing demands for higher data rate 5G tends to utilize larger bandwidths, which in turn put stringent requirements on the linearity of the RF components present in the transceiver systems. Intermodulation distortion (IMD), occurs when two or more signals are input to a nonlinear system, such as in the case of CCs in a CA based system. In such a scenario, the output of the system will not only consist of the original signal frequencies but also the sum and difference frequencies of the input signals together with their harmonics. That is to say, e.g., if a nonlinear system has two signals at the input at frequencies f_1 and f_2, the nonlinearity of the system will give rise to various nonlinear products at the output such as $f_1 + f_2$, $f_1 - f_2$, $2f_1 - f_2$, $2f_2 + f_1$, $2f_1$, $2f_2$, as illustrated in Fig. 3.1, which are also known as the 2^{nd} order intermodulation products, 3^{rd} order intermodulation products and harmonics respectively [69, 75].

For a nonlinear system if the source of the nonlinearity is a passive component or device the nonlinearity is then termed as PIM distortion or PHM distortion [20, 22, 28, 35, 36, 43, 44, 49, 51, 98], [**Publications I-V**]. Before we dive into the details of the sources of PIM distortion, let's first briefly review the fundamentals of PIM distortion.

3.1 Fundamentals of the PIM distortion

Transceivers using FDD have a serious problem with intermodulation distortion when IM frequencies generated at the RF interface, fall onto one of the RX bands. This can lead to partially or completely blocking the desired received signal if the power of the IM distortion is stronger than the received signal thus hampering the signal quality. PIM distortion follows similar behaviour as IMD, however the term passive, since they are generated by the nonlinear passive components. Therefore, it is sufficient to explain PIM in the context of IMD. To elaborate further on IMD mathematically, consider a simple case where the input signal is denoted as x_i, where "i" is the number of tones. The input signal x_i in this case is composed of two tones with frequencies f_1 and f_2

and an amplitude of A_1 and A_2, which can then be written as,

$$x_i(t) = A_1 \cos(2\pi f_1 t) + A_2 \cos(2\pi f_2 t) \tag{3.1}$$

This signal is then subjected to a nonlinear system, a system whose transfer function is given by n^{th}-order power series with coefficients C_1, C_2, C_3,... The output signal X_o of the nonlinear system is then described as,

$$X_o(t) = C_1 X_i + C_2 X_i^2 + C_3 X_i^3 + ... \tag{3.2}$$

Based on (3.2), it is obvious that the larger the C-th coefficient, the more dominant is the nonlinear term. Expanding the series further using trigonometric identities and the Binomial/Multinomial theorems, several other new terms and different frequencies are generated [73]. It should be noted that (3.2) is in fact an approximation derived from Weierstrass Approximation Theorem, which states that polynomials offer a uniform approximation for continuous real-valued functions over a finite interval.

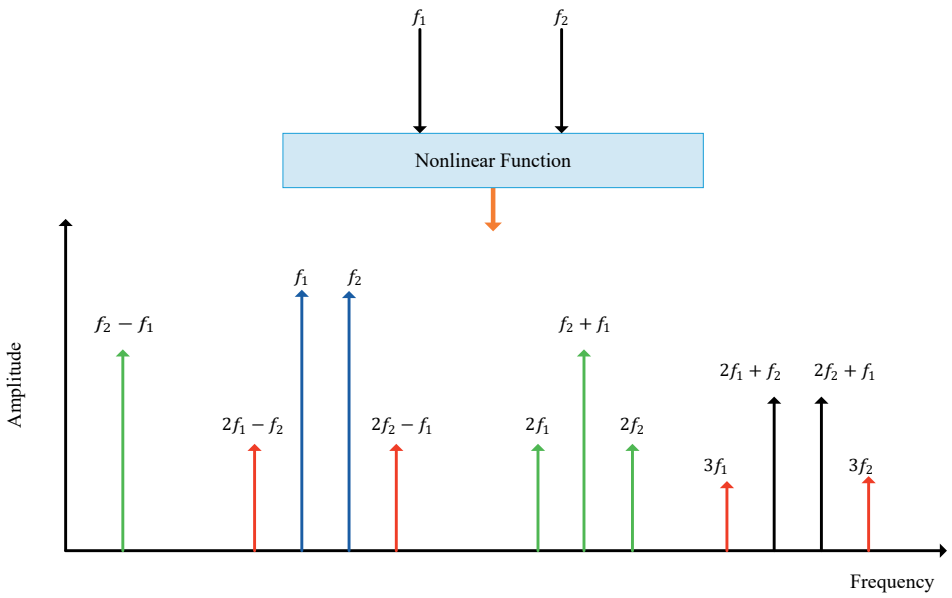

Figure 3.1 Frequency spectrum of intermodulation components in a nonlinear system

The resulting frequency components are either harmonics of the original signal or IM distortion of various orders which results from the sum and difference of the original frequencies. This phenomenon is illustrated in Fig. 3.1 which shows an example of the output spectrum of a nonlinear system when it is subjected to signals with frequencies f_1 and f_2.

Besides the centre frequencies, other significant aspects that must be taken into consideration for a nonlinear communication system are the bandwidth (BW) and power of the signal. The BW of the IM products is wider than the original input signal bandwidth and is scaled according to the order of the IM component. For example, if the input signal BW is 5 MHz, the corresponding 3^{rd}-order IM signal will have a BW of 15 MHz.

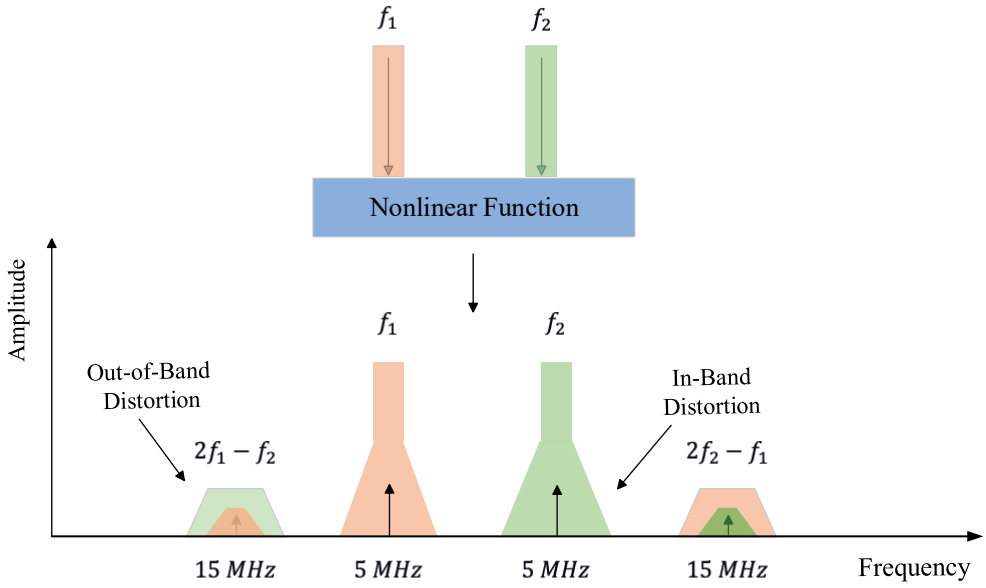

Figure 3.2 Frequency spectrum of the 3^{rd} order IM products illustrating the bandwidth of the IM products is 3 times the bandwidth of the fundamental frequencies

The BW of corresponding IM components will be the order of the IM component times the BW of the input signal if two carriers have the same BW as illustrated in Fig. 3.2. This can be generalized as in (3.3), where m and n are integer coefficients respectively.

$$BW_{IM} = |n|BW_1 + |m|BW_2 \tag{3.3}$$

Fig. 3.2, also shows in-band and out-of-band distortions which are the unwanted changes or alterations within the same frequency band or distortions that occurs outside the frequency band of the original signal. Both in-band and out-of-band distortions can adversely impact the quality and integrity of communication or signal processing systems. It's essential to identify, mitigate, and minimize these distortions to ensure reliable operation and high-quality signal transmission.

The power of the IM products is also a crucial aspect and cannot be ignored. When the power of the input signal is low the power of the IM frequency components is very small. When the input power is increased by 1 dB the (IM3) power increases by 3 dB. Fig. 3.3 shows the third-order intercept point (IP3), which

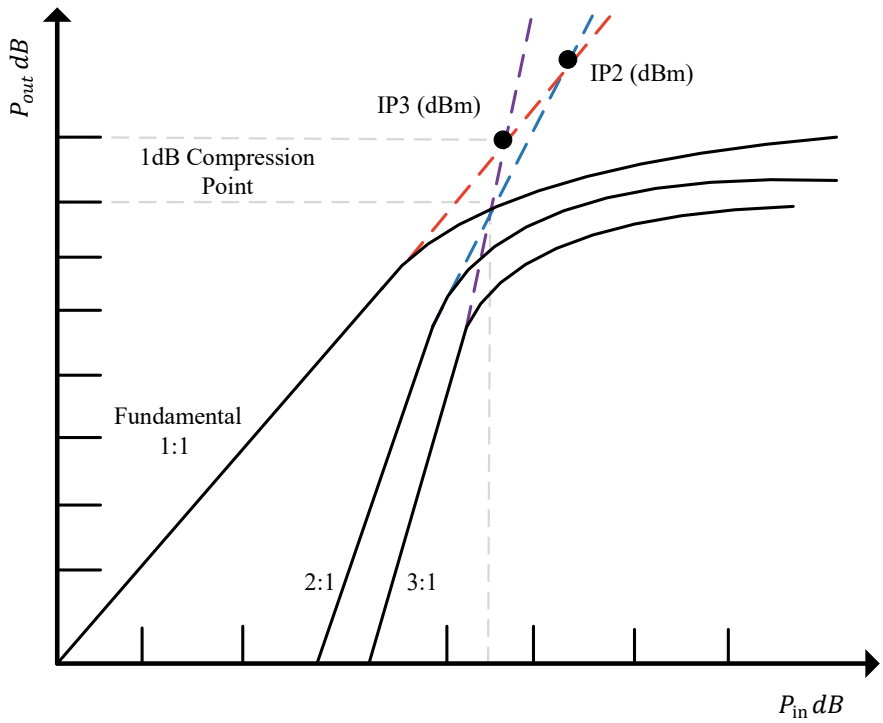

Figure 3.3 Illustration of intersection points (IP) of the 2nd and 3rd order IM products with the desired output power. The dashed lines represent the theoretical slope from the calculation whereas the full line represents the actual plots respectively.

is an intersection point between the theoretical line of the output IM3 signal

and the desired output power. One can argue that IP3 is the most important specification of a receiver dynamic performance as it predicts the performance regarding intermodulation, cross-modulation and RX desensitization [19].

3.2 Classification of PIM Sources

The first investigations regarding PIM date back to 1980-90, when it was identified as a potential source of interference in analogue radiocommunication systems: [34, 45, 61]. However, with the increasing demands for efficient spectrum utilization and the adoption of wideband multicarrier communications such as CA, tackling PIM distortion has now become even more challenging. In general, PIM distortion can be divided into three types: design PIM, where PIM is generated because of how the designers have selected the components to be used in the system, e.g., the quality of the components, size, power, rejection and PIM performance trade-offs. The second one is the assembly PIM, where PIM is generated because of how the system ages over the years. Materials quality, layout, and stability all contribute to PIM as they age. The third one is the "Rusty-Bolt" effect, where the TX signal can produce PIM when reflecting from nearby surfaces in the antenna near-field. Such interference can couple into the RX band and can cause RX desensitization [**Publication-V**].

Overall, the PIM distortion sources can be divided into two categories, i.e., within the radio system called the internal PIM sources and outside the radio system called the external PIM sources. In this thesis, we examine both internal and external sources of PIM when modeling PIM nonlinearities. Therefore, the following subsections provide descriptions of the main PIM generation mechanisms. These sources are not directly used in developing the PIM models discussed later in this thesis but aims to offer the reader insights into these distinct sources.

3.2.1 Internal PIM Sources

In FDD transceivers PIM is caused by several mechanisms, which include electron tunnelling, thin dielectric between metallic contacts, nonlinearities related to dirt and small particles on metal surfaces, electro-thermal (ET) cohesion and

memory effects due to ferromagnetic and ferrimagnetic materials.

Contact mechanisms in RF components have always been thought of as the primary source of internal PIM in modern radio communications systems [88, 99]. However, recent research shows that dirt particles on metal surfaces and ET cohesion are also major factors contributing to PIM distortion. The discussion of the internal sources of PIM in the following Sections will focus on contact mechanisms and ET. This is because the physics of contact mechanisms can help explain why corrosion over time can also generate PIM.

3.2.1.1 Contact Nonlinearities

The nonlinearity in metal contacts is one of the major internal sources of PIM products. There are two types of physical metal contact scenarios that can occur: metal-insulator-metal (MIM) and metal-metal (MM). Each of these contacts has various nonlinear mechanisms of its own. Phenomenons like electron tunnelling, thermionic emissions, and Corona discharge are more likely to happen in MIM structures. MM structures on the other hand can form diode-like junctions due to variations in metal work functions caused by thermal processes such as expansion and thermal fluctuations [98]. These two types of contacts can happen in several ways, especially as they are impacted by the surface and pressure on both ends of the contact.

During fabrication, it is almost impossible to obtain a completely smooth surface on the termination of radio components. When two radio components are coupled, both metal surfaces have multiple peaks in random positions and a local oxide or sulfide layer covers them on a microscopic level. This thickness depends on the type of metal that is used but is usually in the nanometer range. Contacting two metals at this level is almost identical to contacting two needles that have different lengths. Therefore, a contact can be viewed as a combination of both form and structure. By increasing the pressure, mechanical deformation occurs, resulting in more microasperations and expanding the "original" area. Fig. 3.4, illustrates the physical situation in which the current is confined to flow via the microasperities connections, where at high frequencies the current effectively hugs the contacting surfaces and the pattern of the flow of current changes. This change in the current pattern has serious implications for connector design and material selection.

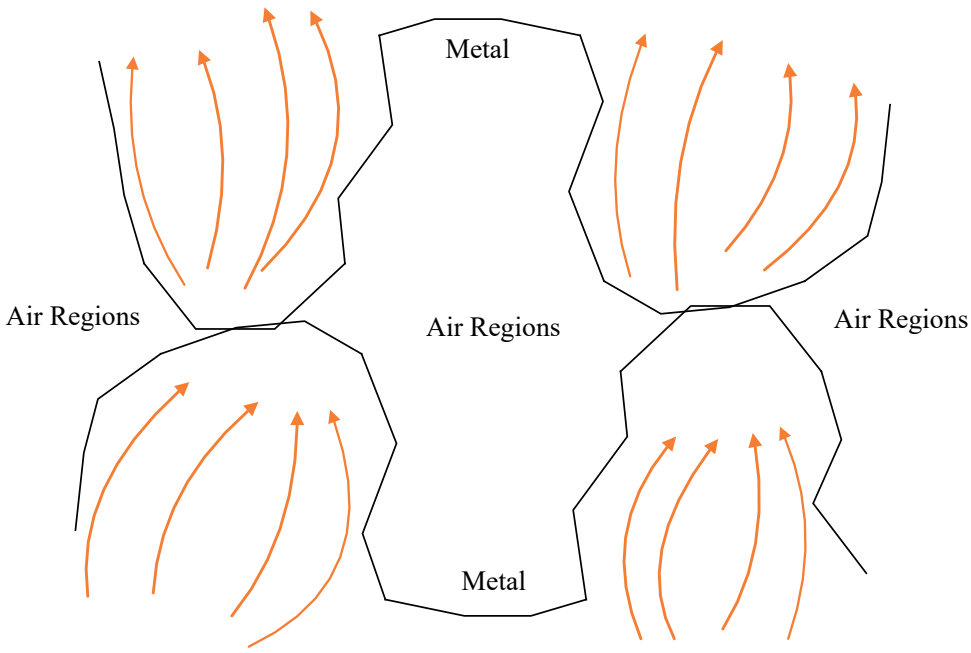

Figure 3.4 Confinement of current in the connections between microaspirities

These mechanisms can be found throughout the RF network, including radio transceivers, transmission lines, mobile units, and metallic junctions and hence cannot be ignored. These mechanisms become even more severe, especially at gNB where high transmit power is utilized.

3.2.1.2 Electro-Thermal PIM Sources

In modern radio communication systems, the transmit power at the gNB in DL is very high since a large service area needs to be covered. Transmit signals with very high power may cause electro-thermal effects which may also in turn lead to the generation of PIM. When a modulated RF signal is travelling, it may experience time-varying linear conductivity due to changes in both the thermal and electrical domains. This may also lead to the formation of PIM distortion. The generation of PIM due to ET conductivity is also one of the key contributing factors to the increasing problem of internal sources of PIM. The science behind this is explained in the following subsection.

3.2.1.3 Distributed Sources of PIM

The passive nonlinearities in modern radio systems can be further categorized as lumped, in which there is one major source of PIM, like MM contacts, and distributed, where the sources are scattered throughout the whole infrastructure. In the base stations, the weak passive nonlinearities generated due to the ET effects and behave like PIM sources are spread throughout the system. This is similar as MIM situation. The influence of the temperature on the conductivity causes significant electrical distortion in the microwave elements and because of the ET phenomenon, the distributed PIM sources are sometimes referred to as a nonlinear transmission line (NTL) [98].

The PIM distortion in an NTL is caused by multiple singular elements in the transmission line. In practice, each of the singular elements is a nonlinear generator whose signal power is proportional to the impedance which also varies throughout the line as illustrated in Fig. 3.5. There are two electric fields generated at each point, forward and reverse. The reverse electric field is, however, negligible after length, $\delta z = \lambda/4$, where "z" is the impedance and "λ" is the signal wavelength. PIM can however be flowed back at the termination of the line.

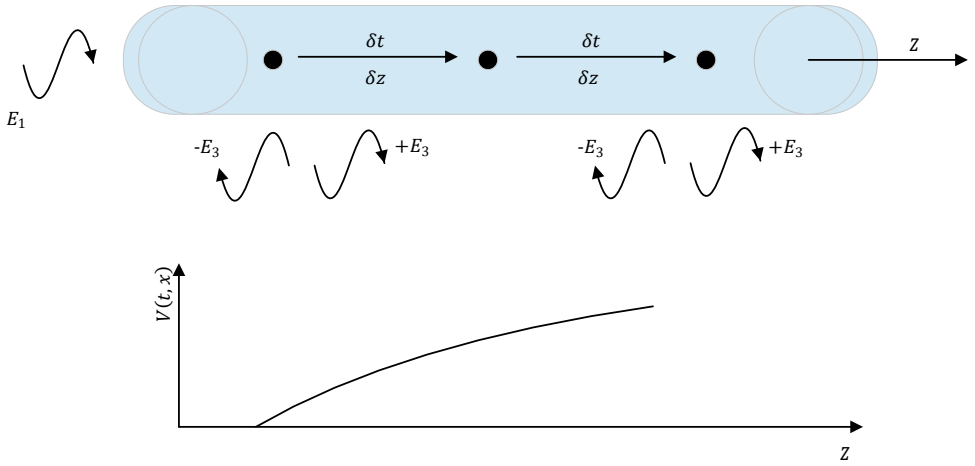

Figure 3.5 The sequential increase in PIM's signal strength due to the generated fields in nonlinear consecutive points in the transmission line.

3.2.2 External Sources of PIM

Up till now, the discussion has been focused on internal nonlinear triggers as the sources of PIM. However, the PIM problem extends beyond the internal components of a radio system. PIM distortion can also be generated externally by unpredictable and uncontrollable sources. In either scenario, indoor or outdoor, the external sources of PIM may result in the problem of self-interference and therefore, it highlights the issues related to the external sources of PIM. Generally, metallic objects in the antenna near-field such as street lamps, rusty metal objects, electric transmission lines, lamps, ceiling lights, and ceiling fans may generate PIM [13, 61, 102] [**Publication-V**]. If any of these objects lie directly in the line of sight of the incident wave the reflection of the wave from the object's uneven surfaces may result in IMD products, which in some cases may fall onto the receiver band of the same antenna or a co-located antenna. In an FDD system, the TX and RX operate simultaneously and are connected to the same antenna. In a co-located scenario where multiple radios are operating at the same time and on different frequency bands, especially while utilizing CA technology, the resulting passive nonlinearities in some cases may fall on one of the RX band and thus lead to receiver desensitization as also discussed at the beginning of this Chapter. The science behind some of the external sources of PIM is discussed in the following subsections.

3.2.2.1 Reflection on Metal Surfaces

Reflections from metal surfaces, "metal flashing" in the RF path can generate PIM. In fact, any finite (naturally occurring rare earth metal) metallic or dielectric component in the beam's path can generate PIM. Fig. 3.6 shows an example where a radio is transmitting in the direction of a metal sheet. The incident waves are reflected from the nonlinear metallic surface. The scattered electric field from the metal surface can be calculated by the physical optics (PO) approach. PO is a well-known and effective method for high-frequency diffraction techniques. The PO approach states that the incident wave induces a local surface current on the illuminated part of the metallic sheet body's surface. For a perfectly conducting body, the postulated surface-current-density

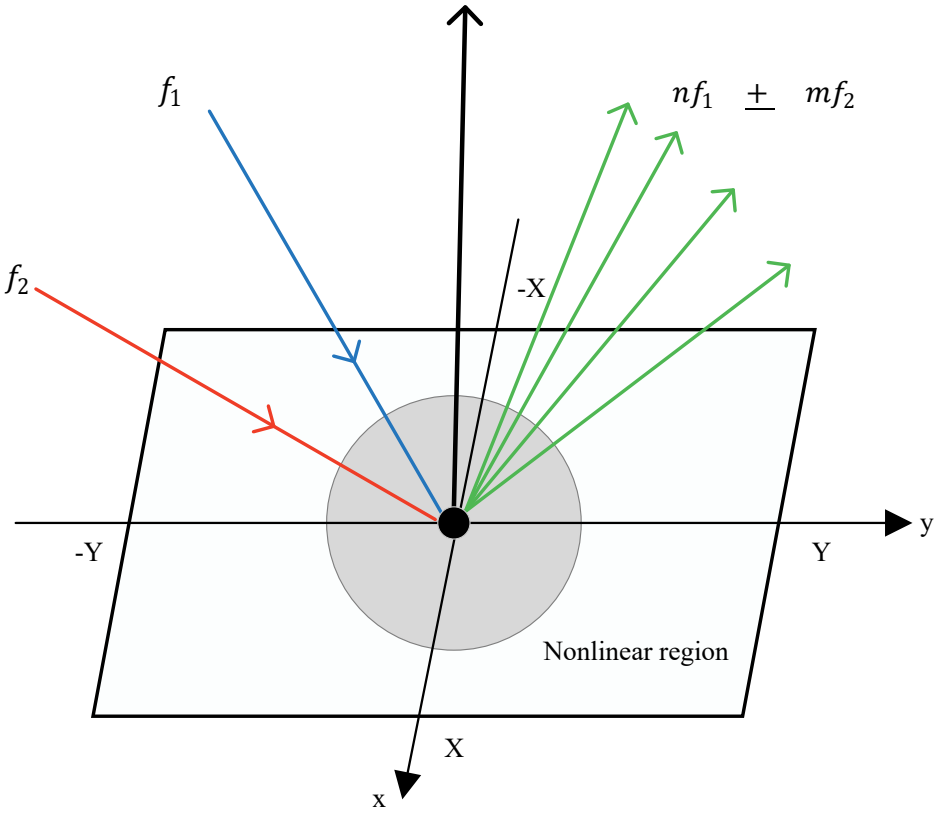

Figure 3.6 Two incident waves f_1 and f_2 lit the area of a plane metallic surface and the resulting IM products are reflected off the nonlinear region.

in the time domain is calculated by time domain physical optics (TDPO) and is described in [63]. The physics of how reflection happens from metal surfaces is not in the scope of this thesis. However, it is sufficient to understand that PIM is generated when a transmit wave hits a metal surface. The dielectric coating and other variables such as wave polarization affect the generation of PIM of the metal surfaces and is elaborated further in the following subsection.

3.2.2.2 Dielectric Coating and Wave Polarization

In the previous Section, we discussed the generation of PIM from smooth metallic surfaces. However, scattering from a metallic object with a dielectric coating is another complex problem, but the scientific approach for studying it remains the same, i.e., TDPO.

The example in Fig. 3.6 presented a simple planar conducting surface, but the TDPO approximation also remains valid for a convex surface that is covered with a dielectric material. Coating with a dielectric material changes the impedance of the object and this directly affects the nonlinear current namely, the direction in which the current is produced and also its strength [12, 31, 63]. Thus, in conclusion, both the dielectric coating and wave polarization affect the nonlinear current produced at the surface of the metallic objects, which in turn may reflect the incident radio wave in a particular direction also generating the PIM and IM products.

3.2.2.3 The Rusty Bolt Effect

In the antenna near-field, the external PIM sources are mainly transmission lines, street lamps, and protective shields on balconies almost all of them are made of steel and iron. Corrosion from rain, humidity and other environmental factors has a strong effect on steel and iron. Typically, if these rusty metallic objects are in the signal path or in the close vicinity of the antenna, they generate very strong PIM distortion. Research suggests that PIM is caused by the semi-conducting oxide of corroded metal. However, further studies show that poorly welded junctions which develop rust over time are usually the major sources of PIM. The generation of PIM due to rusty metallic objects in the signal path is commonly called the "Rusty Bolt Effect".

3.3 Effects of PIM distortion on Network Performance

As discussed in Chapter 1 and Chapter 2, 5G NR utilizes the CA technology. CA helps increase the data rate and efficient spectrum utilization, by utilizing

CCs from different or the same frequency bands in a contiguous or noncontiguous manner. However, combining the CCs in multiband radios may result in acute IMD, when the CCs experience a shared nonlinearity.

If the source of the nonlinearity is the passive components present internally

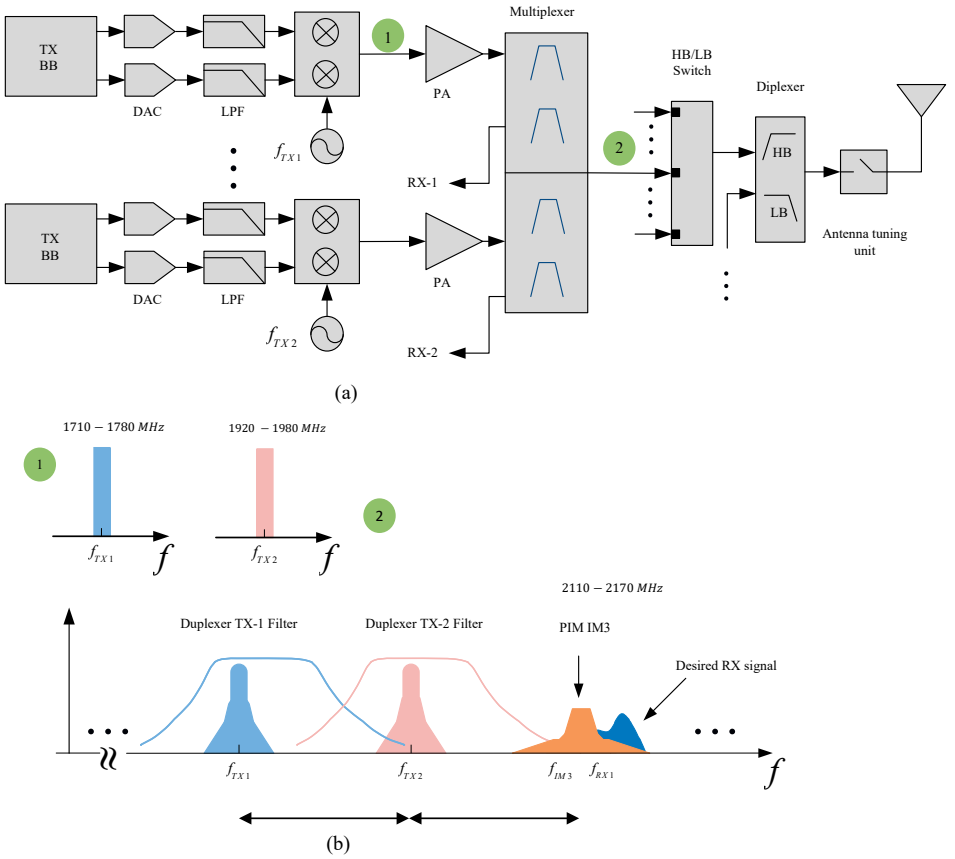

Figure 3.7 (a) Transmitter architecture for inter-band CA FDD transceiver, and (b) a spectral illustration of the unwanted IMD products created due to the nonlinearity of the TX PAs and the passive components, appearing in one of the configured RX operating bands.

in the radio unit or in the antenna near-field then it is called the PIM distortion [34] [**Publications I-V**].

At the lower end of the available spectrum, most frequency ranges, e.g., FR1 utilizes FDD. In FDD, the TX and RX operate at the same time on different centre frequencies to avoid SI. However, such systems are now more

vulnerable to the PIM induced interference, especially when utilizing CCs from multiple frequency bands. This is mainly on the gNB side where the TX power is significantly stronger. However, it can be a problem on the UE side as well. These distortions can sometimes be several dB stronger than the weakest desired received signal. If one of the PIM frequency components falls onto one of the receiver bands, it can lead to RX desensitization and greatly affect network performance.

A concrete example from our work in [**Publication I-IV**], in terms of exact NR bands, is the uplink interband CA transmission at Band 1 $(1920 - 1980)$ MHz and Band 3 $(1710 - 1780)$ MHz, where the upper IM3 falls within the Band 1 downlink $(2110-2170)$ MHz, thus reflecting the SI problem due to PIM. Fig. 3.7, describe this example illustratively. This problem is not restricted to interband CA only but is also valid for intraband CA, for example in intraband CA of Band 2, Band 3 and Band 25. Other, interband NR bands combinations can also experience similar problems such as B3+B8, B2+B4, and B5+B7 and have been acknowledged by several 3GPP documents [59, 71, 82].

In a typical co-site scenario, where there are multiple base stations operating on the same or different frequencies it is standard for PIM interference specifications to meet -150 dBc of the noise floor level. However, in the modern radio network infrastructure, even low-level PIM can significantly affect the network performance. For instance, if a component PIM characteristics degrade even a little due to uncleanliness or other environmental such as mechanical vibrations and temperature changes the noise level rises which in turn affects the UL performance. To further elaborate the effects of PIM on radio network performance, Fig. 3.8 and Fig. 3.9 shows how the effective signal-to-interference-plus-noise ratio (SINR) and channel capacity, which is given by Shannon law of log2(1+SINR) degrades as the PIM level increases for a given signal-to-noise ratio (SNR). As the PIM level increases, interference from spurious emissions and nonlinearities in the system increases, which results in increased distortion and diminished SINR. Consequently, the achievable channel capacity, representing the maximum data rate, decreases, adversely impacting overall network performance.

Therefore, it is essential to find adequate solutions to cancel PIM distortion in an efficient manner without compromising network performance and the link

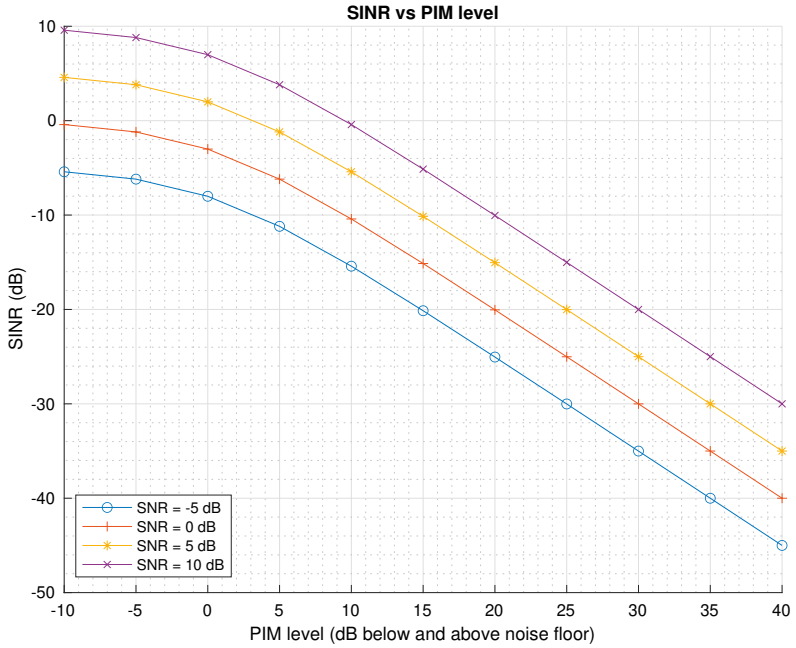

Figure 3.8 Degradation of the effective SINR with increasing PIM level.

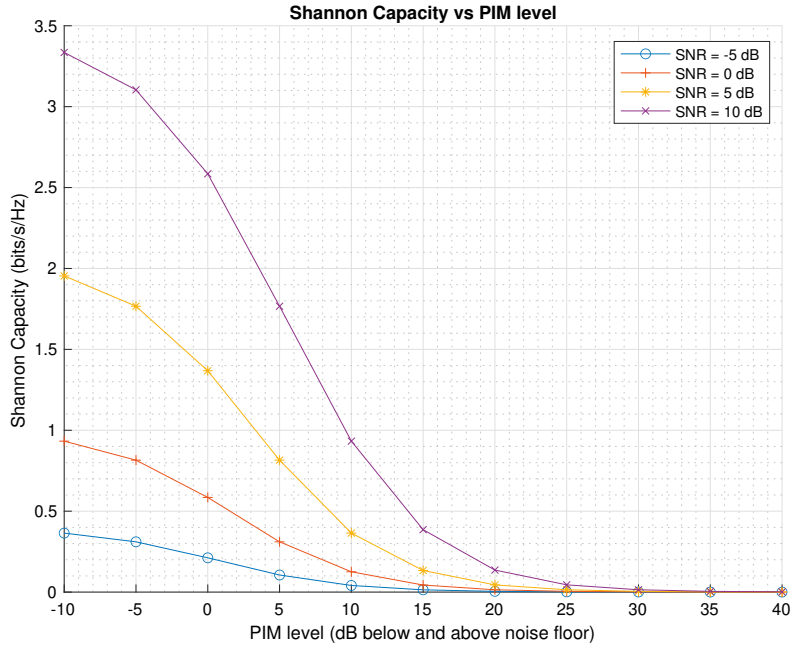

Figure 3.9 Degradation of the channel capacity with increasing PIM level.

budget. Several PIM mitigation techniques have been proposed over time, some of which we will discuss in the following Sections before we dive into the details of digital cancellation of PIM distortion in FDD transceivers.

3.4 Passive Intermodulation Distortion Mitigation Techniques

In principle, the generation of PIM distortion-related interference is unpredictable. The generation of PIM depends on several factors such as the radio operating environment, linearity characteristics of the components and several other characteristics of the PIM generation sources. These factors are impossible to predict and provide a PIM interference-free environment. This makes PIM an extremely challenging problem. The complexity of mitigating PIM further increases with the advancement in radio systems, such as the number of small cells in a small area, higher performing services and complex radio configurations to meet the user data rate demand. However, there are still some techniques to mitigate PIM completely or at least to some extent.

Overall, the PIM mitigation techniques can broadly be divided into two types: physical mitigation techniques and radio-integrated techniques. The physical mitigation techniques of PIM involve employing highly linear components such as diplexer, multiplexer, switches and other radio components or proper antenna planning to avoid generation of PIM by external sources such as metallic objects, rusty metal poles in the antenna near field. Given this as discussed in Section 3.2 of this chapter, the physical PIM mitigation techniques can be further divided into physical mitigation guidelines for external sources of PIM and internal sources of PIM.

3.4.1 Guidelines For Physical Mitigation Of Internal PIM Sources

Mitigation of internal sources of PIM means eliminating or minimizing the effects described in Section 3.2.1. The following guidelines are usually adopted for mitigation of the internal sources of PIM.

- The power of PIM distortion is related to the TX power. If the TX power is high the power of the PIM distortion would be high. Therefore, one way to mitigate the internal PIM is to reduce the TX power also known as MPR in 3GPP context or to reduce the RX reference sensitivity, termed MSD in 3GPP. However, it is not considered to be an efficient approach as it compromises the link budget and the uplink performance.

- Use highly linear internal radio components. This is not considered a feasible approach as highly linear components are costly and it will drastically increase the cost of the device.

- Minimize the metallic contacts and connectors on the circuit board, ensuring that loose metallic contact points and rotating joints are avoided.

- Keep the length of the transmission cable short and use standard semi-rigid coaxial cables.

- Increase the duplexer isolation between the high power TX signal and the desired weak received signal. However, increasing the duplexer isolation is not a feasible option as it will only increase the overall cost of the device. Furthermore, increasing the filter isolation will only help filter out PIM/IMD distortion that is generated in the TX chain before the duplexer. If the PIM/IMD distortion is generated after the duplexer filter, then the duplexer design will not help.

- One way to mitigate internal PIM is proper frequency planning, such that the UL is scheduled or configured to transmit on such frequency which is not affected by the PIM distortion of the DL signal.

All of the above solutions help minimize the electro-thermal effects of the components which have been identified as the main source of PIM. Therefore, in most of the modern radio transceivers low electronic conducting materials are now utilized to ensure that thermal variations are kept to the minimum while employing high power current flows through the RF components of the base station and UE [53].

3.4.2 Guidelines For Physical Mitigation Of External PIM Sources

In order to mitigate the external sources of PIM, it is necessary to minimize or eliminate the effects described in Section 3.2.2. However, mitigating external sources of PIM is more difficult than mitigating internal sources. It is almost impossible to identify all the PIM sources in an open area, for example in the antenna near-field. The TX signal at the gNB DL is very strong. If there is any PIM source in its path, some of the PIM components may fall onto the UL band and affect radio network performance.

Technological advancements have also increased the complexity of the base station, especially in terms of the number of antennas. Antenna isolation is seen as one solution to minimize the effect of PIM interference in co-site base stations. The amount of isolation required depends on many factors such as physical, horizontal and vertical separation between the antennas, polarization of the antennas and the placement of the antennas. In principle, it has been observed that PIM interference improves by increasing the distance between the antennas as well as by increasing electrical down tilt, which helps avoid certain metallic objects in the signal path by adjusting the antenna radiation pattern as needed [42].

3.5 Digital Cancellation of Passive Intermodulation Distortion

As discussed, the guidelines presented for PIM mitigation in Section 3.4 have their limitations. It is possible to mitigate PIM by reducing TX power or using linear components at the radio front-end, but it adversely affects the link budget, throughput, and performance of the radio network. Alternatively, the PIM distortions can be cancelled using digital cancellation techniques [27, 66]. In this thesis, we develop advanced signal models for PIM and present efficient digital cancellation solutions for them. The details about digital cancellation of PIM along with different signal models are presented in the next Chapter.

CHAPTER 4

DIGITAL CANCELLATION OF PIM: SIGNAL MODELS AND ALGORITHMS

4.1 Background and State-of-the-art

Several 3GPP CA documents have acknowledged and reported the self-interference issue in FDD transceivers, which also propose some alternatives to mitigate its effects. Among these are the MPR and MSD - both of which are designed to reduce the strength of interference and enhance receiver sensitivity, respectively. However, these methods compromise the link budget and overall system performance.

To this end, many digital cancellation techniques have been proposed in recent years to solve the SI problem in CA based FDD transceivers. Among these are the PA nonlinearity-induced SI in both interband and intraband CA, for example, [46, 49, 101]. However, these works neglect the problem of PIM. It is therefore considered in the works in [21, 22, 28], which are related to the digital cancellation of SI produced by passive front-end components. However, these works do not take into account the nonlinear distortion produced in the

individual PA, memory effects and the IMD terms greater than the third order. A nonlinear RF imposer network, where the idea is to cancel the nonlinearity by introducing another PIM source derived of the already known PIM sources between the duplexer and the antenna, is proposed in [35] for suppressing PIM.

In this thesis in contrast to the existing solutions, we first develop comprehensive behavioural models for the observable I/Q PIM waveform in the receiver baseband, which includes the combined effects of the nonlinearities of the PAs and the passive RF front-end components while also taking into account the substantial filtering or memory effects of the duplexers and other RF front-end components. Given this, we derive generalized models for the PIM waveform observed at the RX baseband while also taking into consideration the arbitrary nonlinearity order(s) in the involved nonlinear stage(s). Furthermore,

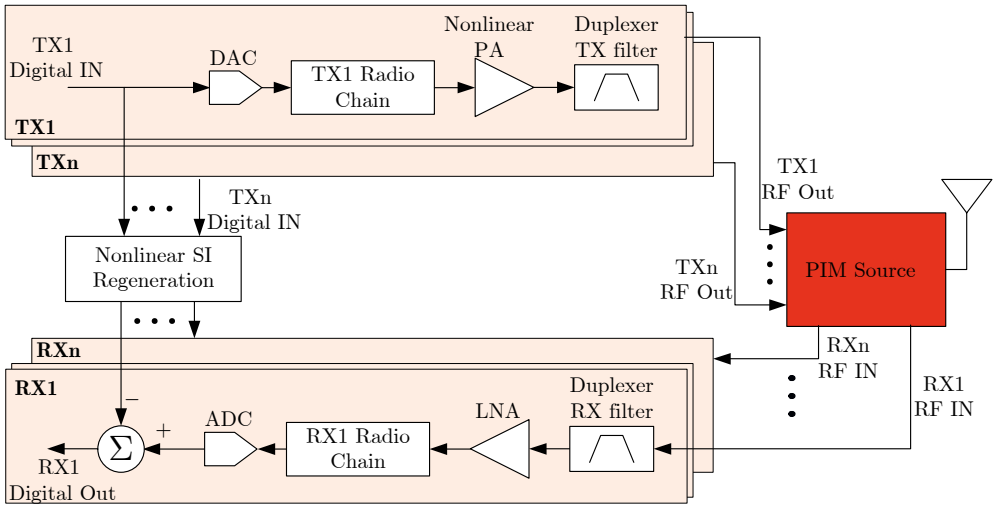

Figure 4.1 Block diagram of a multiband FDD radio transceiver system together with the proposed nonlinear SI generation and cancellation unit, which runs in the transceiver's DFE, **Publication-IV**.

the performance of the proposed digital cancellation solutions are evaluated with real-life RF measurements adopting commercial 5G NR UE and RF components as a practical evaluation platform. Fig. 4.1, illustrates the proposed digital PIM cancellation technique at a conceptual level. The RF measurement results are presented and evaluated in Chapter 5, respectively.

4.2 Signal Models for Passive Intermodulation Distortion

In this Section, we present four different signal models for describing the PIM waveform, which is observed in the RX chain. They differ from each other depending on the assumptions that are made regarding the TX PAs and corresponding memory effects when deriving the signal model. The basic model is based on the assumption that PAs are completely linear, while the second signal model also takes into account the nonlinearities of the PAs. In both of these cases, the actual PIM stage is allowed to have an arbitrary response. In addition, the memory modelling of the involved nonlinear distortion is also taken into account. The third signal model is then based on balancing complexity and performance by putting the memory modelling details into a cascaded or decoupled model. In this model, a common memory model is used for all the nonlinear terms. In the fourth signal model, which is discussed in Section 4.3, a MIMO FDD system is assumed, as well as a model of air-induced PHM distortion that couples into the co-located radio.

For clarity, it is noted and acknowledged that the works in [7, 8, 57] and [49, 91, 101] also address the modelling of nonlinear distortion for interband CA transmitters where a single PA is used for the CCs. However, these works do not take into account the problem of PIM. Furthermore, the modelling and cancellation approach presented in this thesis work is more advanced, due to the fact that the considered system in the generic case contains combined nonlinearities i.e., the nonlinear CC-specific PAs followed by the actual PIM stage. Therefore, even though the centre frequencies of the considered IM products are the same as in [7, 8, 49, 57, 91, 101] but the actual complex waveform is different in the baseband.

The provided modelling principles and methodologies are not limited to specific band combinations. They can be utilized for any 3GPP specified NR band combinations susceptible to the problem of PIM. It should be noted that even single-band radios are susceptible to the problem of PIM if the duplex gap is smaller and noncontiguous CA is deployed. However, for simplicity, we focus on an important example case, i.e., NR Band 1 and Band 3 where the

positive IM3 subband coincides with one of the RX band. In other words, $2\omega_1 - \omega_2 \approx w_{RX}$, where ω_1 and ω_2 are the angular center frequencies of the two CCs, with $\omega_1 > \omega_2$ and ω_{RX} is the angular RX frequency. It is imperative to note here that the assumption of IM3 hitting the receiver band does not limit us to the treatment of third-order nonlinearities alone.

4.2.1 PIM Model With Linear Power Amplifiers

In the existing PIM literature, the PAs have usually been assumed to be linear. Therefore, this first signal model with linear PAs can be considered as a benchmark for the more advanced signal models suggested in this work. To formulate a linear-in-parameter signal model, let us first denote the upconverted I/Q modulated CC signal after linear amplification as:

$$\begin{aligned} \tilde{x}_1[n] =& \mathrm{Re}\big\{\alpha_1 x_1[n] e^{j\omega_1 n}\big\} \\ \tilde{x}_2[n] =& \mathrm{Re}\big\{\alpha_2 x_2[n] e^{j\omega_2 n}\big\}, \end{aligned} \tag{4.1}$$

where, α_1 and α_2 denote the complex gains of the two PAs, where $x_1[n]$ and $x_2[n]$ are the two CCs in the baseband and ω_1 and ω_2 are their respective center frequencies after RF upconversion. Throughout this thesis, we use discrete-time models for all the signals, even though the upconverted signals are continuous time in an actual system. This assumption, however, does not affect the precision of the modelling. The centre frequencies of the CCs are considered only to specify where the nonlinear terms will fall in the frequency domain. The tilde notations such as $\tilde{x}_1[n]$ and $\tilde{x}_2[n]$ indicate the actual I/Q modulated and upconverted RF signals, while the related complex-valued baseband signals are represented without a tilde on top of them.

The summed transmit signal is simply then, $\tilde{x}_{TX}[n] = \tilde{x}_1[n] + \tilde{x}_2[n]$. This summed signal is then subjected to the PIM nonlinearity. In this work, the nonlinearities are modelled as polynomials and thus the signal after undergoing PIM nonlinearity is given by (4.2) as:

$$
\begin{aligned}
\tilde{y}_{\mathrm{PIM}}[n] &= \sum_{p=1}^{P} \beta_p \tilde{x}_{\mathrm{TX}}[n]^p \\
&= \sum_{p=1}^{P} \beta_p \left(\mathrm{Re}\{\alpha_1 x_1[n] e^{j\omega_1 n}\} + \mathrm{Re}\{\alpha_2 x_2[n] e^{j\omega_2 n}\} \right)^p \\
&= \sum_{p=1}^{P} \beta_p \left(\frac{\alpha_1}{2} x_1[n] e^{j\omega_1 n} + \frac{\alpha_1^*}{2} x_1^*[n] e^{-j\omega_1 n} + \frac{\alpha_2}{2} x_2[n] e^{j\omega_2 n} + \frac{\alpha_2^*}{2} x_2^*[n] e^{-j\omega_2 n} \right)^p \\
&= \sum_{p=1}^{P} \sum_{k=0}^{p} \sum_{k_1=0}^{p-k} \sum_{k_2=0}^{p-k-k_1} \gamma_{p,k,k_1,k_2} x_1[n]^k x_1^*[n]^{k_1} x_2[n]^{k_2} x_2^*[n]^{p-k-k_1-k_2} \\
&\qquad \times e^{j[(k-k_1)\omega_1 - (p-k-k_1-2k_2)\omega_2]n}, \qquad (4.2)
\end{aligned}
$$

where β_p denote the p^{th} order coefficient of the PIM nonlinearity and γ_{p,k,k_1,k_2} denotes the coefficients of the resulting nonlinear PIM terms. It is assumed that each of the elicited nonlinear terms also undergoes memory effects such that we have a memory polynomial type of nonlinearity. It should be noted that it is not the only type of polynomial nonlinearity with memory but the simplest one and hence the overall signal model is then given by:

$$
\begin{aligned}
\tilde{y}_{\mathrm{PIM}}[n] &= \sum_{p=1}^{P} \sum_{k=0}^{p} \sum_{k_1=0}^{p-k} \sum_{k_2=0}^{p-k-k_1} \sum_{m=-M_1}^{M_2} \gamma_{p,k,k_1,k_2,m} \\
&\times x_1[n-m]^k x_1^*[n-m]^{k_1} x_2[n-m]^{k_2} x_2^*[n-m]^{p-k-k_1-k_2} \\
&\times e^{j[(k-k_1)\omega_1 - (p-k-k_1-2k_2)\omega_2](n-m)}, \qquad (4.3)
\end{aligned}
$$

where M_1 and M_2 are the numbers of pre-cursor and post-cursor memory taps and thus $M = M_1 + M_2 + 1$ is the total number of taps per filter after the PIM nonlinearity and γ_p, k, k_1, k_2, m is an overall effective coefficient. It is critical to note that the signal models in (4.2) and (4.3) are real-valued. However, the focus here in this thesis is anyway on baseband-equivalent modelling where the signal models are complex-valued by nature.

As we discussed at the beginning of this Section, the analysis in this work is focused on the scenario where the RX band is either fully or partially overlap-

ping with the IM frequency given by, $2\omega_1 - \omega_2$. Therefore, when modelling the PIM distortion affecting the RX band it is sufficient to consider the nonlinear terms in (4.3), which are centred around this frequency. The other nonlinear terms can be filtered out by the duplexer RX filter or later selectivity filtering stages in the RX chain. Given the assumption that the third-order IM falls within the RX band, the signal model in (4.3) can be transformed into the following rules:

$$\begin{cases} k - k_1 = 2 \\ p - k - k_1 - 2k_2 = 1. \end{cases} \tag{4.4}$$

Solving (4.4) for the values of k_1 and k_2 we get,

$$\begin{cases} k_1 = k - 2 \\ k_2 = \dfrac{p+1}{2} - k. \end{cases} \tag{4.5}$$

These rules are derived from (4.3) based on the fact that we are interested in 3^{rd} order terms i.e., $2\omega_1 - \omega_2$ and the rules in (4.4) corresponds to those frequencies. The value of p in (4.5) can now be limited to odd integers, because only odd-order nonlinearities can produce the IM terms on frequency, $2\omega_1 - \omega_2$

Inserting the values of k_1 and k_2 into (4.3) and also updating the sum limits as needed, we get the following baseband-equivalent mathematical expression for the observed PIM distortion at the RX band

$$\begin{aligned} y_{\text{PIM}}[n] = &\sum_{r=1}^{R} \sum_{k=1}^{r} \sum_{m=-M_1}^{M_2} \gamma_{r,k,m} \\ &\times\ x_1[n-m]^{k+1} x_1^*[n-m]^{k-1} \\ &\times\ x_2[n-m]^{r-k} x_2^*[n-m]^{r-k+1} \\ = &\sum_{r=1}^{R} \sum_{k=1}^{r} \sum_{m=-M_1}^{M_2} \gamma_{\mathbf{s},m} \phi_{\mathbf{s}}[n-m], \end{aligned} \tag{4.6}$$

where, $r = (p-1)/2$, $R = (P-1)/2$, p and P are odd, $s = [r\ k]$ is a vector that contains the state of the auxiliary parameters, $\gamma_{s,m}$ is the coefficient of the

nonlinear terms falling onto the RX band, and

$$\phi_{\mathbf{s}}[n] = x_1[n]^{k+1} x_1^*[n]^{k-1} x_2[n]^{r-k} x_2^*[n]^{r-k+1}. \tag{4.7}$$

It should be noted that in theory the signal model in (4.3) will also result in other nonlinear terms which may also fall onto the RX band but they are not given by $2\omega_1 - \omega_2$. To elaborate further, actually all integer solutions of a Diophantine equation which is defined as $\omega_1 x + \omega_2 y = \omega_{RX}$ results in nonlinear terms which overlay the RX band. Nevertheless, it can justified that the only practical solution is $x = 2$ and $y = -1$ since all other solutions are of a very high order, such as $x = 2 - 176t$ and $y = -1 + 195t$, where t is an integer, and therefore, they correspond to extremely high nonlinearity orders, and are usually not observed in a real system. Therefore, it is enough to consider only the case given by, $2\omega_1 - \omega_2$, i.e., $x = 2$ and $y = -1$ [**Publication II-IV**].

4.2.2 PIM model with Nonlinear Power Amplifiers

In [**Publication II-IV**], we have observed that the nonlinearity of the TX PAs also affect the PIM waveform that is observed at the RX band. Therefore, it makes sense to include the PA-induced nonlinearities in the modelling of the PIM distortion itself. Given that, utilizing a memoryless polynomial model for the two considered PAs for each CC, the i^{th} TX signal can be expressed as:

$$\begin{aligned}\tilde{x}_i[n] =& \mathrm{Re}\left\{ \sum_{q=0}^{Q} \alpha_{i,q} x_i[n]^{q+1} x_i^*[n]^q e^{j\omega_i n} \right\} \\ =& \mathrm{Re}\big\{ u_i[n] e^{j\omega_i n} \big\}, \end{aligned} \tag{4.8}$$

where $u_i[n] = \sum_{q=0}^{Q} \alpha_{i,q} x_i[n]^{q+1} x_i^*[n]^q$ and the nonlinearity of the PAs is of the order $2Q + 1$. In this case, the PA induced harmonic IM products are ignored as they are expected to be filtered by the duplexer/multiplexer in the RF front-end. The combined signal is then fed to the PIM nonlinearity similarly to the earlier signal model and the signal after experiencing the static PIM

nonlinearity is then expressed as:

$$\begin{aligned}\tilde{y}_{\mathrm{PIM}}[n] &= \sum_{p=1}^{P} \beta_p(\tilde{x}_1[n] + \tilde{x}_2[n])^p \\ &= \sum_{p=1}^{P} \beta_p(\mathrm{Re}\{u_1[n]e^{j\omega_1 n}\} + \mathrm{Re}\{u_2[n]e^{j\omega_2 n}\})^p, \end{aligned} \tag{4.9}$$

It can be noted that this signal model is structurally similar to the case with linear PAs, only the terms $\alpha_i x_i$ are replaced with $u_i[n]$. Thus, from (4.6), the baseband-equivalent static PIM distortion overlapping with the RX band is given by:

$$y_{\mathrm{PIM}}[n] = \sum_{r=1}^{R}\sum_{k=1}^{r} \gamma_{r,k} u_1[n]^{k+1} u_1^*[n]^{k-1} u_2[n]^{r-k} u_2^*[n]^{r-k+1}, \tag{4.10}$$

After this we expand the exponential terms that involve the PA output signals and their complex conjugates with the help of a binomial expression, which gives us the expression (4.11)

$$\begin{aligned} y_{\mathrm{PIM}}[n] = &\sum_{r=1}^{R}\sum_{k=1}^{r}\sum_{k_{11}=0}^{2k}\sum_{k_{12}=0}^{2k-k_{11}} \cdots \\ &\sum_{k_{1Q}=0}^{2k-\sum_{q=1}^{Q} k_{1q}} \sum_{k_{21}=0}^{2(r-k)+1} \sum_{k_{22}=0}^{2(r-k)+1-k_{21}} \cdots \sum_{k_{2Q}=0}^{2(r-k)+1-\sum_{q=1}^{Q} k_{2q}} \gamma_{r,k,k_{11},\ldots,k_{2Q}} \\ &\times x_1[n]^{(2Q+1)k+1-\sum_{q=1}^{Q}(Q-q+1)k_{1q}} x_1^*[n]^{(2Q+1)k-1-\sum_{q=1}^{Q}(Q-q+1)k_{1q}} \\ &\times x_2[n]^{(2Q+1)(r-k)+Q-\sum_{q=1}^{Q}(Q-q+1)k_{2q}} x_2^*[n]^{(2Q+1)(r-k+1)-Q-\sum_{q=1}^{Q}(Q-q+1)k_{2q}} \end{aligned} \tag{4.11}$$

It can be noted that under the basic case of fully linear PAs the variables $k_{11}, \ldots, k_{2Q}$ do not exist and (4.11) reduces to the signal model presented in Section 4.2.1, (4.6). With some further manipulations the signal model in (4.11) can be further simplified after which the baseband-equivalent expression of the

PIM distortion at RX band including the memory terms is given by:

$$y_{\text{PIM}}[n] = \sum_{r=1}^{R} \sum_{k=1}^{2Q+1} \sum_{q=0}^{(2Q+1)(R-r)+Q} \sum_{m=-M_1}^{M_2} \gamma_{\mathbf{s},m} \phi_{\mathbf{s}}[n-m], \tag{4.12}$$

where now $s = [r \quad k \quad q \quad Q]$ and

$$\phi_{\mathbf{s}}[n] = x_1[n]^{(2Q+1)(r-1)+k+1} x_1^*[n]^{(2Q+1)(r-1)+k-1} \times x_2[n]^q x_2^*[n]^{q+1}. \tag{4.13}$$

4.2.3 Reduced-Complexity Cascaded PIM model With Decoupled Memory

The signal models in (4.12) and (4.13) have high modelling accuracy since they consider both the PA nonlinearities and the PIM nonlinearity. However, these models also have very high modelling complexity. Due to the assumption that each of the nonlinear terms undergoes a memory effect separately, the total number of parameters in the model increases significantly, especially for more high-order nonlinearity. Therefore, in this Section, we develop a model that has a great reduction in computational complexity with a small penalty in modelling accuracy. This is because we assume here that all nonlinearities experience the same memory effects.

Given this, let us first look at the instantaneous PIM signal with nonlinear PAs. Based on (4.12), this signal is presented as:

$$y_{\text{NL}}[n] = \sum_{r=1}^{R} \sum_{k=1}^{2Q+1} \sum_{q=0}^{(2Q+1)(R-r)+Q} \gamma_{\mathbf{s}} \phi_{\mathbf{s}}[n], \tag{4.14}$$

where $\phi_{\mathbf{s}}[n]$ is shown in (4.13) and γ_s denotes the coefficients of the instantaneous basis functions. To take the memory effects into account, the overall signal in (4.14) is put through linear filtering, which in turn means that each of the nonlinear terms experiences common memory effects. One can argue that is typically a more restricted memory model than the one given in (4.6) and (4.12), this is in accordance with the physical phenomenon behind the memory effects since all of the nonlinear terms propagate through the same channel.

With this reasoning, the final cascaded signal model can be then given as:

$$y_{\mathrm{PIM}}[n] = \sum_{m=-M_1}^{M_2} h[n] y_{\mathrm{NL}}[n-m], \tag{4.15}$$

where $h[n]$ is a memory filter modelling the nonlinear response of the PIM source and is decoupled from the rest of the overall response. Just like the other memory models proposed earlier, this filter is also assumed to have M_1 and M_2 precursor and post-cursor memory taps, respectively. The models in (4.14) and (4.15) have one fundamental difference compared to the earlier signal models and that is that these signal models are restricted such that each of the basis functions has their own individual complex scalars as the tunable weights as shown in (4.14) and followed by a global memory filter $h[n]$ given in (4.15).

4.2.4 Comparison of the Signal Models

To compare the attributes of the three signal models, Table 4.1 shows the phenomenon that they are capable of modelling, along with the basis functions resulting from these different signal models for a simple example case, i.e., $R = 1$ and $Q = 0$ (linear PAs) or $Q = 1$(third-order PAs). It can be noted from Table 4.1 that in this case, the model with linear PAs has only one basis function while the models with nonlinear PAs have six basis functions, showing that the basis functions do not increase exceptionally when the PA nonlinearity is taken into account. Furthermore, it should be noted that generally the third-order PIM and third-order PA nonlinearity are of more serious concern.

Assuming the same values of $R = 1$ and $Q = 0$ or $Q = 1$ as in Table 4.1, and considering $M = M_1 + M_2 + 1 = 8$ memory taps in total, the model which considers a linear PAs has 8 parameters, the model with nonlinear PAs has about 48 parameters and the model with decoupled memory only has 14 parameters. This radical difference in the number of parameters between the coupled and decoupled model is also shown in Fig. 4.2

Nevertheless, the models differ in the way they handle linear memory effects. A linear-in-parameter model with coupled memory, which assumes a separate filter for every nonlinear term, leads to a significant number of parameters, as can be seen in Table 4.1, where the third row describing the properties of the

Table 4.1 COMPARISON OF THE THREE SIGNAL MODELS

Signal model	**PA/PIM nonlinearity**	**Memory model**	**Basis functions with $R = 1$ and $Q = 0$ (linear PAs) or $Q = 1$ (nonlinear PAs)**	**Total No. of parameters for arbitrary R and Q**
Linear PAs with coupled memory	No/Yes	Separate for each basis function	$x_1[n]^2x_2^*[n]$	$\frac{R(M_1+M_2+1)(R+1)}{2}$
Nonlinear PAs with coupled memory	Yes/Yes	Separate for each basis function	$x_1[n]^2x_2^*[n]$, $x_1[n]^2x_2[n]x_2^*[n]^2$, $x_1[n]^3x_1^*[n]x_2^*[n]$, $x_1[n]^3x_1^*[n]x_2[n]x_2^*[n]^2$, $x_1[n]^4x_1^*[n]^2x_2^*[n]$, $x_1[n]^4x_1^*[n]^2x_2[n]x_2^*[n]^2$	$R(M_1 + M_2 + 1)(2Q + 1) \times \left[(2Q + 1)\left(\frac{R+1}{2}\right) - Q\right]$
Nonlinear PAs with decou-pled memory	Yes/Yes	Common for all basis functions	$x_1[n]^2x_2^*[n]$, $x_1[n]^2x_2[n]x_2^*[n]^2$, $x_1[n]^3x_1^*[n]x_2^*[n]$, $x_1[n]^3x_1^*[n]x_2[n]x_2^*[n]^2$, $x_1[n]^4x_1^*[n]^2x_2^*[n]$, $x_1[n]^4x_1^*[n]^2x_2[n]x_2^*[n]^2$	$M_1 + M_2 + 1 + R(2Q + 1) \times \left[(2Q + 1)\left(\frac{R+1}{2}\right) - Q\right]$

signal model with nonlinear PAs and coupled memory. Consequently, coupled memory-based models have a complexity that is multiplicative with M, while with decoupled memory-based models, the effect of memory is additive. By contrast, the model with decoupled memory assumes that each nonlinear term has a common memory model. This somewhat reduces the degree of freedom in the model, but it greatly reduces the model complexity. This is because the memory length has only an additive effect on the complexity of the model.

It can be observed from Fig. 4.2 that the number of parameters in the decoupled memory-based model is still moderate and in an acceptable range, in terms of the computation complexity involved when it comes to hardware implementation even when $Q = 5$ or $R = 5$, while in the coupled memory-based model they grow steeply as a function of Q and R. It can be concluded that the decoupled-memory model is a fine trade-off between modeling complexity and accuracy as we will show further in the next Chapter.

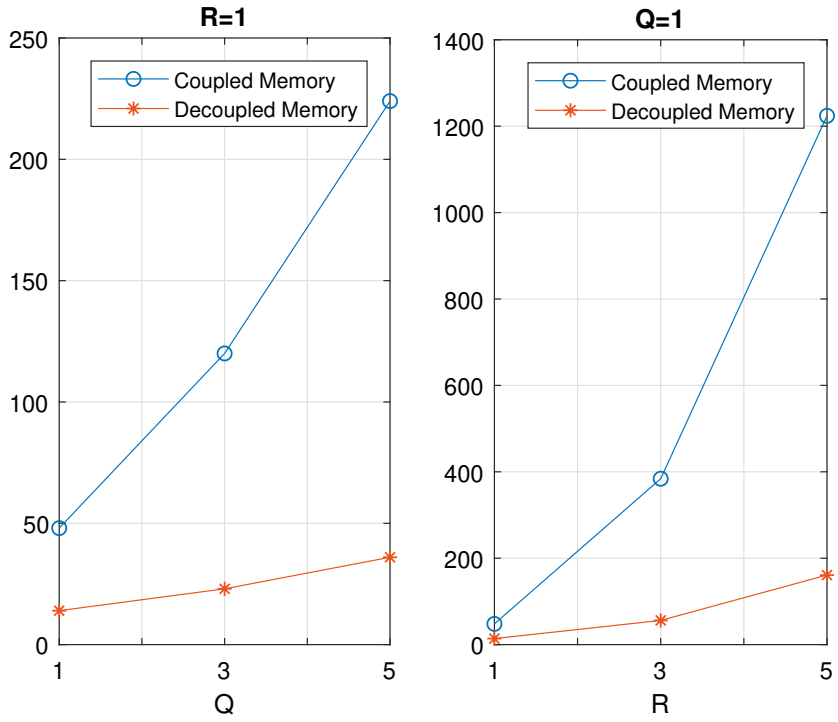

Figure 4.2 Number of parameters in coupled and decoupled memory-based models, where $M1 + M2 + 1 = 8$, for $R = 1$ and $Q = 1$ (left) and changing R (right), **Publication-IV**.

4.3 Signal Model for Passive Harmonic Distortion

So far we presented signal models for PIM distortion, however, practical radio systems employ multiple TXs/RXs with several different frequency band combinations. In some cases, PIM may couple also over the air to the RX band in question, but this is not limited to PIM distortion in some scenarios the PHM distortion may also lead to RX desensitization if the harmonics fall into the RX band. In this Section, we focus on the signal modelling for PHM distortion that couples over the air in a MIMO, FDD setup. In this model, we assume a co-existing 5G NR Band 3 FDD and Band 78 TDD operation, where the passive harmonic distortion of Band 3 lands at the Band 78 RX

band. This phenomenon is illustrated in Fig. 4.3. In this model, we assume a

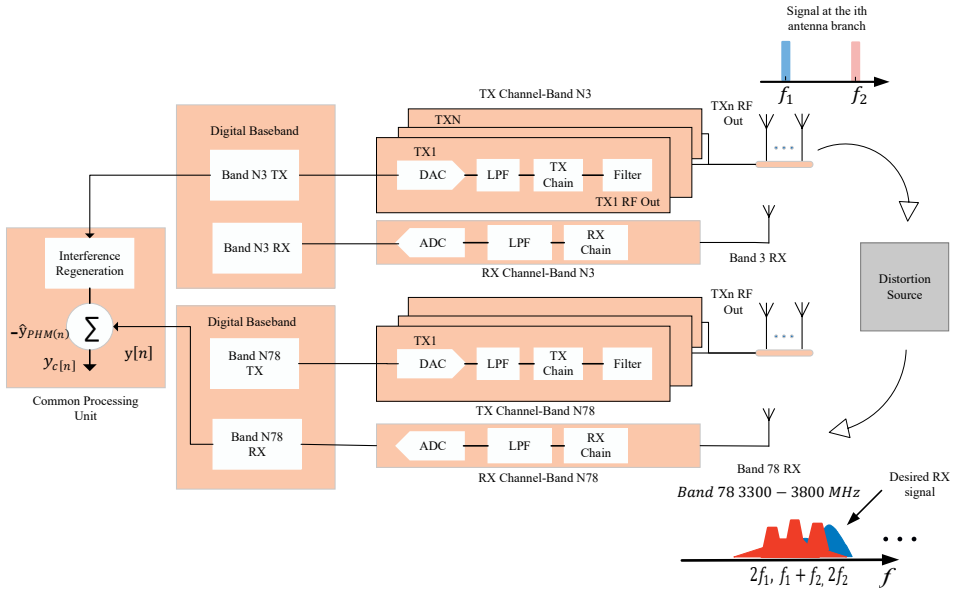

Figure 4.3 Simplified block diagram of the considered setup. The spectral illustration of the 2^{nd} order passive harmonic distortion created by passive metallic objects in the antenna near-field, falling onto the configured RX band is also shown.

generic MIMO-FDD transceiver, where the transmitter has N transmit antennas and utilizes CA with two CCs from Band 3 FDD and Band 78 TDD. The up-converted I/Q modulated signals from the $i-th$ transmitter are given by:

$$\begin{aligned} \tilde{x}_{1i}[n] &= \mathrm{Re}\{\alpha_{1i} x_{1i} e^{j\omega_1 n}\} \\ \tilde{x}_{2i}[n] &= \mathrm{Re}\{\alpha_{2i} x_{2i} e^{j\omega_2 n}\}, \end{aligned} \tag{4.16}$$

where x_{1i} and x_{2i} are the two CCs in the baseband, α_1 and α_2 are the complex gains and ω_1 and ω_2 are the angular centre frequencies of the carriers after upconversion. The combined TX signal on the $i-th$ antenna branch is then the addition of all the CC signals, i.e., $\tilde{x}_i[n] = \tilde{x}_{1i}[n] + \tilde{x}_{2i}[n]$. The signal from all the antennas is incident on a passive harmonic source in the antenna vicinity

and thus the signal after static PHM distortion is given by:

$$\begin{aligned}\tilde{y}_{PHM}[n] &= \sum_{p=1}^{P} \beta_p.(\sum_{i=1}^{N} \tilde{x}_i[n]))^p \\ &= \sum_{p=1}^{P} \beta_p.\{\mathrm{Re}\{(\alpha_{11}x_{11}[n] + \alpha_{12}x_{12}[n] + ... + \alpha_{1N}x_{1N}[n])e^{j\omega_1 n}\} \\ &+ \mathrm{Re}\{(\alpha_{21}x_{21}[n] + \alpha_{22}x_{22}[n] + ... + \alpha_{2N}x_{2N}[n])e^{j\omega_1 n}\}\}^p \\ &= \sum_{p=1}^{P} \beta_p\{\mathrm{Re}\{\psi_1[n]e^{j\omega_1 n}\} + \mathrm{Re}\{\psi_2[n]e^{j\omega_2 n}\}\}^p, \end{aligned} \tag{4.17}$$

where

$$\begin{aligned}\psi_1[n] &= \sum_{i=1}^{N} \alpha_{1,i}x_{1,i}[n] \\ \psi_2[n] &= \sum_{i=1}^{N} \alpha_{2,i}x_{2,i}[n].\end{aligned}$$

Now using the identities of the form

$$\mathrm{Re}\{ue^{jv}\} = 1/2(ue^{jv} + u^*e^{-jv}), \tag{4.18}$$

and

$$(u+v)^p = \sum_{k=0}^{p} \binom{p}{k} u^k v^{p-k}, \tag{4.19}$$

we expand the expression in (4.17) which yields

$$\begin{aligned}\tilde{y}_{PHM}[n] &= \sum_{p=1}^{P} \beta_p \times \\ &\sum_{k=0}^{p} \binom{p}{k} \frac{1}{2^k} \sum_{k_1=0}^{p} \binom{k}{k_1} \psi_1^{k_1} e^{jk_1\omega_1 n} (\psi_1^*)^{k-k_1} e^{j(k-k_1)\omega_1 n} \times \\ &\frac{1}{2^{p-k}} \sum_{k_2=0}^{p-k} \binom{p-k}{k_2} \psi_2^{k_2} e^{jk_2\omega_2 n} (\psi_2^*)^{p-k-k_2} e^{j(k+k_2-p)\omega_2 n}. \end{aligned} \tag{4.20}$$

It should be noted that (4.20) is actually the same as our base signal model in (4.2), only in this case we consider N transmit antennas and harmonic distortion. Evaluating (4.20) further, the passive harmonic distortion along with the basis function and their centre frequencies is then given by:

$$\begin{aligned}\tilde{y}_{PHM}[n] = \sum_{p=1}^{P}\sum_{k_1=0}^{p}\sum_{k_2=0}^{p-k}\gamma_{p,k_1,k_2}\times \\ \psi_1^{k_1}(\psi_1^*)^{k-k_1}\psi_2^{k_2}(\psi_2^*)^{p-k-k_2}\times \\ e^{j\left((2k_1-k)\omega_1+(2k_2+k-p)\omega_2\right)n}.\end{aligned} \tag{4.21}$$

In (4.21) the scaling factors and unknown complex PIM gains have been summed together as denoted by β_p in (4.20) and the overall effective coefficients are given by, γ_p, k_1, k_2. In this signal model, we are interested in the nonlinear terms that appear at the even-order harmonic frequencies, namely $2\omega_1$, $2\omega_2$ and $\omega_1+\omega_2$, which are more likely to appear at the RX band of Band 78. The basis functions for the signals at these frequencies can be obtained from (4.21) by setting certain rules for the positive integers k_1 and k_2. For instance, to obtain the basis functions at $2\omega_1$, we set,

$$\begin{aligned} 2k_1 - k = 2 \quad &\text{and} \quad 2k_2 + k - p = 0 \\ \rightarrow k_1 = \frac{1}{2}k + 1 \quad &\text{and} \quad k_2 = \frac{1}{2}(p-k), \end{aligned}$$

It can be noted that k_1 and k_2 need to be integers, to satisfy this k and p must be even. Similar conditions can be set to obtain basis functions at $2\omega_2$ by setting,

$$\begin{aligned} 2k_1 - k = 0 \quad &\text{and} \quad 2k_2 + k - p = 2 \\ \rightarrow k_1 = \frac{1}{2}k \quad &\text{and} \quad k_2 = 1 + \frac{1}{2}(p-k). \end{aligned}$$

Table. 4.2 shows the basis functions at frequencies $2\omega_1$ and $2\omega_2$, respectively.

Table 4.2 INSTANTANEOUS BASIS FUNCTIONS FOR $p = 2$ AND $p = 4$ FOR HARMONIC FREQUENCIES $2\omega_1$ AND $2\omega_2$

Value of p	**Basis functions,** $2\omega_1$	**Basis functions,** $2\omega_2$
2	$x_{11}^2,\ x_{12}^2, x_{11}x_{12}$	$x_{21}^2,\ x_{22}^2, x_{21}x_{22}$
4	$x_{11}^2,\ x_{12}^2, x_{11}x_{12},\ x_{11}^3x_{11}^*,$ $x_{11}^3x_{12}^*, x_{11}^2x_{12}x_{11}^*,\ x_{11}^2x_{12}x_{12}^*,$ $x_{12}^2x_{11}x_{11}^*,\ x_{12}^2x_{11}x_{12}^*,\ x_{12}^3x_{11}^*,$ $x_{12}^3x_{12}^*,\ x_{11}^2x_{12}x_{11}^*,\ x_{11}^2x_{12}x_{12}^*,$ $x_{11}x_{12}^2x_{11}^*,\ x_{11}x_{12}^2x_{12}^*,\ x_{11}^2x_{21}x_{21}^*,$ $x_{11}^2x_{21}x_{22}^*,\ x_{11}^2x_{22}x_{21}^*,\ x_{11}^2x_{22}x_{22}^*,$ $x_{12}^2x_{21}x_{21}^*,\ x_{12}^2x_{21}x_{22}^*,\ x_{12}^2x_{22}x_{21}^*,$ $x_{12}^2x_{22}x_{22}^*,\ x_{11}x_{12}x_{21}x_{21}^*,$ $x_{11}x_{12}x_{21}x_{22}^*,\ x_{11}x_{12}x_{22}x_{21}^*,$ $x_{11}x_{12}x_{22}x_{22}^*$	$x_{21}^2,\ x_{22}^2,\ x_{21}x_{22},$ $x_{21}^2x_{11}x_{11}^*,x_{21}^2x_{11}x_{12}^*,\ x_{21}^2x_{12}x_{11}^*,$ $x_{21}^2x_{12}x_{12}^*,\ x_{22}^2x_{11}x_{11}^*,\ x_{22}^2x_{11}x_{12}^*,$ $x_{22}^2x_{12}x_{11},\ x_{22}^2x_{12}x_{12}^*,$ $x_{21}x_{22}x_{11}x_{11}^*,\ x_{21}x_{22}x_{11}x_{12}^*,$ $x_{21}x_{22}x_{12}x_{11}^*,\ x_{21}x_{22}x_{12}x_{12}^*,$ $x_{21}^2x_{21}x_{21}^*,\ x_{21}^2x_{21}x_{22}^*,\ x_{21}^2x_{22}x_{21}^*,$ $x_{21}^2x_{22}x_{22}^*,\ x_{22}^2x_{21}x_{21}^*,\ x_{22}^2x_{21}x_{22}^*,$ $x_{22}^2x_{22}x_{21}^*,\ x_{22}^2x_{22}x_{22}^*,$ $x_{21}x_{22}x_{21}x_{21}^*,\ x_{21}x_{22}x_{21}x_{22}^*,$ $x_{21}x_{22}x_{22}x_{21}^*,\ x_{21}x_{22}x_{22}x_{22}^*$

The following rules are set for the corresponding basis functions at $\omega_1 + \omega_2$,

$$\begin{aligned} 2k_1 - k = 1 \qquad &\text{and} \quad 2k_2 + k - p = 1 \\ \rightarrow k_1 = \frac{1}{2}(k+1) \qquad &\text{and} \quad k_2 = \frac{1}{2}(1+p-k). \end{aligned}$$

In this case for k_1 and k_2 to be integers the value of k is set to 1 while again p is always even. The basis functions that are obtained by imposing these rules in (4.21) for $\omega_1 + \omega_2$ are given in Table. 4.3. In Table. 4.2 and Table. 4.3 without the loss of generality, we omit the time-domain index (t) to shorten the notations for better illustration purposes. The PHM distortion generated by a nonlinear source in the antenna near-field is then sensed by a co-located radio and is received with the actual desired signal.

Table 4.3 INSTANTANEOUS BASIS FUNCTIONS FOR $p = 2$ AND $p = 4$ FOR HARMONIC FREQUENCIES $\omega_1 + \omega_2$

Value of p	Basis functions, $\omega_1 + \omega_2$
2	$x_{11}x_{21}$, $x_{11}x_{22}$, $x_{12}x_{21}$, $x_{12}x_{22}$
4	$x_{11}x_{21}$, $x_{11}x_{22}$, $x_{12}x_{21}$, $x_{12}x_{22}$, $x_{11}x_{11}^*x_{11}x_{21}$, $x_{11}x_{11}^*x_{11}x_{22}$, $x_{11}x_{11}^*x_{12}x_{21}$, $x_{11}x_{11}^*x_{11}x_{22}$, $x_{11}x_{12}^*x_{11}x_{21}$, $x_{11}x_{12}^*x_{11}x_{22}$, $x_{11}x_{12}^*x_{12}x_{21}$, $x_{11}x_{12}^*x_{12}x_{22}$, $x_{12}x_{11}^*x_{11}x_{21}$, $x_{12}x_{11}^*x_{11}x_{22}$, $x_{12}x_{11}^*x_{12}x_{21}$, $x_{12}x_{11}^*x_{12}x_{22}$, $x_{12}x_{12}^*x_{11}x_{21}$, $x_{12}x_{12}^*x_{11}x_{22}$, $x_{12}x_{12}^*x_{12}x_{21}$, $x_{12}x_{12}^*x_{11}x_{21}$, $x_{12}x_{12}^*x_{12}x_{22}$, $x_{21}x_{21}^*x_{11}x_{21}$, $x_{21}x_{21}^*x_{11}x_{22}$, $x_{21}x_{21}^*x_{12}x_{21}$, $x_{21}x_{21}^*x_{12}x_{22}$, $x_{21}x_{21}^*x_{11}x_{21}$, $x_{21}x_{22}^*x_{11}x_{22}$, $x_{21}x_{22}^*x_{12}x_{21}$, $x_{21}x_{22}^*x_{12}x_{22}$, $x_{22}x_{21}^*x_{11}x_{21}$, $x_{22}x_{21}^*x_{11}x_{22}$, $x_{22}x_{21}^*x_{12}x_{21}$, $x_{22}x_{22}^*x_{11}x_{21}$, $x_{22}x_{22}^*x_{11}x_{22}$, $x_{22}x_{22}^*x_{12}x_{21}$, $x_{22}x_{22}^*x_{12}x_{22}$

4.4 Digital Cancellation of PIM and Parameter Estimation

In order to achieve cancellation of the PIM distortion at the DFE, a precise estimation of the dominant PIM waveform is needed. Note that in this Section we restrict the parameter estimation and digital cancellation discussion to PIM waveform only. However, the same methods can also be applied to the PHM distortion cancellation and parameter estimation as well for the signal model given in Section 4.3, especially the LS-based estimation which we will discuss in the following Section. Given this, the cancelled signal is expressed formally as,

$$y_{\mathrm{c}}[n] = y[n] - \hat{y}_{\mathrm{PIM}}[n]. \tag{4.22}$$

Where $y[n]$ denotes the cumulative observed received signal and $\hat{y}_{\mathrm{PIM}}[n]$ refers to the PIM waveform estimate, all in baseband. In order to be able to reconstruct the PIM estimate $\hat{y}_{\mathrm{PIM}}(n)$ the unknown model parameters for

the signal models given in Section 4.2 and 4.3 must be estimated. For the estimation of unknown parameters, we proposed the following two solutions.

- *Linear LS-Based estimation:* Relevant only to the linear-in-parameters models in (4.6) and (4.12)
- *Novel Gradient-Descent-Based Adaptive Estimation and Cancellation:* Relevant for all the signal models in (4.6), (4.12) and (4.14) (4.15) (4.20).

Furthermore, it is noted that the gradient-descent-based solution is different for the linear-in-parameter models and for the decoupled memory model. This will be elaborated further later in Section 4.4.2 and the Appendixes. Fig. 4.4, illustrates the overall parameter estimation and cancellation framework at a conceptual level. It is further noted that accurate synchronization, in time and frequency, between the TX and RX signals is considered in the following. Frequency synchronization is easy to accomplish since cancellation processing takes place inside the same transceiver. Time synchronization, or propagation delay between the TX digital baseband and RX digital baseband can easily be estimated offline. This is because this delay is fixed in the hardware and does not necessarily change over time.

4.4.1 Least-Squares-Based Batch Estimation

This cancellation procedure is applicable for the linear-in-parameters models in (4.6), (4.12) and (4.22). For starters, N samples of the observed signal $y[n]$ are collected into a vector as:

$$\mathbf{y} = \begin{bmatrix} y[0] & y[1] & \cdots & y[N-1] \end{bmatrix}^T, \tag{4.23}$$

For a more convenient notation, we start the sample indexing from 0 without losing generality. Derived from the previous modeling results it is then simple to show that the observed signal vector under PIM distortion can be presented as:

$$\mathbf{y} = \mathbf{\Psi}\boldsymbol{\gamma} + \mathbf{z}. \tag{4.24}$$

Where $\mathbf{\Psi}$ is the data matrix that is made up of the known TX data and its

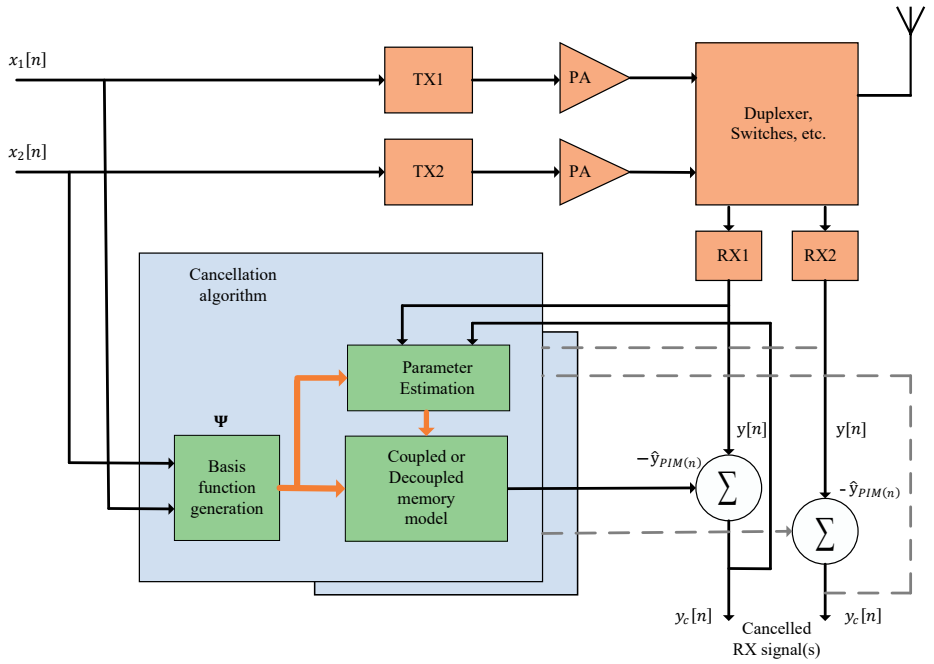

Figure 4.4 Complete estimation and cancellation procedure, including the options for both batch-LS and gradient-descent-based parameter learning algorithms. The option of cancelling PIM at the RX band is also included. The thicker arrows represent the vector inputs and outputs, **Publication-IV**.

basis functions. $\boldsymbol{\gamma}$ contains the unknown coefficients that are to be estimated. $\mathbf{z}$ represents noise and other unmatched signals. Additionally, $\mathbf{z}$ also consists of the originally received signal-of-interest (SoI), if it exists during parameter estimation.

To instantiate the structure of the matrix $\boldsymbol{\Psi}$, we first define the vector for the instantaneous basis functions. This vector collects all the samples of the basis functions at the time of instantiation t. The number of elements in the basis functions vector depends upon the cardinality of all the states of the variable s, which of course depends on the PIM model. To represent the parameter estimation method in a generic manner that can be utilized for both the PIM models in (4.6) and (4.12), the basis function vector is defined as:

$$\boldsymbol{\phi}[n] = \begin{bmatrix} \phi_{\mathbf{s}_1}[n] & \phi_{\mathbf{s}_2}[n] & \cdots & \phi_{\mathbf{s}_C}[n] \end{bmatrix}^T, \tag{4.25}$$

Where s_i represents the different states of the variable s and C is the cardinality of the adopted signal model.

After constructing the instantaneous basis functions vector the overall data matrix is then given by:

$$\boldsymbol{\Psi} = \begin{bmatrix} \boldsymbol{\phi}[M_1]^T & \boldsymbol{\phi}[M_1-1]^T & \cdots & \boldsymbol{\phi}[-M_2]^T \\ \boldsymbol{\phi}[M_1+1]^T & \boldsymbol{\phi}[M_1]^T & \cdots & \boldsymbol{\phi}[-M_2+1]^T \\ \vdots & \vdots & \ddots & \vdots \\ \boldsymbol{\phi}[M_1+N-1]^T & \boldsymbol{\phi}[M_1+N-2]^T & \cdots & \boldsymbol{\phi}[-M_2+N-1]^T \end{bmatrix}, \tag{4.26}$$

where the observed signal y determines the indexing of the block. Using this the LS estimates is then given by [33]

$$\hat{\boldsymbol{\gamma}} = \min_{\boldsymbol{\gamma}} \|\mathbf{y} - \boldsymbol{\Psi}\boldsymbol{\gamma}\|_2^2 = (\boldsymbol{\Psi}^H\boldsymbol{\Psi})^{-1}\boldsymbol{\Psi}^H\mathbf{y}. \tag{4.27}$$

where $\|.\|_2$ is the l^2-norm and $(.)$ is the *Hermitian* transpose.

After learning the coefficients the canceled signal after the online operation of the RX is given by:

$$y_c[n] = y[n] - \boldsymbol{\Psi}_n\hat{\boldsymbol{\gamma}}, \tag{4.28}$$

where,

$$\boldsymbol{\Psi}_n = \begin{bmatrix} \boldsymbol{\phi}[n+M_1]^T & \boldsymbol{\phi}[n+M_1-1]^T & \cdots & \boldsymbol{\phi}[n-M_2]^T \end{bmatrix}. \tag{4.29}$$

The same learned coefficients can be used unless the properties of the effective coupling channel change. Since this whole processing happens inside the transceiver, the parameters are updated rarely, for example, if the operating temperature of the device changes dramatically. In some cases such as when PIM occurs beyond the antenna interface, the parameters might need to be updated repetitively. This is where adaptive estimation methods come in handy,

which we will discuss next.

4.4.2 Gradient Descent-Based Adaptive Estimation

The LS estimate can be computationally heavy, especially when the data size is very large, so iterative solutions are more convenient in many cases. This work proposes a gradient descent-based learning on the instantaneous error. It is important to note that this method is also suitable for the decoupled memory model, as LS is not linear-in-parameter, so it does not work there.

4.4.2.1 Orthogonalized Adaptive Estimation for Linear-in-Parameters Signal Models

For the linear-in-parameter models in (4.6) and (4.12), the signal after cancellation can be rewritten as:

$$y_c[n] = y[n] - \mathbf{\Psi}_n \hat{\boldsymbol{\gamma}}_n, \tag{4.30}$$

where $\hat{\boldsymbol{\gamma}}_n$ is now the vector of the estimates at $n\hat{}th$ iteration. It is evident from this equation that it is a linear-in-parameters model by nature since the cancellation signal can be rewritten as matrix-vector multiplication between the basis functions vector and the parameter estimates. This means that the LMS-type learning can be directly applied as in [33] and without the nonlinear terms. Given this, the basic learning rules can be expressed as follows:

$$\hat{\boldsymbol{\gamma}}_{n+1} = \hat{\boldsymbol{\gamma}}_n + \mu_{\boldsymbol{\gamma}} y_c[n] \mathbf{\Psi}_n^H. \tag{4.31}$$

Where the learning rate is denoted by $\mu_{\boldsymbol{\gamma}}$.

Now the learning rule in (4.31) is widely used and is recognized to be very accurate for linear systems. However, in the case of PIM cancellation, convergence can be slow because of the strong correlation between the basis functions. Therefore, better performance can be obtained by orthogonalizing different elements in $\mathbf{\Psi}_n$ during the parameter update phase. This includes computing the inverse of the correlation matrix for the input vector and using the resulting vector as a multiplier for the learning rule [33, p. 356]. With this method, the

cancellation phase remains the same as in (4.30), though the learning rule is as follows:

$$\hat{\boldsymbol{\gamma}}_{n+1} = \hat{\boldsymbol{\gamma}}_n + \mu_{\boldsymbol{\gamma}} y_c[n] \left(\mathbf{R}^*_{\boldsymbol{\Psi}_n}\right)^{-1} \boldsymbol{\Psi}_n^H, \tag{4.32}$$

where $\mathbf{R}_{\boldsymbol{\Psi}_n} = \mathrm{E}\left[\boldsymbol{\Psi}_n \boldsymbol{\Psi}_n^H\right]$ is the correlation matrix of the input vector to the filter. It should be noted that, now, since the parameter update is presented for the complex conjugate of the classical definition of the learning rule, the correlation matrix must also be complex conjugated.

Next, to be able to determine a more robust expression for $\mathbf{R}^*_{\boldsymbol{\Psi}_n}$, with some assumptions as compared to the original expression we first rewrite it as follows:

$$\begin{aligned}
\mathbf{R}^*_{\boldsymbol{\Psi}_n} =& \mathrm{E}\left[\boldsymbol{\Psi}_n^* \boldsymbol{\Psi}_n^T\right] \\
=& \mathrm{E}\Bigg[\begin{bmatrix}\boldsymbol{\phi}[n+M_1]^T & \boldsymbol{\phi}[n+M_1-1]^T & \cdots & \boldsymbol{\phi}[n-M_2]^T\end{bmatrix}^T \\
& \times \begin{bmatrix}\boldsymbol{\phi}[n+M_1]^T & \boldsymbol{\phi}[n+M_1-1]^T & \cdots & \boldsymbol{\phi}[n-M_2]^T\end{bmatrix}^*\Bigg] \\
=& \mathrm{E}\left[\begin{bmatrix}\boldsymbol{\phi}[n+M_1] \\ \vdots \\ \boldsymbol{\phi}[n-M_2]\end{bmatrix}\begin{bmatrix}\boldsymbol{\phi}[n+M_1]^H & \cdots & \boldsymbol{\phi}[n-M_2]^H\end{bmatrix}\right].
\end{aligned} \tag{4.33}$$

It is evident from (4.33) that the correlation matrix has a blockwise structure, where each of the vectors is of the form $\mathrm{E}\left[\boldsymbol{\phi}[i]\boldsymbol{\phi}[j]^H\right]$. We define two simple assumptions about the transmitted waveform, which can be linked to modern radio communication systems. First, the transmission signals, i.e., the CCs, are both independent and identically distributed with zero mean. As a result, transmit signal properties do not change over time.

Considering the first assumption we can write $\mathrm{E}\left[\boldsymbol{\phi}[i]\boldsymbol{\phi}[j]^H\right] = \mathbf{0}$, when $i \neq j$. That is, the correlation matrix has a block-diagonal structure. Then, considering the second assumption, it states for the remaining diagonal elements that,

$\mathrm{E}\left[\boldsymbol{\phi}[i]\boldsymbol{\phi}[i]^H\right] = \mathrm{E}\left[\boldsymbol{\phi}[j]\boldsymbol{\phi}[j]^H\right]$ for any i and j.

Given these findings, the complex conjugate of the complete correlation matrix can hence, be expressed as, $\mathbf{R}^*_{\mathbf{\Psi}_n} = \text{diag}\left\{\mathbf{R}^*_{\boldsymbol{\phi}}, \ldots, \mathbf{R}^*_{\boldsymbol{\phi}}\right\}$, where $\mathbf{R}_{\boldsymbol{\phi}}$ is the correlation matrix of the basis functions, whose complex conjugate is simply repeated M_1+M_2+1 times on the diagonal. Utilizing this expression, the inverse of the complete correlation matrix is $\left(\mathbf{R}^*_{\mathbf{\Psi}_n}\right)^{-1} = \text{diag}\left\{\left(\mathbf{R}^*_{\boldsymbol{\phi}}\right)^{-1}, \ldots, \left(\mathbf{R}^*_{\boldsymbol{\phi}}\right)^{-1}\right\}$, as defined by the inversion rule of block diagonal matrices. It should be noted it is assumed that the statistical properties of the basis functions are not changed throughout the operation and thus the inverse $\mathbf{R}^*_{\boldsymbol{\phi}}$ can also be calculated offline. Given these facts, the learning rule can then be expressed as follows:

$$\hat{\boldsymbol{\gamma}}_{n+1} = \hat{\boldsymbol{\gamma}}_n + \mu_{\boldsymbol{\gamma}} y_c[n] \text{diag}\left\{\left(\mathbf{R}^*_{\boldsymbol{\phi}}\right)^{-1}, \ldots, \left(\mathbf{R}^*_{\boldsymbol{\phi}}\right)^{-1}\right\} \mathbf{\Psi}_n^H. \tag{4.34}$$

This expression gives considerably reduced computational requirements as compared to the learning rule in (4.32), since during the parameter update phase matrix inversion is not needed. Additionally, the earlier calculated orthogonalizing basis functions samples can be used in each iteration, so computing only the latest basis functions vector is sufficient.

4.4.2.2 Orthogonalized Adaptive Estimation for Decoupled Signal Models

The traditional LMS-based approach is not suitable for the decoupled memory model with cascaded nonlinearity described in Section 4.2 and hence we must formulate the necessary learning rules by resorting to the theory behind gradient descent learning and complex-valued gradients. This adaptive estimation for the decoupled signal models is illustrated conceptually in Fig. 4.5 followed by a detailed discussion as follows:

Based on (4.14) and (4.15) and by using the basis function vector notation, the cancelled signal in this particular case is expressed as:

$$y_{\text{c}}(n) = y(n) - \mathbf{h}_n^H \mathbf{y}_{n,\text{NL}}, \tag{4.35}$$

where $\mathbf{h}_n$ is the memory model estimate in the shape of a vector, and $\mathbf{y}_{n,\text{NL}} = \begin{bmatrix} y_{\text{NL}}(n+M_1) & \cdots & y_{\text{NL}}(n-M_2) \end{bmatrix}$. Furthermore,, $y_{\text{NL}}(n) = \mathbf{g}_n^H \boldsymbol{\phi}(n)$, where $\mathbf{g}_n$ contains the coefficients of the nonlinear basis functions ($\gamma_{\mathbf{s}}$).

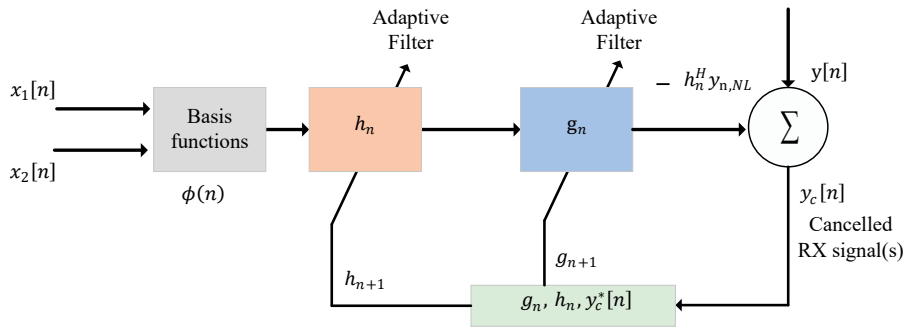

Figure 4.5 Estimation and cancellation procedure with adaptive parameter learning for decoupled signal models

By specifying the cost function as $J(\mathbf{g}_n, \mathbf{h}_n) = |y_{\mathrm{c}}(n)|^2$, the learning rule for the PIM model coefficients can be given as:

$$\mathbf{g}_{n+1} = \mathbf{g}_n - \mu_g \frac{\partial J(\mathbf{g}_n, \mathbf{h}_n)}{\partial \mathbf{g}_n}, \tag{4.36}$$

where μ_g is the PIM coefficient step size. As shown in Appendix A, the complex partial derivative can be expressed as:

$$\frac{\partial J(\mathbf{g}_n, \mathbf{h}_n)}{\partial \mathbf{g}_n} = -2y_{\mathrm{c}}^*(n)\mathbf{\Phi}_n\mathbf{h}_n^*, \tag{4.37}$$

where $\mathbf{\Phi}_n = \begin{bmatrix}\boldsymbol{\phi}(n+M_1) & \cdots & \boldsymbol{\phi}(n-M_2)\end{bmatrix}$. Hence, we can represent the final learning rule for $\mathbf{g}_n$ as:

$$\mathbf{g}_{n+1} = \mathbf{g}_n + \mu_g y_{\mathrm{c}}^*(n)\mathbf{\Phi}_n\mathbf{h}_n^*. \tag{4.38}$$

To learn the memory model, it can be noted that the system is in fact similar to the classical LMS filter with $\mathbf{y}_{n,\mathrm{NL}}$ as the signal at the input, which means that we can adopt a similar learning rule for h_n, given as,

$$\mathbf{h}_{n+1} = \mathbf{h}_n + \mu_h y_{\mathrm{c}}^*(n)\mathbf{y}_{n,\mathrm{NL}}. \tag{4.39}$$

where μ_h is the memory step size.

Now, again because of the mutual correlation between the nonlinear basis

functions $\boldsymbol{\phi}(n)$, the decoupled learning rule in (4.38) also suffers from slow convergence, similarly as in the case of a linear-in-parameter signal model. To resolve this issue, a similar self-orthogonalizing learning rule can be used instead. Utilizing similar steps as in [33, p. 356], in the linear system case we represent the input vector by $\mathbf{u}_n = \boldsymbol{\Phi}_n \mathbf{h}_n^*$. Building on this, the self-orthogonalizing learning rule can be given by:

$$\mathbf{g}_{n+1} = \mathbf{g}_n + \tilde{\mu}_g \mathbf{R}^{-1} e^*(n) \mathbf{u}_n, \tag{4.40}$$

Where $\tilde{\mu}_g$ is the step-size, and $\mathbf{R} = \mathrm{E}\left[\mathbf{u}_n \mathbf{u}_n^H\right]$ is the correlation matrix of the input vector to the filter. One of the drawbacks of this model is that the correlation vector depends on the time-variant model h_n, meaning that the correlation matrix must be computed and inverted upon each iteration, which makes this method extremely complex computationally.

In order to reduce computational complexity and make the self-orthogonalizing rule more acceptable interms of implementation complexity, let us represent the correlation matrix in a more convenient form. By following the steps in Section A.2 the correlation matrix can be given as follows:

$$\mathbf{R} = \mathbf{R}_{\boldsymbol{\phi}} \mathbf{h}_n^H \mathbf{h}_n, \tag{4.41}$$

where $\mathbf{R}_{\boldsymbol{\phi}}$ is the correlation matrix of the basis functions, defined identically as in (4.34) meaning that it is also a block diagonal matrix. It is best to keep in mind that $\mathbf{R}_{\boldsymbol{\phi}}$ is only based on the chosen signal model and the statistical properties of the utilized waveforms, which means that it can be computed offline along with its inverse.

Inferring from the above we can then rewrite the self-orthogonalizing learning rule as:

$$\begin{aligned} \mathbf{g}_{n+1} =& \mathbf{g}_n + \frac{\tilde{\mu}_g}{\mathbf{h}_n^H \mathbf{h}_n} \mathbf{R}_{\boldsymbol{\phi}}^{-1} y_{\mathrm{c}}^*(n) \mathbf{u}_n \\ =& \mathbf{g}_n + \mu_{g,\mathrm{ort}} \mathbf{R}_{\boldsymbol{\phi}}^{-1} y_{\mathrm{c}}^*(n) \boldsymbol{\Phi}_n \mathbf{h}_n^*. \end{aligned} \tag{4.42}$$

where $\mu_{g,\mathrm{ort}}$ is the final step-size. Additionally, it should be noted that the step size as a simplification can be approximated to be fixed with only a small effect on the convergence even though $\mathbf{h}_n^H \mathbf{h}_n$ is is in principle time-variant. However

in practice, h_n is likely to be very slowly varying, therefore this approximation is plausible. Matrix R_{Φ}^{-1} is also fixed and can be precomputed.

4.5 Processing and Learning Complexities and Comparison

In this Section, we discuss the complexity and make comparisons, while focusing only on the proposed gradient descent-based methods. The basic cancellation complexities are studied for the given parameter estimates, and the actual parameter estimation complexities are distinguished.

Resulting directly from the cancellation processing solutions in (4.30) and (4.35), and from the parameter update rules in (4.34), (4.39) and (4.42), the basic complexity numbers in terms of the number of complex multiplications per cancelled sample or per parameter update cycle are provided in Table. 4.4. It is to be noted that the complexities of the coupled and decoupled memory models which also include the nonlinearities of the PAs are expressed for clarity in terms of C, which indicates the total amount of basis functions. It can be expressed generally as:

$$C = R(2Q+1)\left[(2Q+1)\left(\frac{R+1}{2}\right) - Q\right]. \tag{4.43}$$

It is clear from the mathematical expression in 4.4 that the decoupled memory model is especially more efficient in the cancellation phase compared with the basic coupled models. It can be observed that the cancellation complexity of the decoupled model is additive in nature, while for the coupled model it is multiplicative.

In order to elaborate further on the complexity, let us consider the model parameters of $R = 1$, $Q = 2$, and $M = 8$, a parameter which we will also use in the next Chapter when discussing the RF measurement results. Setting these values results in only 1 basis function for the model with linear PAs, while the model with nonlinear PAs have $C = 15$ basis functions. Additionally, in the model with linear PAs, the parameter update phase involves 9 complex multiplications. In contrast, the cancellation phase involves 8 complex multiplications, which in total are 17 complex multiplications. Similarly, for the coupled model

Table 4.4 CANCELLATION PROCESSING AND GRADIENT-BASED PARAMETER UPDATE COMPLEXITIES CORRESPONDING TO THE THREE SIGNAL MODELS. HERE, $M = M_1 + M_2 + 1$, WHILE C IS THE NUMBER OF BASIS FUNCTIONS IN THE MODELS WITH NONLINEAR PAS, EXPRESSED IN (4.43).

Signal model	**Parameter update**	**Cancellation**	**Total**
Linear PAs with coupled memory	$\frac{R(R+1)}{2}\left(\frac{R(R+1)}{2}+M\right)$	$\frac{MR(R+1)}{2}$	$\frac{R(R+1)}{2}\left(\frac{R(R+1)}{2}+2M\right)$
Nonlinear PAs with coupled memory	$C\left(C+M\right)$	CM	$C\left(C+2M\right)$
Nonlinear PAs with decoupled memory	$\left(C+M\right)\left(C+1\right)$	$C+M$	$\left(C+M\right)\left(C+2\right)$

with nonlinear PAs, the parameter update phase consists of 345 complex multiplications, and the cancellation requires further 120 multiplications. Thus the total amount of complex multiplications required per iteration is 465, significantly higher than the simple model with linear PAs. Finally, for the cascaded model with the decoupled memory, the parameter update phase requires 368 complex multiplications while the cancellation requires only 23 complex multiplications, the total number of complex multiplications being only 391. In the decoupled model we notice that the fundamental cancellation processing is 5 times more efficient compared to the coupled memory model and since the PIM in most cases is generated by the device's internal components, there is no need to constantly update the parameters, thus the cascaded model with decoupled memory provides a very attractive complexity reduction.

CHAPTER 5

RF MEASUREMENT RESULTS AND ANALYSIS

In this chapter the performance of the suggested PIM cancellers is studied with the measured signals and LTE-Advanced UE RF components, in the context of Band 1 + Band 3 interband CA, by utilizing all the three signal models given in Section 4.2 and the related digital PIM cancellation solutions. We also briefly discuss the results from **[Publication-II]** where PIM is coupled over-the-air from the main transceiver to the diversity RX branch. For simplicity, the measurement results are categorized as internal PIM sources with UE and external PIM sources with a base station.

5.1 Evaluation of Internal PIM Sources in UE

In this Section, we evaluate the performance of the proposed PIM canceller for the scenarios where PIM is generated by the internal components present in the UE. In this measurement we utilize a hardware similar to UE, however, this is not limited only to the UE but the internal components present in a base station can also generate similar PIM.

5.1.1 Measurement Setup

The RF measurements are performed in an isolated anechoic chamber to avoid interference from external sources. The measurement setup and the test environment are shown in Fig. 5.1 and 5.2. Furthermore, the relevant features of the measurement scenario and the digital canceller are listed in Table. 5.1. In this setup, two CP-OFDM based CCs with QPSK modulation are generated by using the Analog Devices AD9368-2 2×1 transceiver board.

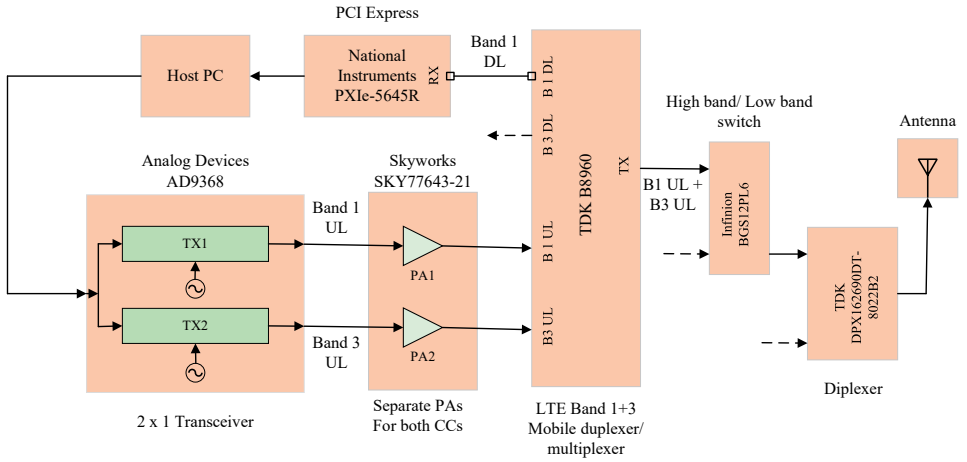

Figure 5.1 Transceiver system structure adopted in the RF measurements. The utilized device and RF component models are shown in the figure, **Publication-IV**.

The CCs are then amplified using two separate Skyworks SKY77643-21 PAs. After the amplification stage, the CCs are combined with a TDK B8960 duplexer/multiplexer, the aggregated TX signal being then fed to an Infineon BGS12PL6 switch and a TDK DPX162690DT-8022B2 diplexer. Towards the end, the diplexer is then connected to an antenna, as can be seen in Fig. 5.1 and 5.2. The National Instruments PXIe-5645R acts as the receiver and digitizer. It should be noted that the AD9368-2 is a pre-commercial not publicly available dual-TX transceiver system with maximum instantaneous BW per channel of 250 MHz and tuning range of $700 - 2800$ MHz. The specification and performance of this board are similar to the commercially available AD9371, however, the frequency tuning range of AD9371 extends further up to 6 GHz.

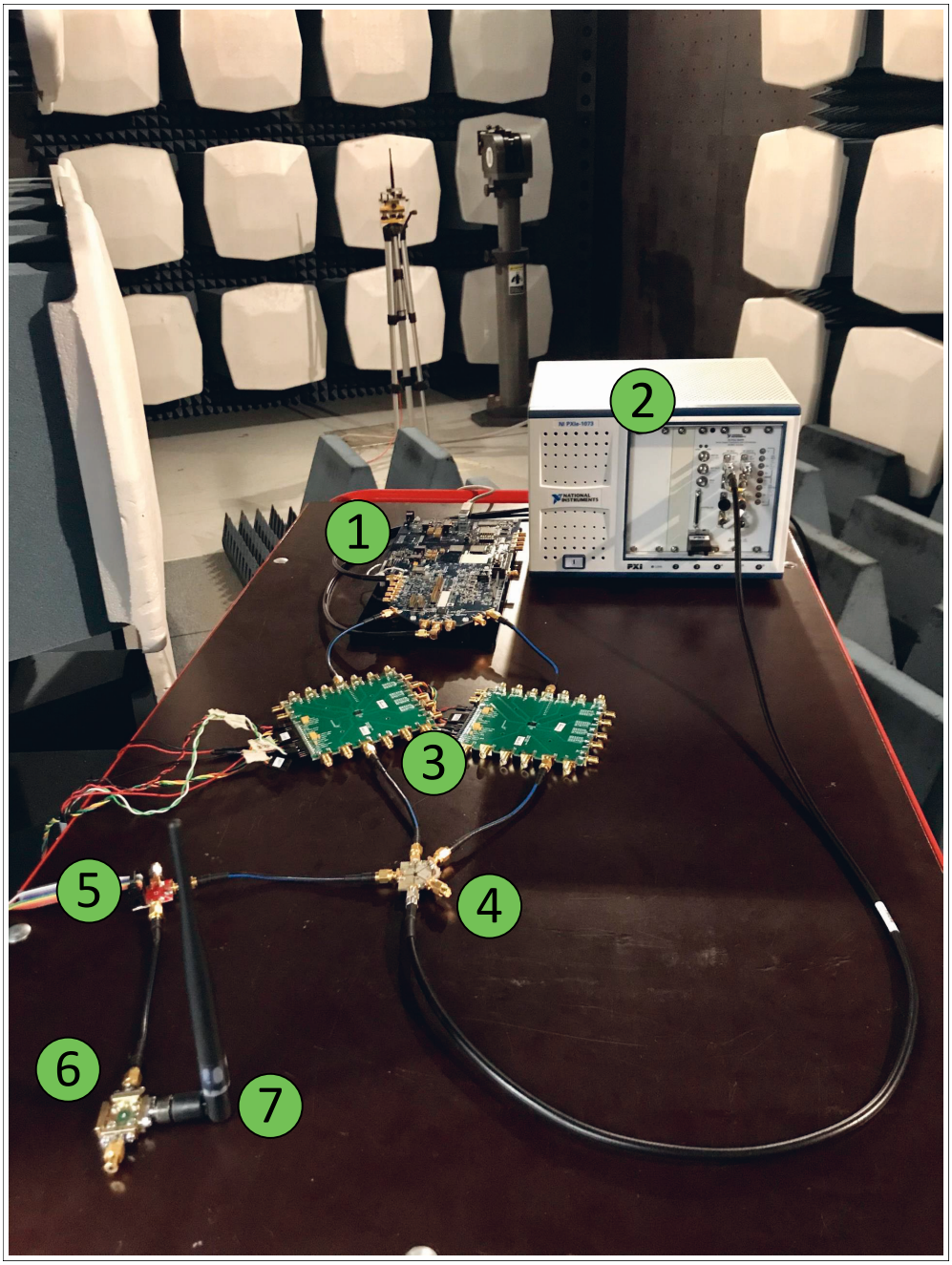

Figure 5.2 Overall RF measurement setup in the isolated chamber, featuring the Analog Devices AD9368-2 board (1), National Instruments PXIe-5645R observation receiver (2), Skyworks SKY77643-21 PAs (3), TDK B8960 multiplexer (4), Infineon BGS12PL6 switch (5), TDK DPX162690DT-8022B2 diplexer (6), and Delta 6A antenna (7), **Publication-IV**.

Table 5.1 LTE-ADVANCED B1+B3 RF MEASUREMENT SCENARIO AND CONSIDERED PIM CANCELLER PARAMETERS. SOME OF THE PARAMETERS ARE ALSO VARIED IN THE MEASUREMENTS.

Feature	Value	
CC bandwidth	5 MHz	10 MHz
CC1 center frequency	1950 MHz	1950 MHz
CC2 center frequency	1760 MHz	1760 MHz
RX center frequency	2140 MHz	2140 MHz
PA gain	28 dB	28 dB
Total TX power at antenna	24 dBm	24 dBm
Cancellation sample rate	31.72 MHz	43.88 MHz
Parameter learning sample size (N)	90 000	120 000
PIM model nonlinearity order ($P = 2R + 1$)	3	3
PA model nonlinearity order ($2Q + 1$)	5	5
Number of PIM pre-cursor taps (M_1)	3	3
Number of PIM post-cursor taps (M_2)	4	4

To obtain proper time synchronization in the measurements, the received sample sequence is correlated with a sequence of the third-order basis function samples, as shown in the first row of Table. 5.1. These can be directly calculated using the TX CC sequences $x_1[n]$ and $x_2[n]$. This is very well justified as the basic third-order basis function is dominant in power compared with the other basis functions. Further details about the measurement setup features can be checked from **Publication-IV** as they are already described there in detail. In the next Section on measurement results, we will study the impact of possible timing offsets. As far as the basic measurement is concerned, no actual SoI was received, however, the impact of SoI on the actual parameter learning is also examined. In addition, we also establish frequency synchronization on the hardware such that both transmitting and receiving entities are frequency-locked. This frequency synchronization is achieved via a MATLAB script. The "Analog Devices" board is fed a clock frequency of 30.72 MHz from an external signal generator and also the TX signal generators are fed from an external signal generator to the "Analog Devices" board. A reference signal is then taken out from one of the signal generator and is fed to the VST for frequnecy synchronization.

5.1.2 Measurement Results

In this Section, we first consider the PIM distortion with the full transmit power of +24 dBm. The essential power spectral densities (PSDs) using the default features listed in Table. 5.1 of each canceller are shown in Fig. 5.3 and 5.4, respectively. Firstly, it is evident that the PIM-induced distortion is a serious problem in FDD transceivers operating on the frequency bands in consideration. The PIM-induced SI is almost 20 dB above the noise floor, even when using state-of-the-art RF components. Secondly, Fig. 5.3 and 5.4 show that each of the proposed signal models, and the related digital cancellers are able to cancel PIM-induced SI efficiently. Furthermore, it is also evident that including the PA nonlinearities in the signal models is indeed beneficial for more accurately suppressing the PIM distortion. Another important finding based on Fig. 5.3 and 5.4 is that the cascaded model with the decoupled memory can achieve almost the same amount of cancellation performance as the much more complex model that has the coupled memory, even though its computational complexity is lower by over five times. In general, when the nonlinear distortion generated by each of the individual PA is taken into consideration, the amount of cancellation is improved by about $4-5$ dB with the 5-MHz carrier and some $2-3$ dB with 10-MHz CCs, in contrast to the linear PA-based canceller.

Next, Fig. 5.5 and 5.6 show the leftover power of the noise and interference with respect to the total transmit power. It is evident that with both the CCs bandwidth the PIM-induced interference is still above the noise level than with the transmit power of as low as 15 dBm if no digital cancellation is performed. However, as proposed modelling and cancelling the PIM even with a simple model assure almost interference-free reception and provide cancellation with transmit power of up to +20 dBm. The range of the transmit power can further be increased by using more advanced signal models that include taking into consideration the PA-induced nonlinearities. The canceller solutions that incorporate the PA nonlinearities of 10 MHz are capable of significantly efficient cancellation with the highest transmit power of +24 dBm. This is even when the CCs are 10 MHz. The results in, Fig. 5.5 and 5.6 also show that the model with decoupled memory is also able to provide nearly identical cancellation as the model with coupled memory thus showing favorable complexity-accuracy

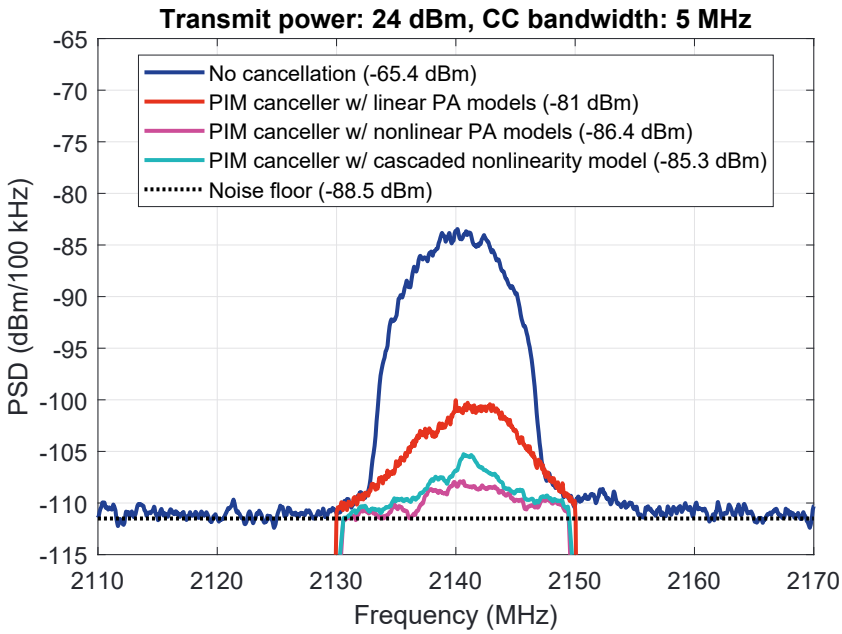

Figure 5.3 Measured PSDs of the PIM distortion at own RX band with different cancellation solutions, using a CC bandwidth of 5 MHz, **Publication-IV**

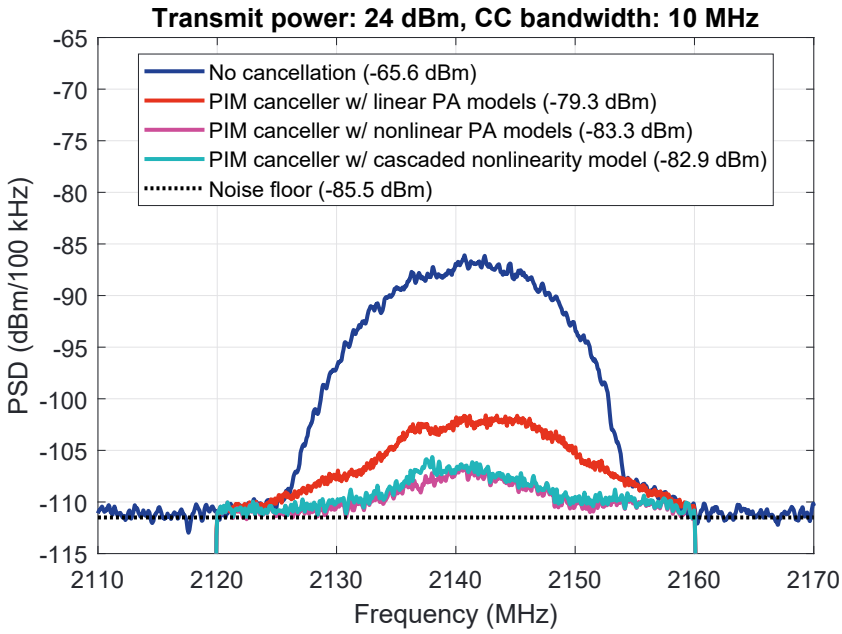

Figure 5.4 Measured PSDs of the PIM distortion at own RX band with different cancellation solutions, using a CC bandwidth of 10 MHz, **Publication-IV**

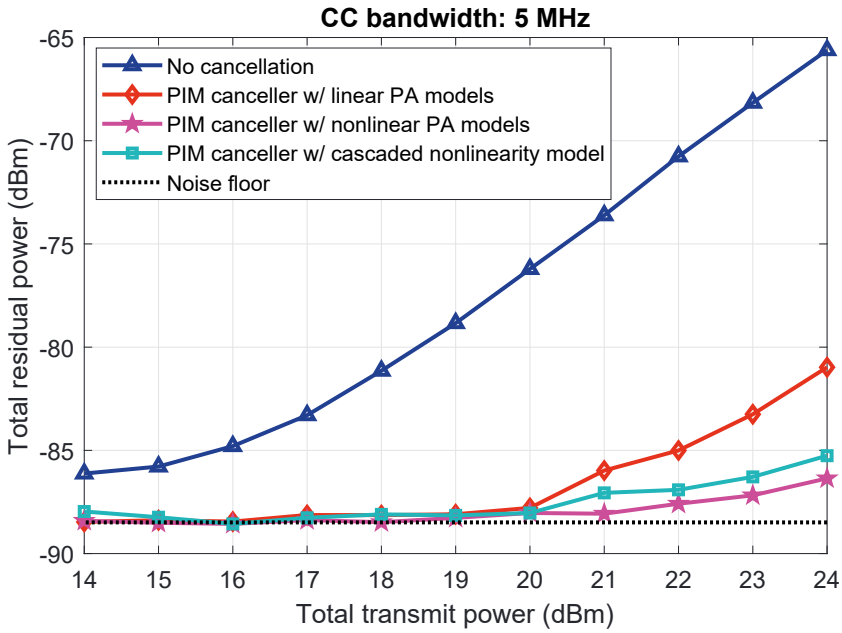

Figure 5.5 Measured PIM cancellation performance with respect to the total transmit power, using a CC bandwidth of 5 MHz, **Publication-IV.**

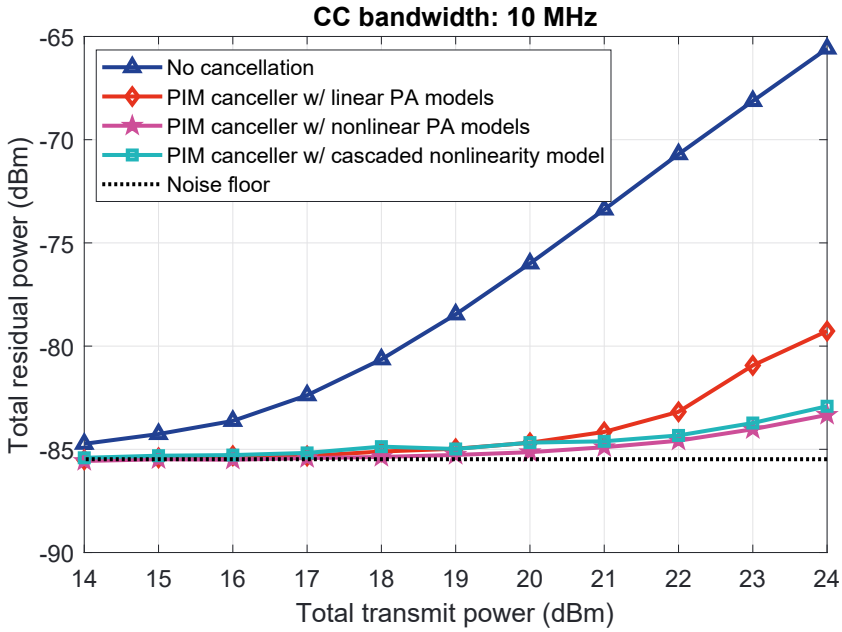

Figure 5.6 Measured PIM cancellation performance with respect to the total transmit power, using a CC bandwidth of 10 MHz, **Publication-IV**

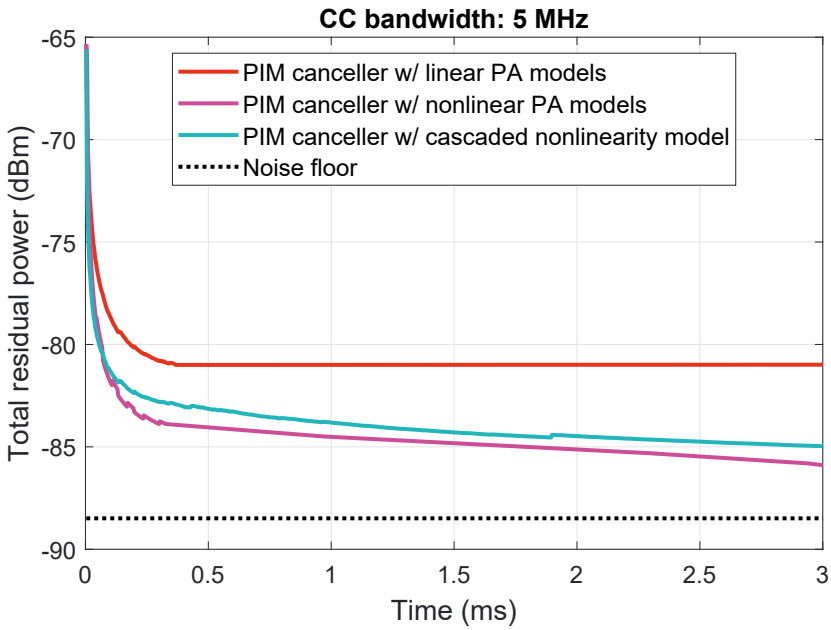

Figure 5.7 Example convergence of the measured residual total power (PIM+noise) over time for the gradient-adaptive PIM cancellers. The CC bandwidth is 5 MHz, and the TX power is +24 dBm, **Publication-IV**.

trade-off of the derived cascaded model.

Gradient-descent-based adaptive learning relies heavily on convergence and learning rate. Therefore, Fig. 5.7 shows the convergence of the residual PIM distortion plus noise power over time, considering an example of the case of CCs of 5 MHz bandwidth. The gradient-descent-based learning rules support accurate convergence for all three canceller types, with the residual power level being very close to the steady state level within $0.5 - 2$ ms. Given the sample rate of 30.72 MHz, this is almost the same as $15000 - 60,000$ samples. It is also noticed that in the simple case of linear PAs the convergence rate is faster because of the fewer number of parameters.

5.1.2.1 Impact of Nonlinearity Orders and Memory Depth

In this Section, we further elaborate on the importance of the PA nonlinearity in the observed PIM distortion, while still keeping the baseline parameters in mind given in Table. 5.1. To this end, Fig. 5.8, shows the remaining PIM-

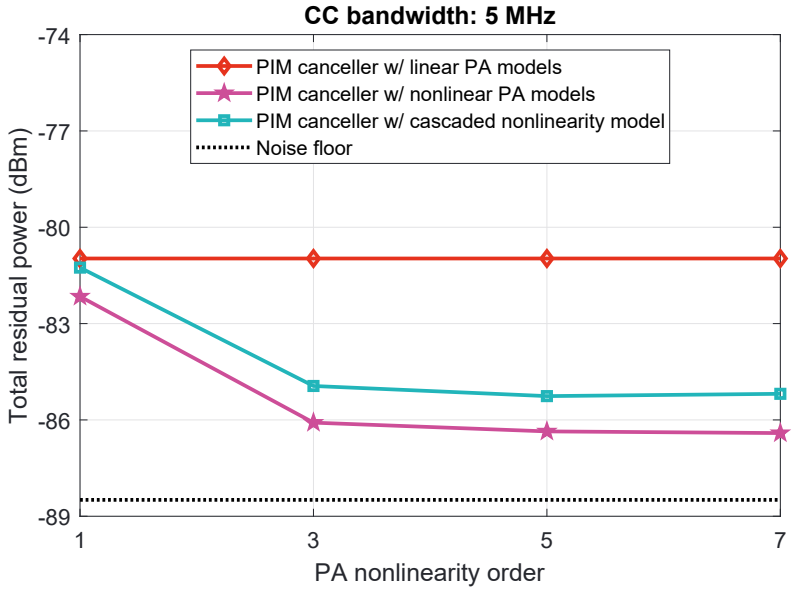

Figure 5.8 Measured PIM cancellation performance with respect to the PA nonlinearity order $(2Q+1)$ and PIM nonlinearity order $(P=2R+1)$ assumed in the canceller, using a CC bandwidth of 5 MHz. TX power is +24 dBm, **Publication-IV**

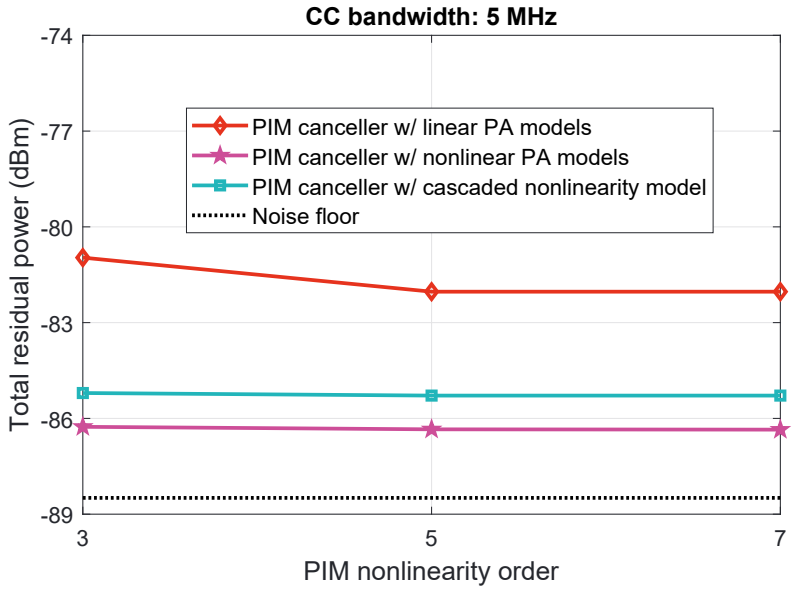

Figure 5.9 Measured PIM cancellation performance with respect to the PIM nonlinearity order $(P=2R+1)$ and PA nonlinearity order $(2Q+1)$ assumed in the canceller, using a CC bandwidth of 5 MHz. TX Power is +24 dBm, **Publication-IV**

plus-noise power when different PA nonlinearity orders used in the cancellation processing, focusing still on the 5-MHz CCs bandwidth case. These results further affirm our stance that modelling the PA nonlinearities greatly enhances the cancellation performance, as can be noted that the third-order PA model-based canceller outperforms the one that is based on the linear-first-order model. It can be further observed that the cancellation performance increases even more with the fifth-order PA. The cancellation performance does not show any significant improvement beyond the fifth-order PA model. The results for the 10 MHz CC are very similar and hence are not discussed here.

Next, we study the effect of the PIM nonlinearity order ($P = 2R + 1$) in the canceller for a given PA nonlinearity order of $2Q + 1 = 5$ and with pre-cursor and post-cursor memory taps of $M_1 = 3$ and $M_2 = 4$, while otherwise, again keeping the baseline parameters in mind as shown in Table. 5.1. The results are given in Fig. 5.9, which again affirms our stance that modelling the PA nonlinearities greatly enhances canceller performance. Furthermore, it can also be noted that increasing the PIM nonlinearity beyond the fifth order does not add any significant gain. Next, Fig. 5.10 shows the canceller performance with respect to the filter memory taps, where for evaluation simplicity, the filters are set to $M_1 = M_2 = M$ and vary M within $M \in \{0, 1, 2, 3, 4\}$ where $M = 0$ means a canceller with no memory. It can be observed that including the memory taps increases the performance by some 3 dB, however, due to the narrow band nature of the signals the amount of memory is fairly mild in this setup.

5.1.2.2 Learning Under the Signal-of-Interest and Timing Offset

Next, we study the sensitivity of the proposed estimation-cancellation methods to the potential timing offsets between the two signals (the observed signal and the cancellation signal). To demonstrate this, timing offsets are introduced to the received signal intentionally, while keeping zero memory in the canceller system i.e., ($M_1 = M_2 = 0$). The obtained results are shown in Fig. 5.11 for the 10-MHz CCs, where we consider the gradient-adaptive cascaded nonlinearity model-based canceller, for better illustration. The results in Fig. 5.11 indicate that the memoryless canceller is extremely sensitive to timing errors. However, when the system is equipped with memory containing both pre and post-cursor

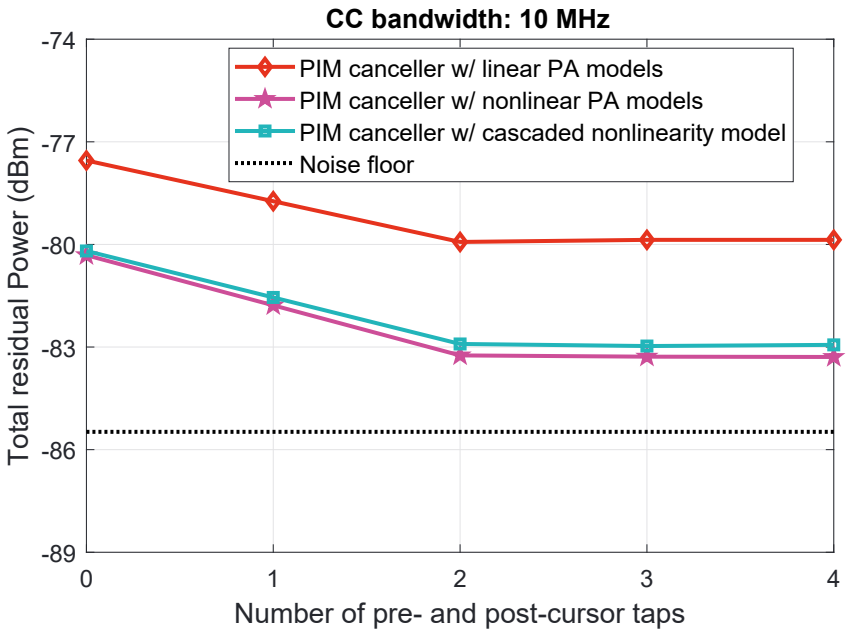

Figure 5.10 Measured PIM cancellation performance with respect to the number of pre-cursor and post-cursor taps ($M_1 = M_2 = M$), PA nonlinearity order ($2Q + 1$) and PIM nonlinearity order ($P = 2R + 1$) assumed in the canceller, using a CC bandwidth of 10 MHz. TX power is +24 dBm, **Publication-IV**.

taps, it becomes quite robust to any timing errors. Finally, we briefly discuss the effect of the presence of the SoI on the canceller parameter learning aspect. We use the same measured signals as in our earlier discussions. However, now we impose an actual LTE-Advanced DL orthogonal OFDM signal on top of the measured I/Q signals whose power varies over time which corresponds to SNR values of the range $(0-15)$. The SoI is a quadrature phase-shift keying (QPSK) modulated OFDM signal with about 300 active subcarriers corresponding to the 5-MHz channel bandwidth specifications. Next, we measure the canceller performance as we did in the earlier examples, however, now also considering the effect of the presence of the SoI on the parameter learning.

The results under different received power levels of the SoI are shown in Fig. 5.12. It is noted that the canceller is quite robust even in the presence of the SoI. However, the canceller performance degrades as the SoI becomes stronger but this is expected since the SoI acts as an additional strong noise from the

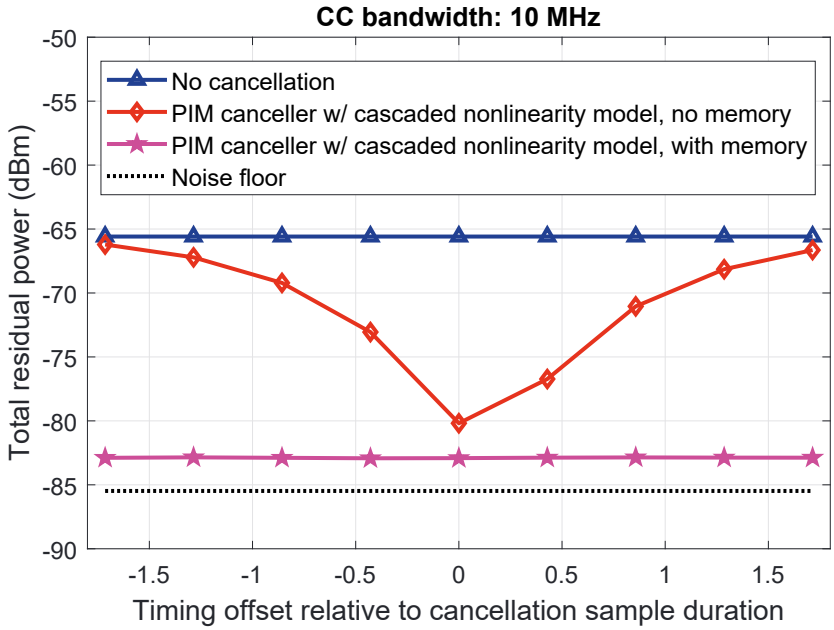

Figure 5.11 Measured PIM cancellation performance with respect to the timing offset, using a CC bandwidth of 10 MHz. TX Power is +24 dBm, **Publication-IV**.

parameter estimation point of view. It is also noted that the performance of the PIM canceller with the linear PA models stays essentially constant with SoI powers up to −79 dBm. This happens because the canceller output at the lower SoI level is still overcome by the nonlinear products resulting from nonlinear PAs and PIM.

5.1.3 Measurement Setup and Results for Coupled PIM

In this subsection, we address the performance evaluations and RF measurements for a special case where the UE is equipped with a diversity RX chain **[Publication-II]**. The results show that PIM coupled over-the-air from the main antenna to the diversity antenna can also be a real problem.

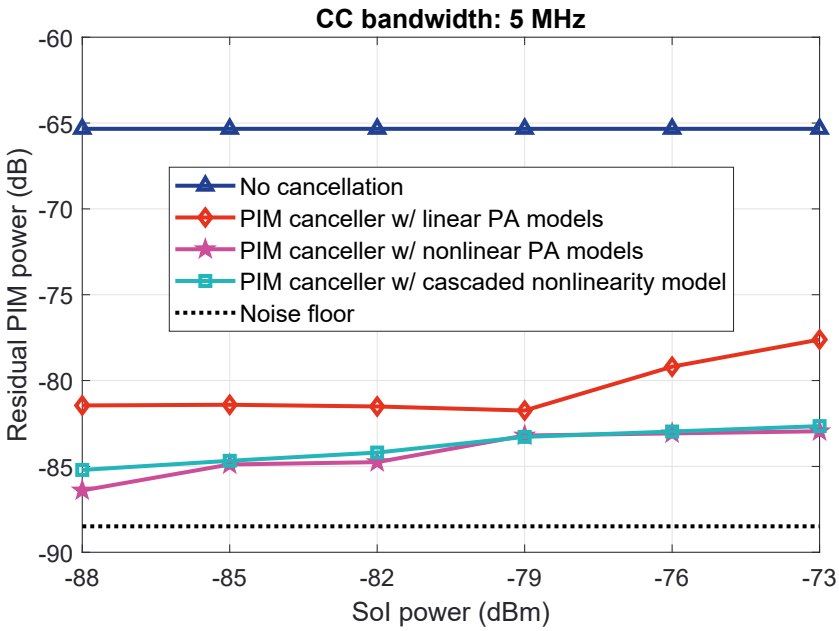

Figure 5.12 Measured PIM cancellation performance in the presence of a signal-of-interest during the parameter learning. CC bandwidth is 5 MHz and TX power is +24 dBm, **Publication-IV**.

5.1.3.1 Measurement Setup

The measurement setup for evaluating the performance of the proposed method is shown in Fig. 5.13 while the relevant setup parameters are shown in Table 5.2.

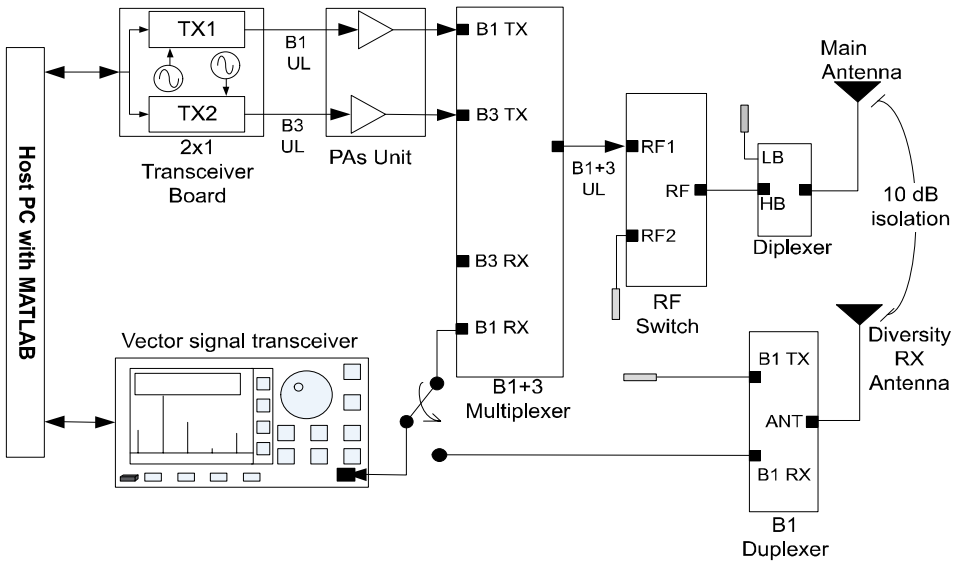

Figure 5.13 The RF measurement setup, showing the corresponding transmitting and receiving units as well as the RF front-end components **Publication-II**.

The measurement setup comprises of Analog Devices AD9368 2×1 transceiver board to generate the corresponding Band 1 and 3 CCTX signals. These signals are then amplified using the Skyworks SKY77643-21 PAs and combined in a multiplexer TDK B8690, which has a common antenna port and separate TX and RX ports. The combined TX signal is next fed to an Infineon switch BGS12PL6 and a diplexer TDK DPX162690DT-8022B2. This diplexer output port is connected to an antenna. For the implementation of the diversity RX chain, to which PIM is coupled over-the-air an additional B1 duplexer is connected to a second antenna which is placed in the close vicinity of the main transceiver. The signals at the main RX ports are fed to the RF input of the National Instrument (NI) PXIe-5645R vector signal transceiver (VST), which are then down-converted and digitized for further processing in MATLAB. In the next Section, the measurement results for the diversity RX branch are presented.

Table 5.2 Basic RF measurement parameters

Parameter	Value
Bandwidths of the TX CCs	5 MHz
Total transmit power	24 dBm
Post PA loss	4 dB
Duplexer insertion loss	3 dB
Switch insertion loss	1 dB
RX center frequency	2140 MHz
LS parameter learning sample size	90000
Number of PIM pre-cursor taps (L_1)	3
Number of PIM post-cursor taps (L_2)	4
Number of TX/PA pre-cursor taps (M_1)	0 or 1
Number of TX/PA post-cursor taps (M_2)	0 or 1

5.1.3.2 Measurement Results

In this subsection, the measurement results for the diversity RX branch are presented which demonstrates that PIM-induced distortion can also couple over-the-air and cause self-interference to the diversity RX branch. The diversity RX antenna is placed at a distance of 5 cm from the main RX antenna, which provides an antenna isolation of 10 dB. Fig. 5.14 shows that the PIM interference is substantially strong and can block the desired RX signal. It can also be observed that the proposed digital cancellation method is able to suppress the over-the-air coupled PIM efficiently very close to the noise floor.

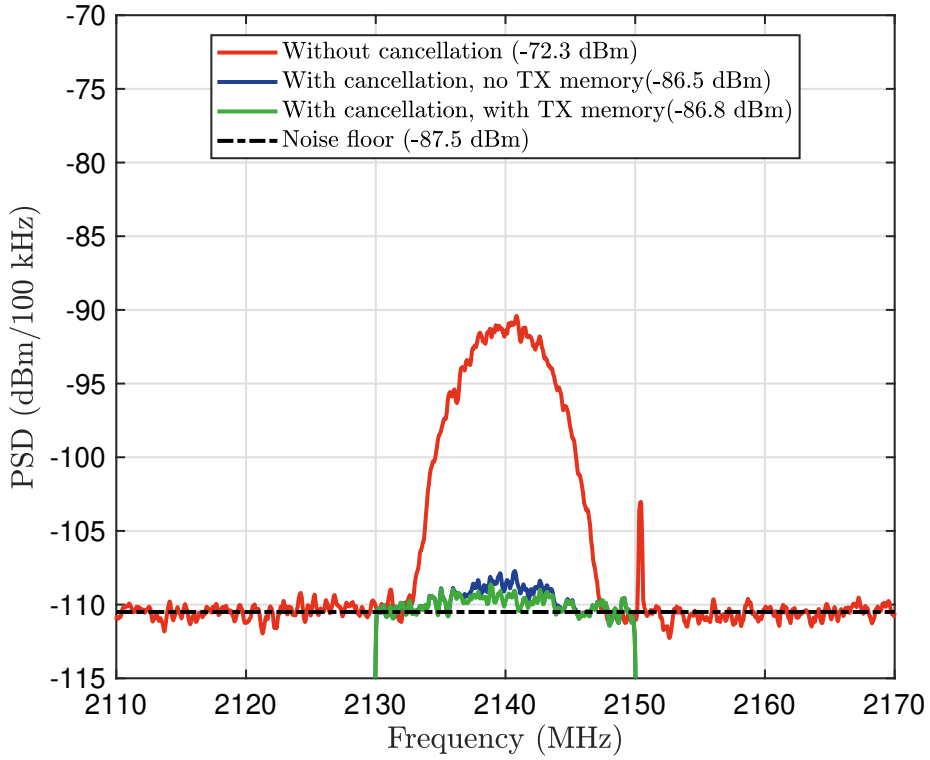

Figure 5.14 Measured PSD curves of the PIM distortion at the diversity RX branch of Band 1 without and with digital cancellation. The TX CC bandwidths at the LTE Bands 1 and 3 are 5 MHz each, and the aggregated TX power is +24 dBm **Publication-II**.

5.2 Evaluation of External PIM sources using Base Station Hardware - PHM Distortion

In this Section, we discuss the RF measurement setup utilized to test the performance of the digital canceller for the signal model discussed in Section 4.2. The digital canceller is based on LS estimation method as described in Section 4.4.1.

5.2.1 Measurement Setup

The measurements are conducted in an anechoic chamber to avoid interference from external sources. To generate passive harmonic distortion, we used rusty metal and other similar sources placed at a distance of 1 meters from the base station. The base station hardware is controlled by a computer located outside the chamber which feeds the input signals and collects the data for post-processing. The measurement setup is shown in Fig. 5.1, while the rest of the relevant features of the measurement system and the digital canceller itself are given in Table. 5.3

Table 5.3 RF MEASUREMENT SETUP CONFIGURATION AND CONSIDERED PHM DISTORTION CANCELLER PARAMETERS

Parameter	Value
Bandwidth of the CCs	5 MHz
Total transmit power	31 dBm
Center frequencies of CCs	1819.0/1866.5 MHz
RX center frequency	3685.0 MHz
RX capture bandwidth	122.8 MHz
Cancellation bandwidth	20 MHz
Signals per carrier frequencies	2
Polynomial order (P)	4
Number of samples used for estimation (N)	90 000

The base station hardware constitutes a dual *TX/RX* system with directional antennas as indicated by label-A in Fig. 5.1. The TX chains then transmit two 5G NR standard CP-OFDM signals as CCs, which has a bandwidth of 5 MHz with a transmit power of about +31 dBm, plus the antenna gain. The centre frequencies of the CCs are 1819.0 MHz and 1866.5 MHz respectively. The RX center frequency is set to 3685.0 MHz, where the observable PHM distortion is also captured as illustrated in Fig. 5.16

5.2.2 Measurement Results

In this Section, we discuss the cancellation results achieved for all the fundamental harmonic distortion products. To this end, Fig. 5.17 shows the cancellation

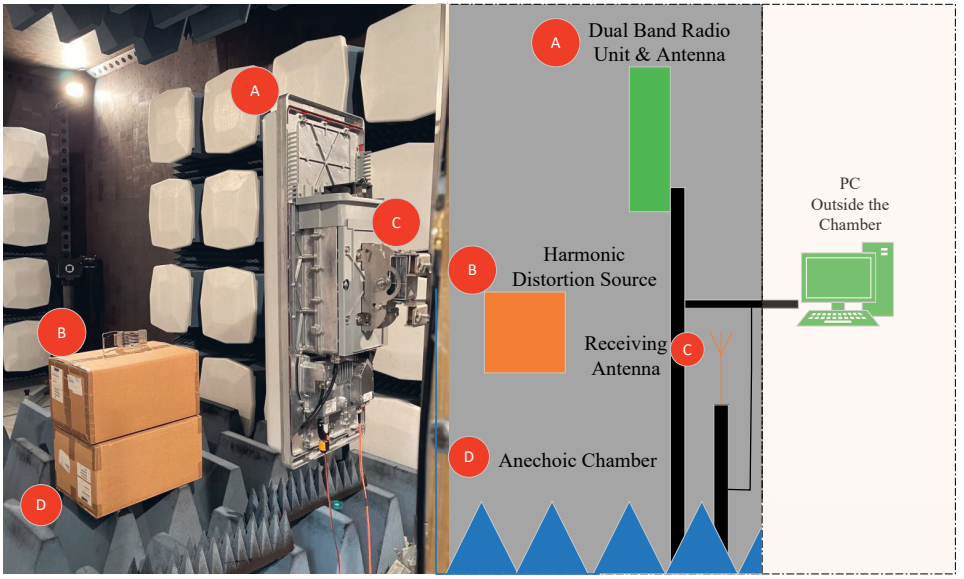

Figure 5.15 Overall RF measurement setup used for evaluating the performance of the proposed digital cancellation method, **Publication-V**.

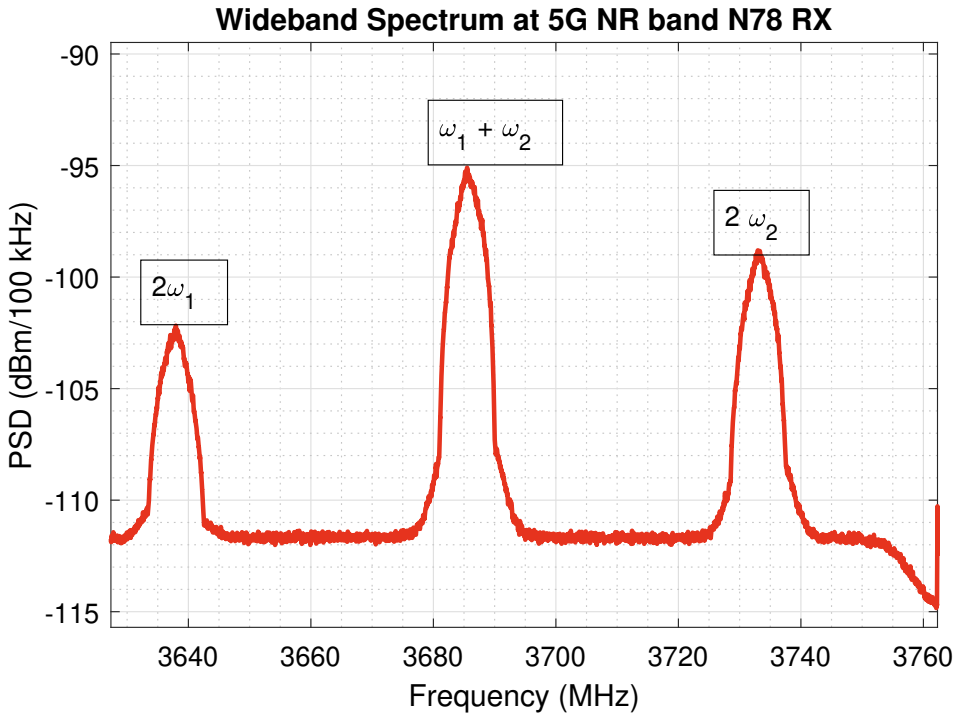

Figure 5.16 Wideband spectrum of the observable PHM distortion at the RX band, **Publication-V.**

results achieved for the frequency $2\omega_1$, where the power of the PHM distortion is about 6.3 dB higher than the noise power and the cancellation achieved is about 5.4 dB.

Similarly, the cancellation results at frequencies $2\omega_2$ and $\omega_1 + \omega_2$ are shown in Fig. 5.18 and Fig. 5.19, where the PHM distortion power is about 8.5 dB and 11.2 dB relative to the noise floor while the cancellation achieved is 6.2 dB and 8.6 dB, relative to the noise floor.

It has been demonstrated in these results that the proposed digital canceller can effectively suppress PHM distortion products, thus enabling efficient utilization of the RF spectrum.

5.3 Main Findings and Inference from the RF Measurement Results

Altogether, the obtained results for the PIM and PHM distortion lead to the following observations:

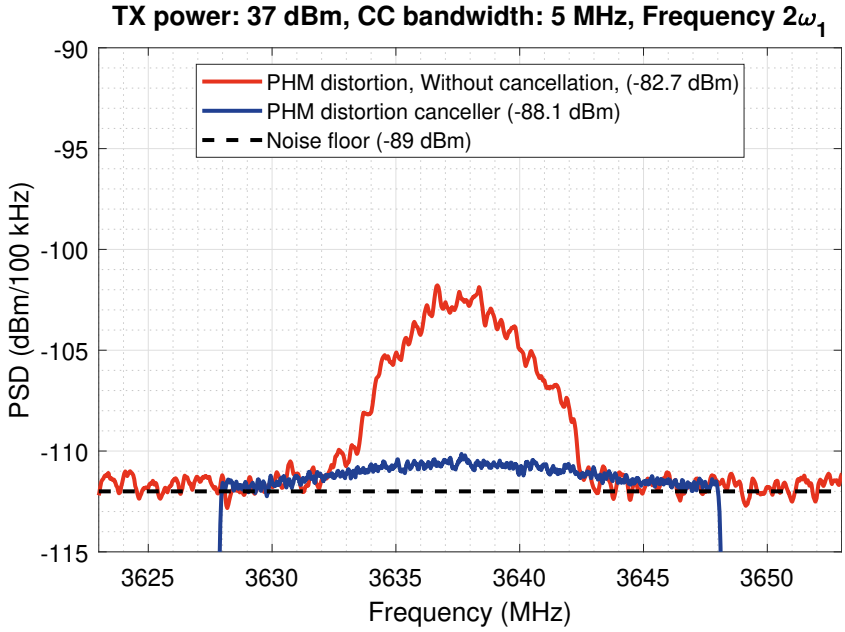

Figure 5.17 The spectra of the observed PHM distortion at frequency $2\omega_1$ and the residual signal after cancellation, **Publication-V**

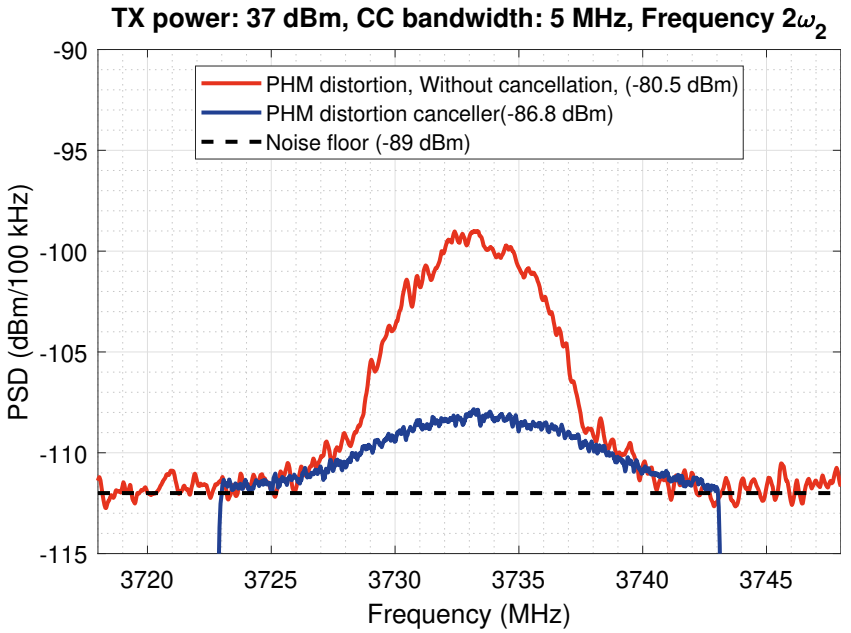

Figure 5.18 The spectra of the observed PHM distortion at frequency $2\omega_2$ and the residual signal after cancellation, **Publication-V.**

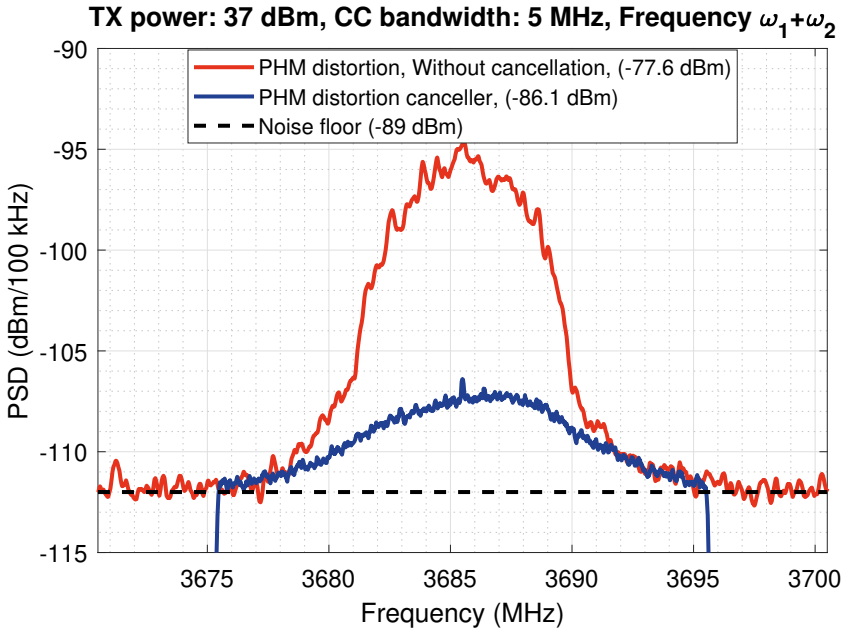

Figure 5.19 The spectra of the observed PHM distortion at frequency $\omega_1 + \omega_2$ and the residual signal after cancellation, **Publication-V.**

- The PIM-PHM induced inteference is a serious problem in FDD transceivers utilizing CA. In this work, we demonstrated it with actual RF measurements utilizing Band 1 and Band 3 where commercial off-the-shelf passive components produced passive distortion which hit one of the RX bands.
- Next, we noticed that the nonlinearity of the PAs must be taken into consideration when developing the interference signal model. Since the PAs already distort the CCs, PAs nonlinearity modelling improves the canceller's performance when taken into account.
- The cascaded model of PIM where there is one decoupled single memory model for all the basis functions greatly reduces the computational complexity of the canceller. It reduces canceller performance slightly, but given the complexity of the model, that is an acceptable trade-off.
- The proposed solutions demonstrated that they are able to perform efficiently in the presence of SoI and timing offsets. This is when an adequate number of precursors and postcursors are present. It was also observed in the case of PHM distortion that the air-induced PHM distortion can also be efficiently cancelled even in FDD-TDD scenario when the radios are co-located.

In the end, the measurement results show that there is still some residual distortion above the noise floor at very high transmit powers. This is most likely due to the potential model mismatch and the residual inaccuracies in the coefficient estimations. The performance can be further improved for example by adopting Volterra-type models but at the cost of increased computational complexity.

CHAPTER 6

THESIS SUMMARY AND FUTURE WORK

In this thesis work, we proposed advanced solutions for modelling and digital cancellation of the passive intermodulation distortion appearing at the own RX band. We focused on the IMD distortion produced as a result of the nonlinearity of the passive components, in CA based FDD transceivers. We also discussed the passive harmonic distortion which may not only be generated by the passive components but may also couple through the air into the RX band, if for example there are metallic objects in the antenna near-field. If left untreated such IMD distortion can seriously degrade the sensitivity of the receiver when operating on certain LTE/NR band combinations. Three different PIM models and one PHM model and the corresponding digital cancellers were proposed, the former trading-off between complexity and modelling accuracy whilst also taking into account the modelling of the PA nonlinearities and the memory effects.

The performance of the proposed digital cancellation solutions was evaluated through real-life RF measurements and the results demonstrate efficient digital cancellation of the residual PIM/PHM interference. For PIM, the advanced signal models incorporating the PAs nonlinearities and the memory effect show

that the corresponding canceller can suppress PIM up to 20 dB. This is very close to the noise floor. The results also show that the proposed cancellers perform very effectively under timing offsets especially when the canceller memory parameterization is done properly. The results obtained throughout this work demonstrate that these digital cancellation solutions improve the network performance by improving the throughput and coverage without limiting the transmit power or having the need to relax the reference sensitivity as otherwise proposed by 3GPP in the context of MPR and MSD which negatively affect the link budget requirements.

The results also indicate nearly perfect mathematical modelling of the nonlinear components present in the TX chain such as the PAs and the passive components since we are able to achieve nearly perfect cancellation with our most advanced signal models and the corresponding digital cancellers. There are 465 complex multiplications per iteration in our model with coupled memory out of which only 120 complex multiplications are required for digital cancellation in contrast to our model with decoupled memory which requires 391 complex multiplications per iteration out of which only 23 complex multiplications are needed for digital cancellation, while the rest of the complex multiplications are needed during the parameter update phase which can also be carried out offline without straining the device in question in real-time operation.

The proposed solutions also help keeping the cost and size of the radio devices small since no expensive highly linear components are needed and there is no need to improve the duplex filter isolation. Furthermore, it is easy to tune the devised solutions for any band combinations without needing to make changes to the actual radio transceiver hardware. The obtained results also indicates that the proposed solution also performs efficiently in MIMO scenarios especially when more than two component carriers are present.

Some of the potential future work items are studying the behaviour of PIM distortion in scenarios where there are more than 2 CCs as opposed to what we discuss as an example in this thesis work. In some cases, for example in the case of three CCs, the IM of all the three CCs at the frequency $\omega_1 + \omega_2 - \omega_3$, coincide with one of the RX band. In such cases, the basis functions can be derived utilizing the equations in Chapter 4, which may yield basis functions of the form $x_1[n]x_2[n]x_3^*[n]$, for the above-mentioned frequency. Another poten-

tial study item could be to study the behaviour of the proposed signal models under different modulation schemes, such as 16QAM, 64QAM, 256QAM and see the impact of proposed cancellers on throughput performance. Some other research directions are to develop advanced signal models for multiple TX/RX antennas; and multiple PIM sources; assess the PIM impact with link and system level simulation, and evaluate the actual hardware implementation-related complexity. The future 6G systems as specified by 3GPP are aiming to utilize the subband full duplex (SBFD) type waveforms and radio access concepts. It would be beneficial to study the behaviour of IM distortions and PIM under such scenarios.

While the research in this domain will continue to flourish in the future, the models and methods proposed in this thesis work greatly relax the passive front-end RF components' linearity requirements, while also increasing the flexibility of the RF spectrum utilization in the existing LTE-Advanced/5G and the upcoming sixth-generation 6G radio networks. This research enables the network operators to increase the data rate while utilizing multiple frequency bands at the same time without the need to have to invest in highly expensive linear components or antenna hardware. It also enables the network operators to operate on full TX power in remote areas and hence providing coverage to a large area which is critical for emergency service providers in areas where network coverage may be limited. The ever increasing demand for user data rate and the growing applications of mobile networks such as flying drones, autonomous vehicles makes it necessary to have more and more radios across the cities and other areas and solutions like the proposed digital canceller are very essential for smooth operations of the mobile networks.

REFERENCES

[1] 3GPP Tech. Rep. 36.850. *Inter-band carrier aggregation.* v11.1.0 (Release 11), July 2013.

[2] 3GPP Tech. Spec. 36.101. *E-UTRA; User Equipment (UE) radio transmission and reception.* v16.0.0 (Release 16), Jan. 2019.

[3] *5G System Overview.* https://www.3gpp.org/technologies/5g-system-overview. August, 2022. 3GPP Tech.

[4] *5G Waveforms & Modulation: CP-OFDM & DFT-s-OFDM.* https://www.electronics-notes.com/articles/connectivity/5g-mobile-wireless-cellular/waveforms-ofdm-modulation.php. December, 2021. Electronic Notes.

[5] *5G/NR - Numerology / SCS (Sub Carrier Spacing).* https://www.sharetechnote.com/html/5G/5G_Phy_Numerology.html. December, 2017. ShareTechNote.

[6] E. AB. *"5G radio access," white paper, 2015. [Online].* https://www.ericsson.com/en/reports-and-papers/white-papers/5g-wireless-access-an-overview. 2015.

[7] M. Abdelaziz, L. Anttila, A. Kiayani and M. Valkama. Decorrelation-Based Concurrent Digital Predistortion With a Single Feedback Path. In: *IEEE Transactions on Microwave Theory and Techniques* 66.1 (2018), 280–293. DOI: 10.1109/TMTT.2017.2706688.

[8] A. Abdelhafiz, A. Kwan, M. Younes, O. Hammi, N. Boulejfen and F. M. Ghannouchi. Augmented Dual-Band Digital Predistorter for Reducing Cross-Band Intermodulation Distortion Using Predictive Injection Technique. In: *IEEE Transactions on Microwave Theory and Techniques* 64.11 (2016), 3518–3527. DOI: 10.1109/TMTT.2016.2603505.

[9] A. Abidi. Direct-conversion radio transceivers for digital communications. In: *Proceedings ISSCC '95 - International Solid-State Circuits Conference*. 1995, 186–187. DOI: 10.1109/ISSCC.1995.535515.

[10] A. Abidi. Low-power radio-frequency ICs for portable communications. In: *Proceedings of the IEEE* 83.4 (1995), 544–569. DOI: 10.1109/5.371966.

[11] M. Agiwal, A. Roy and N. Saxena. Next Generation 5G Wireless Networks: A Comprehensive Survey. In: *IEEE Communications Surveys & Tutorials* 18.3 (2016), 1617–1655. DOI: 10.1109/COMST.2016.2532458.

[12] A. Altintas and P. Russer. Time-domain equivalent edge currents for transient scattering. In: *IEEE Transactions on Antennas and Propagation* 49.4 (2001), 602–606. DOI: 10.1109/8.923321.

[13] ANRITSU. *"Passive Intermodulation (PIM)" ANRITSU, [Online].* https://www.anritsu.com/en-us/test-measurement/technologies/pim. 2022.

[14] O. E. Ayach, S. Rajagopal, S. Abu-Surra, Z. Pi and R. W. Heath. Spatially Sparse Precoding in Millimeter Wave MIMO Systems. In: *IEEE Transactions on Wireless Communications* 13.3 (2014), 1499–1513. DOI: 10.1109/TWC.2014.011714.130846.

[15] T. Bai and R. W. Heath. Coverage and Rate Analysis for Millimeter-Wave Cellular Networks. In: *IEEE Transactions on Wireless Communications* 14.2 (2015), 1100–1114. DOI: 10.1109/TWC.2014.2364267.

[16] S. A. Bassam, W. Chen, M. Helaoui and F. M. Ghannouchi. Transmitter Architecture for CA: Carrier Aggregation in LTE-Advanced Systems. In: *IEEE Microw. Mag.* 14.5 (July 2013), 78–86. ISSN: 1557-9581. DOI: 10.1109/MMM.2013.2259399.

[17] E. Björnson, E. G. Larsson and T. L. Marzetta. Massive MIMO: ten myths and one critical question. In: *IEEE Communications Magazine* 54.2 (2016), 114–123. DOI: 10.1109/MCOM.2016.7402270.

[18] F. Boccardi, R. W. Heath, A. Lozano, T. L. Marzetta and P. Popovski. Five disruptive technology directions for 5G. In: *IEEE Communications Magazine* 52.2 (2014), 74–80. DOI: 10.1109/MCOM.2014.6736746.

[19] J. J. Carr. Chapter 16 - Radio Receiver Basics. In: *The Technician's EMI Handbook*. Ed. by J. J. Carr. Woburn: Newnes, 2000, 163–195. ISBN: 978-0-7506-7233-7. DOI: https://doi.org/10.1016/B978-075067233-7/50016-8. URL: https://www.sciencedirect.com/science/article/pii/B9780750672337500168.

[20] X. Chen, T. Ren, D. J. Pommerenke and M. Yu. Broadband Mechanical Intermodulation Tuner Using Reconfigurable Distributed Nonlinearity. In: *IEEE Transactions on Microwave Theory and Techniques* 70.1 (2022), 5–13. DOI: 10.1109/TMTT.2021.3098850.

[21] H.-T. Dabag, H. Gheidi, S. Farsi, P. S. Gudem and P. M. Asbeck. All-Digital Cancellation Technique to Mitigate Receiver Desensitization in Uplink Carrier Aggregation in Cellular Handsets. In: *IEEE Transactions on Microwave Theory and Techniques* 61.12 (2013), 4754–4765. DOI: 10.1109/TMTT.2013.2287857.

[22] H.-T. Dabag, H. Gheidi, P. Gudem and P. M. Asbeck. All-digital cancellation technique to mitigate self-jamming in uplink carrier aggregation in cellular handsets. In: *2013 IEEE MTT-S International Microwave Symposium Digest (MTT)*. 2013, 1–3. DOI: 10.1109/MWSYM.2013.6697664.

[23] E. Dahlman, S. Parkvall, J. Peisa and H. Tullberg. 5G Evolution and Beyond. In: *2019 IEEE 20th International Workshop on Signal Processing Advances in Wireless Communications (SPAWC)*. 2019, 1–5. DOI: 10.1109/SPAWC.2019.8815418.

[24] E. Dahlman, S. Parkvall and J. Skold. *5G NR: The Next Generation Wireless Access Technology*. 1st. Elsevier Science, 2018. ISBN: 0128143231, 9780128143230.

[25] J. S. Erik Dahlman Stefan Parkvall. *5G NR: The Next Generation Wireless Access Technology*. United States: Academic Press, 2020.

[26] *Further advancements for E-UTRA physical layer aspects*. version 9.0.0, Release 9, Mar. 2010. 3GPP Tech. Rep. 36.814.

[27] A. Gebhard, O. Lang, M. Lunglmayr, C. Motz, R. S. Kanumalli, C. Auer, T. Paireder, M. Wagner, H. Pretl and M. Huemer. A Robust Nonlinear RLS Type Adaptive Filter for Second-Order-Intermodulation Distortion Cancellation in FDD LTE and 5G Direct Conversion Transceivers. In: *IEEE Transactions on Microwave Theory and Techniques* 67.5 (2019), 1946–1961. DOI: 10.1109/TMTT.2019.2896513.

[28] H. Gheidi, H.-T. Dabag, Y. Liu, P. M. Asbeck and P. Gudem. Digital cancellation technique to mitigate receiver desensitization in cellular handsets operating in carrier aggregation mode with multiple uplinks and multiple downlinks. In: *2015 IEEE Radio and Wireless Symposium (RWS)*. 2015, 221–224. DOI: 10.1109/RWS.2015.7129754.

[29] A. Ghosh, T. A. Thomas, M. C. Cudak, R. Ratasuk, P. Moorut, F. W. Vook, T. S. Rappaport, G. R. MacCartney, S. Sun and S. Nie. Millimeter-Wave Enhanced Local Area Systems: A High-Data-Rate Approach for Future Wireless Networks. In: *IEEE Journal on Selected Areas in Communications* 32.6 (2014), 1152–1163. DOI: 10.1109/JSAC.2014.2328111.

[30] J.-C. Guey, P.-K. Liao, Y.-S. Chen, A. Hsu, C.-H. Hwang and G. Lin. On 5G radio access architecture and technology [Industry Perspectives]. In: *IEEE Wireless Communications* 22.5 (2015), 2–5. DOI: 10.1109/MWC.2015.7306369.

[31] J. Guo, H. Yin, L. Man and X. Li. Polarization characteristics and controllability mechanism of passive scattering elements. In: *Journal of Systems Engineering and Electronics* 34.2 (2023), 342–349. DOI: 10.23919/JSEE.2023.000043.

[32] H. Harada, K. Mizutani, T. Matsumura, T. Kato and K. Shioiri. Development of Full-Duplex Cellular System for Beyond 5G and 6G Systems. In: *2022 IEEE 33rd Annual International Symposium on Personal, Indoor and Mobile Radio Communications (PIMRC)*. 2022, 01–05. DOI: 10.1109/PIMRC54779.2022.9977863.

[33] S. Haykin. *Adaptive filter theory*. 4th. Upper Saddle River, NJ: Prentice Hall, 2002.

[34] J. J. Henrie, A. J. Christianson and W. J. Chappell. Linear–Nonlinear Interaction and Passive Intermodulation Distortion. In: *IEEE Trans. Microw. Theory Techn.* 58.5 (May 2010), 1230–1237. ISSN: 1557-9670. DOI: 10.1109/TMTT.2010.2045527.

[35] J. Henrie, A. Christianson and W. J. Chappell. Cancellation of Passive Intermodulation Distortion in Microwave Networks. In: *2008 38th European Microwave Conference*. 2008, 1153–1156. DOI: 10.1109/EUMC.2008.4751663.

[36] J. Henrie, A. Christianson and W. J. Chappell. Engineered Passive Nonlinearities for Broadband Passive Intermodulation Distortion Mitigation. In: *IEEE Microwave and Wireless Components Letters* 19.10 (2009), 614–616. DOI: 10.1109/LMWC.2009.2029733.

[37] H. Holma, A. Toskala and T. Nakamura. *5G Technology: 3GPP New Radio*. Wiley, 2020. ISBN: 9781119236313. URL: https://books.google.fi/books?id=V2s0jgEACAAJ.

[38] S. Hong, J. Brand, J. I. Choi, M. Jain, J. Mehlman, S. Katti and P. Levis. Applications of self-interference cancellation in 5G and beyond. In: *IEEE Communications Magazine* 52.2 (2014), 114–121. DOI: 10.1109/MCOM.2014.6736751.

[39] G. Huang, A. Nix and S. Armour. Impact of Radio Resource Allocation and Pulse Shaping on Papr of SC-FDMA Signals. In: *2007 IEEE 18th International Symposium on Personal, Indoor and Mobile Radio Communications*. 2007, 1–5. DOI: 10.1109/PIMRC.2007.4394297.

[40] T. Hwang, C. Yang, G. Wu, S. Li and G. Ye Li. OFDM and Its Wireless Applications: A Survey. In: *IEEE Transactions on Vehicular Technology* 58.4 (2009), 1673–1694. DOI: 10.1109/TVT.2008.2004555.

[41] M. Iwamura, K. Etemad, M.-h. Fong, R. Nory and R. Love. Carrier aggregation framework in 3GPP LTE-advanced [WiMAX/LTE Update]. In: *IEEE Communications Magazine* 48.8 (2010), 60–67. DOI: 10.1109/MCOM.2010.5534588.

[42] B. Jang, H. Kim, Y. Seo, S. Im and S. Hong. Mitigation of the Third-Order Passive Intermodulation Distortion Interference on Uplink Signal. In: *2019 International Conference on Electronics, Information, and Communication (ICEIC)*. 2019, 1–3. DOI: 10.23919/ELINFOCOM.2019.8706428.

[43] Q. Jin, J. Gao, G. T. Flowers, Y. Wu and G. Xie. Modeling of Passive Intermodulation With Electrical Contacts in Coaxial Connectors. In: *IEEE Transactions on Microwave Theory and Techniques* 66.9 (2018), 4007–4016. DOI: 10.1109/TMTT.2018.2838147.

[44] Q. Jin, J. Gao, H. Huang and L. Bi. Mitigation Methods for Passive Intermodulation Distortion in Circuit Systems Using Signal Compensation. In: *IEEE Microwave and Wireless Components Letters* 30.2 (2020), 205–208. DOI: 10.1109/LMWC.2019.2957989.

[45] H. M. Karaca. Passive Inter-modulation Sources and Cancellation Methods. In: *The European Journal of Research and Development* (2022).

[46] A. Kiayani, M. Abdelaziz, L. Anttila, V. Lehtinen and M. Valkama. Digital Mitigation of Transmitter-Induced Receiver Desensitization in Carrier Aggregation FDD Transceivers. In: *IEEE Trans. Microw. Theory Techn.* 63.11 (Nov. 2015), 3608–3623. ISSN: 0018-9480. DOI: 10.1109/TMTT.2015.2478005.

[47] A. Kiayani, V. Lehtinen, L. Anttila, T. Lähteensuo and M. Valkama. Linearity Challenges of LTE-Advanced Mobile Transmitters: Requirements and Potential Solutions. In: *IEEE Commun. Mag.* 55.6 (June 2017), 170–179. ISSN: 0163-6804. DOI: 10.1109/MCOM.2017.1600651.

[48] A. Kiayani, L. Anttila, M. Kosunen, K. Stadius, J. Ryynänen and M. Valkama. Modeling and Joint Mitigation of TX and RX Nonlinearity-Induced Receiver Desensitization. In: *IEEE Transactions on Microwave Theory and Techniques* 65.7 (2017), 2427–2442. DOI: 10.1109/TMTT.2017.2654222.

[49] A. Kiayani, L. Anttila and M. Valkama. Digital Suppression of Power Amplifier Spurious Emissions at Receiver Band in FDD Transceivers. In: *IEEE Signal Processing Letters* 21.1 (2014), 69–73. DOI: 10.1109/LSP.2013.2291032.

[50] A. Kolackova, S. Saafi, P. Masek, J. Hosek and J. Jerabek. Performance Evaluation of Carrier Aggregation in LTE-A Pro Mobile Systems. In: *2020 43rd International Conference on Telecommunications and Signal Processing (TSP)*. 2020, 627–632. DOI: 10.1109/TSP49548.2020.9163440.

[51] V. Lampu, L. Anttila, M. Turunen, M. Fleischer, J. Hellmann and M. Valkama. Air-Induced Passive Intermodulation in FDD Networks: Modeling, Cancellation and Measurements. In: *2021 55th Asilomar Conference on Signals, Systems, and Computers*. 2021, 983–988. DOI: 10.1109/IEEECONF53345.2021.9723205.

[52] V. Lampu, L. Anttila, M. Turunen, M. Fleischer, J. Hellmann and M. Valkama. Air-Induced PIM Cancellation in FDD MIMO Transceivers. In: *IEEE Microwave and Wireless Components Letters* 32.6 (2022), 780–783. DOI: 10.1109/LMWC.2022.3164718.

[53] S. Lee, K. Hippalgaonkar, F. Yang, J. Hong, C. Ko, J. Suh, K. Liu, K. Wang, J. J. Urban, X. Zhang, C. Dames, S. A. Hartnoll, O. Delaire and J. Wu. Anomalously low electronic thermal conductivity in metallic vanadium dioxide. In: *Science (New York, N.Y.)* 355.6323 (Jan. 2017), 371–374. ISSN: 0036-8075. DOI: 10.1126/science.aag0410. URL: https://doi.org/10.1126/science.aag0410.

[54] S.-Y. Lien, S.-L. Shieh, Y. Huang, B. Su, Y.-L. Hsu and H.-Y. Wei. 5G New Radio: Waveform, Frame Structure, Multiple Access, and Initial Access. In: *IEEE Communications Magazine* 55.6 (2017), 64–71. DOI: 10.1109/MCOM.2017.1601107.

[55] X. Lin. An Overview of 5G Advanced Evolution in 3GPP Release 18. In: *IEEE Communications Standards Magazine* 6.3 (2022), 77–83. DOI: 10.1109/MCOMSTD.0001.2200001.

[56] X. Lin, J. Li, R. Baldemair, J.-F. T. Cheng, S. Parkvall, D. C. Larsson, H. Koorapaty, M. Frenne, S. Falahati, A. Grovlen and K. Werner. 5G New Radio: Unveiling the Essentials of the Next Generation Wireless Access Technology. In: *IEEE Communications Standards Magazine* 3.3 (2019), 30–37. DOI: 10.1109/MCOMSTD.001.1800036.

[57] Y. Liu, C. Li, X. Quan, P. Roblin, M. Rawat, N. Naraharisetti, Y. Tang and K. Kang. Multiband Linearization Technique for Broadband Signal With Multiple Closely Spaced Bands. In: *IEEE Transactions on Microwave Theory and Techniques* 67.3 (2019), 1115–1129. DOI: 10.1109/TMTT.2018.2884413.

[58] H. T. C. Ltd. *"5G: A technology vision," white paper, 2013. [Online].* https://www.huawei.com/minisite/has2015/img/5g_radio_whitepaper.pdf. 2013.

[59] *LTE-Advanced dual uplink inter-band Carrier Aggregation (CA)*. version 13.0.0, Release 13, Jan. 2016. 3GPP Tech. Rep. 36.860.

[60] P. L. Lui. Passive intermodulation interference in communication systems. In: *Electronics and Communication Engineering Journal* 2.3 (June 1990), 109–118. ISSN: 0954-0695.

[61] P. Lui and A. Rawlins. Passive non-linearities in antenna systems. In: *IEE Colloquium on Passive Intermodulation Products in Antennas and Related Structures*. 1989, 6/1–6/7.

[62] G. Macchiarella, G. B. Stracca and L. MiglioIi. Experimental study of passive intermodulation in coaxial cavities for cellular base stations duplexers. In: *Proc. 34th Eur. Microw. Conf., 2004.* Vol. 2. Oct. 2004, 981–984.

[63] H. Mai, A. Zhang and J. Chen. Multilayered Dielectric TDPO method Based on Characteristic Matrix Theory. In: *2019 IEEE International Conference on Computational Electromagnetics (ICCEM)*. 2019, 1–3. DOI: 10.1109/COMPEM.2019.8779114.

[64] T. L. Marzetta. Massive MIMO: An Introduction. In: *Bell Labs Technical Journal* 20 (2015), 11–22. DOI: 10.15325/BLTJ.2015.2407793.

[65] T. Mata, P. Boonsrimuang and P. Boontra. A PAPR Reduction Scheme based on Improved PTS with ABC Algorithm for OFDM Signal. In: *2018 15th International Conference on Electrical Engineering/Electronics, Computer, Telecommunications and Information Technology (ECTICON)*. 2018, 469–472. DOI: 10.1109/ECTICon.2018.8619887.

[66] C. Motz, T. Paireder and M. Huemer. Low-Complex Digital Cancellation of Transmitter Harmonics in LTE-A/5G Transceivers. In: *IEEE Open Journal of the Communications Society* 2 (2021), 948–963. DOI: 10.1109/OJCOMS.2021.3073172.

[67] Nidhi, A. Mihovska and R. Prasad. Overview of 5G New Radio and Carrier Aggregation: 5G and Beyond Networks. In: *2020 23rd International Symposium on Wireless Personal Multimedia Communications (WPMC)*. 2020, 1–6. DOI: 10.1109/WPMC50192.2020.9309496.

[68] Nokia. *"5G masterplan – five keys to create the new communications era," white paper, 2016. [Online].* https://resources.ext.nokia.com/asset/200316. 2016.

[69] M. O'Droma, N. Mgebrishvili and A. Goacher. Theoretical analysis of intermodulation distortion in OFDM signals in the presence of nonlinear RF high power amplifiers. In: *2004 IEEE 59th Vehicular Technology Conference. VTC 2004-Spring (IEEE Cat. No.04CH37514)*. Vol. 3. 2004, 1295–1299 Vol.3. DOI: 10.1109/VETECS.2004.1390462.

[70] C. S. Park, L. Sundström, A. Wallen and A. Khayallah. Carrier aggregation for LTE-Advanced: Design challenges of terminals. In: *IEEE Commun. Mag.* 51.12 (Dec. 2013), 76–84.

[71] C. S. PARK and F. S. PARK. Digital Compensation of IQ Imbalance for Dual-Carrier Double Conversion Receivers. In: *IEICE Transactions on Communications* E95.B.5 (2012), 1612–1619. DOI: 10.1587/transcom.E95.B.1612.

[72] C. S. Park, L. Sundström, A. Wallén and A. Khayrallah. Carrier aggregation for LTE-advanced: design challenges of terminals. In: *IEEE Communications Magazine* 51.12 (2013), 76–84. DOI: 10.1109/MCOM.2013.6685761.

[73] *Passive Inter-modulation Sources and Cancellation Methods.* https://journals.orclever.com/ejrnd/article/view/30. The European Journal of Research and Development. DOI: 10.56038/ejrnd.v2i2.30.

[74] K. I. Pedersen, F. Frederiksen, C. Rosa, H. Nguyen, L. G. U. Garcia and Y. Wang. Carrier aggregation for LTE-advanced: functionality and performance aspects. In: *IEEE Communications Magazine* 49.6 (2011), 89–95. DOI: 10.1109/MCOM.2011.5783991.

[75] J. Pedro and B. Carvalho. *Intermodulation Distortion in Microwave and Wireless Circuits*. Norwood: Artech House, 2003. URL: https://cds.cern.ch/record/995354.

[76] P. Pirinen. Challenges and possibilities for flexible duplexing in 5G networks. In: *2015 IEEE 20th International Workshop on Computer Aided Modelling and Design of Communication Links and Networks (CAMAD)*. 2015, 6–10. DOI: 10.1109/CAMAD.2015.7390471.

[77] R.-A. Pitaval, O. Tirkkonen, R. Wichman, K. Pajukoski, E. Lahetkangas and E. Tiirola. Full-duplex self-backhauling for small-cell 5G networks. In: *IEEE Wireless Communications* 22.5 (2015), 83–89. DOI: 10.1109/MWC.2015.7306541.

[78] H. Pretl and S. Sadjina. Self-Interference in LTE-Advanced and 5G NR Transceivers. In: *2018 IEEE Radio and Antenna Days of the Indian Ocean (RADIO)*. 2018, 1–2. DOI: 10.23919/RADIO.2018.8572347.

[79] *R4-111321, On Passive Intermodulation (PIM) for MSR-NC*. Taipei, Taiwan, Feb. 2011. Ericsson.

[80] *R4-121131, Harmonics and IMD analysis for Inter-band CA Band 3 and Band 8*. Jeju, South Korea, Mar. 2012. KT.

[81] *R4-121219, Way forward for interband Class A2*. Jeju, South Korea, Mar. 2012. Nokia Corporation, AT&T.

[82] *R4-121984, RF Architecture Alternatives for Inter Band CA Class A2*. Jeju, South Korea, Mar. 2012. Motorola Mobility.

[83] W. Roh, J.-Y. Seol, J. Park, B. Lee, J. Lee, Y. Kim, J. Cho, K. Cheun and F. Aryanfar. Millimeter-wave beamforming as an enabling technology for 5G cellular communications: theoretical feasibility and prototype results. In: *IEEE Communications Magazine* 52.2 (2014), 106–113. DOI: 10.1109/MCOM.2014.6736750.

[84] F. Rusek, D. Persson, B. K. Lau, E. G. Larsson, T. L. Marzetta, O. Edfors and F. Tufvesson. Scaling Up MIMO: Opportunities and Challenges with Very Large Arrays. In: *IEEE Signal Processing Magazine* 30.1 (2013), 40–60. DOI: 10.1109/MSP.2011.2178495.

[85] A. Sabharwal, P. Schniter, D. Guo, D. W. Bliss, S. Rangarajan and R. Wichman. In-Band Full-Duplex Wireless: Challenges and Opportunities. In: *IEEE Journal on Selected Areas in Communications* 32.9 (2014), 1637–1652. DOI: 10.1109/JSAC.2014.2330193.

[86] V. D. Sahni, N. Kumar and V. N. Saxena. Novel hybrid technique(s) for PAPR reduction in OFDM systems. In: *2016 International Conference on Signal Processing and Communication (ICSC)*. 2016, 512–515. DOI: 10.1109/ICSPCom.2016.7980634.

[87] Z. Shen, A. Papasakellariou, J. Montojo, D. Gerstenberger and F. Xu. Overview of 3GPP LTE-advanced carrier aggregation for 4G wireless communications. In: *IEEE Communications Magazine* 50.2 (2012), 122–130. DOI: 10.1109/MCOM.2012.6146491.

[88] A. Shitvov, A. G. Schuchinsky, M. B. Steer and J. M. Wetherington. Characterisation of nonlinear distortion and intermodulation in passive devices and antennas. In: *The 8th European Conference on Antennas and Propagation (EuCAP 2014)*. 2014, 1454–1458. DOI: 10.1109/EuCAP.2014.6902055.

[89] R. K. Singh and M. Fidele. An efficient PAPR reduction scheme for OFDM system using peak windowing and clipping. In: *2015 Third International Conference on Image Information Processing (ICIIP)*. 2015, 491–495. DOI: 10.1109/ICIIP.2015.7414822.

[90] *Summary for RAN Rel-18 package*. http://www.3gpp.org/ftp/tsg_ran/TSG_RAN/TSGR_94e/Docs/RP-213469.zip. December, 2021. 3GPP Release 18.

[91] J. Tamminen, M. Turunen, D. Korpi, T. Huusari, Y.-S. Choi, S. Talwar and M. Valkama. Digitally-controlled RF self-interference canceller for full-duplex radios. In: *2016 24th European Signal Processing Conference (EUSIPCO)*. 2016, 783–787. DOI: 10.1109/EUSIPCO.2016.7760355.

[92] O. Tervo, T. Levanen, K. Pajukoski, J. Hulkkonen, P. Wainio and M. Valkama. 5G New Radio Evolution Towards Sub-THz Communications. In: *2020 2nd 6G Wireless Summit (6G SUMMIT)*. 2020, 1–6. DOI: 10.1109/6GSUMMIT49458.2020.9083807.

[98] J. R. Wilkerson, I. M. Kilgore, K. G. Gard and M. B. Steer. Passive Intermodulation Distortion in Antennas. In: *IEEE Transactions on Antennas and Propagation* 63.2 (2015), 474–482. DOI: 10.1109/TAP.2014.2379947.

[99] J. R. Wilkerson, P. G. Lam, K. G. Gard and M. B. Steer. Distributed Passive Intermodulation Distortion on Transmission Lines. In: *IEEE Transactions on Microwave Theory and Techniques* 59.5 (2011), 1190–1205. DOI: 10.1109/TMTT.2011.2106138.

[100] T. Wu et al. A 40nm 4-downlink and 2-uplink RF transceiver supporting LTE-Advanced carrier aggregation. In: *Proc. 2018 IEEE Radio Frequency Integrated Circuits Symp. (RFIC)*. June 2018, 316–319. DOI: 10.1109/RFIC.2018.8428998.

[101] C. Yu, W. Cao, Y. Guo and A. Zhu. Digital Compensation for Transmitter Leakage in Non-Contiguous Carrier Aggregation Applications With FPGA Implementation. In: *IEEE Transactions on Microwave Theory and Techniques* 63.12 (2015), 4306–4318. DOI: 10.1109/TMTT.2015.2495144.

[102] YUPANA. *"Mitigating external sources of Passive Intermodulation" YUPANA, 2022. [Online]*. https://yupanatech.com/media/uploads/PIM_YUPANA.pdf. 2016.

[103] A. A. Zaidi, R. Baldemair, H. Tullberg, H. Bjorkegren, L. Sundstrom, J. Medbo, C. Kilinc and I. Da Silva. Waveform and Numerology to Support 5G Services and Requirements. In: *IEEE Communications Magazine* 54.11 (2016), 90–98. DOI: 10.1109/MCOM.2016.1600336CM.

[104] Y. P. Zhang and D. Liu. Antenna-on-Chip and Antenna-in-Package Solutions to Highly Integrated Millimeter-Wave Devices for Wireless Communications. In: *IEEE Transactions on Antennas and Propagation* 57.10 (2009), 2830–2841. DOI: 10.1109/TAP.2009.2029295.

APPENDIX A

MATHEMATICAL DERIVATIONS

A.1 Calculating the Complex Partial Derivative of the Decoupled Learning Rule

The partial derivative of $J(gn, hn)$ can first be calculated as follows:

$$\begin{aligned}
\frac{\partial J(\mathbf{g}_n, \mathbf{h}_n)}{\partial \mathbf{g}_n} =& \frac{\partial |y_{\mathrm{c}}(n)|^2}{\partial \mathbf{g}_n} = \frac{\partial y_{\mathrm{c}}(n) y_{\mathrm{c}}^*(n)}{\partial \mathbf{g}_n} \\
=& y_{\mathrm{c}}^*(n) \frac{\partial y_{\mathrm{c}}(n)}{\partial \mathbf{g}_n} + y_{\mathrm{c}}(n) \frac{\partial y_{\mathrm{c}}^*(n)}{\partial \mathbf{g}_n} \\
=& - y_{\mathrm{c}}^*(n) \frac{\partial y_{\mathrm{PIM}}(n)}{\partial \mathbf{g}_n} - y_{\mathrm{c}}(n) \frac{\partial y_{\mathrm{PIM}}^*(n)}{\partial \mathbf{g}_n} \\
=& - y_{\mathrm{c}}^*(n) \left(\frac{\partial y_{\mathrm{PIM}}(n)}{\partial \mathbf{g}_{R,n}} + j \frac{\partial y_{\mathrm{PIM}}(n)}{\partial \mathbf{g}_{I,n}} \right) \\
& - y_{\mathrm{c}}(n) \left(\frac{\partial y_{\mathrm{PIM}}^*(n)}{\partial \mathbf{g}_{R,n}} + j \frac{\partial y_{\mathrm{PIM}}^*(n)}{\partial \mathbf{g}_{I,n}} \right) \\
=& - y_{\mathrm{c}}^*(n) \left(\frac{\partial y_{\mathrm{PIM}}(n)}{\partial \mathbf{g}_{R,n}} + j \frac{\partial y_{\mathrm{PIM}}(n)}{\partial \mathbf{g}_{I,n}} \right) \\
& - y_{\mathrm{c}}(n) \left(\left(\frac{\partial y_{\mathrm{PIM}}(n)}{\partial \mathbf{g}_{R,n}} \right)^* + j \left(\frac{\partial y_{\mathrm{PIM}}(n)}{\partial \mathbf{g}_{I,n}} \right)^* \right)
\end{aligned} \tag{A.1}$$

where $\mathbf{g}_n = \mathbf{g}_{R,n} + j\mathbf{g}_{I,n}$.

Recalling that $y_{\mathrm{PIM}}(n) = \mathbf{h}_n^H \mathbf{y}_{n,\mathrm{NL}}$, the partial derivative of $y_{\mathrm{PIM}}(n)$ with respect to $\mathbf{g}_{R,n}$ can then be calculated as

$$\begin{aligned}\frac{\partial y_{\mathrm{PIM}}(n)}{\partial \mathbf{g}_{R,n}} =& \frac{\partial \mathbf{h}_n^H \mathbf{y}_{n,\mathrm{NL}}}{\partial \mathbf{g}_{R,n}} = \frac{\partial \mathbf{y}_{n,\mathrm{NL}}}{\partial \mathbf{g}_{R,n}} \mathbf{h}_n^* \\ =& \left[\frac{\partial y_{\mathrm{NL}}(n+M_1)}{\partial \mathbf{g}_{R,n}} \quad \cdots, \frac{\partial y_{\mathrm{NL}}(n-M_2)}{\partial \mathbf{g}_{R,n}} \right] \mathbf{h}_n^*. \end{aligned} \tag{A.2}$$

A column of $\frac{(\partial y_{n,NL})}{(\partial \mathbf{g}_{R,n})}$ can easily be obtained as follows:

$$\frac{\partial y_{\mathrm{NL}}(n)}{\partial \mathbf{g}_{R,n}} = \frac{\partial \mathbf{g}_n^H \boldsymbol{\phi}(n)}{\partial \mathbf{g}_{R,n}} = \frac{\partial (\mathbf{g}_{R,n}^T - j\mathbf{g}_{I,n}^T)\boldsymbol{\phi}(n)}{\partial \mathbf{g}_{R,n}} = \boldsymbol{\phi}(n). \tag{A.3}$$

Therefore,

$$\frac{\partial y_{\mathrm{PIM}}(n)}{\partial \mathbf{g}_{R,n}} = \begin{bmatrix} \boldsymbol{\phi}(n+M_1) & \cdots & \boldsymbol{\phi}(n-M_2) \end{bmatrix} \mathbf{h}_n^* = \boldsymbol{\Phi}_n \mathbf{h}_n^* \tag{A.4}$$

where $\boldsymbol{\Phi}_n = \begin{bmatrix} \boldsymbol{\phi}(n+M_1) & \cdots & \boldsymbol{\phi}(n-M_2) \end{bmatrix}$. Following a largely similar procedure, the partial derivative of $y_{\mathrm{PIM}}(n)$ with respect to $\mathbf{g}_{I,n}$ can be calculated as

$$\begin{aligned}\frac{\partial y_{\mathrm{PIM}}(n)}{\partial \mathbf{g}_{I,n}} =& \frac{\partial \mathbf{h}_n^H \mathbf{y}_{n,\mathrm{NL}}}{\partial \mathbf{g}_{I,n}} = \frac{\partial \mathbf{y}_{n,\mathrm{NL}}}{\partial \mathbf{g}_{I,n}} \mathbf{h}_n^* \\ =& \left[\frac{\partial y_{\mathrm{NL}}(n+M_1)}{\partial \mathbf{g}_{I,n}} \cdots \frac{\partial y_{\mathrm{NL}}(n-M_2)}{\partial \mathbf{g}_{I,n}} \right] \mathbf{w}_n^* \end{aligned} \tag{A.5}$$

where a column of $\frac{(\partial y_{\mathrm{NL}}(n))}{(\partial \mathbf{g}_{I,n})}$ can now be calculated as

$$\frac{\partial y_{\mathrm{NL}}(n)}{\partial \mathbf{g}_{I,n}} = \frac{\partial \mathbf{g}_n^H \boldsymbol{\phi}(n)}{\partial \mathbf{g}_{I,n}} = \frac{\partial \left(\mathbf{g}_{R,n}^T - j\mathbf{g}_{I,n}^T \right) \boldsymbol{\phi}(n)}{\partial \mathbf{g}_{I,n}} = -j\boldsymbol{\phi}(n). \tag{A.6}$$

As a result, we can write

$$\begin{aligned}\frac{\partial y_{\mathrm{PIM}}(n)}{\partial \mathbf{g}_{I,n}} &= \begin{bmatrix} -j\boldsymbol{\phi}(n+M_1) & \cdots & -j\boldsymbol{\phi}(n-M_2) \end{bmatrix} \mathbf{h}_n^* \\ &= -j\boldsymbol{\Phi}_n \mathbf{h}_n^*. \end{aligned} \tag{A.7}$$

Substituting the hereby obtained expressions into (A.1), we get

$$\begin{aligned}\frac{\partial J(\mathbf{g}_n, \mathbf{h}_n)}{\partial \mathbf{g}_n} &= -y_{\mathrm{c}}^*(n)\left(\frac{\partial y_{\mathrm{PIM}}(n)}{\partial \mathbf{g}_{R,n}} + j\frac{\partial y_{\mathrm{PIM}}(n)}{\partial \mathbf{g}_{I,n}}\right) \\ &\quad - y_{\mathrm{c}}(n)\left(\left(\frac{\partial y_{\mathrm{PIM}}(n)}{\partial \mathbf{g}_{R,n}}\right)^* + j\left(\frac{\partial y_{\mathrm{PIM}}(n)}{\partial \mathbf{g}_{I,n}}\right)^*\right) \\ &= -y_{\mathrm{c}}^*(n)\left(\boldsymbol{\Phi}_n \mathbf{h}_n^* - j^2 \boldsymbol{\Phi}_n \mathbf{h}_n^*\right) \\ &\quad - y_{\mathrm{c}}(n)\left(\boldsymbol{\Phi}_n^* \mathbf{h}_n + j^2 \boldsymbol{\Phi}_n^* \mathbf{h}_n\right) \\ &= -2y_{\mathrm{c}}^*(n)\boldsymbol{\Phi}_n \mathbf{h}_n^* \end{aligned} \tag{A.8}$$

because $j^2 = -1$.

A.2 Calculating the Correlation Matrix of the Orthogonalized Decoupled Learning Rule

We start by rewriting $\mathbf{u}_n$ as follows:

$$\begin{aligned}\mathbf{u}_n = &\boldsymbol{\Phi}_n \mathbf{h}_n^* = \begin{bmatrix} \boldsymbol{\phi}(n+M_1) & \cdots & \boldsymbol{\phi}(n-M_2) \end{bmatrix} \mathbf{h}_n^* \\ = &\begin{bmatrix} \boldsymbol{\phi}_1^T(n) \\ \boldsymbol{\phi}_2^T(n) \\ \vdots \\ \boldsymbol{\phi}_C^T(n) \end{bmatrix} \mathbf{h}_n^* = \begin{bmatrix} \boldsymbol{\phi}_1^T(n)\mathbf{h}_n^* \\ \boldsymbol{\phi}_2^T(n)\mathbf{h}_n^* \\ \vdots \\ \boldsymbol{\phi}_C^T(n)\mathbf{h}_n^* \end{bmatrix} = \begin{bmatrix} \mathbf{h}_n^H \boldsymbol{\phi}_1(n) \\ \mathbf{h}_n^H \boldsymbol{\phi}_2(n) \\ \vdots \\ \mathbf{h}_n^H \boldsymbol{\phi}_C(n) \end{bmatrix} \end{aligned} \tag{A.9}$$

where $\boldsymbol{\phi}_i(n) = \begin{bmatrix} \phi_i(n+M_1) & \cdots & \phi_i(n-M_2) \end{bmatrix}^T$ and $\phi_i(n)$ is the ith PIM basis function. In other words, instead of collecting the different instantaneous basis functions into a single vector $\boldsymbol{\phi}(n-k)$, we now collect the delayed copies of an individual basis function into a single vector $\boldsymbol{\phi}_i(n)$. With this, the correlation

matrix becomes

$$\begin{aligned}\mathbf{R} =& \mathrm{E}\left[\mathbf{u}_n\mathbf{u}_n^H\right] \\ =& \mathrm{E}\left[\begin{bmatrix}\mathbf{h}_n^H\boldsymbol{\phi}_1(n) \\ \vdots \\ \mathbf{h}_n^H\boldsymbol{\phi}_C(n)\end{bmatrix}\begin{bmatrix}\boldsymbol{\phi}_1^H(n)\mathbf{h}_n & \cdots & \boldsymbol{\phi}_C^H(n)\mathbf{h}_n\end{bmatrix}\right].\end{aligned} \tag{A.10}$$

Therefore, the element on the ith row and jth column is

$$\begin{aligned}\{\mathbf{R}\}_{ij} =& \mathrm{E}\left[\mathbf{h}_n^H\boldsymbol{\phi}_i(n)\boldsymbol{\phi}_j^H(n)\mathbf{h}_n\right] \\ =& \mathbf{h}_n^H\mathrm{E}\left[\boldsymbol{\phi}_i(n)\boldsymbol{\phi}_j^H(n)\right]\mathbf{h}_n\end{aligned} \tag{A.11}$$

where the last equality stems from the fact that the analysis is performed for a given memory model. Inspecting then the remaining expected value, it can be rewritten as

$$\begin{aligned}&\mathrm{E}\big[\boldsymbol{\phi}_i(n)\boldsymbol{\phi}_j^H(n)\big] \\ &=\mathrm{E}\left[\begin{bmatrix}\phi_i(n+M_1) \\ \vdots \\ \phi_i(n-M_2)\end{bmatrix}\begin{bmatrix}\phi_j^*(n+M_1) & \cdots & \phi_j^*(n-M_2)\end{bmatrix}\right] \\ &=\mathrm{E}[\phi_i(n)\phi_j^*(n)]\mathbf{I}_M\end{aligned} \tag{A.12}$$

where $M = M_1 + M_2 + 1$ and $\mathbf{I}_M$ is an $M \times M$ identity matrix. The last expression is based on the assumption of i.i.d. stationary transmit signals.

Substituting then (A.12) into (A.11), we get the following form for the element on the ith row and jth column:

$$\begin{aligned}\{\mathbf{R}\}_{ij} =& \mathbf{h}_n^H\mathrm{E}[\phi_i(n)\phi_j^*(n)]\mathbf{I}_M\mathbf{h}_n \\ =& \mathrm{E}[\phi_i(n)\phi_j^*(n)]\mathbf{h}_n^H\mathbf{I}_M\mathbf{h}_n = \mathrm{E}[\phi_i(n)\phi_j^*(n)]\mathbf{h}_n^H\mathbf{h}_n.\end{aligned} \tag{A.13}$$

From this, it is easy to see that the correlation matrix can be written as follows:

$$\begin{aligned}\mathbf{R} =& \mathrm{E}\left[\begin{bmatrix}\phi_1(n)\\ \vdots \\ \phi_C(n)\end{bmatrix}\begin{bmatrix}\phi_1^*(n) & \vdots & \phi_C^*(n)\end{bmatrix}\right]\mathbf{h}_n^H\mathbf{h}_n \\ =& \mathrm{E}\left[\boldsymbol{\phi}(n)\boldsymbol{\phi}^H(n)\right]\mathbf{h}_n^H\mathbf{h}_n = \mathbf{R}_{\boldsymbol{\phi}}\mathbf{h}_n^H\mathbf{h}_n \end{aligned} \tag{A.14}$$

where $\mathbf{R}_{\boldsymbol{\phi}}$ is the correlation matrix of the basis functions.

Publications

PUBLICATION
I

Digital self-interference cancellation in inter-band carrier aggregation transceivers: Algorithm and digital implementation perspectives

M. Z. Waheed, D. Korpi, A. Kiayani, L. Anttila and M. Valkama

2017 IEEE International Workshop on Signal Processing Systems (SiPS), Lorient, France (2017), 1–5
DOI: 10.1109/SiPS.2017.8109983

Digital Self-interference Cancellation in Inter-band Carrier Aggregation Transceivers: Algorithm and Digital Implementation Perspectives

Muhammad Zeeshan Waheed, Dani Korpi, Adnan Kiayani, Lauri Anttila, and Mikko Valkama

Laboratory of Electronics and Communications Engineering, Tampere University of Technology, Finland
e-mail: muhammad.waheed@tut.fi

***Abstract*—In this paper we study and analyze the problem of self-interference in transceivers performing inter-band carrier aggregation, where separate power amplifiers (PAs) are used for each component carrier (CC). The self-interference stems from the nonlinear behaviour of the passive RF components at the transmitter, which results in passive intermodulation terms that in some cases fall onto the RX band. Moreover, also the individual PAs distort the CCs in a nonlinear fashion, which means that the self-interference is in fact produced by a cascade of two nonlinearities. This is something that has largely been ignored in earlier literature. Hence, in this work, a signal model is derived that considers both the nonlinearity of the PAs and the passive components, resulting in a highly efficient digital cancellation solution. Using realistic waveform simulations, it is shown to outperform the existing digital cancellers that neglect the PA-induced nonlinear distortion. Also the computational complexity of the proposed digital canceller is analyzed in detail. All in all, the findings indicate that the developed digital cancellation solution is a feasible option for improving the receiver sensitivity of mobile devices utilizing inter-band carrier aggregation.**

I. Introduction

The continuously increasing user demands for high data throughput in wireless systems can be satisfied by utilizing wider transmission bandwidths. Therefore, modern cellular handsets need to support a wide range of frequency bands, and some of them simultaneously, so that a large aggregated bandwidth can be realized. However, due to current allocation and licensing of the radio spectrum, allocating a continuous spectrum to a single user is practically impossible. To alleviate this issue, the carrier aggregation (CA) technique introduced in LTE-Advanced enables flexible expansion of the transmission bandwidth by aggregating spectrum resources either from the same LTE frequency band (intra-band) or from different frequency bands (inter-band CA) [1]–[3]. With inter-band CA, multiple transmissions can occur simultaneously over different LTE bands, where each contiguous transmit signal is referred to as component carrier (CC), and it greatly enhances the flexibility and efficiency of the radio spectrum usage.

In general, noncontiguous transmission poses a variety of practical implementation related challenges for the radio transceivers [3], [4]. More specifically, when a noncontiguous signal propagates through a nonlinear radio frequency (RF) front-end component, unwanted intermodulation distortion (IMD) products are produced. These IMD products lie at specific intermodulation (IM) sub-bands which are integer linear combinations of the CC center-frequencies [4]. In some cases, some of the IM sub-bands can appear in the own receiver (RX) operating band, causing self-interference. This has recently been acknowledged in 3GPP for various band combinations in inter-band CA [5], [6].

A dominant source of nonlinear distortion in radio transceivers is the transmitter (TX) power amplifier (PA). However, with inter-band CA transmissions where each CC is typically amplified by a separate PA [3], [7], spurious signals generated by the passive RF front-end components can also be significant and, in turn, may cause self-interference to the RX. In recent years, several digital cancellation techniques have been proposed that target to suppress the PA nonlinearity induced self-interference [4]–[9]. On the other hand, the works in [10]–[12] consider only the digital cancellation of passive IMD, while neglecting the nonlinear distortion in the individual TX PAs. In this paper, we develop a complete behavioral model incorporating the joint effects of the cascaded nonlinearities of the PA and the passive components. Then, building on this model, we develop a digital cancellation technique to jointly mitigate the self-interference caused by the nonlinearity of the TX PAs and the passive components in the receiver digital baseband. Waveform simulation results show that the proposed digital cancellation scheme provides substantial self-interference suppression, thus reducing the RF components' linearity requirements, cost, and complexity.

The rest of the paper is organized as follows. In the following section, we discuss the implementation challenges of a radio transceiver supporting inter-band CA. In Section III, essential signal models related to the cascaded nonlinearity of the TX PAs and the passive components are presented, together with the proposed digital cancellation technique. The performance evaluation of the proposed technique with full waveform simulations is reported in Section IV, and conclusions are made in Section V.

II. Inter-band Carrier Aggregation with Non-ideal RF Components

Inter-band CA allows combining the spectrum resources from different LTE operating bands in order to provide increased data rate. It can be divided into CA among the low-

978-1-5386-0446-5/17/$31.00

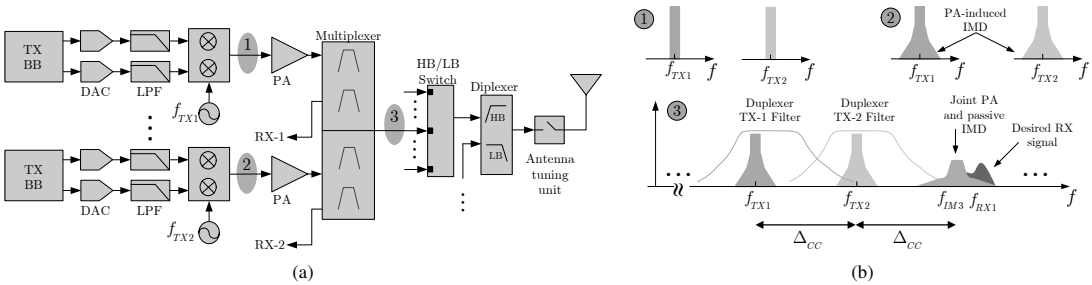

(a) (b)

Fig. 1: (a) Block diagram of the considered transmitter architecture for inter-band CA FDD transceiver, and (b) a spectral illustration of the unwanted IMD products created due to the nonlinearity of the TX PAs and the passive components, appearing in one of the configured RX operating bands.

band ($<$ 1 GHz) carriers and high-band ($>$ 1 GHz) carriers (LB-HB CA) where the CC center-frequencies are further apart, or CA of similar frequencies, i.e., LB-LB CA or HB-HB CA [13]. In this paper, we consider the inter-band CA of similar frequencies, such as CA of LTE Band 1 and Band 3 (CA B1+3), CA B5+13, or CA B4+8, among others. The considered radio architecture, shown in Fig. 1(a), is comprised of separate TX and RX chains for each aggregated LTE band which, in general, is a feasible candidate TX architecture to support a wide range of LTE bands [7]. Each CC is amplified by a separate PA, and different LTE bands are combined using a multiplexer. The radio transceivers of different LTE bands share the same antenna and thereby a band selection switch and a diplexer are also employed.

As discussed earlier, the nonlinear behavior of the RF components in the radio transceiver and RF front-end creates unwanted IMD products. The IMD products created due to the PA nonlinearity appear as spectral regrowth around the transmit CCs, whereas the passive front-end components, such as the multiplexer, the switch, and the diplexer, create IMD products of the CCs which appear at various different center-frequencies. In general, the IM frequencies are linear combinations of the CC center-frequencies, with certain integer coefficients. In some CA band combinations, the center-frequencies of these IMD products can coincide with one of the configured RX frequencies and may lead to RX desensitization, as shown in Fig. 1(b). For example, if we consider the CA of B1+B3 and assume that the center frequency of CC1 is $f_{\mathrm{TX1}} = 1950$ MHz and the center frequency of CC2 is $f_{\mathrm{TX2}} = 1760$ MHz, then the third-order IM sub-band, located at $f = 2f_{\mathrm{TX1}} - f_{\mathrm{TX2}} = 2140$ MHz, falls within the RX band of B1. Other similar band combination examples may include, e.g., CA B3+8, B2+4, B5+7, etc. The relative powers of the IMD components depend on the PA and the passive components' linearity characteristics, and can be very strong even with state-of-the-art RF components.

To prevent the RX desensitization in inter-band CA transceivers, one could consider either reducing the transmit power or alternatively relaxing the receiver reference sensitivity requirements, known as maximum power reduction (MPR) and maximum sensitivity degradation (MSD) in the context of LTE-Advanced, respectively [5], [14]. The former decreases the relative strength of the IMD, while the latter simply takes the IMD-induced interference into account in the link budget calculations. However, such methods will severely compromise the uplink coverage, and consequently a more convenient option might be to just improve the quality of the RF components at the expense of increased overall cost.

Motivated by previous discussion and keeping in view the drawbacks of the above discussed solutions, in this paper we develop an advanced digital self-interference cancellation solution for inter-band CA radio transceivers. This means that the self-interference can be dealt with without any decrease in the uplink coverage, or without significant increase in the overall cost of the transceiver.

III. Passive Intermodulation Modeling and Proposed Digital Cancellation

As already discussed, in this paper we consider a scenario where two UL CCs, transmitted within an LTE mobile device, produce IMD onto the DL frequency band. In particular, assuming that the UL transmission occurs on LTE UL bands 1 and 3, one of the 3rd-order IMD products will fall directly onto the LTE DL Band 1. Note that there are also band combinations that can produce harmful IMD of different orders, but in this work the emphasis is only on this band combination and the 3rd-order IMD that is being produced by the passive components.

A. Self-interference Model and Canceller Structure

In general, denoting the baseband UL signals on Bands 1 and 3 by $s_1(n)$ and $s_3(n)$, respectively, and considering only the 3rd-order passive intermodulation (PIM), we can express the PIM product at RF as

$$s_{\mathrm{PIM}}(n) = \alpha_{\mathrm{PIM}} \left(\alpha_1 \,\mathrm{Re}\left\{s_1(n)e^{j\omega_1 n}\right\} + \alpha_2 \,\mathrm{Re}\left\{s_3(n)e^{j\omega_3 n}\right\}\right)^3 \quad (1)$$

where ω_1 is the center-frequency of the CC on Band 1, ω_3 is the center-frequency of the CC on Band 3, and α_X are unknown coefficients. It is then easy to show by expanding (1)

that the baseband-equivalent self-interference signal falling onto the RX band is as follows:

$$s_{\mathrm{PIM}}^{\mathrm{RX}}(n) = \alpha_{\mathrm{PIM}}^{\mathrm{RX}} s_1(n)^2 s_3^*(n), \tag{2}$$

where we have reverted to baseband-equivalent notation for notational simplicity, the zero frequency corresponding to $2\omega_1 - \omega_3$. Note that (1) generates also several other nonlinear terms but none of them fall near the considered RX band and can consequently be ignored in this analysis.

It is important to note that also the PAs themselves produce some nonlinear distortion, which should be modeled, in addition to PIM. Having also a 3rd-order model for both PAs, we can write

$$s_1(n) = \alpha_{11} x_1(n) + \alpha_{13} x_1(n)^2 x_1^*(n) \tag{3}$$

$$s_3(n) = \alpha_{21} x_3(n) + \alpha_{23} x_3(n)^2 x_3^*(n) \tag{4}$$

where $x_1(n)$ and $x_3(n)$ are the original TX data signals for the two PAs on LTE UL Bands 1 and 3, respectively, and α_{xy} are the coefficients for the PA models. Substituting then (3) and (4) into (2), the final baseband equivalent self-interference signal can be written as

$$\begin{aligned} s_{\mathrm{PIM}}^{\mathrm{RX}}(n) = {} & \alpha_1 x_1(n)^2 x_3^*(n) + \alpha_2 x_1(n)^3 x_1^*(n) x_3^*(n) \\ & + \alpha_3 x_1(n)^4 x_1^*(n)^2 x_3^*(n) + \alpha_4 x_1(n)^2 x_3^*(n)^2 x_3(n) \\ & + \alpha_5 x_1(n)^3 x_1^*(n) x_3^*(n)^2 x_3(n) \\ & + \alpha_6 x_1(n)^4 x_1^*(n)^2 x_3^*(n)^2 x_3(n) \end{aligned} \tag{5}$$

Hence, the final signal model consists of six basis functions, whose coefficients (α_1–α_6) must be estimated in order to regenerate and cancel the PIM-induced self-interference in the receiver.

It should also be noted that the first basis function ($x_1(n)^2 x_3^*(n)$) corresponds to a model with linear PAs, and it can consequently be considered as a benchmark for the proposed digital canceller, which also incorporates the nonlinearity of the PAs. Such a model has been proposed, for instance, in [10], albeit with memory. However, note that the first basis function is still the most dominant one in any practical system as the linear signal term is obviously stronger than any of the nonlinearities.

B. Parameter Estimation

Noting that (5) is in fact a linear-in-parameters model, the parameter estimation can be carried out with linear least squares (LS). For this, let us denote the six basis functions in (5) as follows:

$$\begin{aligned} \phi_1(n) &= x_1(n)^2 x_3^*(n) \\ \phi_2(n) &= x_1(n)^3 x_1^*(n) x_3^*(n) \\ \phi_3(n) &= x_1(n)^4 x_1^*(n)^2 x_3^*(n) \\ \phi_4(n) &= x_1(n)^2 x_3^*(n)^2 x_3(n) \\ \phi_5(n) &= x_1(n)^3 x_1^*(n) x_3^*(n)^2 x_3(n) \\ \phi_6(n) &= x_1(n)^4 x_1^*(n)^2 x_3^*(n)^2 x_3(n) \end{aligned} \tag{6}$$

Then, the data matrix for the nth time instant is as follows:

$$\begin{aligned} & \boldsymbol{\Phi}(n) \\ & = \begin{bmatrix} \phi_1(n-N+1) & \phi_2(n-N+1) & \cdots & \phi_6(n-N+1) \\ \phi_1(n-N+2) & \phi_2(n-N+2) & \cdots & \phi_6(n-N+2) \\ \vdots & \vdots & \ddots & \vdots \\ \phi_1(n) & \phi_2(n) & \cdots & \phi_6(n) \end{bmatrix} \end{aligned} \tag{7}$$

where N is the number of samples used for estimation. The parameter estimate is then simply calculated as

$$\widehat{\boldsymbol{\alpha}} = \left(\boldsymbol{\Phi}^H(n)\boldsymbol{\Phi}(n)\right)^{-1} \boldsymbol{\Phi}^H(n)\boldsymbol{y} \tag{8}$$

where $\hat{\boldsymbol{\alpha}} = \begin{bmatrix} \widehat{\alpha}_1 & \widehat{\alpha}_2 & \cdots & \widehat{\alpha}_6 \end{bmatrix}^T$ contains the estimate for each coefficient, and $\boldsymbol{y}$ is the received signal before any cancellation. Moreover, $(\cdot)^H$ denotes the Hermitian transpose, while $(\cdot)^T$ denotes the regular transpose. The actual cancellation performance can then be evaluated by regenerating the self-interference over another observation period, using the estimated coefficients. The signal after the cancellation can be written as follows:

$$y_{\mathrm{c}}(n) = y(n) - \sum_{i=1}^{6} \widehat{\alpha}_i \phi_i(n), \tag{9}$$

where $y(n)$ is the nth sample of the overall received signal before any cancellation. In the forthcoming results section, the performance of the proposed scheme is compared to the case where linear PAs are assumed, which means that only the first basis function is included in the cancellation processing, as discussed earlier. This is essentially a memoryless version of the digital cancellation solution presented in [10].

C. Computational Complexity of the Cancellation Procedure

Let us then briefly analyze the computational complexity of the proposed digital cancellation solution. The overall cancellation procedure involves in principle two steps, which are as follows:

- Estimating the coefficients with LS
- Regenerating and canceling the self-interference signal

However, considering that the nonlinear behaviour of the PAs and the passive components can be expected to be largely time-invariant, the estimation stage is performed only relatively infrequently. Hence, the overall computational complexity of the digital canceller is mainly determined by the second stage, as it is being performed constantly. For this reason, it is sufficient to consider only the second stage in this analysis.

It can easily be observed from (6) that generating the six basis function samples for one time instant requires 36 complex multiplications. Furthermore, generating the cancellation signal itself, as shown in (9), requires 6 complex multiplications and 5 complex additions per one time instant. Taking into account also the actual cancellation where the regenerated self-interference signal is subtracted from the received signal, the total number of required computations per each received sample is ***42 complex multiplications and 6 complex additions***.

If some latency in generating the basis functions is acceptable, the number of multiplications can be decreased by presenting the basis functions in a recursive form as follows:

$$\begin{aligned}
\phi_1(n) &= x_1(n)^2 x_3^*(n) \\
\phi_2(n) &= \phi_1(n) x_1(n) x_1^*(n) \\
\phi_3(n) &= \phi_2(n) x_1(n) x_1^*(n) \\
\phi_4(n) &= \phi_1(n) x_3(n) x_3^*(n) \\
\phi_5(n) &= \phi_4(n) x_1(n) x_1^*(n) \\
\phi_6(n) &= \phi_5(n) x_1(n) x_1^*(n)
\end{aligned} \tag{10}$$

In this case, it can be calculated from (10) that generating the six basis functions for one time instant requires only 10 complex multiplications. Taking into account also the computations involved in generating the cancellation signal and performing the subtraction, in total ***16 complex multiplications and 6 complex additions*** are needed in this case for each received sample. However, as mentioned, the cost of this decreased computational complexity is the increased latency in generating the basis functions. It should also be mentioned that it might be possible to further reduce the number of multiplications by using alternative representations of the TX signals, although these aspects are out of the scope of this paper.

IV. Simulation Results

A. Simulator Description

The proposed digital cancellation solution is then evaluated using a waveform simulator implemented with Matlab, which is modeling the transceiver illustrated in Fig. 1. The two CCs are transmitted on LTE UL bands 1 and 3, as per the earlier discussions, the transmit waveforms being LTE UL signals. Furthermore, realistic baseband-equivalent models for the different components are also included in the simulator. Firstly, the model for each PA is extracted by measuring the characteristics of an actual real-life PA under the utilized transmit power. The memory effects of the PA are also included in the modeling. The frequency selective behaviour of the duplexer/multiplexer is also considered in the simulator, although results are also provided for a frequency-flat ideal duplexer for reference. The IMD is then produced within the simulator by feeding the sum transmit signal, consisting of two CCs, into a nonlinear model of an RF switch. This produces the PIM component that is falling onto the RX band. The relevant parameters used in the simulations are listed in Table I.

B. Cancellation Performance

The cancellation performance is first measured for a frequency-flat duplexer response. This means that the only memory within the system is that of the PAs. Figure 2 shows the spectra of observed self-interference signal, alongside with the signal spectra after the two different digital cancellers. The cancellation performance of the benchmark scheme with linear PA models, taken from [10], is clearly insufficient for such a weak received signal of interest, as the signal-to-interference-plus-noise ratio (SINR) is in this case negative. On the other hand, when utilizing all the six basis functions, i.e., modeling also the nonlinearity of the PAs, the self-interference can be cancelled almost 10 dB below the noise

TABLE I: The essential simulation parameters.

Parameter	Value
Bandwidth of the CCs	5 MHz
Total transmit power	23 dBm
Center frequencies of CCs	1760/1950 MHz
RX frequency	2140 MHz
IIP3 of the RF switch	70 dBm
Power of the RX signal	-91.5 dBm
Number of samples used for estimation (N)	10 000

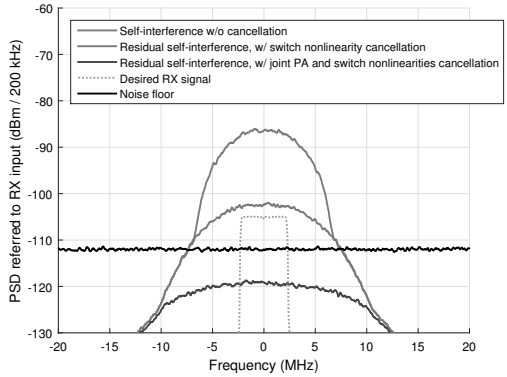

Fig. 2: The spectra of the observed PIM and the residual signals after cancellation. The received signal of interest is also shown for reference. Frequency-flat duplexer response.

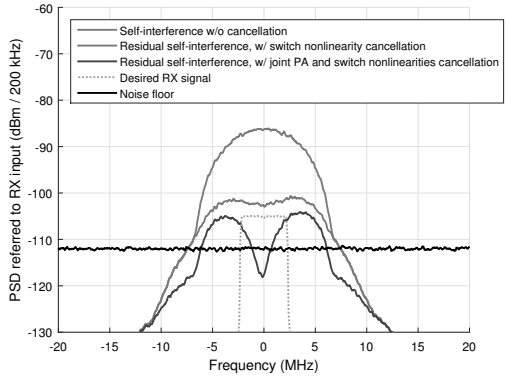

Fig. 3: The spectra of the observed PIM and the residual signals after cancellation. The received signal of interest is also shown for reference. Frequency-selective duplexer response.

floor. This means that the decrease in the SINR is less than half a decibel. Hence, the proposed canceller, with realistic nonlinearity models for the PAs and the passive components, is indeed capable of sufficient cancellation accuracy. Note that the parameter estimation within the simulator is performed using the total received signal that contains also the noise and the desired signal, although each signal component is shown separately in Fig. 2 for a better illustration.

Considering then a more challenging scenario where the duplexer has a frequency-selective response, Fig. 3 shows again the spectra of the different signal components. As can be observed, now the residual self-interference power is much higher also after the proposed canceller with PA nonlinearity modeling. This stems from the fact that the utilized signal model does not have any memory, and consequently it is not capable of modeling any frequency selectivity. This is not an issue when only the PAs have memory, as the resulting frequency selectivity is rather mild in nature. However, the frequency selectivity of the duplexer response is much more severe, and thereby the accuracy of the memoryless model is somewhat reduced. Nevertheless, it still outperforms the benchmark scheme with linear PA models, although now the residual self-interference decreases the SINR with both cancellers.

All in all, these findings confirm the high performance of the proposed digital canceller, thereby indicating that the nonlinearity of the PAs must be modeled when canceling PIM-induced self-interference in the receiver. However, Fig. 3 also demonstrates that the digital canceller should incorporate some memory to fully suppress the self-interference under practical circumstances. This is an important future work item for us, together with performing actual RF measurement–based cancellation experiments.

V. Conclusion

In this paper, we proposed a novel digital cancellation solution for dealing with the self-interference produced in transceivers utilizing inter-band carrier aggregation. The self-interference stems from the nonlinearity of the passive components, as separate power amplifiers are used for each component carrier. However, the nonlinear behaviour of the power amplifiers still affects the self-interference waveform, and hence it is also considered in the proposed digital canceller. Using waveform simulations, the developed digital canceller is shown to outperform the existing solutions, which neglect the nonlinearity of the PAs. As a future work item, we plan to extend the signal model to cover also the various memory effects occurring in the transmitter, while also using actual measured data to evaluate the cancellation performance under real-life conditions.

Acknowledgment

This work was supported by the Academy of Finland (under the projects 304147 In-Band Full-Duplex Radio Technology: Realizing Next Generation Wireless Transmission, and 301820 Competitive Funding to Strengthen University Research Profiles), the Finnish Funding Agency for Innovation (Tekes, under the project 5G Transceivers for Base Stations and Mobile Devices (5G TRx)), Tampere University of Technology Graduate School, Nokia Networks, TDK-EPCOS, Pulse, Sasken, and Huawei Technologies, Finland

References

[1] "Further advancements for E-UTRA physical layer aspects," 3GPP, Tech. Rep. 36.814, Mar. 2010, version 9.0.0, Release 9.

[2] M. Iwamura, K. Etemad, M. H. Fong, and R. Nory, "Carrier aggregation framework in 3GPP LTE-Advanced," *IEEE Communications Magazine*, vol. 48, no. 8, pp. 60–67, Aug. 2010.

[3] C. S. Park, L. Sundström, A. Wallen, and A. Khayallah, "Carrier aggregation for LTE-Advanced: Design challenges of terminals," *IEEE Communications Magazine*, vol. 51, no. 12, pp. 76–84, Dec. 2013.

[4] A. Kiayani, M. Abdelaziz, L. Anttila, V. Lehtinen, and M. Valkama, "Digital mitigation of transmitter-induced receiver desensitization in carrier aggregation FDD transceivers," *IEEE Transactions on Microwave Theory and Techniques*, vol. 63, no. 11, pp. 3608–3623, Dec. 2015.

[5] "LTE; evolved universal terrestrial radio access (E-UTRA); user equipment (UE) radio transmission and reception (3GPP TS 36.101, version 14.1.0, release 14)," ETSI, Sophia Antipolis Cedex, France, Sep. 2016.

[6] "LTE-advanced dual uplink inter-band carrier aggregation (CA) (3GPP TS 36.860, version 13.0.0, release 13)," ETSI, Sophia Antipolis Cedex, France, Jan. 2016.

[7] "Feasibility study for further advancements for E-UTRA (LTE-Advanced)," 3GPP, Tech. Rep. 36.912, Mar. 2013, version 14.0.0, Release 14.

[8] "R4-141306, band 1 and band 3 UE considerations for CA," Qualcomm Incorporated, San Jose Del Cabo, Mexico, 2014.

[9] A. Kiayani, L. Anttila, and M. Valkama, "Digital suppression of power amplifier spurious emissions at receiver band in FDD transceivers," *IEEE Signal Processing Letters*, vol. 21, no. 1, pp. 69–73, Jan. 2014.

[10] H. T. Dabag, H. Gheidi, S. Farsi, P. S. Gudem, and P. M. Asbeck, "All-digital cancellation technique to mitigate receiver desensitization in uplink carrier aggregation in cellular handsets," *IEEE Transactions on Microwave Theory and Techniques*, vol. 61, no. 12, pp. 4754–4765, Dec. 2013.

[11] H. T. Dabag, H. Gheidi, P. S. Gudem, and P. M. Asbeck, "All-digital cancellation technique to mitigate self-jamming in uplink carrier aggregation in cellular handsets," in *Proc. IEEE MTT-S International Microwave Symposium Digest (MTT)*, 2013.

[12] H. Gheidi, H. T. Dabag, Y. Liu, P. M. Asbeck, and P. S. Gudem, "Digital cancellation technique to mitigate receiver desensitization in cellular handsets operating in carrier aggregation mode with multiple uplinks and multiple downlinks," in *Proc. IEEE Radio and Wireless Symposium (RWS)*, 2015.

[13] "Inter-band carrier aggregation (3GPP TS, 36.850, version 1.1.0, release 11)," ETSI, Sophia Antipolis Cedex, France, Jul. 2013.

[14] "Way forward for interband class A2," Nokia Corporation and AT&T, Jeju Island, Korea, 2012.

PUBLICATION II

Digital Cancellation of Passive Intermodulation in FDD Transceivers

M. Z. Waheed, P. P. Campo, D. Korpi, A. Kiayani, L. Anttila and M. Valkama

2018 52nd Asilomar Conference on Signals, Systems, and Computers (2018), 1375–1381
DOI: 10.1109/ACSSC.2018.8645262

Digital Cancellation of Passive Intermodulation in FDD Transceivers

Muhammad Zeeshan Waheed, Pablo Pascual Campo, Dani Korpi, Adnan Kiayani, Lauri Anttila, Mikko Valkama

Laboratory of Electronics and Communications Engineering, Tampere University of Technology, Finland
e-mail: muhammad.waheed@tut.fi

***Abstract*—Modern radio systems and transceivers utilize carrier aggregation (CA) to meet the demands for higher and higher data rates. However, the adoption of CA in the existing Long Term Evolution (LTE)-Advanced and emerging 5G New Radio (NR) mobile networks, in case of frequency division duplexing (FDD), may incur self-interference challenges with certain band combinations. More specifically, the nonlinear distortion products of the transmit signals or component carriers (CCs), stemming from the passive radio frequency (RF) front-end components of the transceiver, can appear in one or more of the configured receiver bands, potentially leading to the receiver desensitization. In this paper, we present advanced baseband equivalent signal models for such passive intermodulation (PIM) distortion viewed from the RX point of view, considering also potential memory effects in the PIM generation. Then, building on these signal models, a digital self-interference cancellation technique operating in the transceiver digital front-end is presented. The performance of the proposed solution is evaluated with real-life RF measurements for LTE-Advanced type user equipment (UE) with dual CC inter-band CA, demonstrating excellent suppression properties. The findings in this work indicate that digital cancellation is a feasible approach for improving the receiver sensitivity of mobile devices that may be prone to RF front-end induced PIM challenges.**

***Index Terms*—4G LTE-Advanced, 5G NR, digital cancellation, frequency division duplexing, nonlinear distortion, passive intermodulation, self-interference.**

I. Introduction

The increasing amounts of data usage by mobile network subscribers imply the need for higher throughputs and higher network capacities. The existing and emerging mobile communication networks, such as 4G long term evolution (LTE)-Advanced and 5G New Radio (NR), are designed to meet these needs and requirements [1]. Carrier aggregation (CA) is one of the key techniques that was introduced in LTE-Advanced to support higher throughput requirements, where multiple component carriers (CCs) at one or multiple LTE bands are aggregated together to form larger transmission bandwidth, and also to facilitate efficient utilization of the available radio spectrum [2]–[4]. In this work, we particularly focus on the case where the aggregated CCs are at different bands, commonly referred to as inter-band CA.

In general, modern radio systems employing wideband multicarrier waveforms are vulnerable to practical analog circuit implementation related challenges and imperfections. One of these challenges is the so called passive intermodulation (PIM) that can severely limit the performance of frequency division duplexing (FDD) based systems. Such PIM is typically generated in the passive components of the radio frequency (RF) transceiver front-end, such as duplexer, diplexer, multiplexer or antenna selection switches. Moreover, the nonlinear junctions typically caused by poor RF connection or the presence of dirt over the metal surfaces in the radio components can also generate PIM. As a consequence, unwanted nonlinear distortion products are created due to the intermodulation of the transmit CCs that generally appear at the specific intermodulation (IM) sub-bands. Depending on the used bands and adopted CC center-frequencies, some of these nonlinear PIM products may appear in one or more of the receiver operating bands as illustrated in Fig. 1. Furthermore, since the PIM is generated in the radio transceiver front-end at or after the duplexer filter, it leaks directly into the receiver and may lead to receiver desensitization.

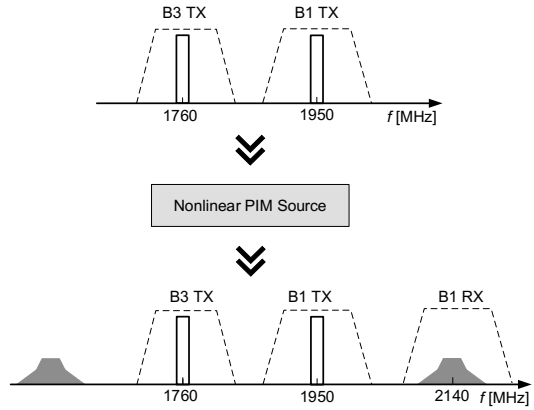

Fig. 1: Spectral illustration of the unwanted PIM products with interband CA of Band 1 and Band 3 at mobile device side. In this example, some of the PIM products hit the Band 1 receiver.

A concrete example case, in terms of exact LTE bands and frequencies, is given in Fig. 1 illustrating uplink inter-band CA transmission at Band 1 (1920-1980 MHz) and Band 3 (1710-1780 MHz). As shown in the figure, the upper third-order IM sub-band (IM3) falls within the Band 1 downlink, reflecting thus the self-interference problem due to PIM. Other LTE

bands that can experience similar problems are, e.g., B3+B8, B2+B4, B5+B7, as discussed and acknowledged also in many inter-band CA related 3GPP technical documents, such as [5], [6]. In general, the problem of PIM-induced self-interference is not only limited to UE devices but can actually be even more pronounced in the base station (BS) transceiver systems [7], [8] where, in addition to internal PIM sources, external sources such as metal objects in the antenna near field and reflections from nearby buildings can cause self-interference. Therefore, PIM can be a big concern also for network vendors and operators.

Obvious solutions to avoid or reduce the PIM-induced self-interference are to either reduce the transmit signal power or to allow for a degradation in the receiver reference sensitivity level. At the UE side, these approaches are referred to as the maximum power reduction (MPR) and maximum sensitivity degradation (MSD), respectively. However, these approaches impact negatively the UL link budget and throughputs [9] and are thus not the most appealing solutions. Alternatively, one could argue to utilize higher quality RF components with good linearity characteristics, however, this may considerably raise the overall radio implementation costs and size.

Some recent works have addressed digital cancellation of PIM. Specifically, Dabag et al. [10] considered third-order PIM cancellation caused by the antenna switch by devising a multiple input single output (MISO) canceller to suppress the frequency-selective PIM with time delay differences between different transmit signals. While showing promising results, the associated parameter estimation complexity is very high. Then, in [11], digital cancellation of second-order PIM due to a diplexer is pursued. In general, these reference techniques do not take into account the nonlinear behavior of the individual PAs in the transmitter chains and the memory effects of the PAs. Since the transmit CCs are distorted in a nonlinear fashion by each of the individual PAs before entering a PIM nonlinearity, this implies that the self-interference is in fact a combination of two nonlinearities. This has been identified recently in [12] and [13], where different digital cancellers for joint mitigation of PA and PIM nonlinerities are proposed and experimented.

In this paper, we develop advanced digital cancellation solutions for suppressing the PIM with memory effects while exclude the PA nonlinearities for simplicity. In addition to PA memory, the proposed method can also account for different mutual time delays of the transmit signals before entering the PIM source, while can also account for memory along and after the PIM generation stage. For presentation simplicity, we focus primarily on modeling and digital cancellation of third-order PIM. The performance of the developed method is evaluated through practical RF measurements, adopting commercial LTE/LTE-Advanced UE transceiver modules and RF components. Moreover, we also address in the performance evaluations and RF measurements an additional practical case where the UE is equipped with a diversity RX chain. Specifically, we show that *PIM coupled over-the-air* from main transceiver to the diversity RX can also be a real problem.

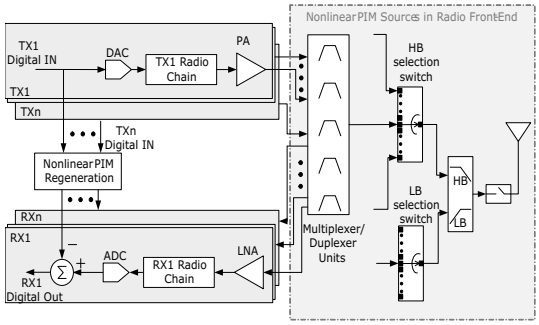

Fig. 2: The considered inter-band CA FDD transceiver architecture at UE side.

Although such PIM coupling over the air can basically be avoided by improving the isolation between the antennas, the isolation is in practice limited by the compact size of the mobile devices. The proposed digital cancellation solution is shown to be able to efficiently suppress the PIM appearing in the main RX branch as well as in the diversity RX branch. Thus, in general, the proposed solution can relax the RF components' linearity requirements and improve the receiver sensitivity by effectively suppressing the PIM, and is applicable in both main RX and diversity RX branches.

The rest of the paper is organized as follows. In Section II, we address baseband equivalent modeling of third-order PIM at RX band under various sources of memory. The corresponding digital cancellation solution and the necessary parameter estimation procedures are presented in Section III. Then, the RF measurement results are reported and analyzed in Section IV. Finally, Section V concludes the paper.

II. Baseband Equivalent Models for Passive Intermodulation at RX Band

In this section, we present the relevant signal models for describing the PIM observed in the RX chain, particularly at digital baseband. A block diagram describing the considered FDD radio transceiver system supporting inter-band CA is shown in Fig. 2. It is assumed that the adopted bands have dedicated TX-RX chains, each, while on the transmit direction the CCs are combined together in a duplexer or a multiplexer [14]. The PIM then occurs in the passive RF components due to cross-modulation between the aggregated transmit signals, and may appear in one or more of the configured receiver bands causing nonlinear self-interference.

Generally speaking, as shown in [12] and [13], the TX PAs can also cause nonlinear distortion to the individual transmit carriers, leading to spectral regrowth around the main transmit carriers. Such nonlinear distortion in the transmit CCs can then affect the overall characteristics of the PIM-induced self-interference and its cancellation. However, in this paper, we restrict our attention to linear transmit chains and PAs, thus basically assuming that the PAs are properly

linearized, e.g., through digital pre-distortion (DPD). It can, however, be argued that the transmit carriers experience some filtering or linear distortion effects before they are combined and thus experience the PIM nonlinearity. Additionally, there can also potentially be multiple PIM sources in the transceiver. As a result, the overall TX-RX PIM coupling path can be viewed as a system of nonlinearities with memory effects. Keeping this in view, we consider two cases for PIM modeling. In the first case, we consider linear and memoryless PAs and pursue frequency-selective behavioral modeling of the nonlinear passive components. In the second case, we also adopt the memory or linear distortion modeling of the individual transmit CCs, prior to the actual PIM stage. As we later demonstrate with practical RF measurements, the latter model can facilitate more accurate PIM modeling and enhanced cancellation.

For presentation purposes and notational simplicity, we focus on third-order PIM effects, while more elaborate higher-order cases as well as coexisting cascaded nonlinearities are addressed in [13].

A. Baseband Equivalent PIM Model: Memoryless TX Chains

Let us denote the complex baseband waveforms of the two transmit CCs by $s_1[n]$ and $s_2[n]$, respectively. The signals are up-converted to their respective RF frequencies and amplified by the PAs. The corresponding aggregated RF signal at the multiplexer/duplexer output, after combining the carriers, can then be expressed as

$$s_{\mathrm{RF}}[n] = \mathrm{Re}\big\{\alpha_1 s_1[n] e^{j\omega_1 n}\big\} + \mathrm{Re}\big\{\alpha_2 s_2[n] e^{j\omega_2 n}\big\}, \quad (1)$$

where α_1 and α_2 denote the complex voltage gains of the two PAs, and ω_1 and $\omega_2 < \omega_1$ are the angular center frequencies of the individual CCs after up-conversion. This signal then travels towards the antenna, however, due to nonlinear passive components, unwanted PIM products of the transmit signal are created. Assuming that the upper third-order IM sub-band, i.e. $2\omega_1 - \omega_2$, lies in the downlink frequency band, similar to Fig. 1, the baseband equivalent complex PIM waveform appearing in the RX band reads then

$$s_{\mathrm{PIM}}[n] = \sum_{l=-L_1}^{L_2} \gamma_l s_1[n-l]^2 s_2^*[n-l] \quad (2)$$

where γ_l denote the impulse response coefficients of the third-order nonlinear term modeling the memory of the PIM generation mechanism, while L_1 and L_2 are the numbers of pre-cursor and post-cursor memory taps in the PIM model, respectively. The total memory length of the PIM generation stage is then $L_1 + L_2 + 1$.

B. Baseband Equivalent PIM Model: TX Chains with Memory

We next generalize the PIM modeling to the case where the individual TX component carrier signals are subject to memory or linear distortion prior to the PIM stage. When complemented with a memory polynomial model for the actual PIM generation stage, this allows for versatile memory modeling, for example in cases where there are mutually different delays along the TX paths, or more generally the frequency responses of the two TX chain are different and both contain memory.

To this end, the two transmit carriers travel through their independent TX chains before arriving at the PIM source, and are subject to linear filtering effects described by the impulse responses $\alpha_{1,m}$ and $\alpha_{2,m}$, respectively. The corresponding RF signal model for the combined signal, prior to the PIM stage, then reads

$$\begin{aligned} s_{\mathrm{RF}}[n] = \mathrm{Re}\Big\{ e^{j\omega_1 n} \sum_{m=-M_1}^{M_2} \alpha_{1,m} s_1[n-m] \Big\} \\ + \mathrm{Re}\Big\{ e^{j\omega_2 n} \sum_{m=-M_1}^{M_2} \alpha_{2,m} s_1[n-m] \Big\}, \end{aligned} \quad (3)$$

where M_1, M_2 are the numbers of the input pre- and post-cursor memory taps for the TX carriers, with the total input memory length being $M_1 + M_2 + 1$. When the above combined signal with memory is subject to a third-order PIM nonlinearity with additional memory, the baseband equivalent PIM waveform at own RX band can be written as shown in (4), next page, where $\gamma_{k_{11},\cdots,k_{1M},k_{21},\cdots,k_{2M}}$ are the effective total memory coefficients for the term defined by the parameters $k_{1M}, k_{21}, \cdots, k_{2M}$, and $M = M_1 + M_2$. Note that in this model, the memory lengths of the transmit CCs and the PIM nonlinearity can be independently chosen, resulting in an overall flexible model from the modeling and cancellation perspective.

To give a concrete example, Table I shows the basis function samples stemming from the two signal models presented in this section, with short memory orders of $L_1 = L_2 = 1$ and $M_1 = M_2 = 1$ for presentation simplicity. As can be observed, the signal model under TX chains with memory has altogether 42 basis functions, opposed to 3 basis functions obtained in the memoryless TX chain case. As a consequence of the different sample delays between the CCs in the basis functions, the more complicated signal model has the potential of better estimating and cancelling also the impacts of any potential timing mismatch errors as well as overall frequency responses in the TX chains. This is achieved, however, at the cost of an increased computational complexity.

III. Proposed Digital PIM Canceller and Parameter Estimation

The proposed digital PIM canceller builds directly on the derived baseband signal models described in the previous section. Specifically, the canceller re-generates the PIM samples, using either (2) or (4), and then subtracts the estimated PIM samples from the actual received baseband signal. In general, the baseband complex samples of the component carriers, $s_1[n]$ and $s_2[n]$, are known in the transceiver. However, the equivalent model parameters, i.e., the γ variables which act as the complex weights of the basis function samples are unknown and thus must be estimated.

$$
\begin{aligned}
s_{\mathrm{PIM}}[n] = \sum_{k_{11}=0}^{2} \sum_{k_{12}=0}^{2-k_{11}} \cdots \sum_{k_{1M}=0}^{2-\sum_{i=1}^{M-1} k_{1i}} \sum_{k_{21}=0}^{1} \sum_{k_{22}=0}^{1-k_{21}} \cdots \sum_{k_{2M}=0}^{1-\sum_{i=1}^{M-1} k_{2i}} \sum_{l=-L_1}^{L_2} \gamma_{l,k_{11},\cdots,k_{1M},k_{21},\cdots,k_{2M}} \times \\
s_1[n-l+M_1]^{k_{11}} s_1[n-l+M_1-1]^{k_{12}} \cdots s_1[n-l-M_2]^{2-\sum_{i=1}^{M} k_{1i}} \times \\
s_2^*[n-l+M_1]^{k_{21}} s_2^*[n-l+M_1-1]^{k_{22}} \cdots s_2^*[n-l-M_2]^{1-\sum_{i=1}^{M} k_{2i}}.
\end{aligned} \tag{4}
$$

TABLE I: Example basis functions of the two considered PIM models

Signal model	**Basis functions when $L_1 = L_2 = 1$**
Memoryless TX Chains	$s_1[n+1]^2 s_2^*[n+1]$, $s_1[n]^2 s_2^*[n]$, $s_1[n-1]^2 s_2^*[n-1]$
TX Chains with Memory, $M_1 = M_2 = 1$	$s_1[n-2]^2 s_2^*[n-2]$, $s_1[n-1]^2 s_2^*[n-1]$, $s_1[n]^2 s_2^*[n]$, $s_1[n-2]^2 s_2^*[n-1]$, $s_1[n-1]^2 s_2^*[n]$, $s_1[n]^2 s_2^*[n+1]$, $s_1[n-2]^2 s_2^*[n]$, $s_1[n-1]^2 s_2^*[n+1]$,$s_1[n]^2 s_2^*[n+2]$, $s_1[n-1] s_1[n-2] s_2^*[n-2]$, $s_1[n] s_1[n-1] s_2^*[n-1]$, $s_1[n+1] s_1[n] s_2^*[n]$, $s_1[n-1] s_1[n-2] s_2^*[n-1]$, $s_1[n] s_1[n-1] s_2^*[n]$, $s_1[n+1] s_1[n] s_2^*[n+1]$, $s_1[n-1] s_1[n-2] s_2^*[n]$, $s_1[n] s_1[n-1] s_2^*[n+1]$, $s_1[n+1] s_1[n] s_2^*[n+2]$, $s_1[n] s_1[n-2] s_2^*[n-2]$, $s_1[n+1] s_1[n-1] s_2^*[n-1]$, $s_1[n+2] s_1[n] s_2^*[n]$, $s_1[n] s_1[n-2] s_2^*[n-1]$, $s_1[n+1] s_1[n-1] s_2^*[n]$, $s_1[n+2] s_1[n] s_2^*[n+1]$, $s_1[n] s_1[n-2] s_2^*[n]$, $s_1[n+1] s_1[n-1] s_2^*[n+1]$, $s_1[n+2] s_1[n] s_2^*[n+2]$, $s_1[n] s_1[n-1] s_2^*[n-2]$, $s_1[n+1] s_1[n] s_2^*[n-1]$, $s_1[n+2] s_1[n+1] s_2^*[n]$, $s_1[n+1] s_1[n+2] s_2^*[n+2]$, $s_1[n+2]^2 s_2^*[n+1]$, $s_1[n+2]^2 s_2^*[n+2]$, $s_1[n]^2 s_2^*[n-2]$, $s_1[n+1]^2 s_2^*[n-1]$, $s_1[n+2]^2 s_2^*[n]$, $s_1[n-1]^2 s_2^*[n-2]$, $s_1[n]^2 s_2^*[n-1]$, $s_1[n+1]^2 s_2^*[n]$, $s_1[n+1]^2 s_2^*[n+1]$, $s_1[n+1]^2 s_2^*[n+2]$, $s_1[n+2] s_1[n+1] s_2^*[n+1]$

Regarding the parameter estimation, the baseband PIM signal models in (2) and (4), and thus the canceller processing structures, are in fact linear in the parameters, i.e., the γ variables. Thus, the parameters can be straight-forwardly estimated with any standard estimator for linear signal models, such as linear least-squares (LS), recursive least squares (RLS), or least mean squares (LMS) [15].

For presentation purposes, we next switch to vector-matrix notations and consider a block of N samples of the received signal. We express the samples of the PIM for the corresponding time duration, stacked into a vector, as

$$
\mathbf{s}_{\mathrm{PIM}} = \boldsymbol{A}\boldsymbol{\theta}, \tag{5}
$$

where $\boldsymbol{A}$ denotes the data matrix that collects the samples of the different nonlinear basis functions while $\boldsymbol{\theta}$ is a vector containing the corresponding unknown coefficients. The structure of the data matrix $\boldsymbol{A}$ depends obviously on which of the two canceller structures is deployed. Using these notations, the LS parameter estimator reads

$$
\widehat{\boldsymbol{\theta}} = \left(\boldsymbol{A}^H \boldsymbol{A}\right)^{-1} \boldsymbol{A}^H \mathbf{y}_{\mathrm{RX}}, \tag{6}
$$

where $(.)^H$ denotes the Hermitian transpose, and $\mathbf{y}_{\mathrm{RX}}$ is the vector of the received complex baseband samples.

After obtaining the estimates of the coefficients, they are used to create a baseband replica of the PIM-induced self-interference in the digital front-end of the radio, during the actual online operation, which is subtracted from the received signal sample by sample. The cancelled signal during the transceiver online operation can thus formally be expressed as

$$
y_{\mathrm{RX,canc}}[n] = y_{\mathrm{RX}}[n] - \boldsymbol{a}^T[n]\hat{\boldsymbol{\theta}}, \tag{7}
$$

where $\boldsymbol{a}^T[n]$ refers to the row vector containing the basis function samples corresponding to the particular time instant n.

In general, the basic approach as described above is that the parameter estimation is carried out offline. In such operating approach, the parameter estimation must then be repeated periodically as the exact PIM characteristics can change over time, e.g., due to changes in the temperature or the transmit power. However, since the PIM is primarily caused by radio transceiver internal front-end components, it is likely that the estimation needs to be repeated only fairly seldom. Alternatively, recursive least squares type of adaptive parameter estimation and tracking approach can also be deployed meaning that the parameters are continuously adapted, sample by sample, during the normal online operation. In this case, it is to be noted that the actual received signal acts as noise from the parameter estimation point of view. In both cases, periodic or continuous parameter estimation, the actual cancellation is anyway running continuously in real-time, using the online transmit data.

IV. RF Measurement Results

A. Measurement Setup and Settings

The performance of the proposed PIM cancellation method is now evaluated through practical RF measurements. A block diagram of the corresponding measurement setup is shown in Fig. 3, while the relevant measurement parameters are listed in Table II. The measurement setup includes the Analog Devices AD9368 2×1 transceiver board to generate the Band 1 and Band 3 CC transmit signals. These signals are next amplified using two separate Skyworks SKY77643-21 PAs and combined in a multiplexer TDK B8690, which has separate TX and RX ports and a common antenna port. The aggregated TX signal is then fed to an Infineon BGS12PL6 switch and

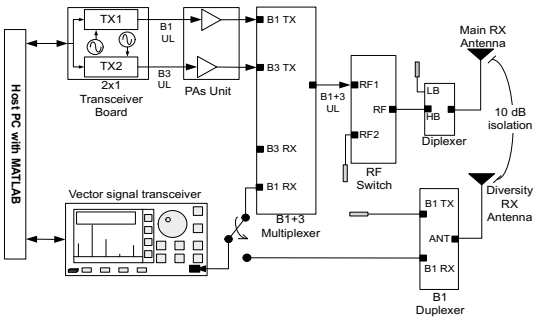

Fig. 3: Illustration of the RF measurement setup, showing the relevant transmitter and receiver units as well as the RF front-end components.

TABLE II: Basic RF measurement parameters

Parameter	Value
Bandwidths of the TX CCs	5 MHz
Total transmit power	24 dBm
Post PA loss	4 dB
Duplexer insertion loss	3 dB
Switch insertion loss	1 dB
RX center frequency	2140 MHz
LS parameter learning sample size	90000
Number of PIM pre-cursor taps (L_1)	3
Number of PIM post-cursor taps (L_2)	4
Number of TX/PA pre-cursor taps (M_1)	0 or 1
Number of TX/PA post-cursor taps (M_2)	0 or 1

a TDK DPX162690DT-8022B2 diplexer. The diplexer output port is connected to an antenna. In addition, to implement a diversity RX chain, an additional B1 duplexer connected to an additional antenna is placed in close proximity of the main transceiver. The signals at the B1 RX ports are fed to the RF input of the National Instrument (NI) PXIe-5645R vector signal transceiver (VST), which is used here for down-conversion and digitization of the received signals for further processing. A host processor with MATLAB is used for post-processing the captured data and for the proposed algorithm evaluation. Block least-squares is used for parameter learning, without actual RX signal. Different sets of transmit signal samples are always used, for parameter learning and for evaluating the cancellation performance. All the measurements are performed in an electromagnetic compatibility (EMC) chamber to avoid any external interferences that might affect the results.

B. Measurement Results for Main RX Branch

In this section, we first present the cancellation results for the main RX branch. The bandwidths of the uplink CCs are assumed to be 5 MHz. When adopting the full transmit power of $+24$ dBm, the essential power spectral density (PSD) curves of the observed PIM before and after the digital cancellation are shown in Fig. 4, containing both canceller cases of

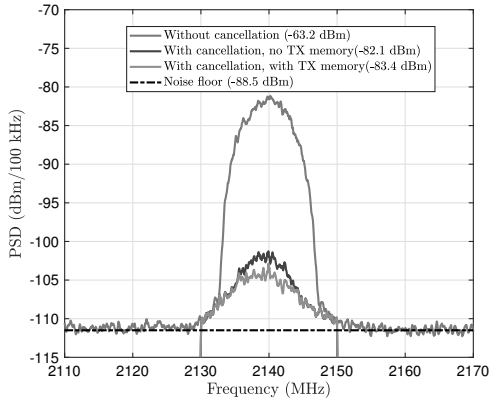

Fig. 4: Measured PSD curves of the PIM distortion at the main RX branch of Band 1 without and with digital cancellation. The TX CC bandwidths at the LTE Bands 1 and 3 are 5 MHz each, and the aggregated TX power is +24 dBm.

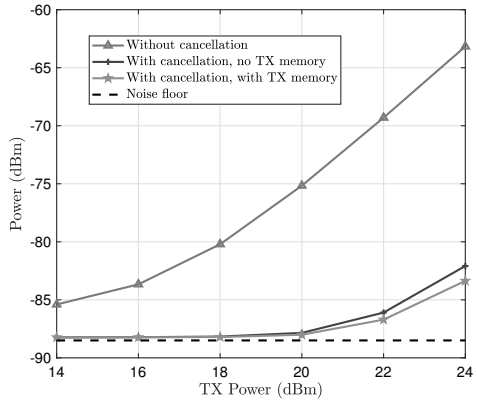

Fig. 5: The measured powers of the PIM distortion at the main RX branch of Band 1 without and with digital cancellation as functions of the aggregated transmit power. The TX CC bandwidths at the LTE Bands 1 and 3 are 5 MHz each.

with and without memory in the TX chains. Notice that for illustration purposes, the PSD curves are all referenced to the actual receiver RF frequencies despite the digital canceller operates at baseband. For one, these results clearly indicate that the PIM induced self-interference is significantly above the receiver noise floor when employing state-of-the-art radio components, and can thus cause RX desensitization. However, the proposed digital cancellation solutions are able to suppress the PIM induced self-interference by up to 21 dB or so. Moreover, it can also be noticed that the memory modeling

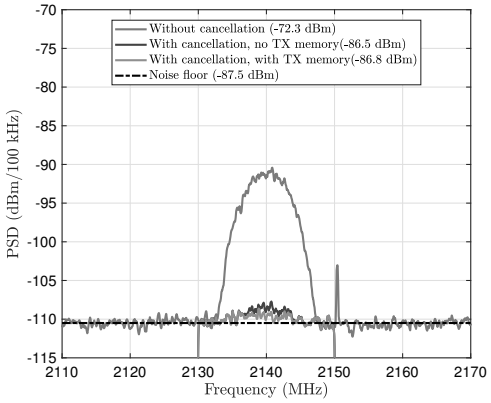

Fig. 6: Measured PSD curves of the PIM distortion at the diversity RX branch of Band 1 without and with digital cancellation. The TX CC bandwidths at the LTE Bands 1 and 3 are 5 MHz each, and the aggregated TX power is +24 dBm.

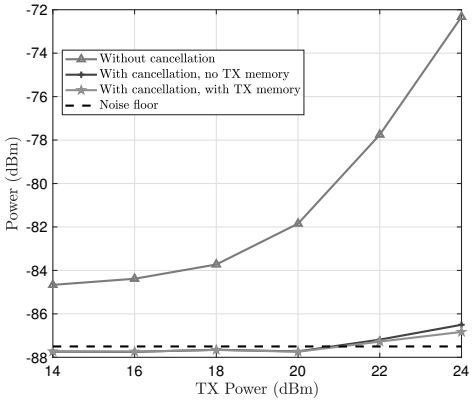

Fig. 7: The measured powers of the PIM distortion at the diversity RX branch of Band 1 without and with digital cancellation as functions of the aggregated transmit power. The TX CC bandwidths at the LTE Bands 1 and 3 are 5 MHz each.

of the PAs, or TX chains overall, prior to the PIM generation stage can further improve the cancellation performance by ca. 1 dB.

Next, Fig. 5 shows the behavior of the PIM-induced self-interference power at Band 1 main RX as a function of the TX power, without and with digital cancellation. The results suggest that the self-interference is already significant even at lower TX powers of some $+14$ dBm, and can heavily degrade the system performance as the TX power is increased. It can also be observed that the proposed cancellation approach can guarantee interference-free reception for the TX powers up to $+20$ dBm, thus substantially extending the usable transmit power range without the risk of receiver desensitization.

C. Measurement Results for Diversity RX Branch

In this subsection, we continue the RF measurements and demonstrate that the PIM-induced distortion can also couple over-the-air and thus cause self-interference, e.g., to a diversity RX branch. To demonstrate this, a diversity RX antenna is placed at a distance of 5 cm from the main RX antenna, which provides an antenna isolation of around 10 dB. Fig. 6 shows then the observed PIM interference coupled over the air from the main transceiver into the diversity RX with the aggregated transmit power of $+24$ dBm. Again, the self-interference is substantial and clearly above the noise floor, and can thus degrade the receiver sensitivity. It can also be observed that the proposed digital cancellation approach is able to suppress the OTA-coupled self-interference efficiently very close to the noise floor. Finally, Fig. 7 shows the PIM-induced distortion power at the diversity RX as a function of the aggregated TX power, evidencing that the proposed digital cancellation is able to efficiently suppress the self-interference close to the noise floor.

D. Further Discussion

While the presented results clearly demonstrate the modeling and cancellation capability of the proposed technique, it can be observed that there is still some residual interference present after the digital cancellation. This is particularly so when larger transmit powers are adopted. The main reason for this is that the developed cancellers consider only third-order PIM while neglect the higher-order distortion terms. The role of such higher-order components is more and more essential when the transmit power increases. Another reason is, despite elementary PA linearization, that also PA induced nonlinear distortion has an impact on the exact PIM waveform. Therefore, developing advanced techniques for joint compensation of PA-induced and PIM nonlinearities, with memory effects, and such that also higher-order nonlinear terms are taken into account [13] forms an important research topic for our future work.

V. Conclusion

In this paper, a novel digital cancellation solution was presented to estimate and cancel the self-interference resulting from the nonlinear passive components in CA-based radio transceivers. Along the self-interference modeling and the corresponding cancellation processing, the memory effects of the TX chains and PAs were also taken into account. The performance of the proposed digital cancellers was tested and analyzed with actual RF measurements using real-life transceivers and RF components for UE devices, demonstrating excellent self-interference suppression. The presented measurement results also show that PIM can couple over the air into the diversity RX branch and thus cause significant interference in the diversity RX. Based on the obtained results, the proposed digital cancellation approach is an effective

solution to suppress the PIM, both in the main RX as well as in the diversity RX chains. Such novel digital cancellation solutions can relax the linearity requirements of the passive RF components, while also enabling efficient utilization of the RF spectrum. Extending the developed cancellation solutions to accommodate higher-order nonlinear products as well as co-existing cascaded nonlinearities were identified as important future research topics.

ACKNOWLEDGMENT

This work was supported by the Academy of Finland (under the grants 304147 and 301820), the Finnish Funding Agency for Innovation (Tekes, under the project "5G Transceivers for Base Stations and Mobile Devices, 5G TRX"), Nokia Bell Labs, RF360, Pulse Finland, Sasken Finland, and Huawei Technologies Finland. The work was also supported by the Tampere University of Technology Graduate School.

REFERENCES

[1] E. Dahlman, S. Parkvall, and J. Sköld, *5G NR: the Next Generation Wireless Access Technology*. Academic Press, 2018.

[2] "Evolved universal terrestrial radio access (E-UTRA); LTE Advanced inter-band carrier aggregation (CA) Rel-15 for 2 downlink (DL) / 2 uplink (UL)," 3GPP Tech. Rep. 36.715-02-02, version 15.0.0, Release 15, July 2018.

[3] "Further advancements for E-UTRA physical layer aspects," 3GPP Tech. Rep. 36.814, version 9.0.0, Release 9, Mar. 2010.

[4] M. Iwamura, K. Etemad, M. H. Fong, and R. Nory, "Carrier aggregation framework in 3GPP LTE-Advanced," *IEEE Communications Magazine*, vol. 48, no. 8, pp. 60–67, Aug. 2010.

[5] "LTE; evolved universal terrestrial radio access (E-UTRA); user equipment (UE) radio transmission and reception (3GPP TS 36.101, version 14.1.0, release 14)," ETSI, Sophia Antipolis Cedex, France, Sep. 2016.

[6] "R4-121131, Harmonics and IMD analysis for inter-band CA band 3 and band 8," KT, Jeju, South Korea, Mar. 2012.

[7] G. Macchiarella, G. B. Stracca, and L. MiglioIi, "Experimental study of passive intermodulation in coaxial cavities for cellular base stations duplexers," in *Proc. 34th European Microwave Conference, 2004.*, vol. 2, Oct. 2004, pp. 981–984.

[8] F. Gao, Y. Gao, and R. Shan, "Analysis and measurement of transmission passive intermodulation distortions," in *Proc. 2017 IEEE International Symposium on Electromagnetic Compatibility Signal/Power Integrity (EMCSI)*, Aug. 2017, pp. 90–93.

[9] A. Kiayani, M. Abdelaziz, L. Anttila, V. Lehtinen, and M. Valkama, "Digital mitigation of transmitter-induced receiver desensitization in carrier aggregation fdd transceivers," *IEEE Transactions on Microwave Theory and Techniques*, vol. 63, no. 11, pp. 3608–3623, Nov. 2015.

[10] H. T. Dabag, H. Gheidi, S. Farsi, P. S. Gudem, and P. M. Asbeck, "All-digital cancellation technique to mitigate receiver desensitization in uplink carrier aggregation in cellular handsets," *IEEE Transactions on Microwave Theory and Techniques*, vol. 61, no. 12, pp. 4754–4765, Dec. 2013.

[11] H. Dabag, H. Gheidi, P. Gudem, and P. M. Asbeck, "All-digital cancellation technique to mitigate self-jamming in uplink carrier aggregation in cellular handsets," in *2013 IEEE MTT-S International Microwave Symposium Digest (MTT)*, 2013, pp. 1–3.

[12] M. Z. Waheed, D. Korpi, A. Kiayani, L. Anttila, and M. Valkama, "Digital self-interference cancellation in inter-band carrier aggregation transceivers: Algorithm and digital implementation perspectives," in *2017 IEEE International Workshop on Signal Processing Systems (SiPS)*, Oct. 2017, pp. 1–5.

[13] M. Z. Waheed, D. Korpi, L. Anttila, A. Kiayani, M. Kosunen, K. Stadius, M. Allen, J. Ryynänen, and M. Valkama, "Passive intermodulation in inter-band carrier aggregation FDD transceivers: Modeling and digital cancellation," *IEEE Transactions on Microwave Theory and Techniques*, 2018, submitted.

[14] "R4-121984, RF architecture alternatives for inter band CA class A2," Motorola Mobility, Jeju, South Korea, Mar. 2012.

[15] S. S. Haykin, *Adaptive filter theory*. Pearson Education India, 2008.

PUBLICATION III

Digital Cancellation of Passive Intermodulation: Method, Complexity and Measurements

M. Z. Waheed, D. Korpi, A. Kiayani, L. Anttila and M. Valkama

2019 IEEE MTT-S International Microwave Conference on Hardware and Systems for 5G and Beyond (IMC-5G) (2019), 1–3
DOI: 10.1109/IMC-5G47857.2019.9160361

Digital Cancellation of Passive Intermodulation: Method, Complexity and Measurements

Muhammad Zeeshan Waheed[†*], Dani Korpi[‡], Adnan Kiayani[*], Lauri Anttila[*], and Mikko Valkama[*]
[*]Tampere University, Dept. Electrical Engineering, Tampere, Finland
[†]Nokia Mobile Networks, Finland; [‡]Nokia Bell Labs, Finland;
Contact email: mikko.valkama@tuni.fi

***Abstract*—This paper addresses digital cancellation of passive intermodulation (PIM) products in simultaneous transmit-receive systems, with specific emphasis on frequency-division duplexing (FDD) based LTE and 5G New Radio (NR) networks. Building on mathematical modeling of the passive intermodulation, a computationally efficient digital cancellation and associated parameter learning solutions are derived and presented. The performance of the method is analyzed through interband carrier aggregation based RF measurements at LTE/NR bands 1 and 3. The measurement results show that the proposed canceller can efficiently cancel the PIM products towards the receiver noise floor. Additionally, the proposed canceller is shown to be of substantially lower complexity compared to the reference methods.**

***Index Terms*—5G NR, LTE, carrier aggregation, radio coexistence, flexible duplex, frequency division duplexing, nonlinear distortion, passive intermodulation.**

I. Introduction

Coexisting and simultaneously operating radio transmitters and receivers are known to be subject to interference challenges [1]. In this paper, we focus on the possible interference of cellular transmitter to cellular receiver in frequency-division duplexing (FDD) based LTE and 5G NR systems and devices. Specifically, as identified in [2], [3], the utilization of carrier aggregation (CA) can lead to challenging self-interference scenarios where intermodulation of the transmit carriers lands directly at one of the own receive bands. Good examples of such cases at the user equipment (UE) side are, e.g., combinations of the LTE/NR bands 1 and 3, or bands 3 and 8 [2]. While band-specific power amplifiers (PAs) relax the problem to certain extent, the passive radio frequency (RF) front-end components, such as switches, diplexers and multiplexers, can be another major source of intermodulation, commonly known as passive intermodulation (PIM) [1], [4]–[6].

The self-interference problem in FDD radio transceivers can potentially be avoided or reduced through a number of approaches. These include, e.g., reducing the transmit power level, known as the maximum power reduction (MPR), or alternatively relaxing the receiver reference sensitivity requirements, commonly referred to as the maximum sensitivity degradation (MSD), in the context of LTE and NR UEs. Another option is to employ expensive high-quality RF components with good linearity characteristics in order to avoid intermodulation. However, these approaches have a negative impact on the uplink (MPR) or downlink (MSD) coverage and throughput, or on the overall radio implementation cost.

Digital cancellation techniques have recently been proposed as an alternative to resolving the self-interference problem in FDD radio transceivers, see, e.g., [4], [5], [6]. In this context, the majority of the works build on polynomial or memory polynomial like linear-in-parameters methods, combined with traditional least-squares (LS), recursive least-squares (RLS), or least mean squares (LMS) type parameter learning schemes. Additionally, in [6], it was recognized that also the band-specific power amplifers and their nonlinear characteristics can contribute to the exact PIM samples, the overall system being a challenging cascaded set of multiple nonlinearities. In such cases, particularly with both memory and nonlinearities in the individual PAs, the complexity of the effective linear in parameters model and the corresponding cancellers largely increases [4]–[6].

In this paper, we present a novel reduced-complexity digital PIM cancellation solution together with novel self-orthogonalizing decoupled parameter learning rules, for suppressing the self-interference stemming from coexisting PA and PIM nonlinearities. The performance of the proposed cancellation technique is evaluated and demonstrated through practical RF measurements adopting interband carrier aggregation at LTE/NR bands 1 and 3 where the third-order intermodulation frequency lands at the band 1 RX. The obtained RF measurement results show that the proposed method can efficiently suppress the nonlinear self-interference, while facilitating substantially lower computational complexity compared to the existing reference methods.

II. Proposed Digital Self-Interference Canceller

A. Nonlinear PIM Model

Let us first define an instantaneous basis function vector as

$$\boldsymbol{\phi}(n) = \begin{bmatrix} \phi_1(n) & \phi_2(n) & \cdots & \phi_C(n) \end{bmatrix}^T \tag{1}$$

where $\phi_i(n)$ denotes an individual basis function, and C is the total amount of basis functions. In this paper, for presentation convenience and practical applicability, we focus on the case of assuming 3rd-order nonlinear behavior in the individual band-specific PAs as well as a 3rd-order nonlinearity in the actual PIM stage. More elaborate scenarios with higher-order nonlinearities in the PAs and PIM interface are covered in our future extended work. The basis function vector $\boldsymbol{\phi}(n)$, forming the basis for nonlinear self-interference modeling at own RX

band, and thus its digital cancellation, reads now [6]

$$\boldsymbol{\phi}(n) = \begin{bmatrix} x_1(n)^2 x_2^*(n) \\ x_1(n)^2 x_2(n) x_2^*(n)^2 \\ x_1(n)^3 x_1^*(n) x_2^*(n) \\ x_1(n)^3 x_1^*(n) x_2(n) x_2^*(n)^2 \\ x_1(n)^4 x_1^*(n)^2 x_2^*(n) \\ x_1(n)^4 x_1^*(n)^2 x_2(n) x_2^*(n)^2 \end{bmatrix} \tag{2}$$

where $x_1(n)$ and $x_2(n)$ are the baseband equivalent signals of the two TX component carriers.

With the above assumptions, and accommodating different unknown relative weigths for the different basis function samples, represented as vector $\mathbf{g}_n$, the baseband equivalent nonlinear self-interference signal model at own RX reads

$$s(n) = \mathbf{g}_n^H \boldsymbol{\phi}(n). \tag{3}$$

To further allow for memory effects in the system, through a filter $\mathbf{w}_n$, the actual nonlinear PIM model is expressed as

$$y(n) = \mathbf{w}_n^H \mathbf{s}_n \tag{4}$$

where $\mathbf{s}_n = \begin{bmatrix} s(n+M_1) & \cdots & s(n-M_2) \end{bmatrix}$, M_1 is the number of pre-cursor memory taps, and M_2 is the number of post-cursor memory taps.

The complexity of the proposed decoupled canceller, i.e., in computing (2)–(4), is $(M_1 + M_2 + 1) + C$ complex multiplications per sample. The complexity of the reference canceller from [6], which adopts a linear-in-parameters model with independent filters for each basis function, is $(M_1+M_2+1)\times C$ complex multiplications per sample. The proposed solution thus yields a considerable reduction in modeling complexity particularly when considering higher-order PA and PIM nonlinearities. Additionally, as we show through RF measurements in Section III, very accurate PIM cancellation can still be obtained, despite the largely reduced complexity.

B. Cancellation and Decoupled Learning

Building on the above nonlinear model for the observable PIM, the signal after the digital cancellation is simply

$$e(n) = d(n) - y(n), \tag{5}$$

where $d(n)$ denotes the received signal. In practice, both the filters $\mathbf{g}$ and $\mathbf{w}$ are, however, unknown and must thus be estimated and possibly also tracked over time if there are time-dependent features in the involved nonlinearities.

For parameter learning and tracking, we define the cost function as $J(\mathbf{g}_n, \mathbf{w}_n) = |e(n)|^2$. Then, the corresponding gradient-based learning rule for the unknown parameter vector $\mathbf{g}$ reads

$$\mathbf{g}_{n+1} = \mathbf{g}_n - \mu_g \frac{\partial J(\mathbf{g}_n, \mathbf{w}_n)}{\partial \mathbf{g}_n}, \tag{6}$$

where μ_g is the learning step-size. After calculating the partial derivatives, the final learning rule can be expressed as

$$\mathbf{g}_{n+1} = \mathbf{g}_n + \mu_g e^*(n) \boldsymbol{\Phi}_n \mathbf{w}_n^*, \tag{7}$$

where $\boldsymbol{\Phi}_n = \begin{bmatrix} \boldsymbol{\phi}(n+M_1) & \cdots & \boldsymbol{\phi}(n-M_2) \end{bmatrix}$. It is noted that the learning rule for $\mathbf{g}$ depends on the other unknown filter $\mathbf{w}$.

As for learning the memory model $\mathbf{w}$, it can be noted that for given $\mathbf{g}$, the system is essentially identical to the classical least mean squares filter with $\mathbf{s}_n$ as the input signal, meaning that an LMS-like learning rule can be adopted. Therefore, the learning rule for $\mathbf{w}_n$ is written as

$$\mathbf{w}_{n+1} = \mathbf{w}_n + \mu_w e^*(n) \mathbf{s}_n, \tag{8}$$

where μ_w is the memory step size. These learning rules are executed in parallel such that both $\mathbf{g}$ and $\mathbf{w}$ are updated simultaneously using the values from the previous iteration.

C. Self-orthogonalized Learning for Faster Convergence

Due to the mutual correlation between the nonlinear basis functions in $\boldsymbol{\phi}(n)$, the learning rule in (7) may suffer from slow convergence. To address this, a self-orthogonalizing learning rule can be used instead. Inspired by [7, p. 356], the filter input vector is expressed as $\mathbf{u}_n = \boldsymbol{\Phi}_n \mathbf{w}_n^*$, and the self-orthogonalizing learning rule can be expressed as

$$\mathbf{g}_{n+1} = \mathbf{g}_n + \tilde{\mu}_g \mathbf{R}^{-1} e^*(n) \mathbf{u}_n, \tag{9}$$

where $\tilde{\mu}_g$ is the step size, and $\mathbf{R} = \mathrm{E}\left[\mathbf{u}_n \mathbf{u}_n^H\right]$ is the correlation matrix of the filter input vector.

Assuming then that the baseband signals of the two transmit carriers are independent and identically distributed (i.i.d.) and stationary, the correlation matrix $\mathbf{R}$ can be easily expressed, for given $\mathbf{w}$, as

$$\mathbf{R} = \mathbf{R}_{\boldsymbol{\phi}} \mathbf{w}_n^H \mathbf{w}_n, \tag{10}$$

where $\mathbf{R}_{\boldsymbol{\phi}}$ is the correlation matrix of the basis functions. Note that $\mathbf{R}_{\boldsymbol{\phi}}$ is only based on the chosen signal model and the statistical properties of the utilized waveforms, meaning that it can be calculated offline, alongside with its inverse. Thus, we can rewrite the self-orthogonalizing learning rule as

$$\begin{aligned} \mathbf{g}_{n+1} &= \mathbf{g}_n + \frac{\tilde{\mu}_g}{\mathbf{w}_n^H \mathbf{w}_n} \mathbf{R}_{\boldsymbol{\phi}}^{-1} e^*(n) \mathbf{u}_n \\ &= \mathbf{g}_n + \mu_{g,\mathrm{ort}} \mathbf{R}_{\boldsymbol{\phi}}^{-1} e^*(n) \boldsymbol{\Phi}_n \mathbf{w}_n^*, \end{aligned} \tag{11}$$

where $\mu_{g,\mathrm{ort}}$ is the final step size. Note that, as a simplification, the step size can be chosen to be static, despite the time-variant term $\mathbf{w}_n^H \mathbf{w}_n$. Therefore, the only additional computation required in this learning rule, opposed to that in (7), is the matrix multiplication since $\mathbf{R}_{\boldsymbol{\phi}}^{-1}$ can be precomputed.

III. RF Measurement Results and Analysis

The performance of the proposed digital self-interference canceller is now evaluated through practical RF measurements. The experimental setup builds on the Analog Devices AD9368 2x1 transceiver board for generating the LTE/NR Band 1 and Band 3 uplink CCs, followed by commercial UE RF modules. Each TX CC is amplified separately using Skyworks multiband PA modules (SKY77643-21), combined in a dual-band multiplexer (TDK B8960), and finally fed to an antenna switch (BGS12PL6). The output RF port of the switch is connected to a wideband mobile antenna. As discussed in the

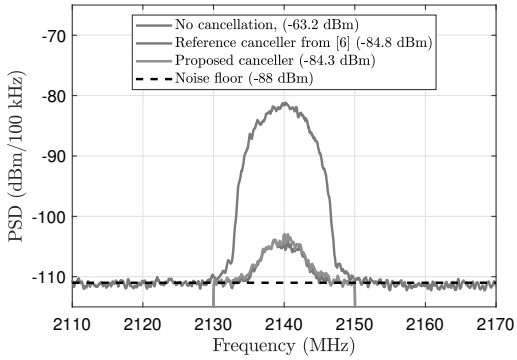

Fig. 1: Measured PIM at Band 1 receiver with and without digital cancellation. The TX power is $+24$ dBm.

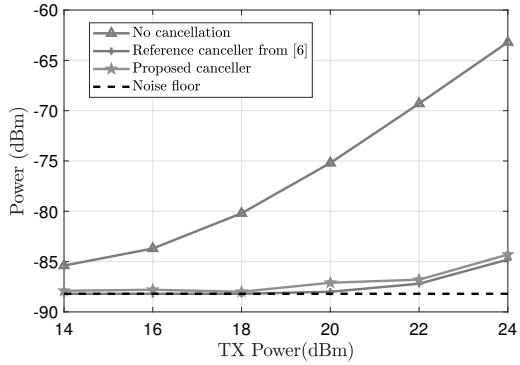

Fig. 2: The measured residual noise+PIM power, with and with digital cancellation, as a function of TX power.

introduction, intermodulation of the transmit carriers leads to self-interference at Band 1 receiver, which is observed and measured at Band 1 receiver port of the multiplexer using a National Instruments vector signal transceiver (VST, PXIe5645R). The VST downconverts and digitizes the signal to baseband, and the digital samples are read from the VST memory and loaded into host processor for post-processing and algorithm evaluation. All the measurements are carried out in an electromagnetic compatibility (EMC) chamber to minimize the impact of external interference signals. For algorithm evaluation, the bandwidths of the TX CCs are assumed to be 5 MHz, each, and the filter $\mathbf{w}_n$ has $M_1 = 3$ pre-cursor and $M_2 = 4$ post-cursor taps, while $C = 6$.

Fig. 1 shows the essential power spectral density (PSD) curves before and after digital cancellation with the full aggregated transmit power of $+24$ dBm. Here, for illustration purposes, x-axis ticks are deliberately labeled as the actual receiver RF frequencies even though the actual processing is done at digital baseband. Firstly, one can observe the substantial level of the PIM-induced self-interference when employing commercial RF components, which can cause receiver desensitization. Secondly, the proposed decoupled-learning based canceller is able to efficiently suppress the self-interference by more than 21 dB, and is capable of achieving almost identical cancellation performance as the reference canceller from [6] with much lower complexity. Specifically, the proposed and reference cancellers need $(M_1+M_2+1)+C = 14$ and $(M_1 + M_2 + 1) \times C = 48$ complex multiplications, respectively, per cancelled sample.

The performance is further assessed by plotting the noise plus self-interference power at Band 1 with respect to different TX power levels, with and without digital cancellation, in Fig. 2. Here, it is interesting to note that the self-interference is already noticeable even at lower TX powers, which can cause receiver sensitivity degradation. The proposed digital cancellation approach is again shown to sufficiently suppress the self-interference such that system noise floor is not heavily degraded, and can thus extend the usable transmit power range.

One can also observe that at highest transmit powers, there is still some residual PIM. These are likely to be stemming from higher-order nonlinear terms and PA memory effects, thus developing advanced cancellation techniques for their mitigation is addressed in our future work.

Conclusion

In this paper, we proposed a novel reduced complexity digital self-interference cancellation algorithm, to mitigate the co-existing PA and PIM induced nonlinearities in FDD transceivers. The proposed technique reduces the computational complexity during the parameter learning in comparison to state-of-the-art linear-in-parameters cancellers. The RF measurement results in LTE/NR Bands 1 and 3 carrier aggregation context demonstrated up to 21 dB suppression of the self-interference. Implementing such algorithms in radio transceivers will enable extending their usable transmit power range, and possibly also relaxing the linearity requirements of the RF components. Our future work will focus on extending the algorithms to incorporate higher-order nonlinearties.

References

[1] E. Dahlman, S. Parkvall, and J. Sköld, *5G NR: the Next Generation Wireless Access Technology*. Academic Press, 2018.

[2] 3GPP Tech. Spec. 36.101, "LTE Evolved Universal Terrestrial Radio Access (E-UTRA) User Equipment (UE) radio transmission and reception," v16.1.0 (Release 16), April 2019.

[3] 3GPP Tech. Spec. 38.101-1, "NR User Equipment (UE) radio transmission and reception; Part 1: Range 1 Standalone," v15.5.0 (Release 15), April 2019.

[4] H. T. Dabag, H. Gheidi *et al.*, "All-digital cancellation technique to mitigate receiver desensitization in uplink carrier aggregation in cellular handsets," *IEEE Trans. Microw. Theory Tech.*, vol. 61, no. 12, pp. 4754–4765, Dec. 2013.

[5] M. Z. Waheed, P. P. Campo *et al.*, "Digital cancellation of passive intermodulation in FDD transceivers," in *2018 52nd Asilomar Conference on Signals, Systems, and Computers*, Oct. 2018, pp. 1375–1381.

[6] M. Z. Waheed, D. Korpi *et al.*, "Digital self-interference cancellation in inter-band carrier aggregation transceivers: Algorithm and digital implementation perspectives," in *2017 IEEE International Workshop on Signal Processing Systems (SiPS)*, Oct. 2017, pp. 1–5.

[7] S. Haykin, *Adaptive Filter Theory*, 4th ed. Prentice Hall, 2002.

PUBLICATION
IV

Passive Intermodulation in Simultaneous Transmit–Receive Systems: Modeling and Digital Cancellation Methods

M. Z. Waheed, D. Korpi, L. Anttila, A. Kiayani, M. Kosunen, K. Stadius, P. P. Campo, M. Turunen, M. Allén, J. Ryynänen and M. Valkama

IEEE Transactions on Microwave Theory and Techniques 68.9 (2020), 3633–3652
DOI: 10.1109/TMTT.2020.2996206

Passive Intermodulation in Simultaneous Transmit-Receive Systems: Modeling and Digital Cancellation Methods

Muhammad Zeeshan Waheed, Dani Korpi, Lauri Anttila, Adnan Kiayani, Marko Kosunen, Kari Stadius, Pablo Pascual Campo, Matias Turunen, Markus Allén, Jussi Ryynänen, and Mikko Valkama

***Abstract*—This article presents novel solutions for suppressing passive intermodulation (PIM) distortion in frequency-division duplexing (FDD) based radio transceivers, stemming from nonlinear radio frequency (RF) components and simultaneous transmission and reception, with special emphasis on modern carrier aggregation networks. With certain transmission band combinations in, e.g., Long Term Evolution (LTE) or the emerging 5G New Radio (NR) mobile radio systems, the nonlinear distortion produced by the passive components of the transceiver RF front-end can result in intermodulation distortion that falls within one of the configured reception bands. While the traditional solution to mitigate this problem is to reduce the transmit power, we take an alternative approach and seek to cancel such PIM in the transceiver digital front-end by using the original transmit data as reference. To generate as accurate cancellation signal as possible, we derive different advanced signal models for the observable intermodulation distortion at own receiver band that incorporate also the power amplifier nonlinearities, together with the passive component nonlinearities and the frequency-selective responses of the duplex filters. The performance and the processing complexity of the devised digital cancellation and parameter estimation solutions are evaluated with real-life RF measurements, where an actual LTE-Advanced user equipment (UE) type transceiver system is utilized. The obtained results show that the proposed cancellers are implementation-feasible and can suppress the self-interference by over 20 dB, cancelling the distortion nearly perfectly up to UE transmit powers of +24 dBm. The results also indicate that in many cases it is necessary to model the nonlinear distortion effects produced by the power amplifiers, even if the individual component carriers are combined after the amplification stage.**

***Index Terms*—5G NR, carrier aggregation, flexible duplex, frequency division duplexing (FDD), LTE-Advanced, nonlinear distortion, passive intermodulation (PIM), self-interference (SI).**

I. Introduction

DRIVEN by new services and applications, the demands for higher and higher data rates are continuously increasing in mobile radio networks [1]. One approach to realize increased throughputs and capacity is to utilize wider transmission bandwidths through aggregating spectral resources simultaneously from multiple frequency channels or bands [1]–[3]. To this end, the so-called carrier aggregation (CA) technique was introduced by the Third Generation Partnership Project (3GPP) in its Release 10, also known as Long Term Evolution (LTE)-Advanced [2], being also supported in 5G New Radio (NR) Release 15 and onwards [3]. The CA technology allows for transmitting and receiving simultaneously over multiple contiguous or non-contiguous parts of the spectrum, thus enabling flexible expansion of the overall transmission bandwidth. Moreover, the spectral resources can be combined from within the same operating frequency band (intra-band CA) or from multiple frequency bands (inter-band CA). The user equipment (UE) can also be simultaneously connected to LTE and NR cells, commonly called LTE-NR dual connectivity, and can thus be transmitting and/or receiving data simultaneously through both LTE and NR carriers [4].

In inter-band CA, the transmission at two or more LTE or NR bands occurs simultaneously, where the transmit signals corresponding to the individual bands are referred to as component carriers (CCs) [1]–[3]. Different deployment scenarios can be further categorized as CA among low-band (< 1 GHz) and high-band (> 1 GHz) carrier frequencies, called LB-HB CA, and CA within more similar frequencies, referred to as LB-LB CA or HB-HB CA. Additionally, in NR, CA can be adopted at both FR1 (below 6 GHz bands) and FR2 (millimeter-wave bands) [4].

A. FDD CA Transceivers and Passive Intermodulation

Fig. 1 (a) shows a frequency-division duplexing (FDD) based radio transceiver architecture supporting inter-band CA, where each aggregated LTE/NR band has a separate transmitter (TX) and receiver (RX) chain, while different LTE/NR bands are supported and combined through band-selection switches and a diplexer [5]–[10]. In general, the growing number of CA frequency band combinations represents a variety of practical challenges for the RF front-end design and implementation, which must now support multiple RF paths simultaneously [5], [7]–[9]. From the unwanted emissions point of view, the nonlinear distortion in the TX power amplifier (PA) is a primary concern, which typically leads to spectral regrowth around the main CCs when each CC is amplified by a separate PA [5]. However, when the aggregated non-contiguous transmit signal propagates through the RF front-end passive components, unwanted passive intermodulation (PIM) products

This paper is an expanded version from the 2019 IEEE MTT-S International Microwave Conference on Hardware and Systems for 5G and Beyond, Atlanta, GA, USA, August 2019 [35].

This work was funded in part by the Academy of Finland (under the projects #304147, #301820, and #319994), in part by the Finnish Funding Agency for Innovation (Business Finland, under the project 5G TRx), and in part by Nokia Bell Labs. (*Corresponding Author: Mikko Valkama*).

M. Z. Waheed, D. Korpi, L. Anttila, A. Kiayani, P. Pascual Campo, M. Turunen, M. Allén, and M. Valkama are with the Department of Electrical Engineering, Tampere University, Tampere, Finland (e-mail: mikko.valkama@tuni.fi).

M. Z. Waheed and D. Korpi are also with Nokia Corporation, Finland.

A. Kiayani is also with Ericsson AB, Sweden.

M. Kosunen, K. Stadius, and J. Ryynänen are with Aalto University, School of Electrical Engineering, Finland.

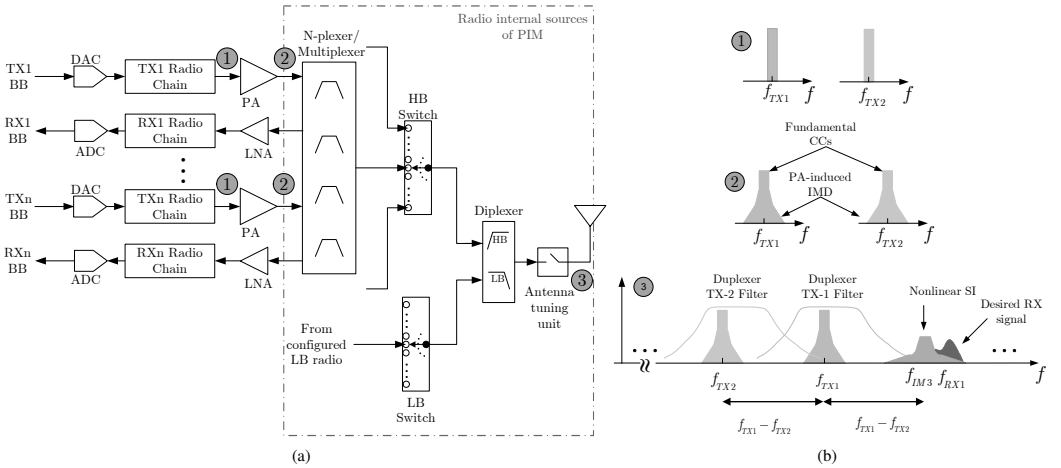

Fig. 1. (a) Block diagram of the considered FDD radio transceiver architecture supporting inter-band carrier aggregation. (b) Relevant signal spectra at different stages of the transceiver illustrating how PIM products can hit the own RX band.

are also created due to cross-modulation of the transmitted signals, see, e.g., [7], [8], [11]–[14], and the references therein. The sources of PIM typically include internal radio front-end components, such as filters, switches, connectors and cables, the antenna system, and even external sources such as corroded metal objects present in the antenna near field [11], [12], [15]–[17]. The resulting PIM products are located at specific intermodulation (IM) sub-bands that are integer linear combinations of the CC center-frequencies. Importantly, in certain LTE or NR band combinations or frequency allocations, some of the IM sub-bands can *coincide with the RX operating band*, as shown in Fig. 1 (b) [13], [16], [18]–[21].

A concrete example of the aforementioned phenomenon is the 3GPP-specified inter-band uplink (UL) CA of Band 1 (1920-1980 MHz) and Band 3 (1710-1785 MHz) (B1+B3), where the third-order IM sub-band (IM3) falls within the downlink (DL) frequencies of band B1. Other example band combinations that are prone to similar problem include, e.g., B3+B8, B2+B4, and B5+B7. Since the PIM is generated after the duplexer TX filter, it experiences only the duplexer insertion loss and therefore goes directly into the receiver, causing *self-interference* that may potentially lead to RX desensitization. Recently, several 3GPP technical documents have identified this issue for various LTE/NR band combinations in inter-band CA, see, e.g., [22]–[24], and this problem is expected to further exacerbate with the introduction of new band combinations in the future. Furthermore, in addition to the UEs, this type of self-interference problem may also become a critical issue in the base station (BS) radio transceiver systems as the operators start to utilize more radio bands in conjunction with the emergence of co-existing LTE and 5G New Radio (NR) systems [25], [26]. In such BS side scenarios, PIM is likely to be even more pronounced due to high transmit power levels [18], [25], [27].

In general, the power of the PIM-induced self-interference depends on the passive components' linearity characteristics, and can be substantially stronger than the desired weak received signal, even with state-of-the-art RF components. Consequently, there is a need to minimize the harmful impact of the self-interference, which can be addressed through various means. A simple technique can be either to decrease the transmit power or alternatively to relax the receiver reference sensitivity requirements, known as the maximum power reduction (MPR) and the maximum sensitivity degradation (MSD), respectively, in the context of LTE-Advanced and NR UEs [23], [28], [29]. These approaches may prevent the receiver desensitization, but will negatively impact the coverage and are thus not very appealing. Another alternative is smart UL and DL resource allocation and scheduling such that inband self-interference is avoided. However, such an approach will not only be very complex but may also hinder full spectrum utilization as well as potentially reduce the peak throughput. Yet an alternative approach to control the self-interference power is to improve the quality and isolation of the RF components. However, the drawback of this solution is the increased overall cost of the device, together with the fact that even with the more expensive components PIM-induced self-interference might not be avoided. Thus, an intriguing approach pursued in this article is to develop and deploy digital PIM cancellation algorithms that exploit the deterministic nature of the self-interference to suppress it in the digital front-end of the transceiver.

It is also shortly noted that simultaneous transmission and reception at the same center-frequency, commonly referred to as inband full-duplex (IBFD), is currently actively researched, see for example [30] and the references therein. One major difference between IBFD and FDD systems is that the self-interference is a fundamental challenge in IBFD transceivers even if all components were purely linear, while in FDD case it is primarily the system and component nonlinearities that cause the inband self-interference. This paper and work indeed focus on the latter, with specific emphasis on the modeling and cancellation of the intermodulation distortion (IMD) induced by the passive components.

B. Prior Art and Novelty

In recent years, various digital cancellation techniques have been proposed to resolve the self-interference problem in CA FDD transceivers. These include digital cancellation of the PA nonlinearity-induced self-interference in intra-band and inter-band CA cases [19]–[21], [31], however, neglecting PIM. The works in [32]–[34], in turn, propose digital self-interference cancellation for suppressing the distortion produced by the passive front-end components. However, these methods do not consider the nonlinear distortion effects in the individual TX PAs while also ignore the memory effects and the IMD terms beyond 3rd order. In [17], on the other hand, a nonlinear RF imposer network at the antenna interface is constructed to suppress PIM.

In this article, contrary to the existing works, we first develop comprehensive behavioral models for the observable I/Q PIM waveform at receiver baseband, incorporating the joint effects of the *cascaded nonlinearities of the PAs and the passive RF front-end components*, while also considering the substantial filtering or memory effects of the duplexers and other RF front-end components. To this end, building on our preliminary work in [35], where the special case of 3rd-order nonlinearities was considered, we derive generalized models for the observable PIM waveform at RX baseband allowing for arbitrary nonlinearity order(s) in the involved nonlinear stage(s). The *first model* considers a combination of linear PAs and a nonlinear PIM stage of arbitrary order, while the *second model* allows for nonlinear distortion of arbitrary orders also in the band-specific PA units. When combined with versatile memory modeling, the processing complexity starts to increase, particularly with the second model. Thus, a *third model* is also derived where the memory modeling of the individual involved basis functions is tailored such that complexity is reduced while still offering close to similar cancellation performance. To facilitate actual digital cancellation building on the derived PIM models, efficient parameter estimation methods are also described, covering both batch least-squares (LS) as well as novel gradient-based adaptive learning methods. Also the fundamental processing complexities of the proposed cancellers and parameter estimation methods are quantitatively addressed and compared.

Additionally, the performance of the proposed digital PIM cancellation techniques, illustrated at conceptual level in Fig. 2, is demonstrated and evaluated through comprehensive RF measurements, adopting commercial LTE-Advanced UE RF components as a practical evaluation platform. The obtained results indicate excellent PIM suppression performance under realistic conditions and implementation-feasible computational complexity, with the best measured cancellation gains exceeding 20 dB. Therefore, the proposed cancellation solutions can contribute to relaxing the RF components' linearity requirements, cost, and complexity while maintaining the RX sensitivity. Furthermore, the developed advanced cancellation techniques can potentially enable new frequency band combinations that would otherwise have to be avoided due to the self-interference challenge. Therefore, the proposed digital cancellation solutions can play an important role in the deployment of the emerging 5G NR radio systems, especially at below 6 GHz bands, as well as in LTE-NR coexistence.

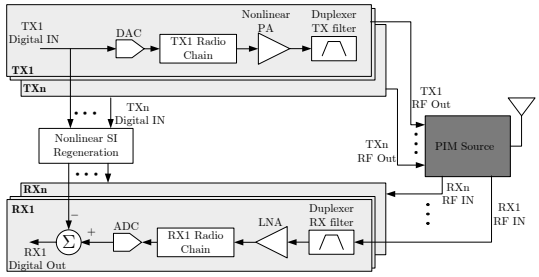

Fig. 2. Block diagram of a multi-band FDD radio transceiver system together with the proposed nonlinear SI regeneration and cancellation unit, which operates in the transceiver's digital front-end.

For clarity, the novelty and contributions of this article, compared to [35] and other existing literature, can be summarized as follows:

- Novel behavioral models for the observable PIM waveform at own RX band are provided, that take into account the co-existing CC-specific PA nonlinearities, or arbitrary orders, and the PIM nonlinearity of arbitrary order, incorporating two different memory models
- Corresponding digital PIM cancellers and novel gradient-adaptive self-orthogonalizing parameter learning rules are derived and proposed
- Computational complexity of the proposed methods are analyzed and reported
- Comprehensive RF measurement results in a practical LTE-Advanced B1+B3 inter-band CA scenario are provided and analyzed, utilizing commercial UE RF components, evidencing that more than 20 dB PIM cancellation can be provided with the most elaborate proposed cancellers

The rest of the article is organized as follows. In Section II, we derive and present three different models for the PIM-induced distortion observed in the receiver, incorporating the potential nonlinearity of the individual PAs and the passive RF front-end components. After this, Section III describes the proposed digital cancellation and parameter estimation procedures, while the RF measurement results are reported and analyzed in Section IV. Finally, Section V concludes the article, while some detailed derivations related to the proposed gradient-descent parameter estimators are provided in Appendices A and B.

II. Signal Models for Passive Intermodulation

In this section, three different signal models for describing the PIM waveform observed in the RX chain are derived and presented. They differ in the underlying assumptions regarding the TX PAs and memory effects that are made when deriving the model. In particular, the simplest model is based on the assumption that the PAs are ideally linear, while the second signal model assumes then nonlinear PA units. In both cases, the actual PIM stage is allowed to have a nonlinear response of arbitrary order, while versatile memory modeling of the involved nonlinear distortion products is also supported. The

$$\begin{aligned}\tilde{y}_{\mathrm{PIM}}[n] &= \sum_{p=1}^{P} \beta_p \tilde{x}_{\mathrm{TX}}[n]^p = \sum_{p=1}^{P} \beta_p \left(\mathrm{Re}\{\alpha_1 x_1[n] e^{j\omega_1 n}\} + \mathrm{Re}\{\alpha_2 x_2[n] e^{j\omega_2 n}\}\right)^p \\ &= \sum_{p=1}^{P} \beta_p \left(\frac{\alpha_1}{2} x_1[n] e^{j\omega_1 n} + \frac{\alpha_1^*}{2} x_1^*[n] e^{-j\omega_1 n} + \frac{\alpha_2}{2} x_2[n] e^{j\omega_2 n} + \frac{\alpha_2^*}{2} x_2^*[n] e^{-j\omega_2 n}\right)^p \\ &= \sum_{p=1}^{P} \sum_{k=0}^{p} \sum_{k_1=0}^{p-k} \sum_{k_2=0}^{p-k-k_1} \gamma_{p,k,k_1,k_2} x_1[n]^k x_1^*[n]^{k_1} x_2[n]^{k_2} x_2^*[n]^{p-k-k_1-k_2} \times e^{j[(k-k_1)\omega_1 - (p-k-k_1-2k_2)\omega_2]n} \end{aligned} \tag{2}$$

third model then seeks to balance between complexity and performance by tailoring the memory modeling details into a so-called cascaded or decoupled model where a common memory model is considered for multiple nonlinear terms.

For clarity, it is noted and acknowledged that modeling of nonlinear distortion for inter-band CA transmitters, with shared PA for the CCs is available, e.g., in [20], [21], [36]–[38]. However, these works do not consider PIM. Additionally, the modeling and cancellation problem considered in this article is substantially more evolved, as the considered system in the general case contains *cascaded nonlinearities*, i.e., the nonlinear CC-specific PAs followed by the actual PIM stage. Hence, while the center-frequencies of the considered intermodulation products are the same as in the works in [20], [21], [36]–[38], the exact complex baseband waveform is different.

In general, the provided modeling principles and methodologies are not limited to any specific band combinations. However, for presentation purposes, we focus on an important example case where the so-called positive IM3 sub-band overlaps with one of the RX bands. In other words, we focus on a scenario where $2\omega_1 - \omega_2 \approx \omega_{\mathrm{RX}}$. Here, ω_1 and ω_2 are the angular center-frequencies of the two CCs, with $\omega_1 > \omega_2$, and ω_{RX} is the angular RX frequency. This corresponds, for example, to the case where the UE performs UL CA on LTE Bands 1 and 3, and thus the PIM-induced distortion falls onto the DL Band 1 desensitizing the UE receiver. This example case of B1+B3 UL CA is also considered in the reported measurement-based evaluations in Section IV. Nevertheless, we wish to emphasize that the analysis presented herein can easily be extended to cover also other types of band combinations, such as the cases where $2\omega_2 - \omega_1 \approx \omega_{\mathrm{RX}}$, corresponding commonly to the BS side. It is additionally noted that the assumption of IM3 frequency hitting the RX band does not limit the treatment to third-order nonlinearities alone.

A. PIM Model with Linear Power Amplifiers

In the existing PIM literature, the typical assumption has been that the PAs are fully linear, and hence this first signal model with linear PAs can be considered the benchmark for the more advanced models proposed in this article. To derive a linear-in-parameters signal model, let us first denote the upconverted I/Q modulated CC signals after the linear amplification as

$$\begin{aligned}\tilde{x}_1[n] &= \mathrm{Re}\{\alpha_1 x_1[n] e^{j\omega_1 n}\} \\ \tilde{x}_2[n] &= \mathrm{Re}\{\alpha_2 x_2[n] e^{j\omega_2 n}\},\end{aligned} \tag{1}$$

where α_1 and α_2 are the complex gains of the two PAs, $x_1[n]$ and $x_2[n]$ are the two CCs in the baseband, and ω_1 and ω_2 are their center frequencies after RF upconversion. Throughout this article, we use discrete-time models for all the signals, although the upconverted signals are obviously continuous-time in a real system. This does not affect the accuracy of the modeling since the center frequencies of the CCs are considered only in order to determine where the resulting nonlinear terms will fall in the frequency domain. Additionally, the tilde-notation is used for the actual I/Q modulated and upconverted RF signals while the corresponding complex-valued baseband signals appear without the tilde on top.

The aggregated transmit signal is then simply $\tilde{x}_{\mathrm{TX}}[n] = \tilde{x}_1[n] + \tilde{x}_2[n]$, which is next subject to the PIM nonlinearity. In this article, the nonlinearities are modeled as polynomials, and hence the signal after the static PIM nonlinearity is as given in (2), at the top of this page, where β_p is the pth-order coefficient of the PIM nonlinearity, and γ_{p,k,k_1,k_2} is the coefficient of the resulting nonlinear PIM terms. Then, each of the resulting nonlinear terms is also assumed to experience memory effects, resulting in the following overall model for the TX signal of the form

$$\begin{aligned}\tilde{y}_{\mathrm{TX}}[n] = &\sum_{p=1}^{P} \sum_{k=0}^{p} \sum_{k_1=0}^{p-k} \sum_{k_2=0}^{p-k-k_1} \sum_{m=-M_1}^{M_2} \gamma_{p,k,k_1,k_2,m} \\ &\times x_1[n-m]^k x_1^*[n-m]^{k_1} x_2[n-m]^{k_2} x_2^*[n-m]^{p-k-k_1-k_2} \\ &\times e^{j[(k-k_1)\omega_1 - (p-k-k_1-2k_2)\omega_2](n-m)},\end{aligned} \tag{3}$$

where M_1 and M_2 are the numbers of pre-cursor and post-cursor memory taps after the PIM nonlinearity, respectively, and $\gamma_{p,k,k_1,k_2,m}$ is the overall effective coefficient. Note that the signal models in (2) and (3) are real-valued, which sets certain conditions on the effective coefficients. However, for clarity of presentation, we omit a more detailed discussion of these conditions in this article as the emphasis is eventually on baseband-equivalent modeling where the signal models are complex-valued by nature.

As already mentioned, we focus the analysis on the scenario where the RX band is at least partially overlapping with the frequency given by $2\omega_1 - \omega_2$. As a result, when modeling the PIM distortion coupling to the RX chain, it is sufficient to consider only those nonlinear terms in (3) that are centered around this frequency, while all other terms will be filtered out by the duplexer RX filter or later selectivity filtering stages in the RX chain. Referring to the signal model in (3), this can be transformed into the following conditions:

$$\begin{cases} k - k_1 = 2, \\ p - k - k_1 - 2k_2 = 1. \end{cases} \tag{4}$$

$$
\begin{aligned}
y_{\mathrm{PIM}}[n] = \sum_{r=1}^{R}\sum_{k=1}^{r}\sum_{k_{11}=0}^{2k}\sum_{k_{12}=0}^{2k-k_{11}}\cdots\sum_{k_{1Q}=0}^{2k-\sum_{q=1}^{Q}k_{1q}}\sum_{k_{21}=0}^{2(r-k)+1}\sum_{k_{22}=0}^{2(r-k)+1-k_{21}}\cdots\sum_{k_{2Q}=0}^{2(r-k)+1-\sum_{q=1}^{Q}k_{2q}}\gamma_{r,k,k_{11},\ldots,k_{2Q}} \\
\times x_1[n]^{(2Q+1)k+1-\sum_{q=1}^{Q}(Q-q+1)k_{1q}} x_1^*[n]^{(2Q+1)k-1-\sum_{q=1}^{Q}(Q-q+1)k_{1q}} \\
\times x_2[n]^{(2Q+1)(r-k)+Q-\sum_{q=1}^{Q}(Q-q+1)k_{2q}} x_2^*[n]^{(2Q+1)(r-k+1)-Q-\sum_{q=1}^{Q}(Q-q+1)k_{2q}},
\end{aligned} \tag{11}
$$

From these, we get

$$
\begin{cases} k_1 = k-2, \\ k_2 = \dfrac{p+1}{2} - k, \end{cases} \tag{5}
$$

where the value of p is now restricted to odd integers since only odd-order nonlinearities can produce terms on the frequency of $2\omega_1 - \omega_2$.

Substituting these into (3) and updating the sum limits accordingly, we obtain the following baseband-equivalent expression for the observed PIM distortion at RX band:

$$
\begin{aligned}
y_{\mathrm{PIM}}[n] &= \sum_{r=1}^{R}\sum_{k=1}^{r}\sum_{m=-M_1}^{M_2}\gamma_{r,k,m} \\
&\quad\times x_1[n-m]^{k+1}x_1^*[n-m]^{k-1} \\
&\quad\times x_2[n-m]^{r-k}x_2^*[n-m]^{r-k+1} \\
&= \sum_{r=1}^{R}\sum_{k=1}^{r}\sum_{m=-M_1}^{M_2}\gamma_{\mathbf{s},m}\phi_{\mathbf{s}}[n-m],
\end{aligned} \tag{6}
$$

where $r = \frac{p-1}{2}$, $R = \frac{P-1}{2}$, p and P are odd, $\mathbf{s} = [r \quad k]$ is a vector containing the state of the auxiliary parameters, $\gamma_{\mathbf{s},m}$ is the coefficient of the nonlinear terms falling on to the RX band, and

$$
\phi_{\mathbf{s}}[n] = x_1[n]^{k+1}x_1^*[n]^{k-1}x_2[n]^{r-k}x_2^*[n]^{r-k+1}. \tag{7}
$$

Note that in theory the complete signal model in (3) will also result in nonlinear terms that fall on to the RX band but are not given by $2\omega_1 - \omega_2$. In fact, all integer results of a Diophantine equation defined as $\omega_1 x + \omega_2 y = \omega_{\mathrm{RX}}$ correspond to nonlinear terms that overlap with the RX band. However, it can easily be shown that the only practical solution is $x = 2$, $y = -1$, since all the other solutions are of extremely high order. Namely, the other solutions are given by $x = 2 - 176t$ and $y = -1 + 195t$, where t is an integer, and therefore they correspond to absurdly high nonlinearity orders, which cannot be observed in real systems. Consequently, it is sufficient to consider only the case given by $2\omega_1 - \omega_2$, i.e., $x = 2$ and $y = -1$. Finally, it is noted that the model in (6)-(7) is structurally similar to the shared PA induced self-interfence at own RX band, addressed in [19]–[21], and thus serves as natural reference.

B. PIM Model with Nonlinear Power Amplifiers

In our recent work, we have observed that also the nonlinearity of the TX PAs affects the exact PIM waveform observed in the receiver [35], [39]. An intuitive interpretation of this is that the intermodulation between the linear and nonlinear components of the transmit signal will in fact be strong enough to be observable in the receiver. This clearly motivates the modeling of the PA-induced nonlinearities, alongside with the PIM distortion itself. Utilizing a memoryless polynomial model for the two involved PAs, the ith TX signal can be expressed as follows:

$$
\begin{aligned}
\tilde{x}_i[n] &= \mathrm{Re}\left\{\sum_{q=0}^{Q}\alpha_{i,q}x_i[n]^{q+1}x_i^*[n]^q e^{j\omega_i n}\right\} \\
&= \mathrm{Re}\big\{u_i[n]e^{j\omega_i n}\big\},
\end{aligned} \tag{8}
$$

where $2Q+1$ is the nonlinearity order of the PAs and $u_i[n] = \sum_{q=0}^{Q}\alpha_{i,q}x_i[n]^{q+1}x_i^*[n]^q$. Herein, the PA-induced intermodulation products at the harmonic frequencies are omitted as they can be expected to be suppressed by the duplexer/multiplexer in the RF front-end. The aggregated TX signal is then fed to the PIM nonlinearity, similar to the earlier signal model. Now, the signal after the static PIM nonlinearity can be expressed as

$$
\begin{aligned}
\tilde{y}_{\mathrm{PIM}}[n] &= \sum_{p=1}^{P}\beta_p\left(\tilde{x}_1[n] + \tilde{x}_2[n]\right)^p \\
&= \sum_{p=1}^{P}\beta_p\left(\mathrm{Re}\big\{u_1[n]e^{j\omega_1 n}\big\} + \mathrm{Re}\big\{u_2[n]e^{j\omega_2 n}\big\}\right)^p.
\end{aligned} \tag{9}
$$

Note that this signal model is structurally identical to the case of linear PAs (the terms $\alpha_i x_i[n]$ are simply replaced by $u_i[n]$), and in accordance with (6), the baseband-equivalent static PIM distortion falling onto the RX band thus reads

$$
y_{\mathrm{PIM}}[n] = \sum_{r=1}^{R}\sum_{k=1}^{r}\gamma_{r,k}u_1[n]^{k+1}u_1^*[n]^{k-1}u_2[n]^{r-k}u_2^*[n]^{r-k+1}. \tag{10}
$$

Expanding then the exponential terms involving the PA output signals and their complex conjugates with the help of the binomial theorem, we arrive at the expression in (11) shown at the top of this page. It should be noted that under the special case of fully linear PAs, the auxiliary variables $k_{11}, \ldots, k_{2Q}$ do not exist, and the above signal model reduces to the one presented in Section II-A.

With some straightforward manipulations, the signal model in (11) can be further simplified, after which the baseband-equivalent expression of the observed PIM distortion at own

TABLE I
COMPARISON OF THE THREE SIGNAL MODELS

Signal model	**PA nonlinearity**	**PIM nonlinearity**	**Memory model**	**Instantaneous basis functions with $R=1$ and $Q=0$ (linear PAs) or $Q=1$ (nonlinear PAs)**	**Total number of parameters for arbitrary R and Q**
Linear PAs with coupled memory	No	Yes	Separate for each basis function	$x_1[n]^2x_2^*[n]$	$\frac{R(M_1+M_2+1)(R+1)}{2}$
Nonlinear PAs with coupled memory	Yes	Yes	Separate for each basis function	$x_1[n]^2x_2^*[n]$, $x_1[n]^2x_2[n]x_2^*[n]^2$, $x_1[n]^3x_1^*[n]x_2^*[n]$, $x_1[n]^3x_1^*[n]x_2[n]x_2^*[n]^2$, $x_1[n]^4x_1^*[n]^2x_2^*[n]$, $x_1[n]^4x_1^*[n]^2x_2[n]x_2^*[n]^2$	$R(M_1+M_2+1)(2Q+1)\times$ $\left[(2Q+1)\left(\frac{R+1}{2}\right)-Q\right]$
Nonlinear PAs with decoupled memory	Yes	Yes	Common for all basis functions	$x_1[n]^2x_2^*[n]$, $x_1[n]^2x_2[n]x_2^*[n]^2$, $x_1[n]^3x_1^*[n]x_2^*[n]$, $x_1[n]^3x_1^*[n]x_2[n]x_2^*[n]^2$, $x_1[n]^4x_1^*[n]^2x_2^*[n]$, $x_1[n]^4x_1^*[n]^2x_2[n]x_2^*[n]^2$	$M_1+M_2+1+R(2Q+1)\times$ $\left[(2Q+1)\left(\frac{R+1}{2}\right)-Q\right]$

RX band, including also the memory, can be written as

$$y_{\mathrm{PIM}}[n]=\sum_{r=1}^{R}\sum_{k=1}^{2Q+1}\sum_{q=0}^{(2Q+1)(R-r)+Q}\sum_{m=-M_1}^{M_2}\gamma_{\mathbf{s},m}\phi_{\mathbf{s}}[n-m], \tag{12}$$

where now $\mathbf{s}=[r \quad k \quad q \quad Q]$ and

$$\phi_{\mathbf{s}}[n]=x_1[n]^{(2Q+1)(r-1)+k+1}x_1^*[n]^{(2Q+1)(r-1)+k-1}\times x_2[n]^q x_2^*[n]^{q+1}. \tag{13}$$

C. Reduced-Complexity Cascaded PIM Model with Decoupled Memory

While the model in (12)-(13) has high modeling accuracy, owing to the fact that it considers both the PA and PIM nonlinearities, it also has relatively high model complexity. Specifically, since it is building on the assumption that each nonlinear term experiences completely independent memory effects, the total amount of parameters in the model grows rapidly for higher nonlinearity orders. For this reason, in this subsection we develop a new model with essentially the same modeling accuracy, but with greatly reduced complexity, by assuming that the nonlinearities experience more similar memory effects.

To this end, let us first consider the instantaneous PIM signal with nonlinear PAs. Based on (12), this signal can be written as

$$y_{\mathrm{NL}}[n]=\sum_{r=1}^{R}\sum_{k=1}^{2Q+1}\sum_{q=0}^{(2Q+1)(R-r)+Q}\gamma_{\mathbf{s}}\phi_{\mathbf{s}}[n], \tag{14}$$

where $\phi_{\mathbf{s}}[n]$ is as shown in (13), while $\gamma_{\mathbf{s}}$ denotes the coefficients of the instantaneous basis functions. Then, to account for the memory, this overall signal $y_{\mathrm{NL}}[n]$ in (14) is subject to linear filtering, which effectively means that each nonlinear term experiences the same memory effects. While this is clearly a more constrained memory model than that of (6) or (12), this corresponds to the physical phenomena behind the memory effects, since the different nonlinear terms propagate together through the same effective channel. With this approach, the final cascaded signal model can be expressed as

$$y_{\mathrm{PIM}}[n]=\sum_{m=-M_1}^{M_2}h[m]y_{\mathrm{NL}}[n-m], \tag{15}$$

where $h[n]$ is the decoupled memory filter. Similar to the earlier memory models, this filter is assumed to contain M_1 and M_2 pre-cursor and post-cursor taps, respectively. However, as a fundamental difference to the previous models, the model in (14)–(15) is constrained such that each of the nonlinear basis functions have their own independent complex scalars as the adjustable weigths, shown in (14), followed then by the global memory filter $h[n]$ in (15).

D. Comparison of the Signal Models

To compare the characteristics of the three signal models, Table I illustrates the phenomena they are capable of modeling, together with the basis functions stemming from these different signal models for a simple example scenario of $R=1$ and $Q=0$ (linear PAs) or $Q=1$ (3rd-order PA models). As can be observed from the table, in this case the model with linear PAs has one basis function, while the models with nonlinear PAs have 6 basis functions. This indicates that the number of basis functions is not dramatically increased even when considering also the PA nonlinearity.

However, the models differ in how they treat the linear memory effects. The linear-in-parameters models with coupled memory implicitly assume independent memory filters for all nonlinear terms, which results in a significant amount of parameters, as is also evident in the last column of Table I. Namely, the effect of memory length on the overall model complexity is *multiplicative* in coupled memory based models. As opposed to this, the cascaded model assumes that each nonlinear term experiences the same memory model. While this somewhat restricts the degrees of freedom in the model, this also greatly limits the complexity since the memory length has only an additive effect on the model complexity.

Considering the same values of $R=1$ and $Q=0$ or $Q=1$ as in Table I, and assuming $M_1+M_2+1=8$ memory taps in total, the model with linear PAs has 8 parameters, the model with nonlinear PAs has 48 parameters, and the decoupled model has only 14 parameters. This fundamental difference in the

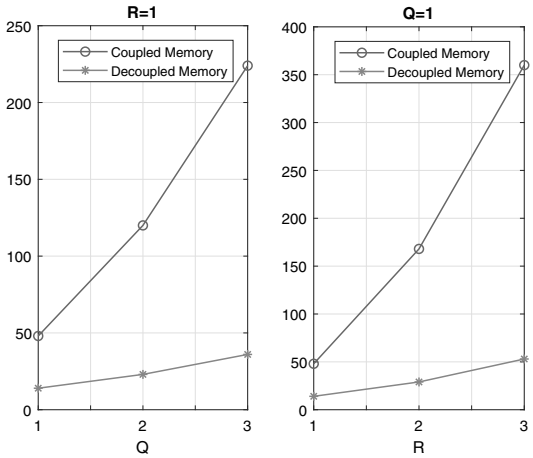

Fig. 3. Number of parameters in the coupled and decoupled memory based models, with $M_1 + M_2 + 1 = 8$, and for $R = 1$ and varying Q (left), and for $Q = 1$ and varying R (right).

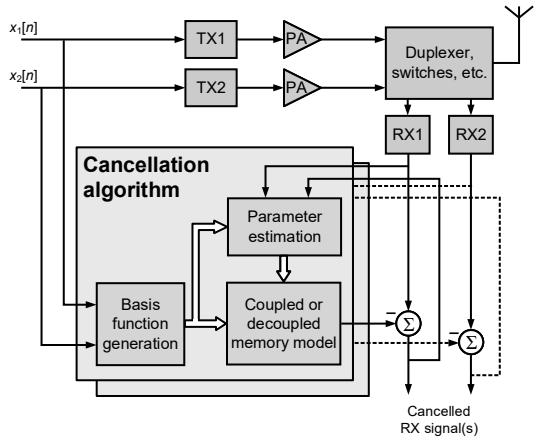

Fig. 4. Overall estimation and cancellation procedure, including options for both batch-LS and gradient-descent-based parameter learning algorithms. Moreover, also the option of cancelling PIM on the other RX band is included. Note that the thicker arrows represent vector inputs and outputs.

numbers of parameters between the coupled and decoupled memory based models is further illustrated in Fig. 3. As can be observed, the number of parameters in the decoupled memory based model is still feasible even if $Q = 3$ or $R = 3$, while that of the coupled memory based model grows very steeply as a function of Q and R. In general, while the linear PA based model is the least complex, it typically suffers from considerably lower modeling accuracy, unlike the two other models that also consider the PA nonlinearity. Therefore, the cascaded model with decoupled memory is an appealing trade-off between modeling accuracy and complexity, as will also be demonstrated through RF measurements in Section IV. The results in Section IV also show that considering the PA nonlinearities in the PIM canceller structure can provide several decibels of additional cancellation gain, compared to the linear PA based canceller.

III. Passive Intermodulation Cancellation and Parameter Estimation

In order to cancel the PIM distortion in the transceiver digital front-end (DFE), an accurate estimation of the prevailing PIM waveform is needed. To express this formally, the cancelled signal reads

$$y_{\mathrm{c}}(n) = y(n) - \hat{y}_{\mathrm{PIM}}(n), \tag{16}$$

where $y[n]$ denotes the overall observed received signal while $\hat{y}_{\mathrm{PIM}}(n)$ refers to the PIM waveform estimate, all at baseband. Now, in order to utilize the derived PIM models from Section II to reconstruct the PIM estimate $\hat{y}_{\mathrm{PIM}}(n)$, the unknown model parameters must be estimated. In this work, we consider and propose the following two alternative solutions for parameter estimation:

- Linear least squares (LS) based estimation; applicable only to the *linear-in-parameters models* in (6) and (12).
- Novel gradient-descent based adaptive estimation and cancellation; applicable to *all signal models* in (6), (12) and (14)–(15).

Moreover, it is noted that the gradient-descent-based solution is different for the linear-in-parameters models and for the reduced complexity decoupled model, as shown through the upcoming derivations in Subsection III-B and the Appendices A and B. The overall parameter estimation and cancellation framework is illustrated on a general level in Fig. 4. The differences between the three models and the corresponding canceller structures are related to the utilized set of basis functions, with examples shown in Table I, and to how the scalar weights and/or memory filters are applied to the basis function samples, while Fig. 4 shows the processing principles at high level. It is additionally noted that proper synchronization, in time and frequency, between the TX and RX is assumed in the following. Frequency synchronization is straight-forward to assume, since the cancellation processing takes place inside one common transceiver system. Additionally, the basic time synchronization or propagation delay between TX digital baseband and RX digital baseband can be easily estimated offline, since it is fixed through the hardware, and thus does not change over time.

A. Least Squares-Based Batch Estimation

The LS-based estimation and cancellation procedure is applicable to the linear-in-parameters models in (6) and (12). As a starting point, N samples of the observed signal $y[n]$ are collected into a vector as

$$\mathbf{y} = \begin{bmatrix} y[0] & y[1] & \cdots & y[N-1] \end{bmatrix}^T, \tag{17}$$

where the sample indexing within the observation block is starting from 0 without loss of generality to achieve a more convenient notation. Building on the previous modeling results, it is then a straightforward matter to show that the observed

signal vector under PIM distortion can be expressed as

$$\mathbf{y} = \mathbf{\Psi}\boldsymbol{\gamma} + \mathbf{z}, \tag{18}$$

where $\mathbf{\Psi}$ is the data matrix constructed from the original TX data based on the adopted signal model and its basis functions, $\boldsymbol{\gamma}$ contains the unknown coefficients, and $\mathbf{z}$ corresponds to noise and potential model mismatch related errors. Additionally, $\mathbf{z}$ contains also the actual received signal-of-interest (SoI) if present during the parameter estimation.

To illustrate the structure of the matrix $\mathbf{\Psi}$, let us first define the so-called instantaneous basis function vector, which collects samples of all the basis functions corresponding to a particular time instant n. The number of elements in the basis function vector depends on the cardinality of the set consisting of all the states of the auxiliary variable vector $\mathbf{s}$, which obviously depends on the considered PIM model. To present the parameter estimation procedure in a generic fashion that can be applied to both PIM models (6) and (12), the instantaneous basis function vector is defined as

$$\boldsymbol{\phi}[n] = \begin{bmatrix} \phi_{\mathbf{s}_1}[n] & \phi_{\mathbf{s}_2}[n] & \cdots & \phi_{\mathbf{s}_C}[n] \end{bmatrix}^T, \tag{19}$$

where $\mathbf{s}_i$ represent the different states of the vector $\mathbf{s}$, and C is the cardinality of the adopted signal model. The expressions of the individual basis functions are given by (7) and (13) for the considered signal models.

Having constructed the instantaneous basis function vector, the overall data matrix itself is obtained as follows:

$$\mathbf{\Psi} = \begin{bmatrix} \boldsymbol{\phi}[M_1]^T & \boldsymbol{\phi}[M_1-1]^T & \cdots & \boldsymbol{\phi}[-M_2]^T \\ \boldsymbol{\phi}[M_1+1]^T & \boldsymbol{\phi}[M_1]^T & \cdots & \boldsymbol{\phi}[-M_2+1]^T \\ \vdots & \vdots & \ddots & \vdots \\ \boldsymbol{\phi}[M_1+N-1]^T & \boldsymbol{\phi}[M_1+N-2]^T & \cdots & \boldsymbol{\phi}[-M_2+N-1]^T \end{bmatrix}, \tag{20}$$

where the indexing of the block corresponds to that of the observed vector $\mathbf{y}$. Using this data matrix, the LS parameter estimate is given by [40]

$$\hat{\boldsymbol{\gamma}} = \min_{\boldsymbol{\gamma}} \|\mathbf{y} - \mathbf{\Psi}\boldsymbol{\gamma}\|_2^2 = \left(\mathbf{\Psi}^H\mathbf{\Psi}\right)^{-1}\mathbf{\Psi}^H\mathbf{y}, \tag{21}$$

where $\|\cdot\|_2$ is the l^2-norm, and $(\cdot)^H$ denotes the Hermitian transpose.

After learning the coefficients, the cancelled signal during the actual online operation of the receiver is then given by

$$y_c[n] = y[n] - \mathbf{\Psi}_n\hat{\boldsymbol{\gamma}}, \tag{22}$$

where

$$\mathbf{\Psi}_n = \begin{bmatrix} \boldsymbol{\phi}[n+M_1]^T & \boldsymbol{\phi}[n+M_1-1]^T & \cdots & \boldsymbol{\phi}[n-M_2]^T \end{bmatrix}. \tag{23}$$

The same coefficients can be used as long as the characteristics of the effective coupling channel remain the same, after which the parameter estimation stage must be repeated. When the whole PIM process occurs inside the transceiver, it is likely that the estimation needs to be repeated only relatively seldom, such as when the temperature of the device changes considerably. On the other hand, in some cases PIM can also take place at or even beyond the antenna interface [12], [27], and thus substantially faster parameter updates may also be needed. This motivates well towards the adaptive estimation methods pursued next.

B. Gradient Descent-Based Adaptive Estimation

Since calculating the LS estimate is known to be computationally heavy, especially when the number of parameters is large, in many cases iterative estimation solutions are more suitable. In this article, we thus next propose the use of gradient descent learning based on the instantaneous error. This approach can be used even for the decoupled model, which does not lend itself to LS estimation as it is not of linear-in-parameters nature. Additionally, as noted above, the iterative methods facilitate also explicit parameter tracking.

1) Orthogonalized Adaptive Estimation for Linear-in-Parameters Signal Models: For the linear-in-parameters models in (6) and (12), let us begin by rewriting the signal after the cancellation as follows:

$$y_c[n] = y[n] - \mathbf{\Psi}_n\hat{\boldsymbol{\gamma}}_n, \tag{24}$$

where $\hat{\boldsymbol{\gamma}}_n$ is now the prevailing estimate of the parameter vector at the nth iteration. The linear-in-parameters nature of the model is evident from this expression, as the cancellation signal can be written as a matrix-vector multiplication between the basis function vector and the parameter estimate. This means that the classical least mean squares (LMS) type learning rule can be directly applied, as it is derived for an identical model, albeit without the nonlinear terms [40]. Therefore, the basic learning rule can be simply written as

$$\hat{\boldsymbol{\gamma}}_{n+1} = \hat{\boldsymbol{\gamma}}_n + \mu_{\boldsymbol{\gamma}} y_c[n]\mathbf{\Psi}_n^H. \tag{25}$$

where $\mu_{\boldsymbol{\gamma}}$ denotes the learning rate.

While the learning rule in (25) is widely-applied and known to be relatively accurate for linear systems, in the PIM cancellation case it suffers from slow convergence due to the strong correlation between the nonlinear basis functions. Therefore, better performance can be obtained by orthogonalizing the different terms in $\mathbf{\Psi}_n$ in the parameter update phase. This involves the computation of the inverse of the correlation matrix for the filter input vector, and using the resulting matrix as a multiplier for the learning rule [40, p. 356]. With this approach, the cancellation phase remains as in (24), while the learning rule reads now

$$\hat{\boldsymbol{\gamma}}_{n+1} = \hat{\boldsymbol{\gamma}}_n + \mu_{\boldsymbol{\gamma}} y_c[n]\left(\mathbf{R}^*_{\mathbf{\Psi}_n}\right)^{-1}\mathbf{\Psi}_n^H, \tag{26}$$

where $\mathbf{R}_{\mathbf{\Psi}_n} = \mathrm{E}\left[\mathbf{\Psi}_n^H\mathbf{\Psi}_n\right]$ is the correlation matrix of the filter input vector. Note that since the parameter update is now presented for the complex conjugate of the classical definition of the learning rule, also the correlation matrix must be complex-conjugated. Using this type of an orthogonalized learning rule ensures faster convergence, with the cost of somewhat higher computational complexity compared to the baseline LMS.

Next, in order to determine a more convenient and computationally efficient expression for $\mathbf{R}^*_{\mathbf{\Psi}_n}$, let us first rewrite it

as follows:

$$\begin{aligned}\mathbf{R}^*_{\boldsymbol{\Psi}_n} &= \mathrm{E}\left[\boldsymbol{\Psi}_n^T\boldsymbol{\Psi}_n^*\right] \\ &= \mathrm{E}\Big[\begin{bmatrix}\boldsymbol{\phi}[n+M_1]^T & \boldsymbol{\phi}[n+M_1-1]^T & \cdots & \boldsymbol{\phi}[n-M_2]^T\end{bmatrix}^T \\ &\quad\times\begin{bmatrix}\boldsymbol{\phi}[n+M_1]^T & \boldsymbol{\phi}[n+M_1-1]^T & \cdots & \boldsymbol{\phi}[n-M_2]^T\end{bmatrix}^*\Big] \\ &= \mathrm{E}\left[\begin{bmatrix}\boldsymbol{\phi}[n+M_1]\\ \vdots \\ \boldsymbol{\phi}[n-M_2]\end{bmatrix}\begin{bmatrix}\boldsymbol{\phi}[n+M_1]^H & \cdots & \boldsymbol{\phi}[n-M_2]^H\end{bmatrix}\right]\end{aligned} \tag{27}$$

From this, it is evident that the correlation matrix has a block-wise structure, where the individual blocks are of the form $\mathrm{E}\left[\boldsymbol{\phi}[i]\boldsymbol{\phi}[j]^H\right]$. Let us now define two simplifying assumptions regarding the transmit waveform, which can be reasonably expected to hold for considered radio communication systems: (*i*) The two transmit signal (CC) sequences are both independent and identically distributed (i.i.d.) with zero mean, as well as mutually independent; (*ii*) The transmit signals are stationary, which means that their statistical properties do not change with respect to time.

By invoking the first assumption, we can write $\mathrm{E}\left[\boldsymbol{\phi}[i]\boldsymbol{\phi}[j]^H\right] = \mathbf{0}$, when $i \neq j$. In other words, the correlation matrix has a block-diagonal structure. Then, by invoking the second assumption, it holds for the remaining diagonal elements that $\mathrm{E}\left[\boldsymbol{\phi}[i]\boldsymbol{\phi}[i]^H\right] = \mathrm{E}\left[\boldsymbol{\phi}[j]\boldsymbol{\phi}[j]^H\right]$ for any i and j.

Using these findings, the complex conjugate of the complete correlation matrix can therefore be expressed as $\mathbf{R}^*_{\boldsymbol{\Psi}_n} = \mathrm{diag}\left\{\mathbf{R}^*_{\boldsymbol{\phi}},\ldots,\mathbf{R}^*_{\boldsymbol{\phi}}\right\}$, where $\mathbf{R}_{\boldsymbol{\phi}}$ is the correlation matrix of the basis functions, whose complex conjugate is simply repeated $M_1 + M_2 + 1$ times on the diagonal. Using this expression, the inverse of the complete correlation matrix is $\left(\mathbf{R}^*_{\boldsymbol{\Psi}_n}\right)^{-1} = \mathrm{diag}\left\{\left(\mathbf{R}^*_{\boldsymbol{\phi}}\right)^{-1},\ldots,\left(\mathbf{R}^*_{\boldsymbol{\phi}}\right)^{-1}\right\}$, as per the inversion rule of block-diagonal matrices. Noting that the statistical properties of the different basis functions remain unchanged throughout the operation, the inverse of $\mathbf{R}^*_{\boldsymbol{\phi}}$ can be precomputed offline. With this, the learning rule can be expressed in the following alternative form:

$$\hat{\boldsymbol{\gamma}}_{n+1} = \hat{\boldsymbol{\gamma}}_n + \mu_{\boldsymbol{\gamma}} y_c[n]\mathrm{diag}\left\{\left(\mathbf{R}^*_{\boldsymbol{\phi}}\right)^{-1},\ldots,\left(\mathbf{R}^*_{\boldsymbol{\phi}}\right)^{-1}\right\}\boldsymbol{\Psi}_n^H, \tag{28}$$

This expression results in considerably reduced computational requirements compared to (26), since there is no need to perform a matrix inversion when calculating the parameter update. That is, the matrix $\left(\mathbf{R}^*_{\boldsymbol{\phi}}\right)^{-1}$ can be precomputed for each known transmit waveform type and stored into memory. Moreover, the earlier computed orthogonalized basis function samples can be reused in each iteration, meaning that it suffices to orthogonalize only the most recent basis function vector.

2) Orthogonalized Adaptive Estimation for Decoupled Signal Models: The classical LMS-based approach is not applicable for the decoupled model with cascaded nonlinearity and memory models, and therefore we must derive the necessary learning rules by resorting to the theory behind gradient descent learning and complex-valued gradients. Based on (14) and (15), and by using the basis function vector notation, the cancelled signal at nth iteration can in this case be first rewritten as

$$y_{\mathrm{c}}(n) = y(n) - \mathbf{h}_n^H\mathbf{y}_{n,\mathrm{NL}}, \tag{29}$$

where $\mathbf{h}_n$ is the memory model estimate in vector form, and $\mathbf{y}_{n,\mathrm{NL}} = \begin{bmatrix}y_{\mathrm{NL}}(n+M_1) & \cdots & y_{\mathrm{NL}}(n-M_2)\end{bmatrix}$. Moreover, $y_{\mathrm{NL}}(n) = \mathbf{g}_n^H\boldsymbol{\phi}(n)$, where $\mathbf{g}_n$ contains the coefficients of the nonlinear basis functions ($\gamma_{\mathbf{s}}$).

Defining then the cost function as $J(\mathbf{g}_n, \mathbf{h}_n) = |y_{\mathrm{c}}(n)|^2$, the learning rule for the PIM model coefficients can be formally expressed as

$$\mathbf{g}_{n+1} = \mathbf{g}_n - \mu_g\frac{\partial J(\mathbf{g}_n,\mathbf{h}_n)}{\partial \mathbf{g}_n}, \tag{30}$$

where μ_g is the PIM coefficient step-size. As shown in Appendix A, the complex partial derivative can be expressed as

$$\frac{\partial J(\mathbf{g}_n,\mathbf{h}_n)}{\partial \mathbf{g}_n} = -2y_{\mathrm{c}}^*(n)\boldsymbol{\Phi}_n\mathbf{h}_n^*, \tag{31}$$

where $\boldsymbol{\Phi}_n = \begin{bmatrix}\boldsymbol{\phi}(n+M_1) & \cdots & \boldsymbol{\phi}(n-M_2)\end{bmatrix}$. Therefore, we can express the final learning rule for $\mathbf{g}_n$ as follows:

$$\mathbf{g}_{n+1} = \mathbf{g}_n + \mu_g y_{\mathrm{c}}^*(n)\boldsymbol{\Phi}_n\mathbf{h}_n^* \tag{32}$$

As for learning the memory model, it can be noted that the system is in fact identical to the classical LMS filter with $\mathbf{y}_{n,\mathrm{NL}}$ as the input signal, meaning that a similar learning rule can be adopted. Therefore, the learning rule for $\mathbf{h}_n$ is

$$\mathbf{h}_{n+1} = \mathbf{h}_n + \mu_h y_{\mathrm{c}}^*(n)\mathbf{y}_{n,\mathrm{NL}}, \tag{33}$$

where μ_h is the memory step-size.

Again, due to the mutual correlation between the nonlinear basis functions in $\boldsymbol{\phi}(n)$, also the decoupled learning rule in (32) suffers from slow convergence, similar to the case with the linear-in-parameter signal models. To address this, a self-orthogonalizing learning rule can be used instead. Following similar steps as in [40, p. 356], in the linear system case, we denote the filter input vector by $\mathbf{u}_n = \boldsymbol{\Phi}_n\mathbf{h}_n^*$. Based on this, the self-orthogonalizing learning rule can be written as

$$\mathbf{g}_{n+1} = \mathbf{g}_n + \tilde{\mu}_g\mathbf{R}^{-1}e^*(n)\mathbf{u}_n, \tag{34}$$

where $\tilde{\mu}_g$ is the step-size, and $\mathbf{R} = \mathrm{E}\left[\mathbf{u}_n\mathbf{u}_n^H\right]$ is the correlation matrix of the filter input vector. However, the challenge with this learning rule is the fact that the correlation matrix depends on the time-variant memory model $\mathbf{h}_n$, which means that the correlation matrix must be computed and inverted during each iteration. This is computationally extremely costly, and renders the learning rule fairly impractical.

In order to reduce the number of required computations and thereby make the self-orthogonalizing learning a practical solution, let us next express the correlation matrix in a more convenient form. Following the steps shown in Appendix B, the correlation matrix can be re-expressed as

$$\mathbf{R} = \mathbf{R}_{\boldsymbol{\phi}}\mathbf{h}_n^H\mathbf{h}_n, \tag{35}$$

where $\mathbf{R}_{\boldsymbol{\phi}}$ is the correlation matrix of the basis functions, defined identically as in (28). Recall that $\mathbf{R}_{\boldsymbol{\phi}}$ is only based on the chosen signal model and the statistical properties of the

TABLE II
CANCELLATION PROCESSING AND GRADIENT-BASED PARAMETER UPDATE COMPLEXITIES CORRESPONDING TO THE THREE SIGNAL MODELS. HERE, $M = M_1 + M_2 + 1$, WHILE C IS THE AMOUNT OF BASIS FUNCTIONS IN THE MODELS WITH NONLINEAR PAS, EXPRESSED IN (37).

Signal model	Parameter update	Cancellation	Total
Linear PAs with coupled memory	$\frac{R(R+1)}{2}\left(\frac{R(R+1)}{2}+M\right)$	$\frac{MR(R+1)}{2}$	$\frac{R(R+1)}{2}\left(\frac{R(R+1)}{2}+2M\right)$
Nonlinear PAs with coupled memory	$C\left(C+M\right)$	CM	$C\left(C+2M\right)$
Nonlinear PAs with decoupled memory	$\left(C+M\right)\left(C+1\right)$	$C+M$	$\left(C+M\right)\left(C+2\right)$

utilized waveforms, meaning that it can be calculated offline, alongside with its inverse.

Stemming from above, we can rewrite the self-orthogonalizing learning rule as follows:

$$\begin{aligned}\mathbf{g}_{n+1} =&\mathbf{g}_n + \frac{\tilde{\mu}_g}{\mathbf{h}_n^H\mathbf{h}_n}\mathbf{R}_{\boldsymbol{\phi}}^{-1}y_{\mathrm{c}}^*(n)\mathbf{u}_n \\ =&\mathbf{g}_n + \mu_{g,\mathrm{ort}}\mathbf{R}_{\boldsymbol{\phi}}^{-1}y_{\mathrm{c}}^*(n)\boldsymbol{\Phi}_n\mathbf{h}_n^*,\end{aligned} \tag{36}$$

where $\mu_{g,\mathrm{ort}}$ is the final step-size. Additionally we note that, as a simplification, the step-size can be chosen to be static, despite the time-variant term $\mathbf{h}_n^H\mathbf{h}_n$. Therefore, the only additional computation required in this learning rule, as opposed to that in (32), is the matrix multiplication since $\mathbf{R}_{\boldsymbol{\phi}}^{-1}$ can be precomputed and remains fixed.

C. Processing and Learning Complexities and Comparison

We next address the complexity analysis and comparisons, focusing on the proposed gradient descent-based methods. We analyze and differentiate between the fundamental cancellation complexities, for given parameter estimates, and the actual parameter estimation complexities.

Stemming directly from the cancellation processing solutions in (24) and (29), as well as from the parameter update rules in (28), (33), and (36), the fundamental complexity numbers in terms of the associated complex multiplications per cancelled sample or per parameter update cycle are provided in Table II. Note that the complexities of the coupled and decoupled models incorporating the nonlinearity of the PAs are expressed for clarity in terms of C, which denotes the total amount of basis functions. It can be expressed in the general case as

$$C = R(2Q+1)\left[(2Q+1)\left(\frac{R+1}{2}\right) - Q\right]. \tag{37}$$

It is clear from the expressions in Table II that the decoupled model is particularly efficient in the cancellation phase, when compared to the naive coupled models. As can be observed, its cancellation complexity is *additive* in nature, while that of the coupled models is *multiplicative*.

In order to gain further insight into the complexity, in terms of a concrete example, let us consider the model parameters of $R = 1$, $Q = 2$, and $M = 8$, which will also be used in processing the RF measurement data in Section IV. These parameters result in one basis function for the model with linear PAs, while the models with nonlinear PAs have $C = 15$ basis functions. Consequently, for the model with linear PAs, the parameter update involves 9 complex multiplications, while the cancellation requires 8 complex multiplications, the total count being 17 complex multiplications. For the coupled model with nonlinear PAs, the parameter update consists of 345 complex multiplications, and the cancellation requires further 120 multiplications. Therefore, the total amount of complex multiplications per iteration is 465, considerably more than for the simple linear model. Finally, for the cascaded model with decoupled memory, the update stage involves 368 complex multiplications, whereas the cancellation requires only 23 complex multiplications. The total amount of complex multiplications per iteration is therefore only 391 for the decoupled model. Most importantly, with the decoupled model, the fundamental cancellation processing with these realistic example parameters is over 5 times more efficient, while the parameter learning is of roughly the same complexity, when compared to the coupled model case. Thus, particularly in cases where PIM is mostly contributed by the internal RF components of the device, there is no need to constantly update the parameters, and the cascaded model with decoupled memory provides a very attractive complexity reduction.

D. Selected Implementation Aspects

We next shortly address selected additional aspects related to the PIM canceller implementation. As the CC signals $x_1[n]$ and $x_2[n]$ may originally exist at the so-called critical sample rate, proper interpolation to higher sample rate is most likely needed, in order to calculate the nonlinear basis functions without aliasing. The exact details depend on the original sample rate and the selected maximum nonlinearity orders. Additionally, the observable PIM in practical receivers may be limited to channel bandwidth, especially if analog channel selection filtering is deployed prior to analog-to-digital converter (ADC). In such cases, the PIM canceller related basis functions can and should also be band-limited, through appropriate digital filtering, and decimated to the same sample rate as the actual RX sample rate. Furthermore, if the intermodulation center-frequency is different from the RX channel center-frequency, digital frequency-shifting of the basis function samples can be deployed. Thus, it can be noted that the devised digital cancellation methods do not impose any additional requirements on the analog RX and ADC interface, considering that properly filtered basis functions are deployed.

Another important implementation related aspect is the potential power consumption of the cancellation engine. It

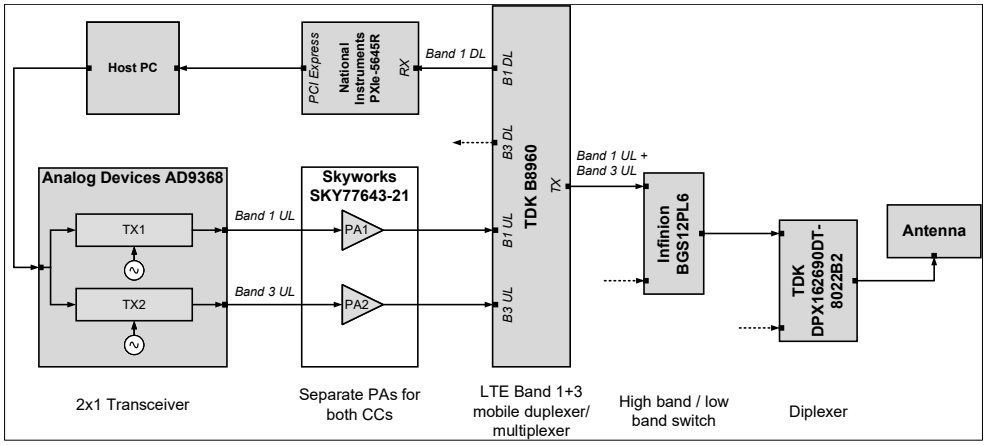

Fig. 5. Transceiver system structure adopted in the RF measurements. The utilized device and RF component models are shown in the figure.

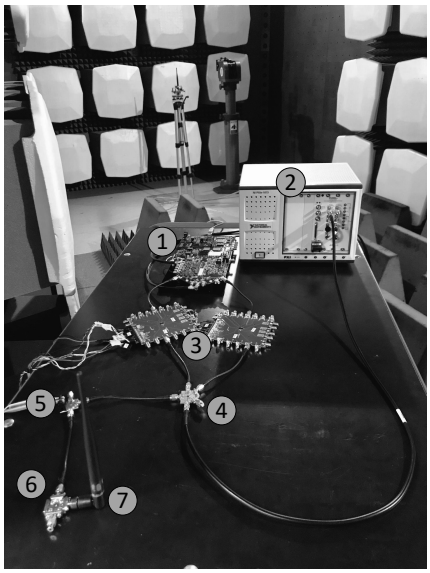

Fig. 6. Overall RF measurement setup in the isolated chamber, featuring the Analog Devices AD9368-2 board (1), National Instruments PXIe-5645R observation receiver (2), Skyworks SKY77643-21 PAs (3), TDK B8960 multiplexer (4), Infinion BGS12PL6 switch (5), TDK DPX162690DT-8022B2 diplexer (6), and Delta 6A antenna (7).

is obvious that the exact power consumption depends on the actual implementation form, with dedicated digital ASICs based implementation yielding the lowest power consumption. As the associated fundamental processing elements (nonlinear transformations, linear filtering) are actually fairly similar to those utilized in polynomial based digital predistortion (DPD) systems, see, e.g., [36]–[38], some ballpark power consumption understanding can be obtained from the reported DPD implementations. While software-based solutions for DPD systems are known to be commonly power hungry, dedicated digital ASIC based implementations have been reported, e.g., in [41], [42] where power consumption is only in the order of few tens of mW. This implies that it is most likely feasible to develop dedicated digital ASICs also for the PIM cancellation purposes, with similar power consumption figures.

IV. RF Measurement Results

A. Considered Scenario and Assumptions

The performance of the proposed PIM cancellers is next evaluated with measured signals and LTE-Advanced UE RF components, in the context of B1+B3 inter-band carrier aggregation, utilizing all three signal models and corresponding digital PIM cancellation solutions. The RF measurements are carried out in an isolated chamber in order to suppress the external interference sources, with the measurement setup and environment being as shown in Figs. 5 and 6. Moreover, the relevant features of the measurement system and the digital canceller are listed in Table III. The two CC signals are generated using the Analog Devices AD9368-2 2×1 transceiver board, after which they are amplified using two separate Skyworks SKY77643-21 PAs. After this, the two TX signals are combined with a TDK B8960 duplexer/multiplexer, the aggregated TX signal being then fed to an Infinion BGS12PL6 switch and a TDK DPX162690DT-8022B2 diplexer. Finally, the diplexer is connected to an antenna, as illustrated in Fig. 5 and Fig. 6. It is noted that AD9368-2 is a pre-commercial non-publicly available dual-TX transceiver system with maximum instantaneous BW per channel of 250 MHz and tuning range of 700 MHz to 2800 MHz. Performance and specifications wise, this board is similar to the commercially available board AD9371, though the tuning range of AD9371 extends further up to 6 GHz.

In this measurement setup with the above components, the linearity of the passive stages is primarily dictated by the switch whose IIP3 value is reported to be +65 dBm. Additionally, to provide the maximum power of +24 dBm at the antenna

interface, the CC-specific PA output powers are +26 dBm since the overall insertion loss from PA outputs to the antenna is approximately 5 dB. Thus, when considering the insertion loss of some 3 dB stemming from the duplexer/multiplexer, it is straight-forward to calculate that the total IMD3 power due to the switch is ca. -52 dBm. Additionally, as discussed also, e.g., in [43], the corresponding share of this total IMD power at the specific intermodulation center-frequency that coincides with the RX operating band is some 10 dB lower. Thus, the observable PIM power at the duplexer/multiplexer RX port is approximately -52 dBm -10 dB -3 dB = -65 dBm.

The CC signals used in the measurements are QPSK modulated single-carrier frequency division multiple access (SC-FDMA) waveforms, following the 3GPP LTE-Advanced uplink specifications with 15 kHz subcarrier spacing. The number of active subcarriers and the FFT size are 300 and 512, respectively, in case of 5 MHz channel bandwidth per CC, while the corresponding numbers are 600 and 1024 in the 10 MHz channel bandwidth case. The peak-to-average-power ratios (PAPR) of the individual CC waveforms are ca. 4.5 dB and 6.5 dB at 1% and 0.01% CCDF levels, respectively. Additionally, when providing the maximum power of +24 dBm at the antenna interface, in the context of Fig. 5, the error vector magnitude (EVM) and the adjacent channel leakage ratio (ACLR) of the individual CCs are ca. 5% and 32 dBc, respectively. The canceller basis functions are limited to 20 MHz and 40 MHz bandwidths, in cases of 5 MHz and 10 MHz CC bandwidths, through digital filtering, and decimated to the rates shown in Table III.

For parameter learning, we focus on the proposed self-orthogonalized gradient-based methods where the related step-sizes are chosen such that convergence is established in roughly 50,000 ... 100,000 samples with the exact sample sizes as shown in Table III. The LS-based parameter learning solutions also work very reliably, but are excluded for presentation brevity. We also note that the canceller corresponding to $Q = 0$ (linear PA models) is the literature reference against which the performance of the more elaborate cancellers building on the joint modeling of CC-specific nonlinear PAs and PIM nonlinearity is to be compared.

To establish proper time synchronization in the measurements, the received sample sequence is correlated with a sequence of the basic third-order basis function samples, shown on the first row of Table I, which can be directly calculated using the TX CC sequences $x_1[n]$ and $x_2[n]$. This is well-justified since the basic third-order basis function is dominant in power, compared to the other basis functions. We also separately study the impacts of the possible timing offsets in the latter part of the experimental results. Additionally, frequency synchronization is established on hardware such that both transmitting and receiving entities are frequency-locked. No actual received signal-of-interest (SoI) is present in the basic measurements, while the impact of SoI on the parameter learning accuracy is also separately studied.

B. Obtained Results

Considering first the PIM distortion with the full transmit power of +24 dBm, Figs. 7 and 8 show the essential power spectral densities (PSDs) using the default features for each canceller as listed in Table III. Firstly, it is clear that PIM-induced distortion is indeed a serious issue in FDD transceivers operating on the frequency bands in question, since the resulting self-interference without cancellation is approximately 20 dB above the noise floor when using these state-of-the-art RF components. The measured PIM power, without cancellation, also very accurately matches with the IIP3 based calculations.

TABLE III
LTE-ADVANCED B1+B3 RF MEASUREMENT SCENARIO AND CONSIDERED PIM CANCELLER PARAMETERS. SOME OF THE PARAMETERS ARE ALSO VARIED IN THE MEASUREMENTS.

Feature	Value	
CC bandwidth	5 MHz	10 MHz
CC1 center frequency	1950 MHz	1950 MHz
CC2 center frequency	1760 MHz	1760 MHz
RX center frequency	2140 MHz	2140 MHz
PA gain	28 dB	28 dB
Total TX power at antenna	24 dBm	24 dBm
Cancellation sample rate	31.72 MHz	43.88 MHz
Parameter learning sample size (N)	90 000	120 000
PIM nonlinearity order ($P = 2R + 1$)	3	3
PA nonlinearity order ($2Q + 1$)	5	5
Number of PIM pre-cursor taps (M_1)	3	3
Number of PIM post-cursor taps (M_2)	4	4

Secondly, Figs. 7 and 8 show that each of the proposed signal models, and each of the corresponding digital cancellers, is capable of efficiently suppressing the PIM-induced self-interference. Additionally, the results also indicate that modeling of the PA nonlinearity is indeed beneficial to more accurately suppress the PIM distortion. In particular, when also the nonlinear distortion produced by the PAs is taken into account, the amount of cancellation is improved by some 4–5 dB with 5 MHz CCs, and some 2–3 dB with 10 MHz CCs, compared to the linear PAs based canceller that can be considered as the literature reference. These are very substantial additional benefits, especially when the actual received signal of interest is close to the fundamental receiver sensitivity level. Another noteworthy finding based on Figs. 7 and 8 is that the cascaded model with decoupled memory can achieve nearly the same cancelling performance as the much more complex model with coupled memory, even though its cancellation complexity is over 5 times lower.

Next, Figs. 9 and 10 show the residual power of the noise and interference with respect to the total transmit power. With both of the considered CC bandwidths, the PIM-induced interference is clearly above the noise floor already with transmit powers in the order of +15 dBm if no cancellation is performed. However, modeling and cancelling the PIM even with the very simplest signal model guarantees nearly interference-free reception up to transmit powers of some +20 dBm. The transmit power range can be further increased by using the more advanced models that incorporate also the PA-induced nonlinearities. With 10 MHz CCs, the canceller solutions incorporating PA nonlinearities are capable of nearly perfect cancellation even with the highest considered transmit power of +24 dBm, as already discussed. Being able to utilize, e.g., 3 dB higher

transmit power, while still protecting the own receiver, is a substantial benefit for the uplink coverage. Furthermore, the nearly identical performance of the models with coupled and decoupled memory is also clearly evident from Figs. 9 and 10, illustrating the excellent complexity-accuracy trade-off of the derived cascaded model.

The learning rate and convergence characteristics are important practical aspects, especially when gradient-descent based adaptive learning rules are applied. To this end, Fig. 11 shows the convergence of the residual PIM interference plus noise power, over time, in the example case of 5 MHz CC bandwidth. As can be observed, with the chosen step-sizes, the developed gradient-descent based learning rules can facilitate reliable convergence for all three canceller types, with the residual power being very close to the final steady-state level already within 0.5-2 ms or so. With the utilized sample rate of 30.72 MHz, this corresponds to some 15,000 ... 60,000 samples. It can also be observed that the linear PA model based canceller converges faster, due to the reduced number of parameters, however, also the steady-state cancellation performance is some 5 dB lower as already concluded earlier.

C. Impact of Nonlinearity Orders and Memory Depth

We next further investigate the significance of the PA nonlinearity in the observed PIM distortion, while otherwise work with the baseline parameterization shown in Table III. To this end, Fig. 12 shows the residual PIM-plus-noise power with different PA nonlinearity orders used in the cancellation processing, focusing on the 5 MHz CC bandwidth case. These results further confirm the conclusion that modeling the PA nonlinearity greatly improves the cancellation performance, as already the 3rd-order PA model based canceller clearly outperforms the one based on linear 1st-order model. Furthermore, it can be observed that the highest performance is achieved with a 5th-order PA model, while increasing the PA nonlinearity order beyond 5 does not observably improve the cancellation performance anymore. The results obtained with 10 MHz CC bandwidth are very similar and thus not explicitly shown.

Next, we experiment the impacts of PIM nonlinearity order ($P = 2R + 1$) in the canceller for given PA nonlinearity order of $2Q + 1 = 5$ and given numbers of precursor and postcursor taps of $M_1 = 3$ and $M_2 = 4$, while otherwise again keeping the baseline parameterization shown in Table III. The obtained results are shown in Fig. 13, again illustrating that modeling the PA induced nonlinearities is beneficial to maximize the cancellation gain. It can also be observed that increasing the PIM nonlinearity order beyond three does not improve the cancellation in this RF component setup.

Additionally, the amounts of precursor and postcursor taps (M_1 and M_2) are varied for given PIM nonlinearity order of $P = 2R + 1 = 3$ and given PA nonlinearity order of $2Q + 1 = 5$, with the results shown in Fig. 14. Here, for evaluation simplicity, we have set $M_1 = M_2 = M$ and vary M within $M \in \{0, 1, 2, 3, 4\}$ where $M = 0$ means a memoryless canceller. As can be observed from the figure, incorporating memory taps in the canceller can improve some 3 dB in the cancellation performance, though due to the relatively narrowband signals, the amount of memory is fairly mild in this measurement setup.

D. Learning Under Timing Offset and Signal-of-Interest

Next we address the sensitivity of the developed estimation-cancellation system on the potential timing offsets between the two signals (observation signal and the cancellation signal) at the cancellation point, while using the baseline parameters from Table III. To this end, we deliberately introduce controlled timing offsets in the receiver signal, relative to the estimated true timing, and execute the parameter learning and cancellation with such signals. The obtained results are shown in Fig. 15 for the 10 MHz CC bandwidth case, where we have focused only on the gradient-adaptive cascaded nonlinearity model based canceller, for readability purposes. We also experiment and show the cancellation performance without memory ($M_1 = M_2 = 0$) and with memory ($M_1 = 3, M_2 = 4$).

As the results in Fig. 15 illustrate, a memoryless canceller is very sensitive to the timing errors – an observation that conforms well with the intuition. However, when the canceller structure is equipped with memory containing both pre-cursor and post-cursor taps, the system can be observed to be very robust against reasonable timing offsets. This is stemming from the fact that a time-offset or time-misalignment in the observed signal can basically be modeled through an additional linear frequency response or impulse response, and thus the memory-based canceller has structural capability to model such phenomenon, assuming that there is a sufficient amount of taps. Thus, as long as the parameter estimation and actual cancellation are carried out under the same time-offset, high-quality cancellation can still be obtained.

Finally, we shortly address the impact of the presence of SoI on the canceller parameter learning. We use the same measured signals, as in the earlier experiments, while add an actual LTE-Advanced downlink OFDM signal on top of the measured I/Q signals. This way, comparisons against the previous results where SoI was not present can be made in a straight-forward manner. The SoI is a QPSK modulated OFDM signal with 300 active subcarriers conforming to the 5 MHz channel bandwidth specifications. The parameter estimation is carried out with the RX signal containing SoI, PIM and thermal noise, while the actual cancellation performance is evaluated after the parameter estimation convergence by using the received signal without SoI. This allows to measure the cancellation performance similar to the earlier examples, while taking explicitly into account the impact of the SoI on the parameter learning.

The obtained results under different received power levels of the SoI are shown in Fig. 16. As can be observed, the different cancellers are relatively robust against reasonable SoI powers, while eventually the parameter estimation accuracy and thereon the cancellation performance start to degrade. This is understandable, since SoI essentially acts as additional strong noise from parameter estimation point of view. However, very reliable parameter estimation is still possible even when the SoI is some 10...15 dB above the thermal noise.

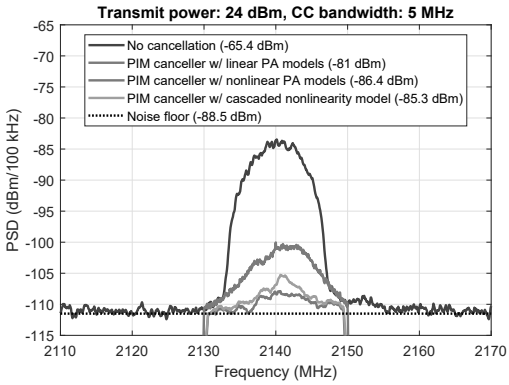

Fig. 7. Measured PSDs of the PIM distortion at own RX band with different cancellation solutions, using a CC bandwidth of 5 MHz.

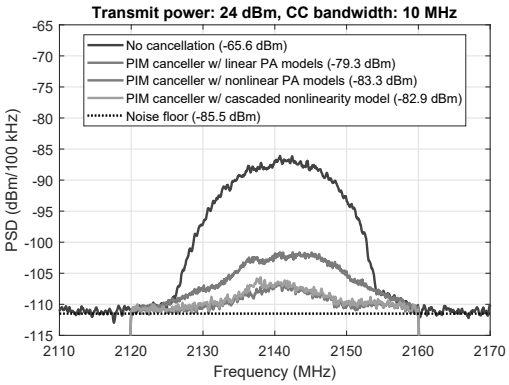

Fig. 8. Measured PSDs of the PIM distortion at own RX band with different cancellation solutions, using a CC bandwidth of 10 MHz.

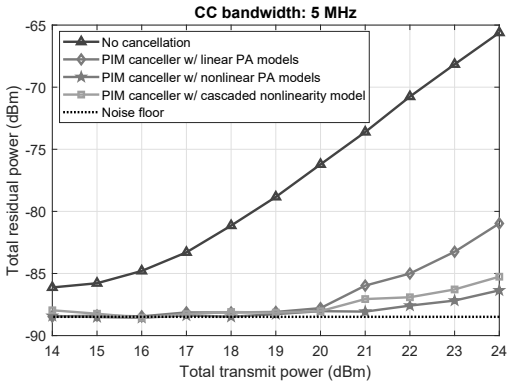

Fig. 9. Measured PIM cancellation performance with respect to the total transmit power, using a CC bandwidth of 5 MHz.

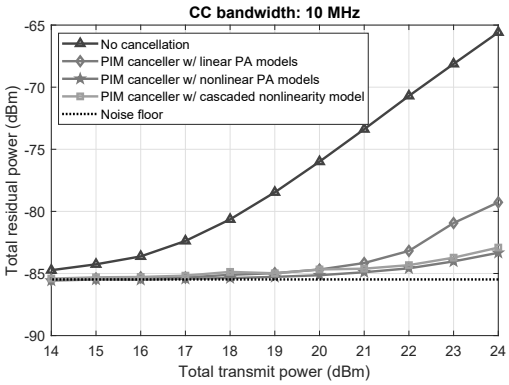

Fig. 10. Measured PIM cancellation performance with respect to the total transmit power, using a CC bandwidth of 10 MHz.

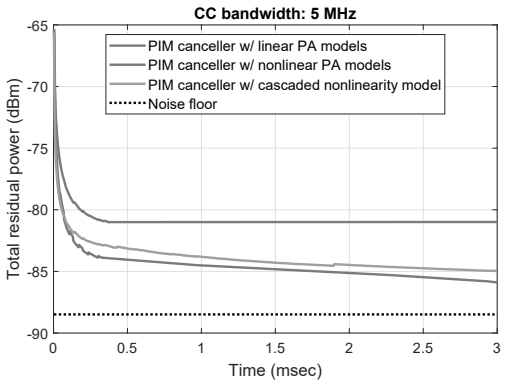

Fig. 11. Example convergence of the measured residual total power (PIM+noise) over time for the gradient-adaptive PIM cancellers. CC bandwidth is 5 MHz and TX power is +24 dBm.

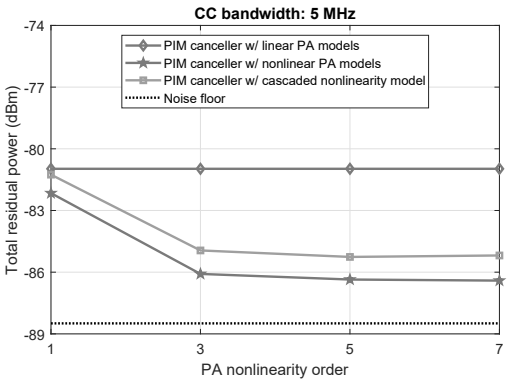

Fig. 12. Measured PIM cancellation performance with respect to the PA nonlinearity order $(2Q+1)$ assumed in the canceller, using a CC bandwidth of 5 MHz. TX power is +24 dBm.

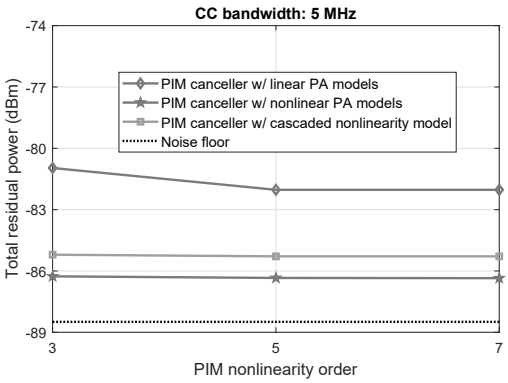

Fig. 13. Measured PIM cancellation performance with respect to the PIM nonlinearity order ($P = 2R + 1$) assumed in the canceller, using a CC bandwidth of 5 MHz. TX Power is +24 dBm.

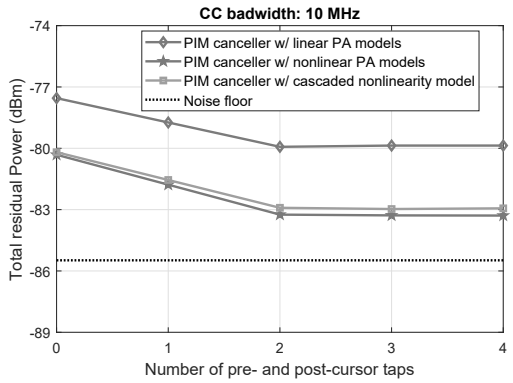

Fig. 14. Measured PIM cancellation performance with respect to the number of pre-cursor and post-cursor taps ($M_1 = M_2 = M$) assumed in the canceller, using a CC bandwidth of 10 MHz. TX power is +24 dBm.

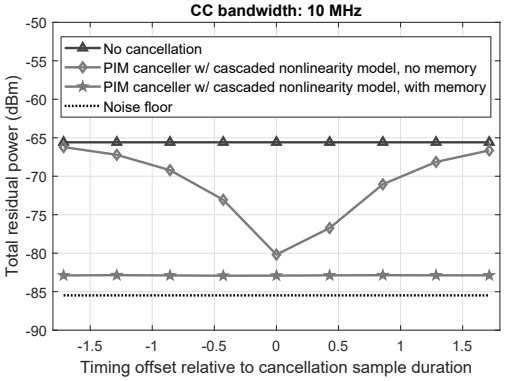

Fig. 15. Measured PIM cancellation performance with respect to the timing offset, using a CC bandwidth of 10 MHz. TX Power is +24 dBm.

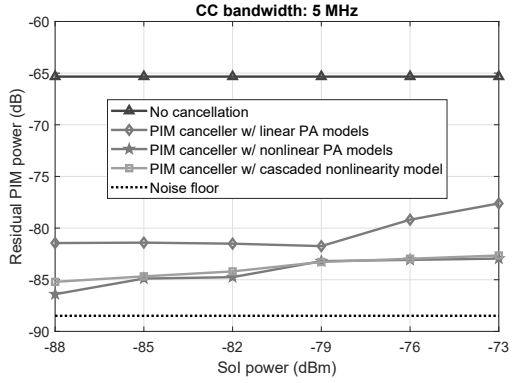

Fig. 16. Measured PIM cancellation performance in the presence of a signal-of-interest during the parameter learning. CC bandwidth is 5 MHz and TX power is +24 dBm.

E. Main Findings and Inference

Altogether, the obtained results give rise to the following observations:

- The PIM-induced interference is a serious issue in FDD transceivers with certain TX and RX frequencies, such as those of LTE Bands 1 and 3. In our work, we demonstrated this with actual RF measurements using 3GPP LTE-Advanced standard compliant waveforms, where commercial off-the-shelf passive components produced significant distortion on to the RX band even when using separate PAs for both CCs.
- The nonlinearity of the PAs must be modeled to obtain as accurate cancellation signal as possible, even when using separate PAs to amplify the individual CCs. In other words, even though the PAs do not contribute to the intermodulation between the CCs, they distort the individual CCs, meaning that the input signals of the PIM nonlinearity are already distorted. As a result, this nonlinear distortion occurring before the PIM and caused by the PAs must be taken into account, in particular at the higher end of the TX powers, when maximum cancellation performance is pursued.
- Modeling the PIM with a cascaded model, where the memory is decoupled from the nonlinear basis functions, achieves excellent cancellation performance despite being very light in terms of the required computations during the cancellation phase. It is therefore a promising candidate for solving the problem of PIM-induced self-interference in mobile radio devices.
- Reliable parameter estimation and cancellation can be achieved, even if there is some time-offset between the cancellation path and the RX path, assuming that the canceller is equipped with both pre-cursor and post-cursor memory taps.
- The proposed solutions where shown to be reasonable robust also against the presence of an actual received signal of interest during the parameter estimation.
- Overall, the PIM distortion can be reliably modeled

and cancelled at transceiver digital front-end, despite the complicated nature of the involved system with cascaded nonlinearities and by-default unknown behavior of the involved RF components and antenna interface. This builds on the efficient problem formulation and the devised parameter learning rules.

Finally, it is noted that the residual distortion above the noise floor, visible in the measurement results at the highest transmit powers, is most likely due to the potential model mismatch and the residual inaccuracies in the estimated canceller coefficients.

F. Potential Extensions

While the canceller derivations and presentation in this article focus on the two-CC carrier aggregation scenario, evolving mobile network specifications allow also transmitting simultaneously with three or even more CCs. Additionally, with some frequency band combinations, also even-order IMD can create nonlinear self-interference at the own RX band [4]. These are both important extensions items, addressed at very preliminary level below, while more rigorous treatments will form important topics for our future work.

First, regarding second-order and fourth-order intermodulation, it is relatively straight-forward to derive the nonlinear basis functions for IMD2 ($p = 2$) and IMD4 ($p = 4$) through the general expression in (2). For $p = 2$, these are $x_1[n]x_2^*[n]$ and $x_1[n]x_2[n]$ at frequencies of $\omega_1 - \omega_2$ and $\omega_1 + \omega_2$, respectively. For $p = 4$, in turn, and if considering example intermodulation frequencies of $3\omega_1 - \omega_2$ and $2\omega_1 - 2\omega_2$, these are of the form $x_1^3[n]x_2^*[n]$ and $x_1^2[n](x_2^*[n])^2$, respectively. While the above expressions do not consider the nonlinearities of the CC-specific PA units, they can be accounted for similarly as in Sub-sections II.B and II.C.

Then, in case with 3 CCs, the pairwise IMD modeling can be carried out as presented earlier in the paper. However, in some cases it can also happen that the intermodulation between all 3 CCs, for example, the frequency $\omega_1 + \omega_2 - \omega_3$ coincides with one of the RX bands. In such cases, the basis functions describing the intermodulation products can be derived as shown in [21], yielding $x_1[n]x_2[n]x_3^*[n]$ for the above noted example frequency. Again, combining the impacts of the involved PA units and their nonlinearities can be done similar to what was shown in Sub-sections II.B and II.C.

V. Conclusions and Summary

In this article, we proposed novel solutions for modeling and digital suppression of the intermodulation distortion at own RX band, produced by the passive components, in carrier aggregation FDD transceivers. If not dealt with, such passive intermodulation can significantly degrade the sensitivity of the receiver when operating on certain LTE/NR band combinations. Three alternative PIM models and the corresponding digital self-interference cancellers were proposed, trading off between the processing complexity and modeling accuracy. The two more evolved models take into account also the component carrier level PA nonlinearities, in addition to the actual PIM, while incorporating also memory effects. To the best of our knowledge, these are the most accurate behavioral signal models for passive intermodulation–induced self-interference in the literature. Additionally, novel gradient-descent based parameter learning rules were derived for the different cancellers.

The proposed methods were evaluated with data measured using an actual carrier aggregation based transceiver system operating on Bands 1 and 3, employing commercial LTE-Advanced UE RF components. The obtained results show that the more advanced cancellers can suppress the self-interference by over 20 dB, canceling it close to the system noise floor, despite being computationally very efficient. Furthermore, the reported results suggest that obtaining such high cancellation performance requires also the modeling of the power amplifier–induced nonlinearities. It was also shown that reliable parameter estimation can be achieved even under TX-RX timings offsets, assuming that the canceller memory parameterization is done properly, as well as under the presence of actual received signal-of-interest up to reasonable power levels. Altogether, the proposed self-interference cancellation solutions can greatly relax the linearity requirements of passive front-end RF components, while also increasing the flexibility of RF spectrum utilization in existing LTE-based and emerging 5G NR radio networks.

Appendix A
Calculating the Complex Partial Derivative of the Decoupled Learning Rule

The partial derivative of $J(\mathbf{g}_n, \mathbf{h}_n)$ can firstly be calculated as follows:

$$\begin{aligned}\frac{\partial J(\mathbf{g}_n,\mathbf{h}_n)}{\partial \mathbf{g}_n} =& \frac{\partial \left|y_{\rm c}(n)\right|^2}{\partial \mathbf{g}_n} = \frac{\partial y_{\rm c}(n) y_{\rm c}^*(n)}{\partial \mathbf{g}_n} \\ =& y_{\rm c}^*(n)\frac{\partial y_{\rm c}(n)}{\partial \mathbf{g}_n} + y_{\rm c}(n)\frac{\partial y_{\rm c}^*(n)}{\partial \mathbf{g}_n} \\ =& -y_{\rm c}^*(n)\frac{\partial y_{\rm PIM}(n)}{\partial \mathbf{g}_n} - y_{\rm c}(n)\frac{\partial y_{\rm PIM}^*(n)}{\partial \mathbf{g}_n} \\ =& -y_{\rm c}^*(n)\left(\frac{\partial y_{\rm PIM}(n)}{\partial \mathbf{g}_{R,n}} + j\frac{\partial y_{\rm PIM}(n)}{\partial \mathbf{g}_{I,n}}\right) \\ & - y_{\rm c}(n)\left(\frac{\partial y_{\rm PIM}^*(n)}{\partial \mathbf{g}_{R,n}} + j\frac{\partial y_{\rm PIM}^*(n)}{\partial \mathbf{g}_{I,n}}\right) \\ =& -y_{\rm c}^*(n)\left(\frac{\partial y_{\rm PIM}(n)}{\partial \mathbf{g}_{R,n}} + j\frac{\partial y_{\rm PIM}(n)}{\partial \mathbf{g}_{I,n}}\right) \\ & - y_{\rm c}(n)\left(\left(\frac{\partial y_{\rm PIM}(n)}{\partial \mathbf{g}_{R,n}}\right)^* + j\left(\frac{\partial y_{\rm PIM}(n)}{\partial \mathbf{g}_{I,n}}\right)^*\right),\end{aligned} \tag{38}$$

where $\mathbf{g}_n = \mathbf{g}_{R,n} + j\mathbf{g}_{I,n}$.

Recalling that $y_{\rm PIM}(n) = \mathbf{h}_n^H \mathbf{y}_{n,\rm NL}$, the partial derivative of $y_{\rm PIM}(n)$ with respect to $\mathbf{g}_{R,n}$ can then be calculated as

$$\begin{aligned}\frac{\partial y_{\rm PIM}(n)}{\partial \mathbf{g}_{R,n}} =& \frac{\partial \mathbf{h}_n^H \mathbf{y}_{n,\rm NL}}{\partial \mathbf{g}_{R,n}} = \frac{\partial \mathbf{y}_{n,\rm NL}}{\partial \mathbf{g}_{R,n}}\mathbf{h}_n^* \\ =& \left[\frac{\partial y_{\rm NL}(n+M_1)}{\partial \mathbf{g}_{R,n}} \quad \cdots \quad \frac{\partial y_{\rm NL}(n-M_2)}{\partial \mathbf{g}_{R,n}}\right]\mathbf{h}_n^*.\end{aligned} \tag{39}$$

A column of $\frac{\partial \mathbf{y}_{n,\rm NL}}{\partial \mathbf{g}_{R,n}}$ can easily be obtained as follows:

$$\frac{\partial y_{\rm NL}(n)}{\partial \mathbf{g}_{R,n}} = \frac{\partial \mathbf{g}_n^H \boldsymbol{\phi}(n)}{\partial \mathbf{g}_{R,n}} = \frac{\partial\left(\mathbf{g}_{R,n}^T - j\mathbf{g}_{I,n}^T\right)\boldsymbol{\phi}(n)}{\partial \mathbf{g}_{R,n}} = \boldsymbol{\phi}(n) \tag{40}$$

Therefore

$$\frac{\partial y_{\mathrm{PIM}}(n)}{\partial \mathbf{g}_{R,n}} = \begin{bmatrix}\boldsymbol{\phi}(n+M_1) & \cdots & \boldsymbol{\phi}(n-M_2)\end{bmatrix}\mathbf{h}_n^* = \boldsymbol{\Phi}_n\mathbf{h}_n^*, \tag{41}$$

where $\boldsymbol{\Phi}_n = \begin{bmatrix}\boldsymbol{\phi}(n+M_1) & \cdots & \boldsymbol{\phi}(n-M_2)\end{bmatrix}$.

Following a largely similar procedure, the partial derivative of $y_{\mathrm{PIM}}(n)$ with respect to $\mathbf{g}_{I,n}$ can be calculated as

$$\begin{aligned}\frac{\partial y_{\mathrm{PIM}}(n)}{\partial \mathbf{g}_{I,n}} =& \frac{\partial \mathbf{h}_n^H \mathbf{y}_{n,\mathrm{NL}}}{\partial \mathbf{g}_{I,n}} = \frac{\partial \mathbf{y}_{n,\mathrm{NL}}}{\partial \mathbf{g}_{I,n}}\mathbf{h}_n^* \\ =& \begin{bmatrix}\frac{\partial y_{\mathrm{NL}}(n+M_1)}{\partial \mathbf{g}_{I,n}} & \cdots & \frac{\partial y_{\mathrm{NL}}(n-M_2)}{\partial \mathbf{g}_{I,n}}\end{bmatrix}\mathbf{w}_n^*,\end{aligned} \tag{42}$$

where a column of $\frac{\partial \mathbf{y}_{n,\mathrm{NL}}}{\partial \mathbf{g}_{I,n}}$ can now be calculated as

$$\frac{\partial y_{\mathrm{NL}}(n)}{\partial \mathbf{g}_{I,n}} = \frac{\partial \mathbf{g}_n^H \boldsymbol{\phi}(n)}{\partial \mathbf{g}_{I,n}} = \frac{\partial\left(\mathbf{g}_{R,n}^T - j\mathbf{g}_{I,n}^T\right)\boldsymbol{\phi}(n)}{\partial \mathbf{g}_{I,n}} = -j\boldsymbol{\phi}(n). \tag{43}$$

As a result, we can write

$$\begin{aligned}\frac{\partial y_{\mathrm{PIM}}(n)}{\partial \mathbf{g}_{I,n}} =& \begin{bmatrix}-j\boldsymbol{\phi}(n+M_1) & \cdots & -j\boldsymbol{\phi}(n-M_2)\end{bmatrix}\mathbf{h}_n^* \\ =& -j\boldsymbol{\Phi}_n\mathbf{h}_n^*.\end{aligned} \tag{44}$$

Substituting the hereby obtained expressions into (38), we get

$$\begin{aligned}\frac{\partial J(\mathbf{g}_n,\mathbf{h}_n)}{\partial \mathbf{g}_n} =& -y_{\mathrm{c}}^*(n)\left(\frac{\partial y_{\mathrm{PIM}}(n)}{\partial \mathbf{g}_{R,n}} + j\frac{\partial y_{\mathrm{PIM}}(n)}{\partial \mathbf{g}_{I,n}}\right) \\ & - y_{\mathrm{c}}(n)\left(\left(\frac{\partial y_{\mathrm{PIM}}(n)}{\partial \mathbf{g}_{R,n}}\right)^* + j\left(\frac{\partial y_{\mathrm{PIM}}(n)}{\partial \mathbf{g}_{I,n}}\right)^*\right) \\ =& -y_{\mathrm{c}}^*(n)\left(\boldsymbol{\Phi}_n\mathbf{h}_n^* - j^2\boldsymbol{\Phi}_n\mathbf{h}_n^*\right) \\ & - y_{\mathrm{c}}(n)\left(\boldsymbol{\Phi}_n^*\mathbf{h}_n + j^2\boldsymbol{\Phi}_n^*\mathbf{h}_n\right) \\ =& -2y_{\mathrm{c}}^*(n)\boldsymbol{\Phi}_n\mathbf{h}_n^*\end{aligned} \tag{45}$$

because $j^2 = -1$.

Appendix B
Calculating the Correlation Matrix of the Orthogonalized Decoupled Learning Rule

We start by rewriting $\mathbf{u}_n$ as follows:

$$\begin{aligned}\mathbf{u}_n =& \boldsymbol{\Phi}_n\mathbf{h}_n^* = \begin{bmatrix}\boldsymbol{\phi}(n+M_1) & \cdots & \boldsymbol{\phi}(n-M_2)\end{bmatrix}\mathbf{h}_n^* \\ =& \begin{bmatrix}\boldsymbol{\phi}_1^T(n)\\ \boldsymbol{\phi}_2^T(n)\\ \vdots \\ \boldsymbol{\phi}_C^T(n)\end{bmatrix}\mathbf{h}_n^* = \begin{bmatrix}\boldsymbol{\phi}_1^T(n)\mathbf{h}_n^*\\ \boldsymbol{\phi}_2^T(n)\mathbf{h}_n^*\\ \vdots \\ \boldsymbol{\phi}_C^T(n)\mathbf{h}_n^*\end{bmatrix} = \begin{bmatrix}\mathbf{h}_n^H\boldsymbol{\phi}_1(n)\\ \mathbf{h}_n^H\boldsymbol{\phi}_2(n)\\ \vdots \\ \mathbf{h}_n^H\boldsymbol{\phi}_C(n)\end{bmatrix},\end{aligned} \tag{46}$$

where $\boldsymbol{\phi}_i(n) = \begin{bmatrix}\phi_i(n+M_1) & \cdots & \phi_i(n-M_2)\end{bmatrix}^T$ and $\phi_i(n)$ is the ith PIM basis function. In other words, instead of collecting the different instantaneous basis functions into a single vector $\boldsymbol{\phi}(n-k)$, we now collect the delayed copies of an individual basis function into a single vector $\boldsymbol{\phi}_i(n)$.

With this, the correlation matrix becomes

$$\begin{aligned}\mathbf{R} =& \mathrm{E}\left[\mathbf{u}_n\mathbf{u}_n^H\right] \\ =& \mathrm{E}\left[\begin{bmatrix}\mathbf{h}_n^H\boldsymbol{\phi}_1(n)\\ \vdots \\ \mathbf{h}_n^H\boldsymbol{\phi}_C(n)\end{bmatrix}\begin{bmatrix}\boldsymbol{\phi}_1^H(n)\mathbf{h}_n & \cdots & \boldsymbol{\phi}_C^H(n)\mathbf{h}_n\end{bmatrix}\right]\end{aligned} \tag{47}$$

Therefore, the element on the ith row and jth column is

$$\begin{aligned}\{\mathbf{R}\}_{ij} =& \mathrm{E}\left[\mathbf{h}_n^H\boldsymbol{\phi}_i(n)\boldsymbol{\phi}_j^H(n)\mathbf{h}_n\right] \\ =& \mathbf{h}_n^H\,\mathrm{E}\left[\boldsymbol{\phi}_i(n)\boldsymbol{\phi}_j^H(n)\right]\mathbf{h}_n,\end{aligned} \tag{48}$$

where the last equality stems from the fact that the analysis is performed for a given memory model. Inspecting then the remaining expected value, it can be rewritten as

$$\begin{aligned}&\mathrm{E}\left[\boldsymbol{\phi}_i(n)\boldsymbol{\phi}_j^H(n)\right] \\ =& \mathrm{E}\left[\begin{bmatrix}\phi_i(n+M_1)\\ \vdots \\ \phi_i(n-M_2)\end{bmatrix}\begin{bmatrix}\phi_j^*(n+M_1) & \cdots & \phi_j^*(n-M_2)\end{bmatrix}\right] \\ =& \mathrm{E}\left[\phi_i(n)\phi_j^*(n)\right]\mathbf{I}_M,\end{aligned} \tag{49}$$

where $M = M_1 + M_2 + 1$ and $\mathbf{I}_M$ is an $M \times M$ identity matrix. The last expression is based on the assumption of i.i.d. stationary transmit signals.

Substituting then (49) into (48), we get the following form for the element on the ith row and jth column:

$$\begin{aligned}\{\mathbf{R}\}_{ij} =& \mathbf{h}_n^H\,\mathrm{E}\left[\phi_i(n)\phi_j^*(n)\right]\mathbf{I}_M\mathbf{h}_n \\ =& \mathrm{E}\left[\phi_i(n)\phi_j^*(n)\right]\mathbf{h}_n^H\mathbf{I}_M\mathbf{h}_n = \mathrm{E}\left[\phi_i(n)\phi_j^*(n)\right]\mathbf{h}_n^H\mathbf{h}_n\end{aligned} \tag{50}$$

From this, it is easy to see that the correlation matrix can be written as follows:

$$\begin{aligned}\mathbf{R} =& \mathrm{E}\left[\begin{bmatrix}\phi_1(n)\\ \vdots \\ \phi_C(n)\end{bmatrix}\begin{bmatrix}\phi_1^*(n) & \vdots & \phi_C^*(n)\end{bmatrix}\right]\mathbf{h}_n^H\mathbf{h}_n \\ =& \mathrm{E}\left[\boldsymbol{\phi}(n)\boldsymbol{\phi}^H(n)\right]\mathbf{h}_n^H\mathbf{h}_n = \mathbf{R}_{\boldsymbol{\phi}}\mathbf{h}_n^H\mathbf{h}_n,\end{aligned} \tag{51}$$

where $\mathbf{R}_{\boldsymbol{\phi}}$ is the correlation matrix of the basis functions.

References

[1] E. Dahlman, S. Parkvall, and J. Skold, *5G NR: The Next Generation Wireless Access Technology*, 1st ed. Elsevier Science, 2018.

[2] 3GPP Tech. Spec. 36.300, "E-UTRA and E-UTRAN; Overall description, stage 2," v10.0.0 (Release 10), June 2010.

[3] 3GPP Tech. Spec. 38.300, "5G NR; Overall description, stage 2," v15.0.0 (Release 15), Jan. 2018.

[4] 3GPP Tech. Spec. 38.101-3, "5G NR; UE Radio Transmission and Reception; part 3," v16.0.0 (Release 16), July 2019.

[5] S. A. Bassam, W. Chen, M. Helaoui, and F. M. Ghannouchi, "Transmitter architecture for CA: Carrier aggregation in LTE-Advanced systems," *IEEE Microw. Mag.*, vol. 14, no. 5, pp. 78–86, July 2013.

[6] J. Lee *et al.*, "A sub-6-GHz 5G New Radio RF transceiver supporting EN-DC with 3.15-Gb/s DL and 1.27-Gb/s UL in 14-nm FinFET CMOS," *IEEE J. Solid-State Circ.*, vol. 54, no. 12, pp. 3541–3552, Dec. 2019.

[7] T. Wu *et al.*, "A 40nm 4-downlink and 2-uplink RF transceiver supporting LTE-Advanced carrier aggregation," in *Proc. 2018 IEEE Radio Frequency Integrated Circuits Symp. (RFIC)*, June 2018, pp. 316–319.

[8] C. S. Park, L. Sundström, A. Wallen, and A. Khayallah, "Carrier aggregation for LTE-Advanced: Design challenges of terminals," *IEEE Commun. Mag.*, vol. 51, no. 12, pp. 76–84, Dec. 2013.

[9] A. Kiayani, V. Lehtinen, L. Anttila, T. Lähteensuo, and M. Valkama, "Linearity challenges of LTE-Advanced mobile transmitters: Requirements and potential solutions," *IEEE Commun. Mag.*, vol. 55, no. 6, pp. 170–179, Jun. 2017.

[10] "R4-121984, RF architecture alternatives for inter band CA class A2," Motorola Mobility, Jeju, South Korea, Mar. 2012.

[11] Q. Jin, J. Gao, G. T. Flowers, Y. Wu, and G. Xie, "Modeling of passive intermodulation with electrical contacts in coaxial connectors," *IEEE Trans. Microw. Theory Techn.*, vol. 66, no. 9, pp. 4007–4016, Sep. 2018.

[12] J. R. Wilkerson, I. M. Kilgore, K. G. Gard, and M. B. Steer, "Passive intermodulation distortion in antennas," *IEEE Trans. Antennas Propag.*, vol. 63, no. 2, pp. 474–482, Feb. 2015.
[13] P. L. Lui, "Passive intermodulation interference in communication systems," *Electronics & Communication Eng. J.*, vol. 2, no. 3, pp. 109–118, June 1990.
[14] A. Shitvov, A. G. Schuchinsky, M. B. Steer, and J. M. Wetherington, "Characterisation of nonlinear distortion and intermodulation in passive devices and antennas," in *The 8th European Conf. Antennas Propag. (EuCAP 2014)*, April 2014, pp. 1454–1458.
[15] J. J. Henrie, A. J. Christianson, and W. J. Chappell, "Linear–nonlinear interaction and passive intermodulation distortion," *IEEE Trans. Microw. Theory Techn.*, vol. 58, no. 5, pp. 1230–1237, May 2010.
[16] "R4-111321, On Passive Intermodulation (PIM) for MSR-NC," Ericsson, Taipei, Taiwan, Feb. 2011.
[17] J. Henrie, A. Christianson, and W. J. Chappell, "Cancellation of passive intermodulation distortion in microwave networks," in *Proc. 2008 38th Eur. Microw. Conf.*, Oct 2008, pp. 1153–1156.
[18] G. Macchiarella, G. B. Stracca, and L. MiglioIi, "Experimental study of passive intermodulation in coaxial cavities for cellular base stations duplexers," in *Proc. 34th Eur. Microw. Conf., 2004.*, vol. 2, Oct. 2004, pp. 981–984.
[19] M. Omer, R. Rimini, P. Heidmann, and J. S. Kenney, "A compensation scheme to allow full duplex operation in the presence of highly nonlinear microwave components for 4G systems," in *2011 IEEE MTT-S Int. Microw. Symp. Digest (IMS)*, June 2011, pp. 1–4.
[20] A. Kiayani, M. Abdelaziz, L. Anttila, V. Lehtinen, and M. Valkama, "Digital mitigation of transmitter-induced receiver desensitization in carrier aggregation FDD transceivers," *IEEE Trans. Microw. Theory Techn.*, vol. 63, no. 11, pp. 3608–3623, Dec. 2015.
[21] C. Yu, W. Cao, Y. Guo, and A. Zhu, "Digital compensation for transmitter leakage in non-contiguous carrier aggregation applications with FPGA implementation," *IEEE Trans. Microw. Theory Techn.*, vol. 63, no. 12, pp. 4306–4318, Dec. 2015.
[22] 3GPP Tech. Rep. 36.850, "Inter-band carrier aggregation," v11.1.0 (Release 11), July 2013.
[23] 3GPP Tech. Spec. 36.101, "E-UTRA; user equipment (UE) radio transmission and reception," v16.0.0 (Release 16), Jan. 2019.
[24] "R4-121131, Harmonics and IMD analysis for inter-band CA band 3 and band 8," KT, Jeju, South Korea, Mar. 2012.
[25] 3GPP Tech. Rep. 37.808, "Passive intermodulation (PIM) handling for base stations (BS)," v12.0.0 (Release 12), Sept. 2013.
[26] 3GPP Tech. Rep. 37.864-41-21, "Dual connectivity (DC) band combinations of LTE xDL/1UL (x=1,2,3,4) + inter-band NR 2DL/1UL," v15.0.0 (Release 15), June 2018.
[27] F. Kearney and S. Chen, "Passive Intermodulation (PIM) Effects in Base Stations: Understanding the Challenges and Solutions," Analog Devices, March 2017.
[28] "R4-121219, Way forward for interband Class A2," Nokia Corporation, AT&T, Jeju, South Korea, Mar. 2012.
[29] 3GPP Tech. Spec. 38.101-1, "5G NR; UE Radio Transmission and Reception; part 1," v16.0.0 (Release 16), July 2019.
[30] K. E. Kolodziej, B. T. Perry, and J. S. Herd, "In-band full-duplex technology: Techniques and systems survey," *IEEE Trans. Microw. Theory Techn.*, vol. 67, no. 7, pp. 3025–3041, July 2019.
[31] A. Kiayani, L. Anttila, and M. Valkama, "Digital suppression of power amplifier spurious emissions at receiver band in FDD transceivers," *IEEE Signal Process. Lett.*, vol. 21, no. 1, pp. 69–73, Jan. 2014.
[32] H. T. Dabag, H. Gheidi, P. Gudem, and P. M. Asbeck, "All-digital cancellation technique to mitigate self-jamming in uplink carrier aggregation in cellular handsets," in *2013 IEEE MTT-S Int. Microw. Symp. Digest (IMS)*, June 2013, pp. 1–3.
[33] H. T. Dabag, H. Gheidi, S. Farsi, P. S. Gudem, and P. M. Asbeck, "All-digital cancellation technique to mitigate receiver desensitization in uplink carrier aggregation in cellular handsets," *IEEE Trans. Microw. Theory Techn.*, vol. 61, no. 12, pp. 4754–4765, Dec. 2013.
[34] H. Gheidi, H. T. Dabag, Y. Liu, P. M. Asbeck, and P. Gudem, "Digital cancellation technique to mitigate receiver desensitization in cellular handsets operating in carrier aggregation mode with multiple uplinks and multiple downlinks," in *Proc. 2015 IEEE Radio Wireless Symp. (RWS)*, Jan 2015, pp. 221–224.
[35] M. Z. Waheed, D. Korpi, A. Kiayani, L. Anttila, and M. Valkama, "Digital cancellation of passive intermodulation: Method, complexity and measurements," in *Proc. IEEE MTT-S Int. Microw. Conf. 5G Hardware Syst. (IMC-5G)*, Aug. 2019.
[36] Y. Liu, C. Li, X. Quan, P. Roblin, M. Rawat, N. Naraharisetti, Y. Tang, and K. Kang, "Multiband linearization technique for broadband signal with multiple closely spaced bands," *IEEE Trans. Microw. Theory Techn.*, vol. 67, no. 3, pp. 1115–1129, March 2019.
[37] M. Abdelaziz, L. Anttila, A. Kiayani, and M. Valkama, "Decorrelation-based concurrent digital predistortion with a single feedback path," *IEEE Trans. Microw. Theory Techn.*, vol. 66, no. 1, pp. 280–293, Jan. 2018.
[38] A. Abdelhafiz, A. Kwan, M. Younes, O. Hammi, N. Boulejfen, and F. M. Ghannouchi, "Augmented dual-band digital predistorter for reducing cross-band intermodulation distortion using predictive injection technique," *IEEE Trans. Microw. Theory Techn.*, vol. 64, no. 11, pp. 3518–3527, Nov. 2016.
[39] M. Z. Waheed, D. Korpi, A. Kiayani, L. Anttila, and M. Valkama, "Digital self-interference cancellation in inter-band carrier aggregation transceivers: Algorithm and digital implementation perspectives," in *Proc. 2017 IEEE Int. Workshop Signal Process. Syst. (SiPS)*, Oct. 2017, pp. 1–5.
[40] S. Haykin, *Adaptive Filter Theory*, 4th ed. Prentice Hall, 2002.
[41] C. Mayer, D. McLaurin, J. Fan, S. Bal, C. Angell, O. Gysel, M. McCormick, M. Manglani, R. Schubert, B. Reggiannini, J. Kornblum, L. Wu, L. Leonard, S. Bhal, A. Kagan, and T. Montalvo, "A direct-conversion transmitter for small-cell cellular base stations with integrated digital predistortion in 65nm CMOS," in *2016 IEEE Radio Frequency Integrated Circuits Symposium (RFIC)*, May 2016, pp. 63–66.
[42] V. N. Manyam, D.-K. G. Pham, C. Jabbour, and P. Desgreys, "A low-power high-performance digital predistorter for wideband power amplifiers," *Analog Integr. Circuits Signal Process.*, vol. 97, no. 3, p. 483–492, Dec. 2018.
[43] A. Kiayani, L. Anttila, M. Kosunen, K. Stadius, J. Ryynänen, and M. Valkama, "Modeling and joint mitigation of TX and RX nonlinearity-induced receiver desensitization," *IEEE Trans. Microw. Theory Techn.*, vol. 65, no. 7, pp. 2427–2442, July 2017.

Muhammad Zeeshan Waheed received the M.Sc. degree (Hons.) in electrical engineering from the Tampere University of Technology, Tampere, Finland, in 2017. He is currently a System-on-a-Chip Engineer with Nokia Mobile Networks, Tampere, while is also pursuing the D.Sc. degree with the newly established Tampere University, Finland. His current research interests include signal processing for flexible radio systems.

Dani Korpi received the M.Sc. and D.Sc. degrees (Hons.) in communications engineering and electrical engineering from Tampere University of Technology, Finland, in 2014 and 2017, respectively. Currently, he is a Senior Specialist with Nokia Bell Labs in Espoo, Finland. His doctoral thesis received an award for the best dissertation of the year in Tampere University of Technology, as well as the Finnish Technical Sector's Award for the best doctoral dissertation of 2017. His research interests include inband full-duplex radios, machine learning for wireless communications, and beyond 5G radio systems.

Lauri Anttila received the M.Sc. degree in 2004 and the D.Sc. degree (with distinction) in 2011 from Tampere University of Technology (TUT), Finland, both in electrical engineering. Since 2016, he has been a University Researcher at the Department of Electrical Engineering, Tampere University (formerly TUT). In 2016-2017, he was a Visiting Research Fellow at the Department of Electronics and Nanoengineering, Aalto University, Finland. His research interests are in radio communications and signal processing, with a focus on the radio implementation challenges in systems such as 5G, full-duplex radio, and large-scale antenna systems.

Adnan Kiayani received the M.Sc. (with honors) and D.Sc. degrees in electrical engineering from Tampere University of Technology, Finland, in 2009 and 2015, respectively. He is currently a Radio System Designer with Ericsson AB, Sweden. His research interests include behavioral modeling of RF systems and signal processing algorithms for flexible radio transceivers.

Marko Kosunen received his M.Sc, L.Sc and D.Sc (with honors) degrees from Helsinki University of Technology, Espoo, Finland, in 1998, 2001 and 2006, respectively. He is currently a Senior Researcher at Aalto University, Department of Electronics and Nanoengineering. Academic years 2017-2019 he visited Berkeley Wireless Reserarch Center, UC Berkeley, on Marie Sklodowska-Curie grant from European Union. His current research interests include programmatic circuit design methodologies, digital intensive and time-based transceiver circuits, and medical sensor electronics.

Kari Stadius received the M.Sc., Lic. Tech., and Doctor of Science degrees in electrical engineering from the Helsinki University of Technology, Helsinki, Finland, in 1994, 1997, and 2010, respectively. He is currently working as a staff scientist at the Department of Micro- and Nanosciences, Aalto University School of Electrical Engineering. His research interests include RF and microwave circuits for communications with especial emphasis on frequency synthesis, analog and mixed-mode circuit design.

Pablo Pascual Campo received his B.Sc. and M.Sc. degrees in Telecommunications and Electrical Engineering in 2012 and 2014, respectively, from Universidad Politécnica de Madrid, Madrid, Spain. He is currently pursuing his D.Sc. degree at Tampere University, Department of Electrical Engineering, Tampere, Finland. His research interests include digital predistortion, full-duplex systems and applications, and signal processing for wireless communications at the mmWave bands.

Matias Turunen is currently pursuing the M.Sc. degree in electrical engineering at Tampere University (TAU), Tampere, Finland, while also working as a Research Assistant with the Department of Electrical Engineering at TAU. His current research interests include in-band full-duplex radios with an emphasis on analog RF cancellation, OFDM radar, and 5G New Radio systems.

Markus Allén received the B.Sc., M.Sc. and D.Sc. degrees in communications engineering from Tampere University of Technology, Finland, in 2008, 2010 and 2015, respectively. He is currently with the Department of Electrical Engineering at Tampere University, Finland, as a University Instructor. His current research interests include software-defined radios, 5G-related RF measurements and digital signal processing for radio transceiver linearization.

Jussi Ryynänen received the M.Sc. and D.Sc. degrees in electrical engineering from the Helsinki University of Technology, Espoo, Finland, in 1998 and 2004, respectively. He is a full professor and the Head of the Department of Electronics and Nanoengineering, Aalto University, Espoo, Finland. His research interests are integrated transceiver circuits for wireless applications. Prof. Ryynänen has served as a TPC Member for the European Solid-State Circuits Conference (ESSCIRC) and the IEEE International Solid-State Circuits Conference (ISSCC), and as a Guest Editor for the IEEE Journal of Solid-State Circuits.

Mikko Valkama received the M.Sc. (Tech.) and D.Sc. (Tech.) Degrees (both with honors) in electrical engineering (EE) from Tampere University of Technology (TUT), Finland, in 2000 and 2001, respectively. In 2003, he was a visiting post-doc research fellow with SDSU, San Diego, CA. Currently, he is a Full Professor and Department Head of Electrical Engineering at the newly formed Tampere University (TAU), Finland. His research interests include radio communications, radio localization, and radio-based sensing, with particular emphasis on 5G and beyond mobile radio networks.

PUBLICATION V

Modeling and Digital Suppression of Passive Nonlinear Distortion in Simultaneous Transmit–Receive Systems

M. Z. Waheed, V. Lampu, A. Kiayani, M. Fleischer, L. Anttila and M. Valkama

2022 56th Asilomar Conference on Signals, Systems, and Computers (2022)
DOI: 10.1109/IEEECONF56349.2022.10051880

Modeling and Digital Suppression of Passive Nonlinear Distortion in Simultaneous Transmit–Receive Systems

Muhammad Zeeshan Waheed*†, Vesa Lampu†, Adnan Kiayani†, Marko Fleischer‡, Lauri Anttila†, and Mikko Valkama†

*Nokia Mobile Networks, Tampere, Finland
†Department of Electrical Engineering, Tampere University, Finland
‡Nokia Mobile Networks, Ulm, Germany
E-mail: muhammad.waheed@nokia.com

***Abstract*—In frequency division duplexing (FDD) based simultaneous transmit-receive systems, nonlinear behavior of the active and passive RF components can cause nonlinear distortion products falling at the receiver band. Such distortion may also arise over-the-air, if there are for example metallic objects in close vicinity of the antenna system. In this work, we focus on the modeling and digital cancellation of such distortion products, especially in case of passive harmonic distortion of the transmit waveform landing at the receiver band. We provide behavioral modeling of the problem, while also use the models to derive corresponding digital distortion cancellers. Practical RF measurement based numerical results are provided, focusing on a timely dual-band cellular transceiver scenario covering 5G NR bands n3 (1.8 GHz) and n78 (3.5 GHz). The RF measurement results demonstrate accurate modeling and distortion cancellation in the considered example cases.**

***Index Terms*—5G, carrier aggregation, duplexing, interference cancellation, nonlinear systems, passive intermodulation, passive harmonic distortion, simultaneous transmission and reception.**

I. Introduction

To support higher peak data rates and improved cell coverage, carrier aggregation (CA) technique was introduced in long term evolution (LTE)-Advanced Release 10, and is also included in 5G new radio (NR) standard. CA allows addition of multiple frequency chunks, called component carriers (CCs), within or across frequency bands, thereby enabling an efficient use of licensed spectrum [1].

In frequency-division duplexing (FDD) networks where transmitter (TX) and receiver (RX) operate simultaneously but at different frequencies, the inter-modulation distortion (IMD) from nonlinear components along the transmit signal path is critical [2]–[4]. The spurious IMD products due to mixing of signals in a passive nonlinear components is referred to as passive inter modulation (PIM), and has also been recognized as a major concern for FDD radios. The presence of PIM in the uplink band results in the elevated receiver noise floor, leading to throughput degradation and impaired end-user experience. The physical mechanism causing PIM can be diverse, for example various passive components in a radio unit such as connectors, combiner, filter, cable assembly, as well as rusty metallic objects in the close vicinity of the antenna can all contribute to PIM generation. The PIM due to rusty metallic objects in antenna near field is referred to as "rusty-bolt" effect, where it can also affect neighboring cells operating on the same site [5].

In practice, PIM can be avoided through proper frequency planning, however, such planning becomes impractical with the growing number of configured bands in a same radio or on a co-located site with FDD and TDD radios. The self-interference issue in FDD transceivers has been acknowledged and reported in several 3GPP CA related documents, such as [6] [7], which have also proposed some alternatives to mitigate its impact. These include, for example, to apply the maximum power reduction (MPR) – to reduce the strength of the interference – or the maximum sensitivity degradation (MSD) – to enhance the receiver sensitivity. However, the adoption of such approaches lead to reduction in cell coverage and throughput loss. Advanced digital cancellation techniques have recently been proposed that exploit the fact that the interference can be regenerated in the receiver digital front-end and removed by subtracting the model output from the actual received signal [8]–[10].

In this paper, we expand our previous work in [11] and [12] on digital self-interference cancellation, but now focus on passive harmonic (PHM) distortion that couples over the air. Furthermore, the proposed framework for digital cancellation now assumes a multiple-input-multiple-output (MIMO) FDD radio setup. The proposed digital cancellation method is tested and verified through practical RF measurements assuming co-existing 5G NR band N3 FDD and band N78 TDD operation, where the second-order passive harmonic distortion of band N3 lands within the receiver band of the band N78, as shown in Fig. 1. The rest of the paper is organized as follows. In Section II, we address baseband equivalent model of PHM distortion generated at RX band by external sources in the antenna near field and the relevant digital cancellation methods and parameter estimation procedures. In section III, the performance of the proposed digital cancellation method is evaluated with practical radio frequency (RF) measurements. Finally, Section IV concludes the paper.

978-1-5386-0446-5/17/$31.00 ©2021 IEEE

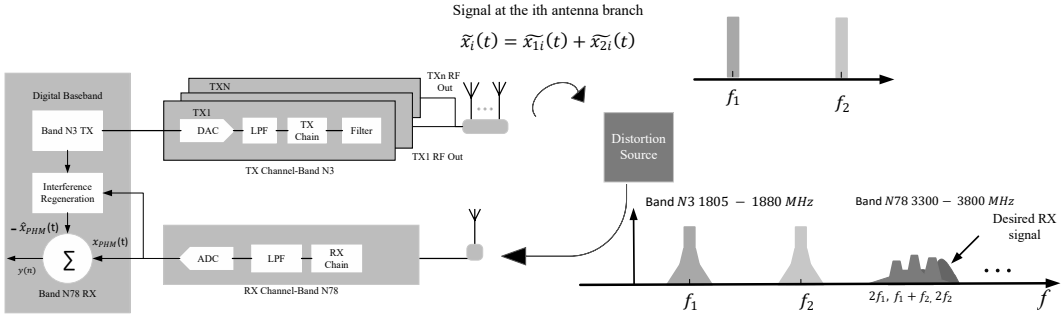

Fig. 1. Simplified block diagram of the considered setup showing modeling-related notations and spectral illustration of the second-order passive harmonic distortion that is created by passive metallic objects in the antenna near field, appearing in one of the configured RX bands.

II. Passive Harmonic Distortion: Modeling and Proposed Digital Cancellation Methods

We begin by formulating the self-interference problem, assuming a MIMO FDD system and air-induced passive harmonic distortion (PHM) that couples into a co-located TDD radio. Building on the proposel signal modeling, we then develop a linear-in-parameters model for digital estimation and cancellation.

A. Self-Interference Model

We consider a generic MIMO-FDD transceiver, as shown in Fig 1, where the transmitter has N transmit antennas and employs carrier aggregation with two CCs. The up-converted I/Q modulated CC signals from $i-$th transmitter are given as

$$\begin{aligned}\tilde{x}_{1i} &= \mathrm{Re}\{\alpha_{1i}x_{1i}e^{j\omega_1 n}\}\\ \tilde{x}_{2i} &= \mathrm{Re}\{\alpha_{2i}x_{2i}e^{j\omega_2 n}\},\end{aligned} \tag{1}$$

where x_{1i} and x_{2i} are the two CCs in the baseband, α_1 and α_2 represent the complex gains, and ω_1 and ω_2 are center-frequency of the corresponding CCs after up-conversion. It is noted that the up-converted I/Q modulated CC signals are continuous-time in an actual system. However, this does not impact the accuracy of the modelling since we consider the center frequencies of the CCs only in order to determine where the resulting nonlinear terms will fall in the frequency domain.

In practice, the components carriers may belong to the same RF band (intra-band CA) or can be aggregated across different bands (inter-band CA). For the latter case, the RF CC signals may be combined after the PA in a diplexer when they have a separate TX/RX line-up or before a *multi-band PA* if the RF spacing between the bands is small. For notational simplicity, we assume in this paper intra-band CA scenario and restrict our focus to only two CCs; nevertheless, the proposed modeling is applicable to inter-band CA as well since the PHM distortion source is assumed to be outside the radio. The aggregated TX signal of the $i-$th antenna branch is then a sum of all CC signals, i.e., $\tilde{x}_i(t) = \tilde{x}_{1i}(t) + \tilde{x}_{2i}(t)$.

The signal from all transmit antenna branches propagate and are incident on a PHM distortion source, which is assumed to be in close proximity of antenna unit. Using a polynomial model, the signal after static PHM nonlinearity is given by

$$\begin{aligned}\tilde{x}_{PHM}(t) &= \sum_{p=1}^{P}\beta_p.(\sum_{i=1}^{N}\tilde{x}_i(t)))^p\\ &= \sum_{p=1}^{P}\beta_p.\{\mathrm{Re}\{(\alpha_{11}x_{11}(t)+\alpha_{12}x_{12}(t)+.....+\alpha_{1N}x_{1N}(t))e^{j\omega_1 n}\}\\ &+ \mathrm{Re}\{(\alpha_{21}x_{21}(t)+\alpha_{22}x_{22}(t)+.....+\alpha_{2N}x_{2N}(t))e^{j\omega_1 n}\}\}^p\\ &= \sum_{p=1}^{P}\beta_p\{\mathrm{Re}\{\psi_1(t)e^{j\omega_1 n}\}+\mathrm{Re}\{\psi_2(t)e^{j\omega_2 n}\}\}^p\end{aligned} \tag{2}$$

where

$$\begin{aligned}\psi_1(t) &= \sum_{i=1}^{N}\alpha_{1,i}x_{1,i}(t)\\ \psi_2(t) &= \sum_{i=1}^{N}\alpha_{2,i}x_{2,i}(t).\end{aligned}$$

Now using the identities of the form

$$\mathrm{Re}\{ue^{jv}\} = 1/2(ue^{jv}+u^*e^{-jv}), \tag{3}$$

and

$$(u+v)^p = \sum_{k=0}^{p}\binom{p}{k}u^k v^{p-k}, \tag{4}$$

we expand the expression in (2) which yields

$$\begin{aligned}\tilde{x}_{PHM}(t) &= \sum_{p=1}^{P}\beta_p\times\\ &\sum_{k=0}^{p}\binom{p}{k}\frac{1}{2^k}\sum_{k_1=0}^{p}\binom{k}{k_1}\psi_1^{k_1}e^{jk_1\omega_1 t}(\psi_1^*)^{k-k_1}e^{j(k-k_1)\omega_1 t}\times\\ &\frac{1}{2^{p-k}}\sum_{k_2=0}^{p-k}\binom{p-k}{k_2}\psi_2^{k_2}e^{jk_2\omega_2 t}(\psi_2^*)^{p-k-k_2}e^{j(k+k_2-p)\omega_2 t}.\end{aligned} \tag{5}$$

TABLE I
INSTANTANEOUS BASIS FUNCTIONS FOR $p = 2$ AND $p = 4$

Value of p	**Basis functions,** $2\omega_1$	**Basis functions,** $2\omega_2$	**Basis functions,** $\omega_1 + \omega_2$
2	$x_{11}^2,\ x_{12}^2, x_{11}x_{12}$	$x_{21}^2,\ x_{22}^2, x_{21}x_{22}$	$x_{11}x_{21},\ x_{11}x_{22},\ x_{12}x_{21},\ x_{12}x_{22}$
4	$x_{11}^2,\ x_{12}^2, x_{11}x_{12},\ x_{11}^3x_{11}^*,\ x_{11}^3x_{12}^*,$ $x_{11}^2x_{12}x_{11}^*,\ x_{11}^2x_{12}x_{12}^*,\ x_{12}^2x_{11}x_{11}^*,$ $x_{12}^2x_{11}x_{12}^*,\ x_{12}^3x_{11}^*,\ x_{12}^3x_{12}^*,$ $x_{11}^2x_{12}x_{11}^*,$ $x_{11}^2x_{12}x_{12}^*,\ x_{11}x_{12}^2x_{11}^*,\ x_{11}x_{12}^2x_{12}^*,$ $x_{11}^2x_{21}x_{21}^*,\ x_{11}^2x_{21}x_{22}^*,\ x_{11}^2x_{22}x_{21}^*,$ $x_{11}^2x_{22}x_{22}^*,$ $x_{12}^2x_{21}x_{21}^*,\ x_{12}^2x_{21}x_{22}^*,\ x_{12}^2x_{22}x_{21}^*,$ $x_{12}^2x_{22}x_{22}^*,\ x_{11}x_{12}x_{21}x_{21}^*,$ $x_{11}x_{12}x_{21}x_{22}^*,\ x_{11}x_{12}x_{22}x_{21}^*,$ $x_{11}x_{12}x_{22}x_{22}^*$	$x_{21}^2,\ x_{22}^2, x_{21}x_{22},\ x_{21}^2x_{11}x_{11}^*,$ $x_{21}^2x_{11}x_{12}^*,\ x_{21}^2x_{12}x_{11}^*,\ x_{21}^2x_{12}x_{12}^*,$ $x_{22}^2x_{11}x_{11}^*,\ x_{22}^2x_{11}x_{12}^*,\ x_{22}^2x_{12}x_{11},$ $x_{22}^2x_{12}x_{12}^*,\ x_{21}x_{22}x_{11}x_{11}^*,$ $x_{21}x_{22}x_{11}x_{12}^*,$ $x_{21}x_{22}x_{12}x_{11}^*,\ x_{21}x_{22}x_{12}x_{12}^*,$ $x_{21}^2x_{21}x_{21}^*,$ $x_{21}^2x_{21}x_{22}^*,\ x_{21}^2x_{22}x_{21}^*,\ x_{21}^2x_{22}x_{22}^*,$ $x_{22}^2x_{21}x_{21}^*,\ x_{22}^2x_{21}x_{22}^*,\ x_{22}^2x_{22}x_{21}^*,$ $x_{22}^2x_{22}x_{22}^*,\ x_{21}x_{22}x_{21}x_{21}^*,$ $x_{21}x_{22}x_{21}x_{22}^*,$ $x_{21}x_{22}x_{22}x_{21}^*,\ x_{21}x_{22}x_{22}x_{22}^*$	$x_{11}x_{21},\ x_{11}x_{22},\ x_{12}x_{21},\ x_{12}x_{22},$ $x_{11}x_{11}^*x_{11}x_{21},\ x_{11}x_{11}^*x_{11}x_{22},$ $x_{11}x_{11}^*x_{12}x_{21},\ x_{11}x_{11}^*x_{11}x_{22},$ $x_{11}x_{12}^*x_{11}x_{21},$ $x_{11}x_{12}^*x_{11}x_{22},\ x_{11}x_{12}^*x_{12}x_{21},\ x_{11}x_{12}^*x_{12}x_{22},$ $x_{12}x_{11}^*x_{11}x_{21},\ x_{12}x_{11}^*x_{11}x_{22},\ x_{12}x_{11}^*x_{12}x_{21},$ $x_{12}x_{11}^*x_{12}x_{22},\ \ x_{12}x_{12}^*x_{11}x_{21},\ x_{12}x_{12}^*x_{11}x_{22},$ $x_{12}x_{12}^*x_{12}x_{21},$ $x_{12}x_{12}^*x_{11}x_{21},\ x_{12}x_{12}^*x_{12}x_{22},\ x_{21}x_{21}^*x_{11}x_{21},$ $x_{21}x_{21}^*x_{11}x_{22},\ x_{21}x_{21}^*x_{12}x_{21},\ x_{21}x_{21}^*x_{12}x_{22},$ $x_{21}x_{21}^*x_{11}x_{21},\ x_{21}x_{22}^*x_{11}x_{22},\ x_{21}x_{22}^*x_{12}x_{21},$ $x_{21}x_{22}^*x_{12}x_{22},$ $x_{22}x_{21}^*x_{11}x_{21},\ x_{22}x_{21}^*x_{11}x_{22},\ x_{22}x_{21}^*x_{12}x_{21},$ $x_{22}x_{22}^*x_{11}x_{21},$ $x_{22}x_{22}^*x_{11}x_{22},\ x_{22}x_{22}^*x_{12}x_{21},\ x_{22}x_{22}^*x_{12}x_{22}$

Resulting from (5), the PHM distortion with the basis functions (BFs) and their center frequencies is then given by

$$\begin{aligned}\tilde{x}_{PHM}(t) = \sum_{p=1}^{P}\sum_{k_1=0}^{p}\sum_{k_2=0}^{p-k}\gamma_{p,k_1,k_2}\times \\ \psi_1^{k_1}(\psi_1^*)^{k-k_1}\psi_2^{k_2}(\psi_2^*)^{p-k-k_2}\times \\ e^{j\left((2k_1-k)\omega_1+(2k_2+k-p)\omega_2\right)t}\end{aligned} \tag{6}$$

where, for notational simplicity, we have lumped all the scaling factors with the unknown complex PIM gain β_p and denote the overall effective coefficient as γ_{p,k_1,k_2}.

In this work, we are only interested in even-order passive harmonic distortion products, namely at frequencies $2\omega_1$, $2\omega_2$ and $\omega_1 + \omega_2$, which are likely to appear at the RX band in LTE-A and 5G FDD-TDD defined band combinations and also typically have high power to cause throughput degradation. The corresponding signals at these frequencies can be obtained by appropriately setting the value for the positive integers k_1 and k_2 in Equation (6). For instance, the signals at $2\omega_1$ can be obtained by imposing the following rules for the positive integers k_1 and k_2 in (6):

$$\begin{aligned} 2k_1 - k = 2 \qquad &\text{and} \quad 2k_2 + k - p = 0 \\ \rightarrow k_1 = \frac{1}{2}k + 1 \qquad &\text{and} \quad k_2 = \frac{1}{2}(p-k), \end{aligned}$$

where we can see that k_1 and k_2 needs to be integers, given that k and p must be even. Similar rules can be imposed for the BFs at $2\omega_2$ by setting

$$\begin{aligned} 2k_1 - k = 0 \qquad &\text{and} \quad 2k_2 + k - p = 2 \\ \rightarrow k_1 = \frac{1}{2}k \qquad &\text{and} \quad k_2 = 1 + \frac{1}{2}(p-k) \end{aligned}$$

and for the corresponding BFs at $\omega_1 + \omega_2$

$$\begin{aligned} 2k_1 - k = 1 \qquad &\text{and} \quad 2k_2 + k - p = 1 \\ \rightarrow k_1 = \frac{1}{2}(k+1) \qquad &\text{and} \quad k_2 = \frac{1}{2}(1+p-k). \end{aligned}$$

Finally, in order for k_1 and k_2 to be integers, the value of k must be adjusted accordingly, while p is always even. The value of k e.g., for the case $\omega_1 + \omega_2$ is set to 1.

For completeness of the modeling, the resulting nonlinear terms for $p = 2$ and $p = 4$ in a dual-band inter-CA scenario for all the three passive harmonic distortion frequencies are shown in Table I, where without loss of generality we drop the time-domain index (t) to shorten the notations.

Finally, the PHM distortion generated in a nonlinear passive source and sensed by a collocated radio is received together with the actual received signal of interest. The digital BB received signal after down-conversion and channel filtering is therefore given by

$$x_{BB}[n] = x_D[n] + \eta_{BB}[n] + x_{PHM}[n] \tag{7}$$

where $x_D[n]$ is the desired received signal and η_{BB} is additive noise.

B. Digital Cancellation and Parameter Estimation

The derived baseband signal models discussed in the previous section serve as the basis for the proposed digital PHM distortion canceller. The canceller specifically creates new PHM distortion samples using the basis functions from Table I, which are then subtracted from the actual received baseband signal.

The general assumption here is that the PHM is a nonlinear function of the transmit data that stems from the same site, and there's a single digital baseband unit with access to all aggressor and victim carriers, thus the PHM distortion can be digitally estimated and canceled in the digital baseband. The variables that serve as the complex weights of the basis function samples, or the equivalent model parameters, as denoted by γ_p in (6) are unknown and must thus be estimated.

Noting that Equation (6) is in fact a linear-in-parameters model, the parameter estimation can be carried out with linear least squares (LS). As a starting point, consider M samples of the observed baseband received signal $x_{BB}[n]$ in equation

(7) which, under observed PHM distortion, can be expressed as

$$\mathbf{x}_{BB} = \mathbf{\Phi}\boldsymbol{\gamma} + \mathbf{z}, \tag{8}$$

where $\mathbf{\Phi}$ is the nonlinear data matrix containing relevant basis functions that are constructed from the original TX data, $\boldsymbol{\gamma}$ denotes unknown coefficients that need to be estimated, and the desired received signal and noise in equation (6) are lumped into a single variable $\mathbf{z}$.

We shortly elaborate the structure of the matrix $\mathbf{\Phi}$ by restricting our focus to the example frequency of $2\omega_1$ and assuming $p = 2$, for which the instantaneous basis functions read as follows:

$$\begin{aligned} \phi_1[n] &= x_{11}^2[n] \\ \phi_2[n] &= x_{12}^2[n] \\ \phi_3[n] &= x_{11}[n]x_{12}[n]. \end{aligned} \tag{9}$$

Then, the nonlinear data matrix $\mathbf{\Phi}$ is obtained as follows:

$$\mathbf{\Phi}[n] = \begin{bmatrix} \phi_1[n-M+1] & \phi_2[n-M+1] & \cdots & \phi_3[n-M+1] \\ \phi_1[n-M+2] & \phi_2[n-M+2] & \cdots & \phi_3[n-M+2] \\ \vdots & \vdots & \ddots & \vdots \\ \phi_1[n] & \phi_2[n] & \cdots & \phi_3[n] \end{bmatrix} \tag{10}$$

and the parameter estimation is simply carried out as

$$\widehat{\boldsymbol{\gamma}} = \left(\mathbf{\Phi}^H[n]\mathbf{\Phi}[n]\right)^{-1}\mathbf{\Phi}^H[n]\mathbf{x}_{BB}[n] \tag{11}$$

where $\hat{\boldsymbol{\gamma}} = \begin{bmatrix}\widehat{\gamma}_1 & \widehat{\gamma}_2 & \widehat{\gamma}_3\end{bmatrix}^T$ contains the estimates for each coefficient, $(\cdot)^H$ denotes the Hermitian transpose, while $(\cdot)^T$ denotes the regular transpose.

Having estimated the coefficients using M observation samples, the actual cancellation performance can then be evaluated by regenerating the interference and then subtracting it from the received signal. In an online operation of the receiver, the received signal with interference cancellation is given by

$$y_c[n] = x_{BB}[n] - \mathbf{\Phi}[n]\hat{\boldsymbol{\gamma}}. \tag{12}$$

Next, in the following section, we analyze the accuracy and performance of our proposed digital cancellation methods with practical RF measurements. The measurement setup and results are presented and discussed.

III. RF Measurement Setup and Results

This section covers the description of the RF measurement setup utilized to evaluate the performance of the proposed digital cancellation method alongside the actual measured cancellation results.

A. Measurement Setup

The measurement setup is presented in Fig. 2. The measurements are conducted in an anechoic chamber with a true base-station hardware, where rusty metal and other similar test PHM distortion sources are also deployed at a distance of at least 1m from the base-station. The base-station hardware is controlled by a PC located outside the chamber to feed the input signals and to collect data from the base-station for post-processing. Furthermore, other relevant features of the measurement system and the digital canceller itself are show in Table II.

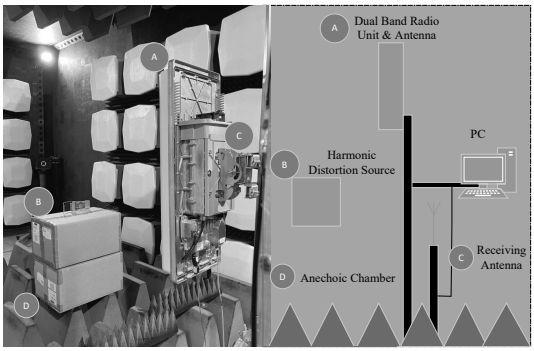

Fig. 2. Overall RF measurement setup used for evaluating the performance of the proposed digital cancellation method. Different parts of the system are also highlighted.

TABLE II
RF MEASUREMENT SETUP CONFIGURATION AND CONSIDERED PHM DISTORTION CANCELLER PARAMETERS

Parameter	Value
Bandwidth of the CCs	5 MHz
Total transmit power	31 dBm
Center frequencies of CCs	1819.0/1866.5 MHz
RX center frequency	3685.0 MHz
RX capture bandwidth	122.8 MHz
Cancellation bandwidth	20 MHz
Signals per carrier frequencies	2
Polynomial order (P)	4
Number of samples used for estimation (N)	90 000

The base-station hardware comprises of a dual TX/RX system with directive antennas as show in Fig. 2 labeled as (A). The TX chains transmit two 5G NR standard-compliant CP-OFDM signals as CCs, with a bandwidth of 5 MHz and the transmit power being set to +31 dBm plus the antenna gain. In both the TX chains, each of the individual carriers lies at 5G NR band n3, at TX frequencies of 1819.0 MHz and 1866.5 MHz. The RX center frequency is set to 3685.0 MHz in the RX chain which correspond to the fundamental frequency of the 2nd passive harmonic distortion of the form $\omega_1 + \omega_2$. The data for post processing is utilized from the RX chain as indicated in Fig. 1.

The RX capture bandwidth is set to 122.8 MHz and the even-order harmonics at different frequencies are all captured at once which are then processed separately. The following section shows the cancellation results achieved for all the even-order harmonics, i.e., $\omega_1 + \omega_2$, $2\omega_1$, $2\omega_2$.

Furthermore, the proposed digital cancellation method considers polynomial order up to ($P = 4$), with the basis functions being shown in Table I. For the case of $2\omega_1$, there are a

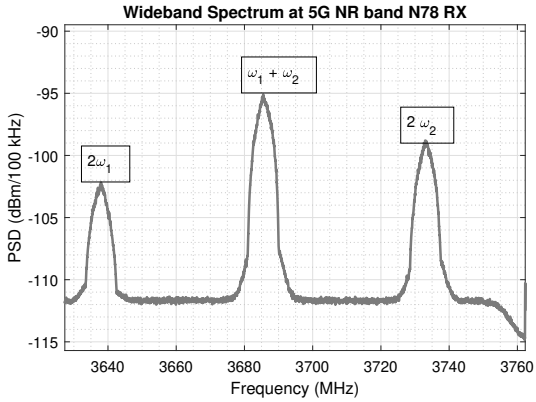

Fig. 3. Wideband spectrum of the observable PHM distortion at the RX band.

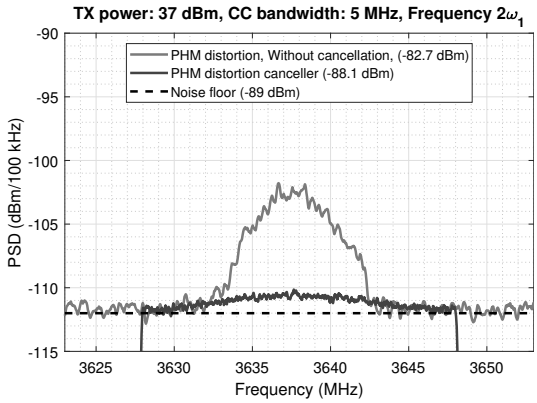

Fig. 4. The spectra of the observed PHM distortion at frequency $2\omega_1$ and the residual signal after cancellation.

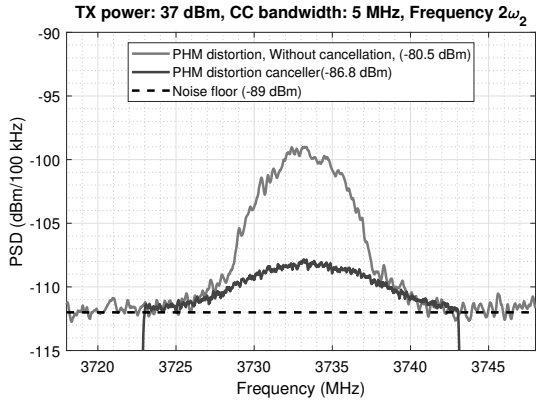

Fig. 5. The spectra of the observed PHM distortion at frequency $2\omega_2$ and the residual signal after cancellation.

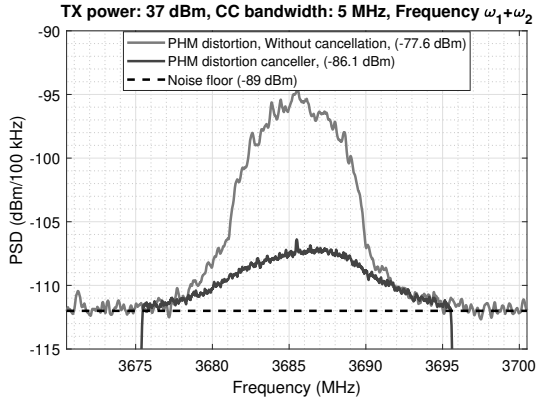

Fig. 6. The spectra of the observed PHM distortion at frequency $\omega_1 + \omega_2$ and the residual signal after cancellation.

total of 27 BFs as a concrete example. Similarly, the BFs for other even-order harmonics such as $\omega_1 + \omega_2$, and $2\omega_2$ are also illustrated in Table I.

B. Measurement Results

In this section the performance of the proposed digital cancellation method is evaluated. The observable PHM distortion products appearing at the 5G NR band n78 RX are illustrated in Fig. 3.

Next, the actual cancellation results achieved for all these fundamental harmonic distortion products are shown. For example, Fig. 4 shows the cancellation results for the frequency $2\omega_1$ where the PHM distortion power is about $6.3\,$dB above the thermal noise floor, and the cancellation achieved with the proposed cancellation method is about $5.4\,$dB using a polynomial order of $P = 4$. Hence, the residual distortion is only some $0.9\,$dB above the noise floor.

Similarly, the cancellation results for the frequency $2\omega_2$ with polynomial order of $P = 4$ are shown in Fig. 5, where the original PHM distortion power is about $8.5\,$dB, relative to the noise floor, and the achieved cancellation gain is $6.2\,$dB.

Finally, Fig. 6 shows the cancellation results achieved for frequency $\omega_1 + \omega_2$ with a polynomial order of $P = 4$. The original PHM distortion power observed here is about $11.2\,$dB, when again referenced to the thermal noise floor, while the achieved cancellation gain is $8.6\,$dB. These results demonstrate that the proposed digital cancellation method can cancel the fundamental PHM distortion products quite efficiently, thus enabling the utilization of the RF Spectrum efficiently in LTE-advanced and the 5G NR radio networks with collocated radio transceivers.

IV. Conclusion

In this paper, we proposed a novel digital cancellation solution for dealing with air-induced passive harmonic distortion in

FDD transceivers and other collocation scenarios with simultaneously active transmitters and receivers. The air-induced PHM distortion stems from the built environment close to the transceiver antenna system, that can be a serious problem in simultaneous transmit-receive systems with certain band and carrier combinations and coexisting scenarios. Behavioral models of the air-induced PHM distortion were derived and a corresponding linear-in-parameters digital canceller scheme was proposed. The performance of the proposed digital canceller was tested with actual RF measurements in an example case with coexistence of 5G NR bands n3 and n78. The air-induced PHM distortion was successfully cancelled, by up to around 9 dB in the measurements. Our future work will consider extending the cancellation solutions such that both passive harmonic and intermodulation distortion products can be efficiently modelled and suppressed.

ACKNOWLEDGMENT

This work was funded in part by the Academy of Finland (under the projects #319994, #338224, and #332361), and in part by Nokia Corporation.

REFERENCES

[1] 3GPP, "Base station (bs) radio transmission and reception," *Technical Specification (TS)*, vol. 36, pp. v8–2, 2008.

[2] A. Kiayani, V. Lehtinen, L. Anttila, T. Lahteensuo, and M. Valkama, "Linearity challenges of lte-advanced mobile transmitters: Requirements and potential solutions," *IEEE Communications Magazine*, vol. 55, no. 6, pp. 170–179, 2017.

[3] S. A. Bassam, W. Chen, M. Helaoui, and F. M. Ghannouchi, "Transmitter architecture for ca: Carrier aggregation in lte-advanced systems," *IEEE Microwave Magazine*, vol. 14, no. 5, pp. 78–86, 2013.

[4] C. S. Park, L. Sundström, A. Wallén, and A. Khayrallah, "Carrier aggregation for lte-advanced: design challenges of terminals," *IEEE Communications Magazine*, vol. 51, no. 12, pp. 76–84, 2013.

[5] V. Lampu, L. Anttila, M. Turunen, M. Fleischer, J. Hellmann, and M. Valkama, "Air-Induced PIM Cancellation in FDD MIMO Transceivers," *IEEE Microwave and Wireless Components Letters*, vol. 32, no. 6, pp. 780–783, 2022.

[6] "LTE; evolved universal terrestrial radio access (E-UTRA); user equipment (UE) radio transmission and reception (3GPP TS 36.101, version 14.1.0, release 14)," ETSI, Sophia Antipolis Cedex, France, Sep. 2016.

[7] "LTE-advanced dual uplink inter-band carrier aggregation (CA) (3GPP TS 36.860, version 13.0.0, release 13)," ETSI, Sophia Antipolis Cedex, France, Jan. 2016.

[8] M. Z. Waheed, D. Korpi, A. Kiayani, L. Anttila, and M. Valkama, "Digital self-interference cancellation in inter-band carrier aggregation transceivers: Algorithm and digital implementation perspectives," in *2017 IEEE International Workshop on Signal Processing Systems (SiPS)*, 2017, pp. 1–5.

[9] M. Zeeshan Waheed, P. P. Campo, D. Korpi, A. Kiayani, L. Anttila, and M. Valkama, "Digital cancellation of passive intermodulation in fdd transceivers," *arXiv e-prints*, pp. arXiv–1812, 2018.

[10] H.-T. Dabag, H. Gheidi, S. Farsi, P. S. Gudem, and P. M. Asbeck, "All-digital cancellation technique to mitigate receiver desensitization in uplink carrier aggregation in cellular handsets," *IEEE Transactions on Microwave Theory and Techniques*, vol. 61, no. 12, pp. 4754–4765, 2013.

[11] M. Z. Waheed, D. Korpi, L. Anttila, A. Kiayani, M. Kosunen, K. Stadius, P. P. Campo, M. Turunen, M. Allén, J. Ryynänen, and M. Valkama, "Passive intermodulation in simultaneous transmit–receive systems: Modeling and digital cancellation methods," *IEEE Transactions on Microwave Theory and Techniques*, vol. 68, no. 9, pp. 3633–3652, 2020.

[12] M. Z. Waheed, P. P. Campo, D. Korpi, A. Kiayani, L. Anttila, and M. Valkama, "Digital cancellation of passive intermodulation in fdd transceivers," in *2018 52nd Asilomar Conference on Signals, Systems, and Computers*, 2018, pp. 1375–1381.